

Ministry of Education and Science of the Russian Federation  
Saint Petersburg National Research University of Information  
Technologies, Mechanics, and Optics

***NANOSYSTEMS:***  
***PHYSICS, CHEMISTRY, MATHEMATICS***

2015, volume 6(4)

**Наносистемы: физика, химия, математика**

2015, том 6, № 4



# NANOSYSTEMS:

**PHYSICS, CHEMISTRY, MATHEMATICS**

## ADVISORY BOARD MEMBERS

**Chairman:** V.N. Vasiliev (*St. Petersburg, Russia*),  
V.M. Ievlev (*Voronezh*), P.S. Kop'ev (*St. Petersburg, Russia*),  
V.N. Parmon (*Novosibirsk*), A.I. Rusanov (*St. Petersburg, Russia*).

## EDITORIAL BOARD

**Editor-in-Chief:** N.F. Morozov (*St. Petersburg, Russia*)  
**Deputy Editor-in-Chief:** I.Yu. Popov (*St. Petersburg, Russia*)

### Section Co-Editors:

Physics – V.M. Uzdin (*St. Petersburg, Russia*),  
Chemistry, material science – V.V. Gusarov (*St. Petersburg, Russia*),  
Mathematics – I.Yu. Popov (*St. Petersburg, Russia*).

### Editorial Board Members:

V.M. Adamyan (*Odessa, Ukraine*); O.V. Al'myasheva (*St. Petersburg, Russia*);  
A.P. Alodjants (*Vladimir, Russia*); S. Bechta (*Stockholm, Sweden*); J. Behrndt (*Graz, Austria*);  
M.B. Belonenko (*Volgograd, Russia*); V.G. Bepalov (*St. Petersburg, Russia*); J. Brasche  
(*Clausthal, Germany*); A. Chatterjee (*Hyderabad, India*); S.A. Chivilikhin (*St. Petersburg,  
Russia*); A.V. Chizhov (*Dubna, Russia*); A.N. Enyashin (*Ekaterinburg, Russia*), P.P. Fedorov  
(*Moscow, Russia*); E.A. Gudilin (*Moscow, Russia*); V.K. Ivanov (*Moscow, Russia*),  
H. Jónsson (*Reykjavik, Iceland*); A.A. Kiselev (*Madison, USA*); Yu.S. Kivshar (*Canberra,  
Australia*); S.A. Kozlov (*St. Petersburg, Russia*); P.A. Kurasov (*Stockholm, Sweden*);  
A.V. Lukashin (*Moscow, Russia*); V.A. Margulis (*Saransk, Russia*); I.V. Melikhov (*Moscow,  
Russia*); G.P. Miroshnichenko (*St. Petersburg, Russia*); I.Ya. Mittova (*Voronezh, Russia*);  
H. Neidhardt (*Berlin, Germany*); K. Pankrashkin (*Orsay, France*); B.S. Pavlov (*Auckland,  
New Zealand*); A.V. Ragulya (*Kiev, Ukraine*); V. Rajendran (*Tamil Nadu, India*);  
A.A. Rempel (*Ekaterinburg, Russia*); V.Ya. Rudyak (*Novosibirsk, Russia*); D Shoikhet  
(*Karmiel, Israel*); P Stovicek (*Prague, Czech Republic*); V.M. Talanov (*Novocherkassk,  
Russia*); A.Ya. Vul' (*St. Petersburg, Russia*); V.A. Zagrebnov (*Marseille, France*).

### Editors:

I.V. Blinova; A.I. Popov; A.I. Trifanov; E.S. Trifanova (*St. Petersburg, Russia*),  
R. Simoneaux (*Philadelphia, Pennsylvania, USA*).

**Address:** University ITMO, Kronverkskiy pr., 49, St. Petersburg 197101, Russia.

**Phone:** +7(812)232-67-65, **Journal site:** <http://nanojournal.ifmo.ru/>,

**E-mail:** [popov1955@gmail.com](mailto:popov1955@gmail.com)

## AIM AND SCOPE

The scope of the journal includes all areas of nano-sciences. Papers devoted to basic problems of physics, chemistry, material science and mathematics inspired by nanosystems investigations are welcomed. Both theoretical and experimental works concerning the properties and behavior of nanosystems, problems of its creation and application, mathematical methods of nanosystem studies are considered.

The journal publishes scientific reviews (up to 30 journal pages), research papers (up to 15 pages) and letters (up to 5 pages). All manuscripts are peer-reviewed. Authors are informed about the referee opinion and the Editorial decision.

# Content

<b>From the Editorial Board</b>	<b>459</b>
L.Ts. Adzhemyan, T.L. Kim, M.V. Kompaniets, V.K. Sazonov <b>Renormalization group in the infinite-dimensional turbulence: determination of the RG-functions without renormalization constants</b>	<b>461</b>
E.S. Kraynyukov, A.A. Karetnikov, A.P. Kovshik, E.I. Ryumtsev, E.V. Aksyonova, V.P. Romanov <b>The study of the local director orientation in chiral liquid crystals</b>	<b>470</b>
A.E. Kuchma, A.K. Shchekin <b>Evolution of size and composition of a multicomponent gas bubble in liquid solution</b>	<b>479</b>
D.A. Murich, V.P. Romanov, S.V. Ul'yanov <b>The interaction of polarization charges in freely suspended smectic-C* films</b>	<b>489</b>
E.A. Polyakov, P.N. Vorontsov-Velyaminov <b>Exact classical stochastic representations of the many-body quantum dynamics</b>	<b>501</b>
I.A. Silanteva, P.N. Vorontsov-Velyaminov <b>Entropic sampling of star-shaped polymers with different number of arms: temperature dependencies of structural properties</b>	<b>513</b>
A.Yu. Val'kov, V.L. Kuzmin, V.P. Romanov, M.A. Nikitina, V. Meglinskii <b>Boundary effect on multiple scattering of elastic waves in a half-space</b>	<b>524</b>

## Regular paper

### MATHEMATICS

M.M. Lipovich, I.S. Lobanov

**On construction of evolutionary operator for rectangular linear optical multiport** 537

### PHYSICS

E.D. Eidelman

**Estimation of the contact area of solids by electrothermal analogy** 547

I.V. Melihov, O.V. Alekseev, V.N. Rudin,  
E.D. Kozlovsky, A.V. Noskov

**The kinetics of formation and morphological memory of polymeric nanostructures** 551

A.G. Petrashen, N.V. Sytenko

**Stimulated emission of an atomic system under coherent excitation** 562

### CHEMISTRY AND MATERIAL SCIENCE

A.N. Sinitsin, V.V. Zuev

**Dielectric relaxation of fulleroid materials filled PA6 composites and the study of its mechanical performance** 570

G.S. Zakharova, Y. Liu, I.S. Popov, A.N. Enyashin

**Structural hierarchy of  $\text{NH}_4\text{V}_3\text{O}_7$  particles prepared under hydrothermal conditions** 583

D.A. Zhrebtssov, V.Sh. Mirasov, D.G. Kleschev, E.V. Polyakov

**Nanodisperse oxide compounds of iron formed in the  $\text{FeSO}_4 - \text{KOH} - \text{H}_2\text{O} - \text{H}_2\text{O}_2$  system ( $4.0 \leq \text{pH} \leq 13.0$ )** 593

## From the Editorial Board

In this issue, we present papers of colleagues and students of the late professor Vadim Petrovich Romanov, professor of the Statistical Physics Department, Faculty of Physics, St Petersburg State University.

First of all, it should be said that V.P. was an outstanding scientist and teacher. He used to tell us that once when he started working at a physics department, Faculty of Physics, being a fresh graduate, the department chief told him: “Teaching could be performed in two ways – first way is when the scientific activity hinders teaching and the second way is when teaching hinders your scientific work. At our department the second way is preferred and accepted”. It should be pointed out that V.P. himself never preferred either of these extremes, always managing to successfully combine both - research and education.



Science has much in common with art and sport – in both there is a place for brilliant guess and unexpected discovery; for prolonged learning, training, repetition and hard every-day work; for struggle to achieve the best results in certain area. In all these endeavors, people communicate with colleagues from various places within the country and all over the world. The role of V.P. could be best of all described by words concerning to sport, i.e. he was a real “player-manager”; or by words from the theatrical world – he was a director-producer who simultaneously played several principal roles in the piece.

However, V.P. was primarily a physicist. He possessed a rare feeling for physics and could qualitatively foresee possible interesting effects based on a semi-intuitive and skillfully simplified perception. Being a theoretician, he collaborated frequently with the experimentalists and often suggested ideas for new experiments. He did it in such an interesting and eloquent way that it later

gave rise to a whole series of scientific works, jointly written with experimentalists. This was the case when he worked on the statistical physics of liquid crystals, on the theory of electromagnetic and acoustic wave propagation and scattering in strongly anisotropic media. The results of these studies attained wide scientific recognition.

His regular friendliness and patience were also characteristic features of Vadim Petrovich when working with students and colleagues. He never hesitated to put, as he called them himself, “foolish questions”, he was always ready to spend his time to aid his students in overcoming scientific difficulties, readily sharing with his colleagues his reach research and teaching experience. It was always clear that when V.P. entered a room, talks, conversations and discussions began around. He truly facilitated the joyful discussions and interactions of people with different ideas.

V.P. very much disliked all sorts of paper-bureaucratic “assistance” for the scientific-educational process, which, over the last few years, became catastrophically strong, clearly harming both education and science. The scientist, as a researcher, and as a teacher, has to neglect his basic work with students and acolytes in order to create all manner of “plans”, “reports”, “projects”, “programs” and a lot of other “very important papers”. However, V. P. was an optimist, and hence, no negative tendencies could be considered by him in any other way than as temporal obstacles which should be overcome with minimal damage.

V.P. was a harmonic person, a loving family man, and research was his passion. If the scientific problem occupied his mind, nothing could prevent him from thinking on it at any time and any place. It would be right to say that science and teaching, together with his family, were for him the main guiding points of life. For us, his students and colleagues, V.P. is and will further remain a benchmark teacher and scholar.

# Renormalization group in the infinite-dimensional turbulence: determination of the RG-functions without renormalization constants

L. Ts. Adzhemyan<sup>1</sup>, T. L. Kim<sup>1</sup>, M. V. Kompaniets<sup>1</sup>, V. K. Sazonov<sup>1,2</sup>

<sup>1</sup> Department of Theoretical Physics, St. Petersburg State University, Uljanovskaja 1, St. Petersburg, Petrodvorez, 198504 Russia

<sup>2</sup> Institute of Physics, Department of Theoretical Physics, University of Graz, Universitätsplatz 5, A-8010 Graz, Austria

l.adzhemyan@spbu.ru, mkompan@gmail.com, vasily.sazonov@uni-graz.at

PACS 05.10.Cc, 05.10.Gg, 05.45.Jn

DOI 10.17586/2220-8054-2015-6-4-461-469

We calculate renormalization-group functions in the developed turbulence model for infinite dimensional space  $d \rightarrow \infty$  using an operating method without renormalization constants. The renormalization fixed point and index  $\omega$ , obtained within the considered three loop approximation, are in agreement with previous calculations. The results demonstrate the efficiency of the method and the possibility of its complete automation, which is crucially important in higher order perturbation theory computations.

**Keywords:** turbulence, renormalization group (RG).

*Received: 20 June 2015*

## 1. Introduction

The explanation for the anomalous scaling in fully developed turbulence, which describes the deviations from the Kolmogorov phenomenological theory, is an actual problem of the modern statistical mechanics. Currently, the anomalous exponents have been calculated and anomalous scaling was obtained only in the simplified turbulence model – the rapid-change model of the passive scalar advection. It was shown in [1] that in spaces with large dimensions  $d$ , this model is reduced to the Kolmogorov theory and that the exponents of the anomalous scaling tends to zero, as  $d \rightarrow \infty$ . These exponents were calculated in [1] up to the first order in  $1/d$ .

There are indications that in turbulence theory, based on the Navier-Stokes equations, the limiting dimension  $d \rightarrow \infty$  plays a role of the critical dimension of the space, for which the Kolmogorov theory becomes valid [2]. For the analysis of this asymptotic theory the renormalization group method and  $\varepsilon$ -expansion were applied in [3]. The studies in [3] revealed significant simplifications in the limit  $d \rightarrow \infty$ . This allowed the authors to perform the three loop analytical calculations of the RG-fixed point and the index  $\omega$  and then to guess the formula for these quantities analogous to the corresponding one in the Heisenberg model for the developed turbulence [4]. It would be highly interesting to verify the correctness of this formula, comparing its predictions with those of fourth order perturbation theory. However, such verification is not a trivial task, because of the number of diagrams dramatically increases with the increasing order of the perturbation theory (there are 1692 four-loop Feynman diagrams). Thus, the automation of the computational process is required.

In the current work, we apply the method of automatic computations for the renormalization group functions developed in [5], [6] in application to three-loop calculations. The method described in [5], [6] allows one to represent the renormalization group functions without using the renormalization constants in terms of the non-singular in  $\varepsilon$  integrals. All necessary terms of the  $\varepsilon$ -expansion can be found by expanding the integrands of these integrals into a Taylor series.

The automatic three-loop calculations confirm the  $\omega$  index value obtained in [3]. The value for the charge in the fixed point differs from the corresponding one in [3], because of the utilization of different renormalization schemes.

## 2. The model

The microscopic model of the fully developed, homogeneous, isotropic turbulence of the incompressible viscous fluid or gas is usually described by the stochastic Navier-Stokes equation with a random driving force:

$$\partial_t v_i = -\partial_i P - (v_j \partial_j) v_i + \nu_0 \partial^2 v_i + f_i, \quad (1)$$

where  $v_i$  is the velocity field,  $P$  and  $\nu_0$  are the pressure and the kinematic viscosity, respectively,  $f_i$  is the random force per unit mass. Equation (1) is complemented by the incompressibility condition  $\partial_i v_i = 0$ , which leads to the transverseness of the velocity field and force. We assume for  $f$  a Gaussian distribution with zero mean and correlator:

$$\langle f_i(t_1, \mathbf{x}_1) f_j(t_2, \mathbf{x}_2) \rangle \equiv D_{ij}^f(t_1 - t_2, \mathbf{x}_1 - \mathbf{x}_2), \quad (2)$$

$$D_{ij}^f(t, \mathbf{k}) = \delta(t) P_{ij}(\mathbf{k}) d_f(k), \quad (3)$$

where  $P_{ij}(\mathbf{k}) \equiv \delta_{ij} - k_i k_j / k^2$  is the transverse projector. In the inertial interval of the wavenumbers  $m \ll k \ll k_{diss}$  ( $m^{-1} = L$  is the external turbulence scale,  $k_{diss}$  is the dissipative scale) one can use the power-law model

$$d_f(k) = D_0 k^{4-d-2\varepsilon} \theta(k - m), \quad (4)$$

where  $\varepsilon$  is analogous to the  $4 - d$  parameter in the Wilson theory of the phase transitions. The physical value of  $\varepsilon$  is equal to 2 and corresponds to an ideal pumping of the energy into the system by infinitely-sized vortices.

According to the fundamental theorem [7], the stochastic equation (1) is equivalent to quantum field theory with a double set of transverse fields determined by the action:

$$S_0 = v' D^f v' / 2 + v' (-\partial_t v_i - (v \partial) v + \nu_0 \partial^2 v). \quad (5)$$

Here, all the necessary integrations and summations over indices are meant. The contribution of the pressure in (5) is omitted due to the transverseness of the auxiliary field  $v'$ .

The diagrams of the perturbation theory determined by the action (5) contain ultraviolet (UV) divergences, when  $\varepsilon \rightarrow +0$ . The invariance of the action under the Galilean transformations results in the only singly divergent 1-irreducible correlation function,

$\Gamma_{ij}^{(0)} = \langle v_i v_j' \rangle_{1-ir}$  (1-irreducible response function). To cancel divergences in this function, one needs the only one counterterm of the type  $v' \partial^2 v$ . The renormalized action is given by:

$$S = v' D^f v' / 2 + v' (-\partial_t v_i - (v \partial) v + \nu Z_\nu \partial^2 v), \quad (6)$$

which is obtained from (5) by the multiplicative renormalization of the parameters:

$$D_0 = g_0 \nu_0^3 = g \mu^{2\varepsilon} \nu^3, \quad \nu_0 = \nu Z_\nu, \quad g_0 = g \mu^{2\varepsilon} Z_g, \quad Z_g = Z_\nu^{-3}, \quad (7)$$

where  $\mu$  is the renormalization mass,  $g$  is the dimensionless renormalized charge and the renormalization of the fields is not required.

In the following, we use the renormalization scheme, analogous to the renormalization on the zero frequencies and moments, complemented by the extra condition  $\mu = m$ . Let  $\Gamma_{ij}(\mathbf{k}, \omega)$  be the 1-irreducible response function calculated in accordance with action (6) with the renormalization constant  $Z_\nu = 1$ . This function is proportional to the transverse projector:

$$\Gamma_{ij}(\mathbf{k}, \omega) = P_{ij}(\mathbf{k})\Gamma(k, \omega), \quad \Gamma(k, \omega) = \frac{\Gamma_{ii}(\mathbf{k}, \omega)}{d-1}. \quad (8)$$

Let us now define a normalized function equal to unity in the zero (loop-less) approximation:

$$\bar{\Gamma}(k, \omega) = \frac{\Gamma(k, \omega)}{-\nu k^2}. \quad (9)$$

Then, for its renormalized version, we require the following normalization conditions:

$$\bar{\Gamma}^R \Big|_{k=0, \omega=0, \mu=m} = 1, \quad (10)$$

namely, all diagrammatic contributions to the renormalized function  $\bar{\Gamma}^R$  must be canceled out by the counterterms in the normalization point  $k = 0, \omega = 0, \mu = m$ . This condition defines the subtraction scheme and the form of the renormalization constant  $Z_\nu$ .

The Feynman diagrammatic technique, corresponding to the model (6), (3), (4), contains the following propagators, given in the  $(\mathbf{k}, \mathbf{t})$ -representation by:

$$\langle v_i(t_1)v_j(t_2) \rangle = \frac{d_f(k)}{2\nu k^2} \exp[-\nu k^2|t_1 - t_2|] P_{ij}(\mathbf{k}) = \text{---} \quad (11)$$

$$\langle v_i(t_1)v'_j(t_2) \rangle = \theta(t_1 - t_2) \exp[-\nu k^2(t_1 - t_2)] P_{ij}(\mathbf{k}) = \text{---}+ \quad (12)$$

The interaction in (6) is represented by the triple vertex  $-v'(v\partial)v = v'_j V_{jst} v_s v_t$  with the vertex factor:

$$V_{jst} = ik_s \delta_{jl} = \text{---}+ \begin{array}{c} \bullet \\ \diagup \\ \diagdown \end{array} \quad (13)$$

where  $k_s$  is the momentum argument of the field  $v'$ . The crossed endpoint in (13) corresponds to the field  $v'$ , the endpoint marked by the bold dot corresponds to the field  $v_s$  contracted with  $ik_s$  and the plain line stands for the field  $v_t$ .

We represent the perturbation series for the function  $\bar{\Gamma}$  as:

$$\bar{\Gamma}(k, \omega, m, \mu) = \sum_{n \geq 1} u^n \mu^{n\varepsilon} \sum_i \chi_n^{(i)}(k, \omega, m), \quad u \equiv \frac{S_d g}{(2\pi)^d}, \quad (14)$$

where the  $i$ -summation runs over all  $n$ -loop diagrams of the function  $\bar{\Gamma}$ . For convenience, we introduce a normalized charge  $u$ , in which  $S_d$  is the surface area of the unit sphere in the  $d$ -dimensional space.

### 3. Renormalization group equations, RG-functions expressed in terms of the renormalized Green functions

In our renormalization scheme the renormalization constants  $Z_\nu$  and  $Z_g$  (similar to the MS scheme) depend only on the space dimension  $d$  and parameter  $\varepsilon$  and do not depend on the ratio  $m/\mu$ . The equations of the renormalization group are obtained from the independence

of the non-renormalized Green functions on the parameter  $\mu$  at fixed  $\nu_0$  and  $g_0$ . The RG-equations look exactly the same as in the MS scheme [8]. In particular, the equation for the 1-irreducible function  $\Gamma^R$  is given by:

$$(\mu\partial_\mu + \beta(g)\partial_g - \gamma_\nu(g)\nu\partial_\nu)\Gamma^R = 0, \quad (15)$$

where

$$\gamma_i(g) = \frac{-2\varepsilon g\partial_g \ln Z_i}{1 + g\partial_g \ln Z_g}, \quad \beta(g) = -g(2\varepsilon + \gamma_g) = -g(2\varepsilon - 3\gamma_\nu). \quad (16)$$

The latter equation in (16) is a consequence of the relation between the renormalization constants  $Z_g$  and  $Z_\nu$  in (7). The equations (16) define the  $\beta$  and  $\gamma_\nu$  RG-functions in terms of the renormalization constants. These functions are finite and do not contain poles in  $\varepsilon$ , because of the renormalizability of the theory. However, the required preliminary calculation of the singular in  $\varepsilon$  renormalization constants is complicated, especially for the numerical evaluation of  $\beta$  and  $\gamma_\nu$ . Using equation (15), we express these RG-functions in term of the renormalized Green function  $\Gamma^R$ .

First of all, we derive the RG-equation for the normalized function  $\bar{\Gamma}^R$ . Employing (9) and (10) we find:

$$(\mu\partial_\mu + \beta(g)\partial_g - \gamma_\nu(g)\nu\partial_\nu)\bar{\Gamma}^R = \gamma_\nu\bar{\Gamma}^R. \quad (17)$$

Considering this equation in the normalization point  $k = 0$ ,  $\omega = 0$ ,  $\mu = m$  and taking into account that:

$$\bar{\Gamma}^R|_{k=0,\omega=0}(m, \mu, \nu) = \bar{\Gamma}^R|_{k=0,\omega=0}(m/\mu), \quad \partial_g\bar{\Gamma}^R|_{k=0,\omega=0,\mu=m} = 0, \quad (18)$$

we obtain:

$$\gamma_\nu(g) = -(m\partial_m\bar{\Gamma}^R)|_{k=0,\omega=0,\mu=m}. \quad (19)$$

In (19), the RG-function  $\gamma_\nu$  is written in terms of the renormalized function  $\bar{\Gamma}^R$ . Usually, computation of the renormalized functions involves calculation of the divergent in  $\varepsilon$  renormalization constants. For calculations involving finite objects, we need to take into account the counterterms by the  $R$ -operation, acting on the diagrams of the basic action, where  $Z_\nu = 1$ ,

$$\Gamma^R = R\Gamma = (1 - K)R'\Gamma. \quad (20)$$

Here, the  $R'$ -operation eliminates divergences in the subgraphs of diagrams and the operation  $(1 - K)$  removes the remaining superficial divergence. The  $R'$ -operation can be expressed as [9]:

$$R'\Gamma = \prod_j (1 - K)_j\Gamma, \quad (21)$$

where, for each diagram from  $\Gamma$ , the product runs over all its divergent subgraphs. The renormalization operation (20) eliminates the divergences in the function  $\Gamma^R$  as a whole and separately in each diagram.

The formal UV-divergence index of the 1-irreducible function  $\langle vv' \rangle_{1-ir}$  equals 2. This leads to the possible counterterms of the  $k^2$  and  $i\omega$  types. However, as is seen from (13), the external leg  $v'$  of this function is always multiplied by the external moment  $k$ , therefore, only the divergence of the  $k^2$ -type remains. In our renormalization scheme, this corresponds to the following subtraction operations for the whole function  $\bar{\Gamma}$  and for the 1-irreducible subgraphs of diagrams  $\chi_n^{(i)}$  from (14), respectively:

$$\begin{aligned} (1 - K)\bar{\Gamma}(k, \omega, m, \mu) &= \bar{\Gamma}(k, \omega, m, \mu) - \bar{\Gamma}|_{k=0,\omega=0,\mu=m}, \\ (1 - K)\chi_j(k_j^2, \omega_j, m) &= \chi_j(k_j^2, \omega_j, m) - \chi_j|_{k_j=0,\omega=0}, \end{aligned} \quad (22)$$

where  $k_j$  and  $\omega_j$  are the moment and frequency incoming to the subgraph  $\chi_j$ . The subtraction of the divergences in the subgraphs leads to the finite integrals corresponding to the renormalized Feynman diagrams.

Note that the dimensionless counterterm  $\bar{\Gamma} |_{k=0,\omega=0,\mu=m}$  does not depend on  $m$ , then, taking into account (19), we obtain:

$$\gamma_\nu(g) = -(m\partial_m R\bar{\Gamma}) |_{k=0,\omega=0,\mu=m} = -(m\partial_m R'\bar{\Gamma}) |_{k=0,\omega=0,\mu=m} . \tag{23}$$

Substituting expansion (14) in (23), we find

$$\gamma_\nu(g) = \sum_{n \geq 1} u^n (\gamma_\nu)_n , \quad (\gamma_\nu)_n = -m^{-2n\varepsilon} \sum_i (m\partial_m R' \chi_n^{(i)}) |_{k=0,\omega=0,\mu=m} . \tag{24}$$

This is the main relation for the calculation of the RG-function  $\gamma_\nu$ .

#### 4. Large $d$ limit

Let us consider the diagrams in the momentum representation in the spherical coordinate system. Then, the dimension of the space  $d$  enters into the integration measure  $\int_0^\infty dk k^{d-1} \int_0^\pi d\theta (\sin \theta)^{d-2} \dots$  and into the lines  $vv$  of diagrams as  $k^{2-d-2\varepsilon}$ . The number of  $vv$ -lines in diagrams of the function  $\Gamma$  coincides with the number of loops, consequently the pure integration momenta can be always associated with  $vv$ -lines. Then, the factor  $\theta(k-m)k^{2-d-2\varepsilon}$  from (4) changes  $\int_0^\infty dk k^{d-1}$  to  $\int_m^\infty dk k^{1-2\varepsilon}$  and the dependence on  $d$  in the radial part disappears. When  $d \rightarrow \infty$ , the angular weight  $(\sin \theta)^{d-2}$  has a sharp maximum at  $\theta = \pi/2$ . Since  $\cos(\pi/2) = 0$ , the inner products of the different internal integration moments vanish. Then, in the leading approximation at  $d \rightarrow \infty$  one may consider the internal integration moments to be orthogonal to each other and to the external moment  $p$ . In this approximation, the integrands do not depend on angles and the angular integrations give a factor  $S_d$ , included in the definition of the charge  $u$  (14). The latter charge is finite in the renormalization group fixed point.

Therefore, the main contribution to the Green functions at  $d \rightarrow \infty$  is given by the diagrams without the inner products, which drastically decreases the number of diagrams. In the one loop approximation from four diagrams in Fig. 1, only the first one gives the non-zero contribution:

$$\chi_1^{(1)} |_{k=0,\omega=0} = \int_m^\infty dk \frac{k^{1-2\varepsilon}}{4k^2} . \tag{25}$$

Then, from equation (24), we find the one-loop expression for the anomalous dimension  $\gamma_\nu$ :

$$(\gamma_\nu)_1 = -m^{2\varepsilon} m\partial_m \chi_1^{(1)} |_{k=0,\omega=0} = \frac{1}{4} . \tag{26}$$

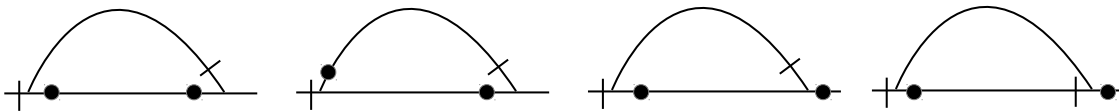


FIG. 1. One-loop diagrams.

In the two-loop approximation in the leading order for large  $d$ , only 6 of the 120 diagrams contribute. Let us consider the diagram in Fig. 2, as an example. Its integration over time gives:

$$\chi_2^{(1)} |_{k=0,\omega=0} = \frac{-1}{32} \int_m^\infty dk k^{1-2\varepsilon} \int_m^\infty dq q^{1-2\varepsilon} k^2 \left( \frac{2}{k^4(k^2 + q^2)} + \frac{1}{k^2(k^2 + q^2)^2} \right) . \tag{27}$$

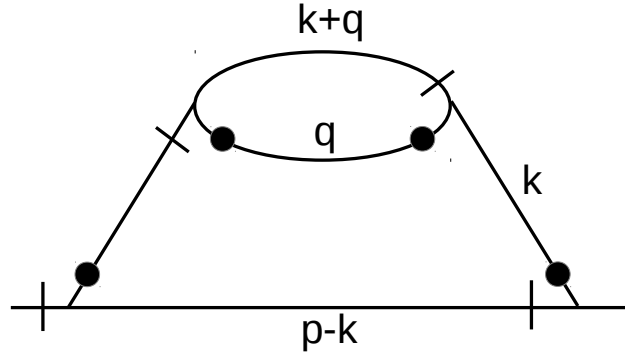


FIG. 2. Example of the two-loop diagram.

This diagram has a divergent subgraph with the circulating (internal) moment  $q$  and external moment  $k$ . The corresponding divergence of the integral over  $q$  at  $\varepsilon = 0$  is logarithmic and localized in the first summand in (27). Acting on this subgraph by the subtraction operation  $(1 - K)$  and using (21), we obtain:

$$R' \chi_2^{(1)} |_{k=0, \omega=0} = \frac{-1}{32} \int_m^\infty dk k^{1-2\varepsilon} \left\{ \int_m^\infty dq q^{1-2\varepsilon} \frac{k^2}{k^2(k^2 + q^2)^2} + \left[ \int_m^\infty dq q^{1-2\varepsilon} \frac{2k^2}{k^4(k^2 + q^2)} - \int_\mu^\infty dq q^{1-2\varepsilon} \frac{2k^2}{k^4 q^2} \right] \right\}. \tag{28}$$

In accordance with (24), the contribution of this diagram to the  $(\gamma_\nu)_2$  is given by:

$$-\left( \mu^{4\varepsilon} m \partial_m R' \chi_2^{(1)} |_{k=0, \omega=0} \right) |_{\mu=m} = \frac{-1}{32} \int_1^\infty dq q^{1-2\varepsilon} \left[ \frac{2}{1 + q^2} - \frac{2}{q^2} + \frac{1}{(1 + q^2)^2} \right] + \frac{-1}{32} \int_1^\infty dk k^{1-2\varepsilon} \left[ \frac{2}{k^2(1 + k^2)} + \frac{1}{(1 + k^2)^2} \right]. \tag{29}$$

Changing the variables, as  $q^2 = x$  and  $k^2 = x$  and joining the integrals, we rewrite (29) as:

$$-\left( \mu^{4\varepsilon} m \partial_m R' \chi_2^{(1)} |_{k=0, \omega=0} \right) |_{\mu=m} = -\frac{1}{32} \int_1^\infty dx \frac{x^{-\varepsilon}}{(x + 1)^2}. \tag{30}$$

The calculation of the remaining two loop diagrams leads to

$$(\gamma_\nu)_2 = \frac{1}{16} \int_1^\infty dx \frac{x^{-\varepsilon}}{(x + 1)^2}. \tag{31}$$

In the MS-scheme the RG-functions do not depend on  $\varepsilon$ . In our scheme, the one loop result (26) is also independent of  $\varepsilon$ . The dependence on  $\varepsilon$  of the two loop result can be found by expanding the integrand of (31) into the Taylor series. The number of the needed terms of this series is determined by the global desired precision. For the third order expansion in  $\varepsilon$ , taking into account that the charge  $u$  in the fixed point  $u_* = O(\varepsilon)$ , it is necessary to know two following terms

$$(\gamma_\nu)_2 = \frac{1}{32} (1 - 2\varepsilon \ln 2) + O(\varepsilon^2). \tag{32}$$

Next, we consider an example of three-loop diagram calculation.

When the integration over time is performed, the diagram in Fig. 3 is given by the integral:

$$\chi_3^{(1)} |_{k=0, \omega=0} = \frac{1}{156} \int_m^\infty dk k^{1-2\varepsilon} \int_m^\infty dq q^{1-2\varepsilon} \int_m^\infty ds s^{1-2\varepsilon} \frac{1}{k^2(k^2 + q^2)(k^2 + q^2 + s^2)}. \tag{33}$$

The diagram in Fig. 3 contains two divergent subgraphs: the one-loop subgraph with internal circulating momentum  $s$  and external moments  $k$  and  $q$  ("subgraph 1") and the two-loop subgraph with internal circulating moments  $q$  and  $s$  and external momentum  $k$  ("subgraph 2"). The action of the  $R'$ -operation is reduced to the consistent application of two subtraction operations  $(1 - K)_2(1 - K)_1$  on the subgraphs in an arbitrary order. Then, from (33), we

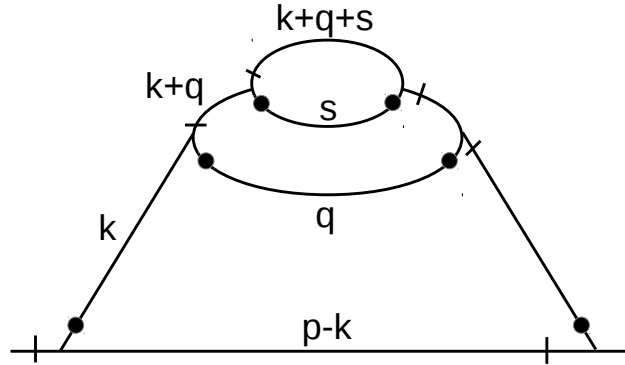


FIG. 3. Example of the three-loop diagram.

obtain:

$$R'\chi_3^{(1)}|_{k=0,\omega=0} = \frac{1}{156} \int_m^\infty dk k^{-1-2\epsilon} \left\{ \int_m^\infty dq \frac{q^{1-2\epsilon}}{(k^2 + q^2)} \left[ \int_m^\infty ds \frac{s^{1-2\epsilon}}{(k^2 + q^2 + s^2)} - \int_\mu^\infty ds \frac{s^{1-2\epsilon}}{s^2} \right] - \int_\mu^\infty dq \frac{q^{1-2\epsilon}}{q^2} \left[ \int_\mu^\infty ds \frac{s^{1-2\epsilon}}{(q^2 + s^2)} - \int_\mu^\infty ds \frac{s^{1-2\epsilon}}{s^2} \right] \right\}. \quad (34)$$

Here, the first two summands are the results of the action of the operation  $(1 - K)_1$  on the one-loop subgraph; the third and fourth summands are the results of the action of  $(1 - K)_2$  on the whole diagram after the action of  $(1 - K)_1$ . Differentiating (34) with respect to  $m$ , one can easily see that  $-\left(\mu^{6\epsilon} m \partial_m R'\chi_3^{(1)}|_{k=0,\omega=0}\right)|_{\mu=m} = 0$ , i.e. this diagram does not contribute to  $(\gamma_\nu)_3$ .

The total amount of the three-loop diagrams is 4080 and only 83 of those survive in the limit  $d \rightarrow \infty$ . Their contribution is given by:

$$(\gamma_\nu)_3 = \frac{1}{512}(7 + 6 \ln 2) + O(\epsilon). \quad (35)$$

Therefore, from (24), (26), (32) and (35), it follows that the anomalous dimension  $\gamma_\nu$  in the three-loop approximation is:

$$\gamma_\nu = \frac{u}{4} + \frac{u^2}{32}(1 - 2\epsilon \ln 2) + \frac{u^3}{512}(7 + 6 \ln 2) + O(u^4). \quad (36)$$

Substituting (36) into the  $\beta$ -function (16) and solving the equation  $\beta(u_*) = 0$ , we find the value of the charge in the fixed point in terms of the  $\epsilon$ -expansion

$$u_* = \frac{8\epsilon}{3} - \frac{8\epsilon^2}{9} - \frac{4\epsilon^3}{9}(1 - 2 \ln 2). \quad (37)$$

According to (16), (36) and (37), the index  $\omega = \beta'(u_*)$  is:

$$\omega = 2\epsilon + \frac{2}{3}\epsilon^2 + \frac{10}{9}\epsilon^3. \quad (38)$$

The latter expression coincides with one obtained in [3].

## 5. Conclusions

We have performed calculations for the anomalous dimension  $\gamma_\nu$  and exponent  $\omega$  in the three-loop approximation in the fully developed turbulence model for large numbers of dimensions in space, by determining the of RG-functions without renormalization constants. Our calculations demonstrated the efficiency of the applied method. Its main advantage is that for the computation of the  $n$ -loop results, one needs to evaluate the set of the  $(n - 1)$ -dimensional integrals, free from the singularities in  $\varepsilon$ . The computation procedure can be automated with relative ease. The main difficulty in higher order perturbation theory calculations is in the rapidly increasing number of diagrams with vector fields and the triple interaction vertex. In the considered limit,  $d \rightarrow \infty$ , the number of the diagrams is notably decreased. Thus, in four loops, only 1692 diagrams remain of the original 417872.

The significant decrease in the number of diagrams may indicate that the  $\varepsilon$ -expansion of the function  $\gamma_\nu(\varepsilon)$  has a finite radius of convergence in the limit  $d \rightarrow \infty$ , in contrast to the general case, when one observes a factorial growth of the corresponding series coefficients. A similar thing occurs in phase transition theory when the anomalous dimensions  $\gamma(\varepsilon, n)$  is calculated. Here  $\varepsilon = 4 - d$ , where  $d$  is the dimension of the space and  $n$  is the number of the field components. At fixed  $n$  the coefficients of the  $\varepsilon$ -expansion grow factorially, but the coefficients of the  $(1/n)$ -expansion have a finite radius of the convergence, as the series in  $\varepsilon$  [8]. Currently, in turbulence theory only the third order in  $\varepsilon$  at  $d \rightarrow \infty$  of the double  $(\varepsilon, 1/d)$ -expansion is known. However, the results obtained in the current work and in [3] have revealed some simplicity for this expansion. It is seen from the equations (37) and (38) that the irrational contribution to  $u_*$  (the charge at the fixed point depends on the renormalization scheme) with  $\ln 2$  disappearing in the physical quantity of the index  $\omega$ . The contributions of some particular diagrams proportional to  $\ln^2 2$ ,  $\pi^2$ ,  $\text{dilog}(3/2)$ , typical for the series of critical exponents in critical dynamics models, are all canceled out in the total sum of diagram. The coefficients of (38) are rational numbers. This gives the possibility to sum the series and find the function  $\gamma_\nu(\varepsilon)$  at  $d \rightarrow \infty$  without using the  $\varepsilon$ -expansion.

## Acknowledgements

The work of LTsA, TLK and MVK was supported by Saint-Petersburg State University (project 11.38.185.2014). VKS acknowledges the support by the Austrian Science Fund FWF Grants Nr. I 1452-N27 and Nr. P21970-N16.

## References

- [1] M. Chertkov, G. Falkovich, I. Kolokolov, and V. Lebedev, Normal and anomalous scaling of the fourth-order correlation function of a randomly advected passive scalar. *Phys. Rev. E*, 1995, **52**, 4924. M. Chertkov and G. Falkovich, Anomalous Scaling Exponents of a White-Advection Passive Scalar. *Phys. Rev. Lett.*, 1996, **76**, P. 2706.
- [2] J.-D. Fournier, U. Frisch, H. A. Rose. Infinite-dimensional turbulence. *J. Phys. A*, **11**(1), 1978, P. 187–198.
- [3] L. Ts. Adzhemyan, N.V. Antonov, P.B. Gol'din, T.L. Kim and M.V. Kompaniets. Renormalization group in the infinite-dimensional turbulence: third-order results, *Journal of Physics A: Mathematical and Theoretical*, 2008, **41**(49), P. 495002.
- [4] L.Ts. Adzhemyan, N.V. Antonov, Renormalization group in turbulence theory: Exactly solvable Heisenberg model. *Theoretical and Mathematical Physics*, **115**, 1098, P. 562–574.
- [5] L.Ts. Adzhemyan, M.V. Kompaniets, S.V. Novikov, V.K. Sazonov. Representation of the  $\beta$ -function and anomalous dimensions by nonsingular integrals: Proof of the main relation, *Theoretical and Mathematical Physics*, 2013, **175**, P. 717–726.

- [6] L.Ts. Adzhemyan, M.V. Kompaniets, Five-loop numerical evaluation of critical exponents of the  $\phi^4$  theory. *Journal of Physics: Conference Series*, 2014, **523**, P. 012049.
- [7] P.C. Martin, E.D. Siggia, H.A. Rose. Statistical Dynamics of Classical Systems. *Phys.Rev.*, 1973, **A8**, P. 423.
- [8] A. N. Vasil'ev *The Field Theoretic Renormalization Group in Critical Behavior Theory and Stochastic Dynamics* (Routledge Chapman & Hall 2004); ISBN 978-0-415-31002-4
- [9] O. I. Zavialov, *Renormalized Quantum Field Theory*, (Dordrecht :Kluwer, 1990).

## The study of the local director orientation in chiral liquid crystals

E. S. Kraynyukov, A. A. Karetnikov, A. P. Kovshik,  
E. I. Ryumtsev, E. V. Aksyonova, V. P. Romanov

The Faculty of Physics of the Saint Petersburg State University,  
198504, St. Petersburg, Petrodvorets, Russia

bacoom888@gmail.com, akaret@mail.ru, sashakovshik@yandex.ru,  
rei39@mail.ru, aksev@mail.ru, vpromanov@mail.ru

**PACS 42.70.Df; 42.25.Bs; 42.25.Fx; 42.25.Gy DOI 10.17586/2220-8054-2015-6-4-470-478**

The refraction of an extraordinary light wave in a layer of a chiral liquid crystal with the director rotated  $90^\circ$  has been studied. In this structure, if a light wave is incident on the surface of the liquid crystal at a large angle and the light passes through the whole layer, it refracts at the opposite boundary of the layer. The angular dependence of the light transmission through the liquid crystal layer has been researched. It has been demonstrated that the electric field changed the character of the refraction of the extraordinary wave and the light started to pass through the layer. The threshold voltage of the light transmission has been determined, as well as its dependence on the light incidence angle. The effect dynamics have been studied and the angular dependence of the light transmission decay time has been determined.

**Keywords:** refraction, chiral liquid crystal, relaxation time.

*Received: 20 June 2015*

### 1. Introduction

The use of liquid crystals (LC) in display technology is based on the control of the optical properties of LC thin layers with the help of an electric field. Under the influence of an electric field, the director of an LC (the direction of preferential orientation of molecules) changes its position in space, affecting the intensity of the light transmitting through the liquid crystal layer. Associated with the director reorientation, the light transmission switch-on and switch-off times  $\tau_{\text{on}}$  and  $\tau_{\text{off}}$  are the most important performance characteristics of liquid crystal devices. Due to this, there is a need to study the changes of orientation structure of liquid crystals under the influence of external electric fields, as well as the dependence of  $\tau_{\text{on}}$  and  $\tau_{\text{off}}$  on various parameters for liquid crystal layers. The research of the LC director reorientation dynamics at different distances from the LC layer boundary is of particular interest.

Such investigation can be performed for a liquid crystal layer with a helical structure, using the phenomena of refraction [1–3]. Refraction was observed in plain liquid crystal layers, displaced between glass surfaces, on the surface of which the director was parallel to the surfaces and had the same direction. In the middle of the layer, the director was rotated  $90^\circ$  from the director position at the boundaries. The extraordinary ray, incident from the glass to the liquid crystal layer at angles exceeding the angle of total internal reflection of the ordinary ray, entered the LC, refracted inside the layer, and returned back through the same glass surface. Calculated predictions showed that the distance from the surface layer to the ray refraction point decreased, when the angle of incidence for the light to the LC layer was increased. The application of an electric field led to distortion of the LC layer structure orientation and a change in the ray's path. When the magnitude of the electric field exceeded the Fréedericksz threshold,

refraction was disturbed – the ray passed through the layer. In works [3–5], the intensity of the transmitted light, the threshold voltage, and the cell transmission switch-on and switch-off time dependencies on the light angle of incidence were studied. Varying the angle of incidence allowed us to study the change in the local orientation of the LC director under the influence of an electric field with a smooth change of the depth of the ray penetration into the layer.

When using liquid crystals in a variety of electro-optical devices, there are several sets of boundary conditions that allow the creation of the necessary structure for LC director orientation, thereby changing the optical characteristics of the devices. Therefore, comparison of the characteristics for a system with  $180^\circ$  rotation of the director, studied in works [3–5], with the characteristics of other helical structures having different boundary conditions is of great scientific and practical interest. In this regard, the purpose of this work was to study light refraction in the layer of the plane-oriented, chiral liquid crystal (used in works [3–5]), in which the direction of the director on surfaces differs by  $90^\circ$ .

## 2. Experiment

The experimental cell for studying the refraction in chiral liquid crystal layers was composed of two glass trapezoidal prisms (1) and (2) with a base size of  $50 \times 25$  mm and height of 18 mm (Fig. 1). The inclination of the entrance faces to the base was  $68^\circ$ . The refractive index of the prisms  $n_{gl}$  was 1.7002 for the wavelength  $\lambda = 632.8$  nm. There were transparent conductive coatings (electrodes) and thin polyimide layers at the prism bases. By rubbing the latter, the planar orientation was set with the surface for the liquid crystal providing strong anchoring for the LC director. At the same time, the LC director at the layer's first boundary, where the ray of light was incident, was directed perpendicular to the plane of the figure (Fig. 1). At the second boundary of the layer the director lies in the plane of the figure. The required LC layer thickness of  $8 \mu\text{m}$  was set with the help of Teflon spacers. The space between the prisms was filled with the chiral liquid crystal mixture (previously used in works [4, 5]) with the helical pitch  $P_0 = 32 \mu\text{m}$  that consisted of LC-1466 (NIOPIK) with the chiral dopant VIH-3 (Vilnius State University, Lithuania). The dielectric anisotropy  $\Delta\varepsilon$  of LC-1466 was 11.7 for a frequency of 1 kHz. The principal refractive indices values for the ordinary and extraordinary rays  $n$  and  $n_0$ , for wavelength  $\lambda = 632.8$  nm were 1.691 and 1.511 respectively. For a given layer thickness and helical pitch, the LC director was rotated by  $90^\circ$  when passing from one layer's boundary to the other.

The scheme of the experimental setup is shown in Fig. 2 (top view). The beam of light from a helium-neon laser with wavelength  $\lambda = 632.8$  nm and the diameter of 1 mm was incident to the studied cell with the liquid crystal (LC-cell) through the half-wave plate  $\lambda/2$ . With the half-wave plate, the polarization vector of the incident ray was parallel to the LC director at the interface between the liquid crystal and glass. Next, the light fell on the photodetector Ph, whose signal was recorded with the digital oscilloscope Osc (ASK-3106) and the computer. For signal control, we used a bipolar rectangular voltage generator ANR-3122, forming voltage pulses up to 10 V with the duration of 0.1 – 5.0 seconds and carrier frequency  $f = 1$  kHz. The controlled voltage from the generator was applied to the electrodes of the cell and the oscilloscope. In order to change the angle of incidence  $\delta$  for the ray to the liquid crystal layer, the cell was mounted on the rotating table with the angle-reading device with an accuracy of 1 minute.

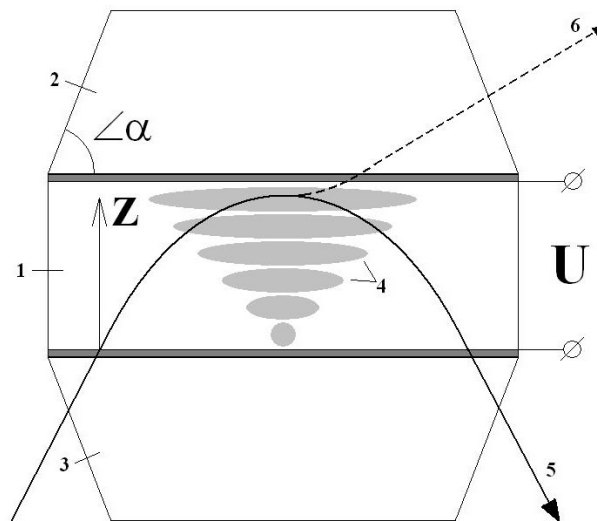


FIG. 1. LC-cell: 1 – liquid crystal layer; 2,3 – glass prisms; 4 – director configuration in liquid crystal layer; 5 – the trajectory of the extraordinary ray in the absence of an electric field; 6 – the trajectory of the extraordinary ray when electric field is applied;  $U$  – control voltage

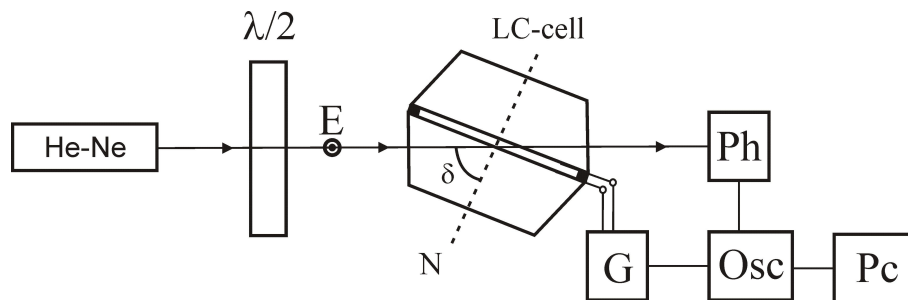


FIG. 2. Scheme of experimental setup: He-Ne – laser;  $\lambda/2$  – half wave plate; LC-cell – liquid crystal cell; Ph – photodetector; G – generator; Osc – oscilloscope; PC – computer

### 3. Experimental results

Primarily, the dependence of the intensity of the light passing through the cell at the angle of incidence for the extraordinary ray to the LC layer was obtained (Fig. 3). The figure shows that with angles of incidence smaller than the critical angle of total internal reflection for the ordinary ray ( $\delta = 62.7^\circ$  when  $n_0 = n_\perp = 1.511$ ), the intensity of the transmitted light is maximized. The observed intensity oscillations in the areas of max transmission of the cell may be caused by interference between the rays refracted from the first and second layer boundaries, since a change in the angle of incidence results in a phase difference change between the interfering rays. In the  $62.0^\circ - 63.1^\circ$  angular range, the LC-cell light transmission changes from its maximum value to zero. The decreasing intensity deviations from monotony in this area are also associated with the interference of the rays reflected from both boundaries of the LC layer. The value of the critical angle of refraction (the extraordinary ray return back near second interface), which was  $62.7^\circ$  (within experimental error), coincided with the limit angle of refraction for the LC-cell which had its director rotated by  $180^\circ$  [3–5].

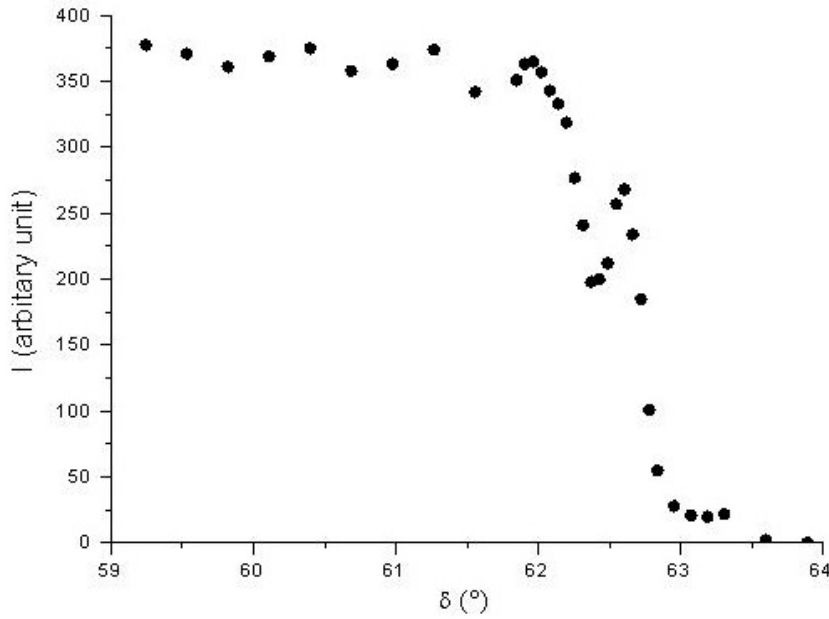


FIG. 3. The dependence of the intensity  $I$  of the light passing through the cell on the incidence angle  $\delta$  of the extraordinary ray to the LC layer

With angles of incidence larger than the critical angle of refraction ( $62.7^\circ$ ), the effects of the electric field of sufficient magnitude on the cell led to the disturbance (cut-off) of extraordinary ray refraction and light passing through the cell. The oscillograms of the control voltage  $U = 8$  V at frequency of 1 kHz (a) and the optical response (b) for an angle of incidence of  $63^\circ$  are shown in Fig. 4. For comparison, there are also optical responses of the LC-cell to the applied electric field, when the light falls perpendicular to the LC layer in an electrically-controlled birefringent mode (c) and the cut-off of the Mauguin regime (d), specific to the twist cells with a  $90^\circ$  rotation of the director. From the obtained oscillograms, it follows that the times for establishing maximum transmission in these modes differ. The time for complete refraction cut-off  $\tau_1$  is significantly higher than the similar parameter in electrically-controlled birefringent modes  $\tau_2$  and the cut-off of the Mauguin regime  $\tau_3$ . Upon cancellation of the electric field, the fastest cessation for light transmission is specific to the refraction recovery mode.

The refraction cut-off mode, similar to the electrically-controlled birefringent modes and the Mauguin regime cut-off, has a threshold value. The threshold voltage of light transmission through the cell  $U_{th}$  was determined by using the dependence of the transmitted light intensity  $I$  on the applied voltage  $U$ . As an example, Fig. 5 shows the dependence of  $I$  on  $U$  for the angle of incidence of  $62.8^\circ$ .

The increase in the light angle of incidence to the liquid crystal layer within the  $62.8^\circ - 79.7^\circ$  range resulted in an increase in the threshold voltage from 1.1 V to 8.2 V (Fig. 6). A similar dependence was also observed in the LC cell with  $180^\circ$  rotation of the director, studied in work [3]. To interpret the results, the depth of the ray penetration into the layer at different angles of incidence was calculated using the formula:

$$z(\delta) = d - \frac{2d}{\pi} \operatorname{asin} \sqrt{\frac{\left(1 - \frac{n_0^2}{n_{gl}^2 \sin^2 \delta}\right) n_e^2}{n_e^2 - n_0^2}}, \quad (1)$$

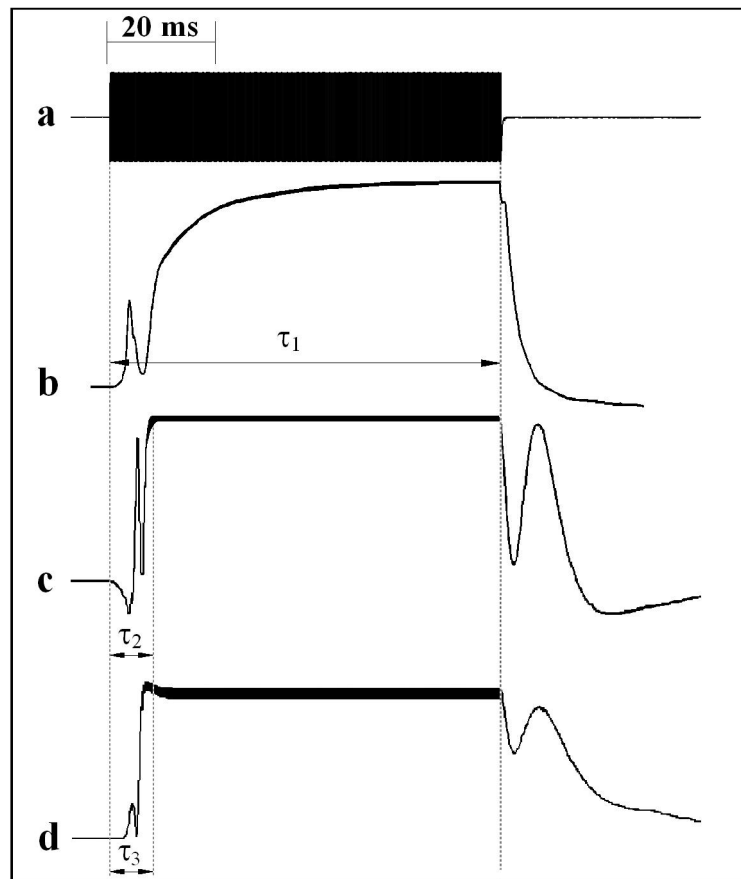


FIG. 4. Oscillograms of control voltage and optical response. (a) – Control voltage  $U = 8$  V, and carrier frequency  $f = 1000$  Hz. (b) – cut-off refraction mode, the angle of incidence of light on the layer  $\delta = 63^\circ$ ,  $z = 7.3$   $\mu\text{m}$ . (c) – electrically-controlled birefringence mode, (d) – cut-off Mauguin mode. Oscillograms (c) and (d) are obtained for the light incidence along the normal to the layer

where,  $d$  – the thickness of the LC,  $\delta$  – the angle of incidence for the extraordinary ray to the layer,  $z$  – the depth of the ray penetration into the layer. The dependence of  $z$  on  $\delta$  is shown in Fig. 7. It is seen from Fig. 7 that as the angle of light incidence to the layer increases, the penetration depth decreases. When  $z$  decreases, the dependence of  $U_{\text{th}}$  on  $z$  shows an increase in the threshold voltage. The increase of  $U_{\text{th}}$  when  $\delta$  increases, i.e. when the depth of the ray penetration into the layer decreases, can be attributed to the fact that the deviation of the LC director at the same angle close to the surface requires more voltage than in the layer depth [2]. It should be noted that a change of 1 in the angle of incidence results in a change of the ray penetration depth by 250 nm (Fig. 7). The latter provides a unique opportunity to study the local orientation structure of the LC director and its change dynamics in external electric fields. Therefore, we also studied the reorientation of the LC director upon switching off of the electric field for different angles of light incidence to the layer, and hence for the penetration depth  $z$ . The magnitude of the control voltage, disturbing the terms of refraction, exceeded the threshold voltage corresponding to all achievable values of  $z$  and was the same ( $U = 8$  V) for all the angles of incidence (the depth of the ray penetration into the layer). In this case, in the layer with the equally deformed LC structure, we studied the relaxation of the local deformation of

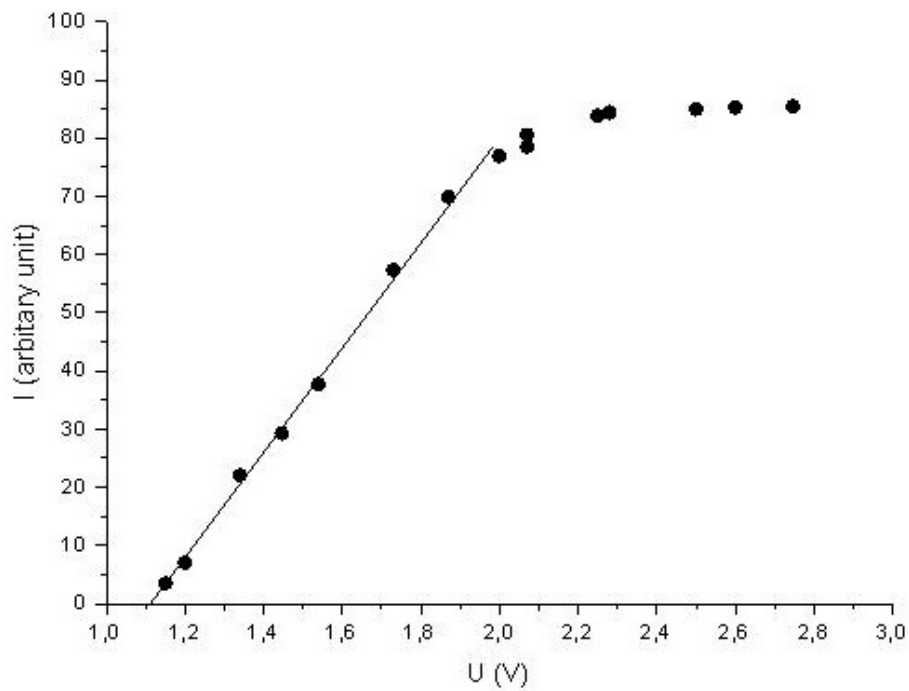


FIG. 5. The intensity of the transmitted light on the control voltage applied at an angle of incidence of the extraordinary ray in the LC layer.  $\delta = 63^\circ$

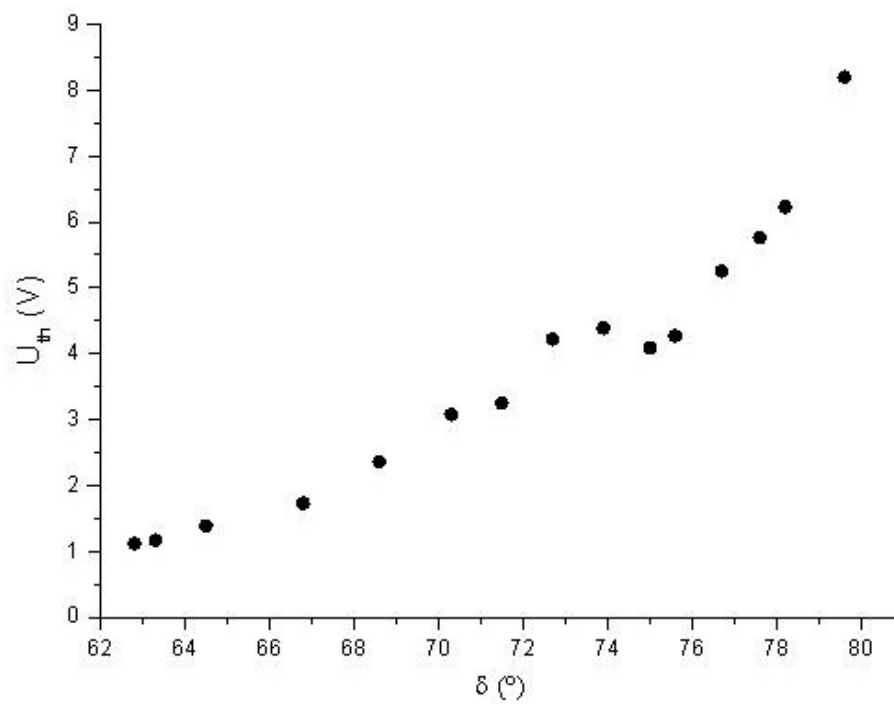


FIG. 6. The dependence of the threshold voltage  $U_{th}$  on the angle of incidence of the extraordinary ray  $\delta$  on the LC layer

the director, which differed at different distances from the layer boundary. The recovery time of the optical transmission of the cell  $\tau_r$  was determined using the oscillograms of the optical response to the electric field. The relaxation times correspond to the time taken to relax from 100% to 10% of the maximum transmission. As an example, the oscillograms for the optical response relaxation for several angles of incidence are shown in Fig. 8.

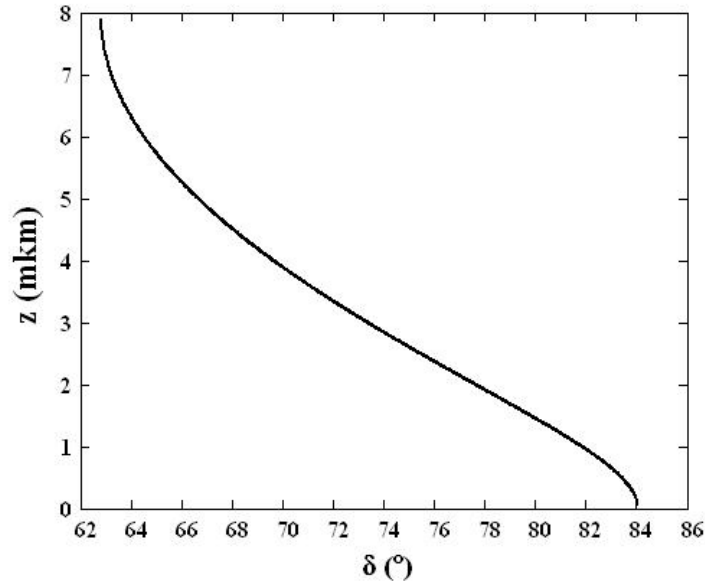


FIG. 7. The dependence of the penetration depth  $z$  extraordinary ray in the liquid crystal layer on the incidence angle  $\delta$

The dependence of  $\tau_r$  on the depth of the ray penetration into the layer  $z$  for the voltage of 8 V is shown in Fig. 9. The figure shows that the recovery time for optical transmission  $\tau_r$  decreases along with the depth of the light penetration into the liquid crystal layer. Qualitatively, such dependence can be explained by the fact that the recovery rate of the LC initial orientation is proportional to the magnitude of elastic torque that affects the LC director. This elastic torque is at its maximum in the area of the LC layer, where there is a maximum orientation gradient of the director, when the field is off. We can assume that this is why  $\tau_r$  decreases along with the distance from the boundary of the layer  $z$  [5].

#### 4. Conclusion

The refraction of light in the chiral liquid crystal layer (helical pitch of 32  $\mu\text{m}$ ) with the 90° rotation of the director at different angles of incidence to the LC layer (the depth of the extraordinary ray penetration into the layer) has been studied. The effect of the electric field on the extraordinary ray refraction at different distances from the LC layer surface has been researched. The threshold character of the refraction cut-off (the light transmission of the cell) has been found. The dependencies of the threshold voltage of the refraction cut-off  $U_{th}$  and the refraction recovery time  $\tau_r$  of the electric field switching off on the depth of the ray penetration into the LC layer have been obtained.

The comparison of the results of the experimental research of the electric field influence on the extraordinary ray refraction in the helical liquid crystal structures with the 90° and 180° director rotation of the showed that in both structures, the minimum threshold voltage for the refraction disturbance  $U_{th(min)}$  corresponds to the minimum angle of incidence to the layer. At

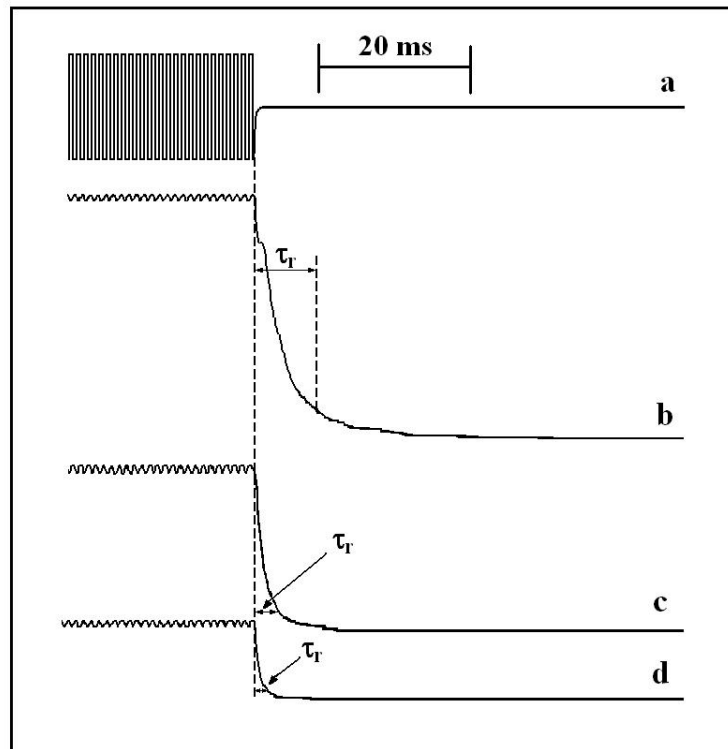


FIG. 8. The trailing edge of the optical response of the cell after the field at different depths of penetration of the beam in the LC layer. a) pulse voltage,  $U = 8 \text{ V}$ ,  $f = 1 \text{ kHz}$ . b) – d) optical feedback for  $z = 7.2 \mu\text{m}$ ,  $z = 5.1 \mu\text{m}$  and  $z = 4.0 \mu\text{m}$ , respectively

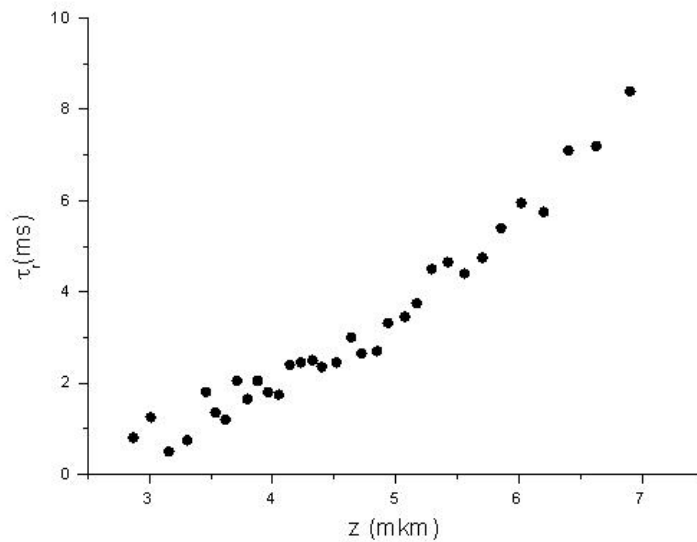


FIG. 9. Dependence of refraction recovery time  $\tau$  on penetration depth  $z$  extraordinary ray in the liquid crystal layer for voltage  $8 \text{ V}$

the same time, for the structure with the  $180^\circ$  rotation of the director,  $U_{\text{th}(\text{min})}$  causes refraction disturbance in the middle layer [3], and in the cell with  $90^\circ$  rotation – at the layer boundary opposite to the input surface. The refraction recovery time  $\tau_r$  is maximum in both structures for the minimum angle of incidence to the layer. For the structure with  $180^\circ$  director rotation,  $\tau_{r(\text{max})}$  corresponds to the director orientation recovery, necessary for recovering the refraction in the middle of the LC layer. At the same time, in the LC structure rotated  $90^\circ$   $\tau_{r(\text{max})}$  is required for the refraction recovery near the layer boundary opposite to the input surface, i.e. at the maximum depth of the ray penetration into the liquid crystal layer.

The study showed that the lowest threshold voltage for the refraction cut-off and the longest refraction recovery time corresponds to the maximum depth of the extraordinary ray penetration into the layer, regardless of the boundary conditions on the surfaces of the LC layer and the ray rotation point in the middle of the layer (rotation of the director by  $180^\circ$ ), or at the far boundary of the layer (rotation of the director by  $90^\circ$ ).

The theoretical background of the results is a rather complex issue, especially in the case of sufficiently strong electrical fields exceeding the Fréedericksz threshold. The solution to this problem is expected to be found at some point in the future.

Thus, the combined experimental and theoretical research of the light refraction in helical-structured liquid crystals and the effect of electric field on refraction will allow investigation of the process for local director reorientation at different distances from the interfaces between liquid crystals and glass.

## References

- [1] E.V. Aksenova, A.A. Karetnikov, A.P. Kovshik et al. Return back of the extraordinary beam for oblique incidence in helical liquid crystals with large pitch. *Europhys. Lett.*, 2005, **69**, P. 68–74.
- [2] E.V. Aksenova, A.A. Karetnikov, A.P. Kovshik et al. Propagation of Light through a Forbidden Zone in Chiral Media. *J. Opt. So. Amer.*, 2008, **6** (104), P. 909–919.
- [3] A.A. Karetnikov, N.A. Karetnikov, A.P. Kovshik, et al. Electric Field Effect on Refraction of Light in a Layer of Chiral Liquid Crystal with Large Pitch. *Opt. Spectr.*, 2010, **6** (108), P. 947–953.
- [4] A.A. Karetnikov, N.A. Karetnikov, A.P. Kovshik et al. Local Dynamics of Director Reorientation under Electric Field in Helical LC Structure. *Mol. Cryst. Liq. Cryst.*, 2012, **561**, P. 97–106.
- [5] E.V. Aksenova, B.B. Divinsky, A.A. Karetnikov, et al. Particular the propagation of light in the cells of chiral liquid crystals in an external electric field. *Journal of Experimental and Theoretical Physics*, 2014, **2** (145), P. 369–380.

## Evolution of size and composition of a multicomponent gas bubble in liquid solution

A. E. Kuchma, A. K. Shchekin

Department of Statistical Physics, Faculty of Physics, St. Petersburg State University,  
Ulyanovskaya 1, Petrodvoretz, St. Petersburg, 198504, Russia

akshch@list.ru

**PACS** 05.70.Fh, 05.70.Np, 47.55.db, 47.57.eb, 68.35.Rh

**DOI** 10.17586/2220-8054-2015-6-4-479-488

The equations describing the transient and steady stages of size and composition evolution for a gas bubble which grows or shrinks due to the diffusion of several gases dissolved in liquid solution have been derived. The diffusion fluxes for gases in the liquid mixture caused by the bubble growth or dissolution were assumed to be quasi-stationary and the mixture of the gases in the bubble was treated as ideal. The analytical solutions for the obtained evolution equations have been found for bubbles of any size with an arbitrary number of components in the case of equal products of diffusivities and solubilities of dissolved gases in the liquid solution, and for sufficiently large binary bubbles for which capillary effects can be neglected.

**Keywords:** bubble, multicomponent, supersaturated solution, diffusion, kinetics of growth.

*Received: 20 June 2015*

### 1. Introduction

This paper presents several analytical results in the theoretical description for the growth or dissolution kinetics of a single gas bubble in a supersaturated or undersaturated gas-liquid solution in the case when the bubble is comprised of several gases. Evidently, finding such description is a fundamental issue because it turns to be a necessary element for the general theory on the decay of multicomponent metastable liquid solutions [1,2]. As discussed previously, the formation of gas bubbles is widely applied in technological processes for the creation of new porous materials and nano- and microcontainers [3,4]. The rapid, explosive growth of water vapor and accompanying dissolved gas bubbles in magmatic melt is one contributing mechanism for volcanic eruptions [5–7]. The control of gas bubble growth and dissolution in blood and biological tissues is a very important issue for those undergoing decompression [8]. These examples highlight how the problem of theoretically describing bubble growth or dissolution is still very relevant.

The diffusion growth of single-component bubbles in a supersaturated solution of gas in liquid has been previously considered under the assumption of a quasi-stationary state for the concentration fields of dissolved gas in the vicinity of bubble and with the use of a self-similar solution for the non-stationary diffusion equation [9–13]. Quasi-steady-state diffusion approaches to the description of multicomponent bubble evolution were considered by Ramos [14,15] and Cable and Frade [16]. In particular, it was reported in [15,16] that large enough bubbles reach a state of stationary growth with fixed composition and growth rate and may demonstrate a nonmonotonic change in their radius during the initial stage of their evolution. Formulation of the theory of non-stationary self-similar growth of a binary bubble

with stationary composition in the case of high supersaturation had been done by Gor and Kuchma [17].

Recently, we have formulated and analyzed a set of equations for the size, composition and temperature of a droplet consisting of a binary or multicomponent solution, which non-isothermally condenses or evaporates under a quasi-steady-state diffusion regime in a multicomponent mixture of vapors and non-condensable carrier gas [18–22]. Some of these equations have been analytically solved. The problem of a multicomponent droplet growing or evaporating in the diffusion regime in the vapor-gas mixture is similar to the problem of growth or dissolution of a multicomponent bubble in the liquid solution with several dissolved gas. In this paper, we will extend the analytical approach which was useful for a small droplet to the case of a multicomponent bubble.

## 2. General relations

We consider a multicomponent spherical bubble of radius  $R$  which grows or shrinks due to the diffusion of several gases dissolved in liquid solution at fixed absolute temperature  $T$  and pressure  $P$ . Under mechanical equilibrium of the bubble and the solution, the total pressure  $P_{tot}(R)$  in the bubble depends on its radius  $R$  and pressure  $P$  in the solution according to the formula:

$$P_{tot}(R) = P + \frac{2\sigma}{R}, \quad (1)$$

where  $\sigma$  is the surface tension at the bubble-liquid interface. Let  $n_i$  be the volume concentration of the molecules of  $i$ -th gas ( $i = 1, 2, \dots, k$ ) within the bubble, then the total gas concentration  $n$  in the bubble equals:

$$n = \sum_{i=1}^k n_i. \quad (2)$$

Assuming the gas mixture in the bubble is ideal, we have:

$$n = \frac{P_{tot}}{k_B T} = \frac{P}{k_B T} \left( 1 + \frac{2\sigma}{PR} \right) = \bar{n} \left( 1 + \frac{R_*}{R} \right), \quad (3)$$

where  $k_B$  is the Boltzmann constant, and we have introduced the new notation:

$$\bar{n} \equiv \frac{P}{k_B T}, \quad R_* \equiv \frac{2\sigma}{P}. \quad (4)$$

For characterization of the composition of the bubble, we will use the molecular fractions  $x_i$  of  $i$ -th component determined as:

$$x_i = \frac{n_i}{n} = \frac{N_i}{N} \quad (i = 1, 2, \dots, k), \quad (5)$$

where  $N_i$  is the number of molecules of  $i$ -th gas and  $N = \sum_{i=1}^k N_i$  is the total number of gas molecules in the bubble. Because  $\sum_{i=1}^k x_i = 1$ , only  $k - 1$  molecular fractions  $x_i$  can be considered to be independent. In light of Eqs. (3) and (4), the total number  $N$  of molecules in the bubble can also be expressed as:

$$N = \frac{4\pi}{3} n R^3 = \frac{4\pi}{3} \bar{n} R^3 \left( 1 + \frac{R_*}{R} \right) = \frac{4\pi}{3} \bar{n} R^2 (R + R_*). \quad (6)$$

The emission and absorption of gas molecules by the bubble produce the diffusion profiles of each component around the bubble in a liquid solution. We denote the local volume concentration of  $i$ -th component at distance  $r \geq R$  from the center of the bubble as  $\rho_i(r, t)$ . Correspondingly, the initial bulk volume concentration of the  $i$ -th component in liquid is  $\rho_{i0} = \rho_i(r \rightarrow \infty, t)$ . We will assume that the concentration  $\rho_i(R, t)$  at the boundary of the bubble is determined by conditions of chemical equilibrium for the  $i$ -th component in the bubble and solution and is related in this way with the volume concentration  $n_i$  within the bubble. Henry's law gives:

$$\rho_i(R, t) = s_i n_i = s_i x_i n \quad (i = 1, 2, \dots, k), \tag{7}$$

where  $s_i$  is the solubility of  $i$ -th component of the gas mixture in the liquid solution.

### 3. The equations governing the evolution of the composition and size of the bubble

Differentiating both sides of definition (5) with respect to time gives:

$$\dot{x}_i = \frac{\dot{N}_i}{N} - x_i \frac{\dot{N}}{N} \quad (i = 1, 2, \dots, k), \tag{8}$$

where the dot over the quantity marks the time derivative or rate of the corresponding quantity. The expression for the rates  $\dot{N}_i$  and  $\dot{N}$  have the following form under assumption of stationary diffusion of the dissolved gases in solution:

$$\dot{N}_i = 4\pi R D_i [\rho_{i0} - \rho_i(R, t)] \quad (i = 1, 2, \dots, k), \tag{9}$$

$$\dot{N} = 4\pi R \sum_{i=1}^k D_i [\rho_{i0} - \rho_i(R, t)], \tag{10}$$

where  $D_i$  is the diffusivity of  $i$ -th component of the gas mixture in the liquid solution. Substitution of Eqs. (9) and (10) into the right-hand side of Eq. (8) and using Eqs. (4) and (6) yields:

$$\dot{x}_i = \frac{3}{\bar{n}R(R + R_*)} \left( D_i [\rho_{i0} - \rho_i(R, t)] - x_i \sum_{j=1}^k D_j [\rho_{j0} - \rho_j(R, t)] \right) \quad (i = 1, 2, \dots, k). \tag{11}$$

Let us now introduce the  $i$ -th gas supersaturation in solution as:

$$\zeta_i \equiv \frac{\rho_{i0}}{s_i \bar{n}} - 1 \quad (i = 1, 2, \dots, k). \tag{12}$$

Eqs. (3) and (7) allows us to write:

$$\rho_i(R, t) = s_i x_i \bar{n} \left( 1 + \frac{R_*}{R} \right) \quad (i = 1, 2, \dots, k). \tag{13}$$

Substituting Eqs. (12) and (13) in Eq. (11) yields:

$$\dot{x}_i = \frac{3}{R(R + R_*)} \left[ D_i s_i \left( \zeta_i + 1 - x_i \left( 1 + \frac{R_*}{R} \right) \right) - x_i \sum_{j=1}^k D_j s_j \left( \zeta_j + 1 - x_j \left( 1 + \frac{R_*}{R} \right) \right) \right] \quad (i = 1, 2, \dots, k). \tag{14}$$

Analogously, differentiating both sides of definition (6) with respect to time and using Eq. (3) gives:

$$\dot{N} = 4\pi n R^2 \dot{R} + \frac{4\pi}{3} \dot{n} R^3 = 4\pi \bar{n} \left(1 + \frac{R_*}{R}\right) R^2 \dot{R} - \frac{4\pi}{3} \bar{n} \frac{R_*}{R^2} \dot{R} R^3 = 4\pi \bar{n} R \dot{R} \left(R + \frac{2}{3} R_*\right), \quad (15)$$

while substituting Eqs. (7) and (12) in Eq. (10) yields:

$$\dot{N} = 4\pi R \bar{n} \sum_{i=1}^k D_i s_i \left[ \zeta_i + 1 - x_i \left(1 + \frac{R_*}{R}\right) \right]. \quad (16)$$

After comparing Eqs. (15) and (16), we obtain:

$$\dot{R} \left(R + \frac{2}{3} R_*\right) = \sum_{i=1}^k D_i s_i \left( \zeta_i + 1 - x_i \left(1 + \frac{R_*}{R}\right) \right). \quad (17)$$

Finally, we have coupled evolution equations (14) and (17) for the bubble's composition and radius with initial conditions  $x_i(t=0) = x_{i0}$ ,  $R(t=0) = R_0$ . Note that in the case of a single-component gas in solution and bubble ( $x_1 = 1$ ,  $\zeta_i + 1 = 0$  at  $i \geq 2$ ), Eq. (17) is obviously reduced to the equation for the bubble radius in the known form:

$$R \dot{R} \frac{R + R_\sigma}{\zeta_1 R - R_*} = D_1 s_1, \quad (18)$$

where

$$R_\sigma \equiv \frac{2}{3} R_*. \quad (19)$$

For a supersaturated gas-liquid solution, when  $\zeta_1 > 0$ , Eq. (18) can be rewritten:

$$R \dot{R} \frac{R + R_\sigma}{R - R_c} = D_1 s_1 \zeta_1, \quad (20)$$

where  $R_c = \frac{R_*}{\zeta_1} = \frac{2\sigma}{P\zeta_1}$  is the radius of the critical bubble (at  $R_0 > R_c$  the size of the bubble increases monotonically with time, while at  $R_0 < R_c$ , the bubble dissolves irreversibly). The growth dynamics of a supercritical bubble in a highly supersaturated ( $\zeta_1 \gg 1$ ) gas-liquid solution, determined by Eq. (20), was studied in detail in [11]. If there is  $\zeta_1 \leq 0$ , a bubble of any initial size irreversibly dissolves.

#### 4. Analytical solution of evolution equations in the case of equal products of diffusivities and solubilities of dissolved gases

Let us now consider the conditions on the system parameters which allows us to find analytical solutions for Eqs. (14) and (17). In the particular case when  $D_i s_i \equiv D_s$ , for any gas component, (i.e. when the diffusivity and solubility products for dissolved gases in liquid solution are equal) Eqs. (14) and (17) take the form:

$$\dot{x}_i = \frac{3D_s}{R(R + R_*)} [\zeta_i + 1 - x_i (\bar{\zeta} + 1)] \quad (i = 1, 2, \dots, k), \quad (21)$$

$$R \dot{R} \frac{R + R_\sigma}{R - R_*/\bar{\zeta}} = D_s \bar{\zeta}, \quad (22)$$

where we have introduced new notation:

$$\bar{\zeta} \equiv \sum_{i=1}^k (\zeta_i + 1) - 1. \quad (23)$$

As is seen from Eqs. (20) and (22), changing the bubble size with time does not depend in this particular case on the bubble's composition and is described by the same equation as in the case of single-component bubble. The role of supersaturation is played now by the quantity  $\bar{\zeta}$ , and we have  $R_*/\bar{\zeta}$  instead of  $R_c$ . Proceeding by analogy with [11], taking into account the initial value  $R(t=0) = R_0$  and Eq. (19), we find for the bubble radius at  $\bar{\zeta} \neq 0$ :

$$\frac{R^2 - R_0^2}{2} + \left(1 + \frac{2\bar{\zeta}}{3}\right) \frac{R_*}{\bar{\zeta}} \left(R - R_0 + \frac{R_*}{\bar{\zeta}} \ln \left| \frac{\bar{\zeta}R - R_*}{\bar{\zeta}R_0 - R_*} \right| \right) = Ds\bar{\zeta}t. \quad (24)$$

In the case  $\bar{\zeta} = 0$ , it follows from Eq. (22) that the bubble radius satisfies the equation:

$$R\dot{R} \left( \frac{R}{R_*} + \frac{2}{3} \right) = -Ds. \quad (25)$$

It is clear from Eq. (25) that  $\dot{R} < 0$  and the bubble irreversibly dissolves in this case. Using the initial condition for the bubble radius, we find the solution of Eq. (25) in the form:

$$\frac{1}{3} \left( \frac{R^3 - R_0^3}{R_*} + R^2 - R_0^2 \right) = -Dst. \quad (26)$$

Setting  $R(t_d) = 0$ , we can find the time  $t_d$  of complete dissolution of the bubble of initial radius  $R_0$  at  $\bar{\zeta} = 0$  as:

$$t_d(R_0) = \frac{R_0^2}{3Ds} \frac{R_0 + R_*}{R_*}. \quad (27)$$

There is a special case when  $\zeta_i + 1 = 0$  for all gas components, and, correspondingly,  $\bar{\zeta} + 1 = 0$ . This case refers to the dissolution of a gas bubble in pure solvent. As follows from Eq. (21), we have  $\dot{x}_i = 0$  for each gas component within the bubble in this case, and the composition of the bubble in the dissolution process remains unchanged. Such situation is fully equivalent to the description of the single-component bubble dissolution in the pure solvent. Substituting  $\bar{\zeta} = -1$  into Eq. (24), we find:

$$\frac{R^2 - R_0^2}{2} - \frac{1}{3}R_* \left[ R - R_0 - R_* \ln \left( \frac{R + R_*}{R_0 + R_*} \right) \right] = -Dst. \quad (28)$$

As follows from Eq. (28), the time  $\bar{t}_d$  of complete dissolution of the bubble of initial radius  $R_0$  at  $\bar{\zeta} = -1$  is determined as:

$$\bar{t}_d(R_0) = \frac{1}{Ds} \left[ \frac{R_0^2}{2} - \frac{1}{3}R_* \left( R_0 - R_* \ln \left( \frac{R_0}{R_*} + 1 \right) \right) \right]. \quad (29)$$

In the case  $R_0 \ll R_*$ , this time approximately equals:

$$\bar{t}_d(R_0) \approx \frac{R_0^2}{3Ds} \left( 1 + \frac{R_0}{3R_*} \right). \quad (30)$$

Let us now consider a relation between the bubble radius and composition. If  $\bar{\zeta} + 1 > 0$ , then we have from Eq. (21):

$$\dot{x}_i = -\frac{3Ds(\bar{\zeta} + 1)}{R(R + R_*)} (x_i - x_{is}), \quad (i = 1, 2, \dots, k), \quad (31)$$

where:

$$x_{is} \equiv \frac{\zeta_i + 1}{\bar{\zeta} + 1}, \tag{32}$$

is the stationary value of molecular fraction of  $i$ -th component of the gas mixture in the bubble. With the help of Eq. (22), we can find from Eq. (31) the relation between differentials  $dx_i$  and  $dR$ :

$$\frac{dx_i}{x_i - x_{is}} = - \frac{3(\bar{\zeta} + 1)(R + R_\sigma)dR}{(R + R_*)(\bar{\zeta}R - R_*)} \quad (i = 1, 2, \dots, k). \tag{33}$$

The solution of Eq. (33) at  $\bar{\zeta} \neq 0$  and  $R(t = 0) = R_0, x_i(t = 0) = x_{i0}$  ( $i = 1, 2, \dots, k$ ) has the form:

$$\left| \frac{x_i - x_{is}}{x_{i0} - x_{is}} \right| = \frac{R_0 + R_*}{R + R_*} \left| \frac{\bar{\zeta}R_0 - R_*}{\bar{\zeta}R - R_*} \right|^{\frac{2\bar{\zeta} + 3}{\bar{\zeta}}}. \tag{34}$$

Equation (34) shows that molecular fractions of all gas components in the bubble relax to their steady-state values according to one and the same power law. If  $R \gg R_*/|\bar{\zeta}|$  and  $R_0 \gg R_*/|\bar{\zeta}|$ , Eq. (34) simplifies as:

$$\left| \frac{x_i - x_{is}}{x_{i0} - x_{is}} \right| = \left| \frac{R_0}{R} \right|^{3\frac{\bar{\zeta} + 1}{\bar{\zeta}}} \quad (i = 1, 2, \dots, k), \tag{35}$$

or

$$R^2 = R_0^2 \left( \frac{x_{i0} - x_{is}}{x_i - x_{is}} \right)^{\frac{2}{3}\frac{\bar{\zeta}}{\bar{\zeta} + 1}}. \tag{36}$$

In the case when  $\bar{\zeta} = 0$ , the dependence  $x_i(R)$  ( $i = 1, 2, \dots, k$ ) can be easily found by two ways. First we can set  $\bar{\zeta} = 0$  just in Eq. (33) for  $x_i$  and solve it to obtain:

$$\left| \frac{x_i - x_{is}}{x_{i0} - x_{is}} \right| = \frac{R_0 + R_*}{R + R_*} \exp\left(-3\frac{R_0 - R}{R_*}\right) \quad (i = 1, 2, \dots, k). \tag{37}$$

The same result can also be obtained by taking the limit  $\bar{\zeta} \rightarrow 0$  in the solution (34) and using the relation:

$$\left| \frac{\bar{\zeta}R_0 - R_*}{\bar{\zeta}R - R_*} \right|^{\frac{2\bar{\zeta} + 3}{\bar{\zeta}}} = \left| \frac{1 - \bar{\zeta}R_0/R_*}{1 - \bar{\zeta}R/R_*} \right|^{\frac{2\bar{\zeta} + 3}{\bar{\zeta}}} \approx \left(1 - \bar{\zeta}\frac{R_0 - R}{R_*}\right)^{\frac{3}{\bar{\zeta}}} \xrightarrow{\bar{\zeta} \rightarrow 0} \exp\left(-3\frac{R_0 - R}{R_*}\right).$$

### 5. Analytical solution of evolution equations in the case of neglecting the capillary contributions

For sufficiently large bubbles, when  $R_0 \gg R_*$  and  $R \gg R_*$ , we can neglect the capillary contributions to the evolution equations (14) and (17) and write:

$$\dot{x}_i = \frac{3}{R^2} \left( D_i s_i (\zeta_i + 1 - x_i) - x_i \sum_{j=1}^k D_j s_j (\zeta_j + 1 - x_j) \right), \tag{38}$$

$$R\dot{R} = \sum_{i=1}^k D_i s_i (\zeta_i + 1 - x_i). \tag{39}$$

An analytical solution for this set of equations is possible for  $k = 2$  (for a binary gas bubble). In this case, Eqs. (38) and (39) are reduced to the form:

$$\dot{x}_1 = \frac{3}{R^2} f(x_1), \quad (40)$$

$$f(x_1) = -D_1 s_1 [(\gamma - 1)x_1^2 + (\zeta_1 + \gamma\zeta_2 + 2)x_1 - \zeta_1 - 1], \quad (41)$$

$$R\dot{R} = g(x_1), \quad (42)$$

$$g(x_1) = D_1 s_1 [\zeta_1 + 1 + \gamma\zeta_2 + x_1(\gamma - 1)], \quad (43)$$

where:

$$\gamma \equiv \frac{D_2 s_2}{D_1 s_1}. \quad (44)$$

This set of equations is similar to the set of equations describing the evolution of a two component droplet in the gas mixture, which has been studied in [18].

Recognizing that the case of  $\gamma = 1$  (when  $D_2 s_2 = D_1 s_1 = Ds$ ) was completely described in the previous section for multicomponent bubbles of any size, we consider further the situation with  $\gamma \neq 1$ , assuming for definiteness  $\gamma > 1$ . It is convenient to rewrite Eq. (41) in the form:

$$f(x_1) = -D_1 s_1 (\gamma - 1) (x_1 - x_{1s}) (x_1 - \tilde{x}_{1s}), \quad (45)$$

where  $x_{1s}$  and  $\tilde{x}_{1s}$  are the roots of function  $f(x_1)$ :

$$x_{1s} = \frac{-(\zeta_1 + 2 + \gamma\zeta_2) + \sqrt{[\zeta_1 + 2 + \gamma\zeta_2]^2 + 4(\gamma - 1)(\zeta_1 + 1)}}{2(\gamma - 1)}, \quad (46)$$

$$\tilde{x}_{1s} = \frac{-(\zeta_1 + 2 + \gamma\zeta_2) - \sqrt{[\zeta_1 + 2 + \gamma\zeta_2]^2 + 4(\gamma - 1)(\zeta_1 + 1)}}{2(\gamma - 1)}. \quad (47)$$

As follows from Eq. (47), at  $\gamma > 1$ , the root  $\tilde{x}_{1s}$  is negative,  $\tilde{x}_{1s} < 0$ , and has no physical meaning. The root  $x_{1s}$  lies in the interval  $0 < x_1 < 1$  and corresponds to the stationary composition of the bubble. As follows from Eqs. (42) and (43), the stationary rate  $(R\dot{R})_s$  of the changing the bubble size is determined as:

$$(R\dot{R})_s = g(x_{1s}) = D_1 s_1 [\zeta_1 + 1 + \gamma\zeta_2 + x_{1s}(\gamma - 1)], \quad (48)$$

or, in view of Eq. (46), as:

$$(R\dot{R})_s = \frac{\gamma}{1 + (\gamma - 1)x_{1s}} D_1 s_1 (\zeta_1 + \zeta_2 + 1). \quad (49)$$

As one can see from Eq. (49), the size of the bubble increases monotonically in the stationary case at  $\zeta_1 + \zeta_2 + 1 > 0$ . If the opposite inequality holds, the bubble dissolves.

Since function  $f(x_1)$  monotonically decreases over the  $0 < x_1 < 1$  interval, it then follows from Eq. (40) that molecular fraction  $x_1$  tends monotonically with time to its stationary value  $x_{1s}$ . This allows us to use the current value  $x_1(t)$  as the independent variable for solving the system of equations for the evolution of the composition and size of the bubble. Accordingly, we find from Eqs. (40) and (42) the following differential equation:

$$\frac{dR^2}{R^2} = \frac{2g(x_1)}{3f(x_1)} dx_1, \quad (50)$$

the solution of which at  $R(t = 0) = R_0, x_1(t = 0) = x_{10}$  has the form:

$$R^2(x_1) = R_0^2 \exp\left(\frac{2}{3} \int_{x_{10}}^{x_1} \frac{g(y)}{f(y)} dy\right). \tag{51}$$

Substituting Eq. (51) in Eq. (40) yields another differential equation:

$$\frac{dx_1}{dt} = \frac{3}{R^2} f(x_1) = \frac{3}{R_0^2 \exp\left(\frac{2}{3} \int_{x_{10}}^{x_1} \frac{g(y)}{f(y)} dy\right)} f(x_1), \tag{52}$$

the solution of which can be written as:

$$t(x_1) = \frac{R_0^2}{3} \int_{x_{10}}^{x_1} \frac{dy}{f(y)} \exp\left(\frac{2}{3} \int_{x_{10}}^y \frac{g(z)}{f(z)} dz\right). \tag{53}$$

It is convenient to transform expression (43) for function  $g(x_1)$  as:

$$g(x_1) = D_1 s_1 (\gamma - 1) (x_1 - x_{1*}), \tag{54}$$

where:

$$x_{1*} = \frac{\zeta_1 + \gamma \zeta_2 + 1}{1 - \gamma}. \tag{55}$$

Using Eqs. (45) and (54) allows us to represent the ratio  $g(x_1)/f(x_1)$  in the form:

$$\frac{g(x_1)}{f(x_1)} = -\frac{x_1 - x_{1*}}{(x_1 - x_{1s})(x_1 - \tilde{x}_{1s})} = \frac{1}{x_{1s} - \tilde{x}_{1s}} \left( \frac{\tilde{x}_{1s} - x_{1*}}{x_1 - \tilde{x}_{1s}} - \frac{x_{1s} - x_{1*}}{x_1 - x_{1s}} \right), \tag{56}$$

and to perform integration:

$$\exp\left(\frac{2}{3} \int_{x_{10}}^x \frac{g(y)}{f(y)} dy\right) = \left(\frac{x_{10} - x_{1s}}{x_1 - x_{1s}}\right)^{\frac{2}{3} \frac{x_{1s} - x_{1*}}{x_{1s} - \tilde{x}_{1s}}} \left(\frac{x_1 - \tilde{x}_{1s}}{x_{10} - \tilde{x}_{1s}}\right)^{\frac{2}{3} \frac{\tilde{x}_{1s} - x_{1*}}{x_{1s} - \tilde{x}_{1s}}}. \tag{57}$$

Using Eq. (57) in Eqs. (51) and (53), we finally obtain for the square of the radius,  $R^2(x)$  and time,  $t(x)$  the following expressions:

$$R^2(x_1) = R_0^2 \left(\frac{x_{10} - x_{1s}}{x_1 - x_{1s}}\right)^{\frac{2}{3} \frac{x_{1s} - x_{1*}}{x_{1s} - \tilde{x}_{1s}}} \left(\frac{x_1 - \tilde{x}_{1s}}{x_{10} - \tilde{x}_{1s}}\right)^{\frac{2}{3} \frac{\tilde{x}_{1s} - x_{1*}}{x_{1s} - \tilde{x}_{1s}}}, \tag{58}$$

$$t(x_1) = \frac{R_0^2}{3f(x_{10})} \int_{x_{10}}^{x_1} dy \left(\frac{x_{10} - x_{1s}}{y - x_{1s}}\right)^{\frac{2}{3} \frac{x_{1s} - x_{1*}}{x_{1s} - \tilde{x}_{1s}}} + 1 \left(\frac{y - \tilde{x}_{1s}}{x_{10} - \tilde{x}_{1s}}\right)^{\frac{2}{3} \frac{\tilde{x}_{1s} - x_{1*}}{x_{1s} - \tilde{x}_{1s}}} - 1. \tag{59}$$

The dependence  $x_1(t)$  can be found by reversing the dependence  $t(x_1)$  obtained with the help of Eq. (59). Substituting the reversal function  $x_1(t)$  in Eq. (58) determines the dependence  $R^2(t)$ .

Let us now consider the possibility of nonmonotonic behavior for rate  $R\dot{R}$  as a function of system parameters and an initial bubble composition. As is clear from Eqs. (42) and (54), a nonmonotonic growth or dissolution of the bubble becomes possible when the parameter  $x_{1*}$ , determined by Eq. (55), appears within the  $0 < x_{1*} < 1$  interval, and the concentration  $x_1(t)$  passes during the bubble evolution through the value  $x_1 = x_{1*}$ . In such a case, we have  $\dot{R} > 0$  at  $x_1 < x_{1*}$  and  $\dot{R} < 0$  at  $x_1 > x_{1*}$ . According to Eq. (55), the condition  $0 < x_{1*} < 1$  is

reached if the double inequality  $1 - \gamma < \zeta_1 + \gamma\zeta_2 + 1 < 0$  is fulfilled. Moreover, if we have  $0 < x_{1*} < x_{1s} < 1$  and  $x_{10} < x_{1*}$ , then the bubble radius will diminish at the initial stage of its evolution until the concentration  $x_1 = x_{1*}$  is reached and then grow monotonically after that. Note that, as follows from Eqs. (46) and (55), inequality  $x_{1*} < x_{1s}$  fulfils at  $\zeta_1 + \zeta_2 + 1 > 0$ .

To control our results, we will check the case when  $\gamma \rightarrow 1$  in Eq. (58). Setting  $\gamma \rightarrow 1$  in Eqs. (46), (47) and (55) and recognizing with the help of Eq. (23) that  $\bar{\zeta} \equiv \zeta_1 + \zeta_2 + 1$  in the case of two dissolved gases, we find:

$$x_{1s} \rightarrow \frac{\zeta_1 + 1}{\bar{\zeta} + 1}, \quad \tilde{x}_{1s} \sim -\frac{\bar{\zeta} + 1}{\gamma - 1} \rightarrow \infty, \quad x_{1*} \sim -\frac{\bar{\zeta}}{\gamma - 1} \rightarrow \infty, \quad (60)$$

$$\frac{x_{1s} - x_{1*}}{x_{1s} - \tilde{x}_{1s}} \rightarrow \frac{\bar{\zeta}}{\bar{\zeta} + 1}, \quad \left( \frac{x_1 - \tilde{x}_{1s}}{x_{10} - \tilde{x}_{1s}} \right)^{\frac{2}{3}} \frac{\tilde{x}_{1s} - x_{1*}}{x_{1s} - \tilde{x}_{1s}} \rightarrow 1. \quad (61)$$

Using Eqs. (60) and (61) in Eq. (58), we obtain  $R^2(x_1) \xrightarrow{\gamma \rightarrow 1} R_0^2 \left( \frac{x_{10} - x_{1s}}{x_1 - x_{1s}} \right)^{\frac{2}{3} \frac{\bar{\zeta}}{\bar{\zeta} + 1}}$ . As expected, this result coincides with Eq. (36) for the case when  $D_1 s_1 = D_2 s_2 \equiv Ds$  and  $R \gg R_*/|\bar{\zeta}|$ ,  $R_0 \gg R_*/|\bar{\zeta}|$  which was considered in section 3.

## Acknowledgements

This work was supported by the Russian Foundation for Basic Research (project No. 13-03-01049-a) and the Program of Development of St. Petersburg State University (project No. 11.37.183.2014).

## References

- [1] Skripov V.P. *Metastable Liquid*. New York: Wiley, 1974.
- [2] Baidakov V.G. *Explosive Boiling of Superheated Cryogenic Liquids*. Berlin: Wiley-VCH, 2007.
- [3] Kolasinski K.W. Bubbles: A review of their relationship to the formation of thin films and porous materials. *Mesoporous Biomaterials*, 2014, **1**, P. 49–60.
- [4] Liu P.S., Chen G.F. *Porous Materials: Processing and Applications*. Amsterdam: Elsevier, 2014.
- [5] Gonnermann H.M. and Manga M. The fluid mechanics inside a volcano. *Annu. Rev. Fluid Mech.*, 2007, **39**, P. 321–356.
- [6] Kuchma A.E., Kuni F.M., and Shchekin A.K. Nucleation stage with nonsteady growth of supercritical gas bubbles in a strongly supersaturated liquid solution and the effect of excluded volume. *Phys. Rev. E*, 2009, **80**, 061125.
- [7] Chernov A.A., Kedrinsky V.K., and Pil'nik A.A. Kinetics of gas bubble nucleation and growth in magmatic melt at its rapid decompression. *Physics of Fluids*, 2014, **26**, 116602.
- [8] Srinivasan R.S., Gerth W.A., Powell M.R. Mathematical model of diffusion-limited evolution of multiple gas bubbles in tissue. *Ann. Biomed. Eng.*, 2003, **31** (4), P. 471–81.
- [9] Epstein P.S. and Plesset M.S. On the Stability of Gas Bubbles in Liquid-Gas Solutions. *J. Chem. Phys.*, 1950, **18**, P. 1505–1509.
- [10] Grinin A.P., Kuni F.M., Gor G.Y. Theory of nonsteady diffusion growth of a gas bubble in a supersaturated solution of gas in liquid. *Colloid Journal*, 2009, **71** (1), P. 46–54.
- [11] Kuchma A.E., Gor G.Y., Kuni F.M. Stages of Steady Diffusion Growth of a Gas Bubble in Strongly Supersaturated Gas-Liquid Solution. *Colloid Journal*, 2009, **71** (4), P. 520–528.
- [12] Grinin A.P., Kuni F.M., Gor G.Y. The rate of nonsteady gas bubble growth in liquid supersaturated with gas. *J. Mol. Liq.*, 2009, **148** (1), P. 32–34.
- [13] Gor G.Y., Kuchma A.E. Dynamics of gas bubble growth in a supersaturated solution with Sievert's solubility law. *J. Chem. Phys.*, 2009, **131**, 034507.
- [14] Ramos J.I. Growth of multicomponent gas bubbles. *Chem. Eng. Commun.*, 1986, **40**, P. 321–334.
- [15] Ramos J.I. Multicomponent Gas Bubbles. I. Growth of Stationary Bubbles. *J. Non-Equilib. Thermodyn.*, 1988, **13**, P. 1–25.

- [16] Cable M. and Frade J.R. Diffusion-controlled growth of multi-component gas bubbles. *Journal of Materials Science*, 1987, **22** (3), P. 919–924.
- [17] Gor G.Y., Kuchma A.E. Steady-state composition of a two-component gas bubble growing in a liquid solution: self-similar approach. *J. Chem. Phys.*, 2009, **131**, 234705.
- [18] Kuchma A.E., Shchekin A.K., Kuni F.M. Simultaneous establishing of stationary growth rate and composition of supercritical droplets at isothermal binary condensation in the diffusion-controlled regime. *Physica A*, 2011, **390**, P. 3308–3316.
- [19] Martyukova D.S., Kuchma A.E., Shchekin A.K. Dynamics of variations in size and composition of a binary droplet in a mixture of two condensing vapors and a passive gas under arbitrary initial conditions. *Colloid Journal*, 2013, **75** (5), P. 571–578.
- [20] Kuchma A.E., Martyukova D.S., Lezova A.A., Shchekin A.K. Size, temperature and composition of a spherical droplet as a function of time at the transient stage of nonisothermal binary condensation or evaporation. *Colloids and Surfaces A*, 2013, **432** (5), P. 147–156.
- [21] Kuchma A.E., Shchekin A.K., Lezova A.A., Martyukova D.S. On the Evolution of a Multicomponent Droplet during Nonisothermal Diffusion Growth or Evaporation. *Colloid Journal*, 2014, **76** (5), P. 576–584.
- [22] Kuchma A.E., Shchekin A.K., Martyukova D.S., Lezova A.A. Growth or evaporation of a free microdroplet. General equations for the regime of nonstationary diffusion and heat transfer in multicomponent vapor-gas environment. *Aerosol Science & Technology*, submitted 2015.

# The interaction of polarization charges in freely suspended smectic-C\* films

D. A. Murich<sup>1</sup>, V. P. Romanov<sup>1</sup>, S. V. Ul'yanov<sup>1,2</sup>

<sup>1</sup>Saint Petersburg State University, Ul'yanovskaya, 1, Petrodvoretz, Saint Petersburg 198504, Russia

<sup>2</sup>Saint Petersburg State University of Commerce and Economics, Saint Petersburg 194021, Russia

murichdim@mail.ru, ulyanov\_sv@mail.ru

PACS 61.30.Dk, 61.30.Gd, 42.79.Hp, 42.70.Df

DOI 10.17586/2220-8054-2015-6-4-489-500

The fluctuations of the director orientation in a freely suspended smectic-C\* film were theoretically investigated. In the free energy expression of the film, not only were the elastic energy and the weak external electric field interaction considered, the interaction of polarization charges arising from fluctuations of the polarization vector were also included. The correlation function of the director fluctuations was obtained for a film of finite thickness. Calculations of light scattering intensity were provided. It has been found that due to the interaction of polarization charges, the angular dependence of the scattering intensity significantly depends on the magnitude of spontaneous polarization.

**Keywords:** smectic-C\*, freely suspended films, polarization charges, correlation function, light scattering intensity.

*Received: 20 June 2015*

## 1. Introduction

Smectic-C\* liquid crystals have attracted wide attention from researchers for several decades. This is primarily due to the unique physical properties inherent to these substances [1]. Smectics-C\* (Sm-C\*) are well-documented as layered systems consisting of monomolecular layers composed of elongated molecules which are inclined relative to the normal to the layers. This leads to the creation of a director vector,  $\mathbf{n}$ , which gives the average direction of preferred molecule orientation, and is inclined at an angle  $\theta$  relative to the normal  $\mathbf{N}$  to the smectic layers. At constant temperature, the angle  $\theta$  can be considered constant throughout the liquid crystal. Each layer in Sm-C\* can be considered as a two-dimensional liquid. In addition, the Sm-C\* possesses spontaneous polarization, and the polarization vector  $\mathbf{P}$  in each point of the liquid crystal is perpendicular to both the director  $\mathbf{n}$ , and the normal  $\mathbf{N}$ . In bulk Sm-C\* samples, when passing from layer to layer, the polarization vector  $\mathbf{P}$  rotates around the normal  $\mathbf{N}$  by a certain angle that is the same for all layers. The number of layers over which the vector  $\mathbf{P}$  makes a full rotation may vary from five or six to thousands [1-3]. As a result, the director  $\mathbf{n}$  also uniformly rotates about the normal  $\mathbf{N}$  when passing from one smectic layer to the next, forming a helical structure. In the bulk samples of Sm-C\*, the vector  $\mathbf{P}$  can experience several full rotations, and therefore, throughout the entire sample, the polarization is zero.

In free-standing Sm-C\* films, an average a constant direction of the polarization vector  $\mathbf{P}$  can be achieved by an external electric field, or by a small film thickness. Due

to fluctuations of the director orientation  $\mathbf{n}$ , fluctuations of the polarization  $\mathbf{P}$  may also arise. The occurrence of spatial inhomogeneities for spontaneous polarization leads to the appearance of polarization charges with density  $\rho = -\text{div}\mathbf{P}$ . The electrostatic interaction of the polarization charges changes the spatial correlation function of the director fluctuations and it can be manifested in light scattering experiments. It is usually assumed that the interaction of the polarization charges is completely or partially screened by impurity charges [1]. At the same time, the contribution of the unscreened Coulomb interaction was observed in the light scattering experiments which were performed on highly-pure Sm-C\* samples [4-8].

The Coulomb interaction of polarization charges in Sm-C\* is usually assumed to be isotropic [1]. As was shown in [9], screened Coulomb interaction in thin Sm-C\* films may lead to renormalization of the bend elastic modulus. For thin freely suspended Sm-C\* films in [4-8] the correlation function of orientation fluctuations was calculated and experiments were performed on highly-purified Sm-C\* samples which revealed the Coulomb interaction contribution to the angular dependence of the light scattering. For a plane Sm-C\* cell with bookshelf geometry, the calculations of the correlation function for orientation fluctuations were carried out in [10], taking into account the finite thickness of the cell. The angular dependence of light scattering intensity for Sm-C\* was calculated for different spontaneous polarization values. Anisotropy of the Coulomb interaction in the bulk samples of Sm-C\* was considered in the theoretical description performed in [11].

In the present work, the correlation function of orientation fluctuations is calculated for a freely suspended Sm-C\* film, taking into account the finite film thickness and the Coulomb interaction of polarization charges. The results of the calculations are used to find the angular dependence of scattered light intensity.

## 2. Basic equations

Let's assume that in a freely suspended Sm-C\* film the helical structure of director  $\mathbf{n}$  is unwound. This can be achieved by an external electric field,  $\mathbf{E}$ , which is directed along the smectic layers. We assume that the field applied is not too large, so that it was possible to consider only the interaction of a field with the polarization vector  $\mathbf{P}$ . In this case, the free energy of distortion in the film Sm-C\* can be represented as the sum of three terms:

$$F = F_{Fr} + F_P + F_C. \quad (2.1)$$

Here,  $F_{Fr}$  – the elastic free energy of distortion of the director field, which, in the unwound Sm-C\*, can be represented in the following form:

$$F_{Fr} = \frac{1}{2} \int d\mathbf{r} [K_{11}(\text{div } \mathbf{n})^2 + K_{22}(\mathbf{n} \cdot \text{rot } \mathbf{n})^2 + K_{33}(\mathbf{n} \times \text{rot } \mathbf{n})^2]. \quad (2.2)$$

Here,  $K_{11}$ ,  $K_{22}$ ,  $K_{33}$  are Frank modules. The second term in Eq. (2.1) arises from the interaction of the spontaneous polarization  $\mathbf{P}$  with external electric field  $\mathbf{E}$ :

$$F_P = - \int d\mathbf{r} (\mathbf{P} \cdot \mathbf{E}). \quad (2.3)$$

The last term in Eq. (2.1) considers Coulomb interaction between the polarization charges arising in the inhomogeneous ferroelectric Sm-C\*. Neglecting anisotropy of the dielectric constant, and taking it as equal to the average value of  $\varepsilon$ , for this contribution, we have:

$$F_C = \frac{1}{2} \int d\mathbf{r} \int d\mathbf{r}' \frac{\text{div } \mathbf{P}(\mathbf{r}) \text{div}' \mathbf{P}(\mathbf{r}')}{\varepsilon |\mathbf{r} - \mathbf{r}'|}. \quad (2.4)$$

The layers are flat in a free standing Sm- $C^*$  film at equilibrium. In the description of the director  $\mathbf{n}$ , fluctuation deformations of the layered structure are usually neglected. This is due to the fact that the possibility of free rotation of the director  $\mathbf{n}$  around the normal  $\mathbf{N}$  to the smectic layers, leads to much greater distortions of the director  $\mathbf{n}$  field than small change the direction of the normal  $\mathbf{N}$ . In a Sm- $C^*$  film in which the helical structure is unwound by an external electric field, the orientation of the director  $\mathbf{n}$  is uniform.

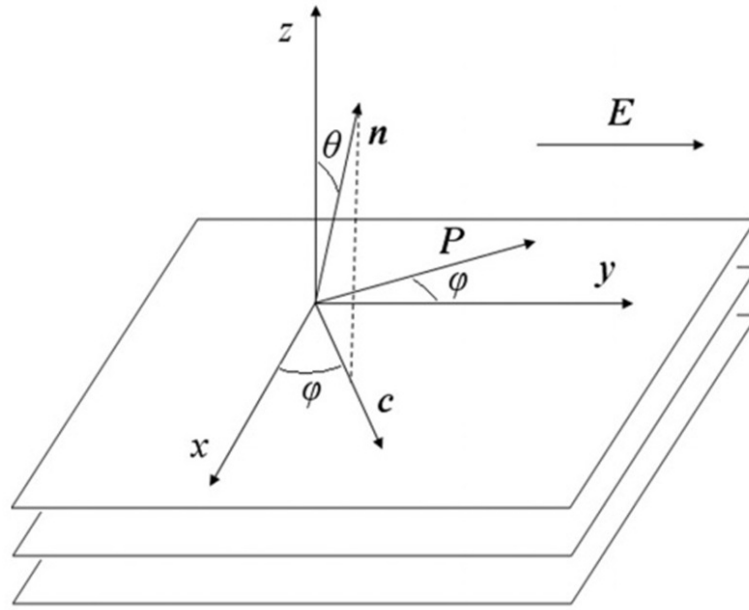


FIG. 1. The system coordinates and vectors  $\mathbf{n}, \mathbf{c}, \mathbf{P}$ . The electric field is directed along the  $y$  axis

For the calculations, it is convenient to use a coordinate system in which the  $xy$  plane is parallel to the smectic layers and is located in the middle of the film. The direction of the  $y$ -axis is chosen along the external field,  $\mathbf{E}$ , and the  $z$ -axis is normal to the layers. The orientation structure in Sm- $C^*$  conveniently described by  $\mathbf{c}$ -director, which is a unit vector codirectional with the projection of the director  $\mathbf{n}$  onto the plane of the smectic layer. Director  $\mathbf{n}$  is defined by angles  $\theta$  and  $\varphi$  as shown in Fig. 1. The angle  $\theta$  determines the slope of director  $\mathbf{n}$  with respect to the normal to the layers. This angle depends on the temperature, which we assumed to be constant. The angle  $\varphi$  describes the deviation of  $\mathbf{c}$ -director from the equilibrium direction along the  $x$ -axis. The polarization vector  $\mathbf{P}$  is given by:

$$\mathbf{P} = P [\mathbf{N} \times \mathbf{c}] \tag{2.5}$$

where  $P$  - the polarization of Sm- $C^*$ . The vectors  $\mathbf{n}, \mathbf{c}, \mathbf{P}$  have the coordinates:

$$\begin{aligned} \mathbf{n} &= (\sin \theta \cos \varphi, \sin \theta \sin \varphi, \cos \theta) \\ \mathbf{c} &= (\cos \varphi, \sin \varphi, 0) \\ \mathbf{P} &= P(-\sin \varphi, \cos \varphi, 0). \end{aligned} \tag{2.6}$$

Believing the  $\mathbf{c}$ -director fluctuations and hence the angle  $\varphi$  fluctuations are small, we have:

$$\begin{aligned} \mathbf{n} &\approx \left[ \left(1 - \frac{\varphi^2}{2}\right) \sin \theta, \varphi \sin \theta, \cos \theta \right], \\ \mathbf{c} &\approx \left(1 - \frac{\varphi^2}{2}, \varphi, 0\right), \end{aligned} \tag{2.7}$$

$$\mathbf{P} \approx P(-\varphi, 1 - \frac{\varphi^2}{2}, 0).$$

The contribution of the  $\mathbf{c}$ -director fluctuations to the free energy in the Gaussian approximation can be represented as follows:

$$\begin{aligned} \delta F = \frac{1}{2} \int d\mathbf{r} \left[ B_1 \left( \frac{\partial \varphi}{\partial x} \right)^2 + B_2 \left( \frac{\partial \varphi}{\partial y} \right)^2 + B_3 \left( \frac{\partial \varphi}{\partial z} \right)^2 + 2B_{13} \left( \frac{\partial \varphi}{\partial x} \right) \left( \frac{\partial \varphi}{\partial z} \right) + \right. \\ \left. + PE\varphi^2 + \frac{P^2}{\varepsilon} \int d\mathbf{r}' \frac{\frac{\partial \varphi(\mathbf{r})}{\partial x} \frac{\partial \varphi(\mathbf{r}')}{\partial x'}}{|\mathbf{r}-\mathbf{r}'|} \right]. \end{aligned} \quad (2.8)$$

Here:

$$\begin{aligned} B_1 &= K_{22} \sin^2 \theta \cos^2 \theta + K_{33} \sin^4 \theta, \\ B_2 &= K_{11} \sin^2 \theta, \\ B_3 &= K_{22} \sin^4 \theta + K_{33} \sin^2 \theta \cos^2 \theta, \\ B_{13} &= \sin^2 \theta \cos \theta (K_{33} - K_{22}). \end{aligned} \quad (2.9)$$

We will consider a film of finite thickness, located in the area  $[-L/2; L/2]$ , where  $L$  is the film thickness. In the  $xy$  plane, the film has a macroscopic size and therefore it is convenient to use the following Fourier representation:

$$\begin{aligned} \varphi_{\mathbf{q}_\perp}(z) &= \int d\mathbf{r}_\perp e^{-i\mathbf{q}_\perp \cdot \mathbf{r}_\perp} \varphi(\mathbf{r}_\perp, z), \\ \varphi(\mathbf{r}_\perp, z) &= \frac{1}{(2\pi)^2} \int d\mathbf{q}_\perp e^{i\mathbf{q}_\perp \cdot \mathbf{r}_\perp} \varphi_{\mathbf{q}_\perp}(z). \end{aligned} \quad (2.10)$$

In expression (2.8), for the free energy, we turn to the Fourier representation and take into account the ratio:

$$\int d\mathbf{r}_\perp \frac{e^{i\mathbf{q}_\perp \cdot \mathbf{r}_\perp}}{\sqrt{r_\perp^2 + (z-z')^2}} = \frac{2\pi}{q_\perp} e^{-q_\perp |z-z'|}. \quad (2.11)$$

The result is as follows:

$$\begin{aligned} \delta F = \frac{1}{2(2\pi)^2} \int d\mathbf{q}_\perp \left[ \int_{-\frac{L}{2}}^{\frac{L}{2}} dz \varphi_{\mathbf{q}_\perp}^*(z) \left( B_1 q_x^2 + B_2 q_y^2 + PE - B_3 \frac{\partial^2}{\partial z^2} - 2B_{13} i q_x \frac{\partial}{\partial z} \right) \varphi_{\mathbf{q}_\perp}(z) + \right. \\ \left. + \frac{2\pi P^2}{q_\perp \varepsilon} q_x^2 \int_{-\frac{L}{2}}^{\frac{L}{2}} dz \int_{-\frac{L}{2}}^{\frac{L}{2}} dz' e^{-q_\perp |z-z'|} \varphi_{\mathbf{q}_\perp}^*(z') \varphi_{\mathbf{q}_\perp}(z) + \right. \\ \left. + \left( B_3 \varphi_{\mathbf{q}_\perp}^*(z) \frac{\partial \varphi_{\mathbf{q}_\perp}(z)}{\partial z} + 2B_{13} i q_x \varphi_{\mathbf{q}_\perp}^*(z) \varphi_{\mathbf{q}_\perp}(z) \right) \Big|_{-\frac{L}{2}}^{\frac{L}{2}} \right]. \end{aligned} \quad (2.12)$$

The free energy (2.12) is a quadratic form,  $\frac{1}{2} (\varphi, \hat{M}\varphi)$ . We select by square brackets kernel of the operator explicitly:

$$\begin{aligned} \delta F = \frac{1}{2(2\pi)^2} \int d\mathbf{q}_\perp \int_{-\frac{L}{2}}^{\frac{L}{2}} dz \varphi_{\mathbf{q}_\perp}^*(z) \int_{-\frac{L}{2}}^{\frac{L}{2}} dz' \left[ \delta(z-z') \left( B_1 q_x^2 + B_2 q_y^2 + PE - \right. \right. \\ \left. \left. - B_3 \frac{\partial^2}{\partial z'^2} - 2B_{13} i q_x \frac{\partial}{\partial z'} \right) + \frac{2\pi P^2}{q_\perp \varepsilon} q_x^2 e^{-q_\perp |z-z'|} \right. \\ \left. + \delta(z-z') \left( \delta \left( z' - \frac{L}{2} \right) - \delta \left( z' + \frac{L}{2} \right) \right) \left( B_3 \frac{\partial}{\partial z'} + 2B_{13} i q_x \right) \right] \varphi_{\mathbf{q}_\perp}(z'). \end{aligned} \quad (2.13)$$

The resulting expression for the free energy enables us to find the correlation function for the angle  $\varphi$ , ie,  $\mathbf{c}$ -director fluctuations:

$$g_{\mathbf{q}_\perp}(z, z') = \int d\mathbf{r}_\perp e^{-i\mathbf{q}_\perp \cdot \mathbf{r}_\perp} \langle \varphi(\mathbf{r}_\perp, z) \varphi(\mathbf{0}, z') \rangle. \quad (2.14)$$

Here  $\langle \dots \rangle$  represents the statistical averaging over all configurations of the angle  $\varphi$  field. Correlation function  $g_{\mathbf{q}_\perp}(z, z')$  is the core of inverse operator  $\hat{M}^{-1}$ , multiplying by

$k_B T$ , where  $T$  is the temperature and  $k_B$  is the Boltzmann constant. Hence, the correlation function  $g_{\mathbf{q}_\perp}(z, z')$  must satisfy the equation:

$$\hat{M}g = k_B T \delta(z - z'), \tag{2.15}$$

or in explicit form:

$$\begin{aligned} & \left( B_1 q_x^2 + B_2 q_y^2 + PE - B_3 \frac{\partial^2}{\partial z^2} - 2B_{13} i q_x \frac{\partial}{\partial z} \right) g_{\mathbf{q}_\perp}(z, z') + \\ & + \int_{-\frac{L}{2}}^{\frac{L}{2}} dz'' \frac{2\pi P^2}{q_\perp \varepsilon} q_x^2 e^{-q_\perp |z-z''|} g_{\mathbf{q}_\perp}(z'', z') + \\ & + \left( \delta\left(z - \frac{L}{2}\right) - \delta\left(z + \frac{L}{2}\right) \right) \left( B_3 \frac{\partial}{\partial z} + 2B_{13} i q_x \right) g_{\mathbf{q}_\perp}(z, z') = k_B T \delta(z - z') \end{aligned} \tag{2.16}$$

To solve the integral-differential equation, it is convenient to enter the following function  $v_{\mathbf{q}_\perp}(z, z')$ , defined as:

$$v_{\mathbf{q}_\perp}(z, z') = q_\perp \int_{-\frac{L}{2}}^{\frac{L}{2}} dz'' e^{-q_\perp |z-z''|} g_{\mathbf{q}_\perp}(z'', z'). \tag{2.17}$$

This allows us to solve the following system of differential equations instead of the integral-differential equation:

$$\begin{cases} \left( -\partial_z^2 - 2b_{13} i q_x \partial_z + b_1 q_x^2 + b_2 q_y^2 + \frac{PE}{B_3} \right) g_{\mathbf{q}_\perp}(z, z') + \\ + \frac{2\pi P^2}{B_3 q_\perp \varepsilon} q_x^2 v_{\mathbf{q}_\perp}(z, z') = \frac{k_B T}{B_3} \delta(z - z') \\ \left( -\partial_z^2 + q_\perp^2 \right) v_{\mathbf{q}_\perp}(z, z') - 2q_\perp^2 g_{\mathbf{q}_\perp}(z, z') = 0, \end{cases} \tag{2.18}$$

Here, we use the notations:

$$\begin{aligned} \partial_z &= \frac{\partial}{\partial z}, & \partial_z^2 &= \frac{\partial^2}{\partial z^2}, \\ b_1 &= \frac{B_1}{B_3}, & b_2 &= \frac{B_2}{B_3}, & b_{13} &= \frac{B_{13}}{B_3}. \end{aligned}$$

The boundary conditions for the system (2.18) have the form:

$$\begin{cases} \pm \partial_z v_{\mathbf{q}_\perp}(z = \pm \frac{L}{2}, z') + q_\perp v_{\mathbf{q}_\perp}(z = \pm \frac{L}{2}, z') = 0 \\ \partial_z g_{\mathbf{q}_\perp}(z = \pm \frac{L}{2}, z') + 2i q_x b_{13} g_{\mathbf{q}_\perp}(z = \pm \frac{L}{2}, z') = 0. \end{cases} \tag{2.19}$$

The first of these conditions permits the removal of terms with  $\delta$ -functions from the left-hand side of Eq. (2.16), and the second follows from the rule for differentiating of the function  $v_{\mathbf{q}_\perp}(z, z')$  at the boundary of the film.

For the solution of the system (2.18) with boundary conditions (2.19), it is convenient to enter two four-dimensional vectors in the same way as it was done in [10]:

$$\begin{aligned} \mathbf{W} &= (g, v, \partial_z g, \partial_z v)^T, \\ \mathbf{D} &= \frac{k_B T}{B_3} (0, 0, 1, 0)^T. \end{aligned} \tag{2.20}$$

Here, the upper index “ $T$ ” denotes the transposition. In the given notations, the system (2.18) has the form:

$$(\partial_z - \hat{H})\mathbf{W} = -\mathbf{D}\delta(z - z'), \tag{2.21}$$

where:

$$\hat{H} = \begin{pmatrix} 0 & 0 & 1 & 0 \\ 0 & 0 & 0 & 1 \\ a & b & -f & 0 \\ -2q_\perp^2 & q_\perp^2 & 0 & 0 \end{pmatrix}. \tag{2.22}$$

We have introduced here the following notation:

$$\begin{aligned} a &= b_1 q_x^2 + b_2 q_y^2 + \frac{PE}{B_3}, \\ b &= \frac{2\pi P^2 q_x^2}{B_3 q_{\perp}^2 \varepsilon}, \\ f &= 2b_{13} q_x i. \end{aligned}$$

The boundary conditions for the Eq. (2.21), as it follows from (2.19), take the following form:

$$\hat{\Gamma}_{\sigma} \mathbf{W}_{\mathbf{q}_{\perp}} \left( z = \sigma \frac{L}{2}, z' \right) = 0, \quad (2.23)$$

where  $\sigma = \pm$  corresponds to  $z = \pm L/2$ , and the matrix  $\hat{\Gamma}_{\sigma}$  has the form:

$$\hat{\Gamma}_{\sigma} = \begin{pmatrix} f & 0 & 1 & 0 \\ 0 & q_{\perp} & 0 & \sigma 1 \end{pmatrix}. \quad (2.24)$$

The boundary conditions (2.23) are satisfied by the vectors proportional to the following linearly independent vectors:

$$\begin{aligned} \mathbf{w}^{(1)} &= (1, 0, -f, 0)^T, \\ \mathbf{w}^{(\sigma)} &= (0, \sigma 1, 0, -q_{\perp})^T, \end{aligned}$$

Therefore, the solution of Eq. (2.21) satisfying the boundary condition (2.23) can be found in the form:

$$\mathbf{W}_{\mathbf{q}_{\perp}}^{\sigma}(z, z') = e^{(z-\sigma \frac{L}{2})\hat{H}} (\mathbf{w}^{(1)} C_{\sigma}^{(1)}(z') + \mathbf{w}^{(\sigma)} C_{\sigma}^{(2)}(z')). \quad (2.25)$$

Here,  $\mathbf{W}_{\mathbf{q}_{\perp}}^{+}(z, z')$  corresponds to  $\mathbf{W}_{\mathbf{q}_{\perp}}(z, z')$  at  $z > z'$  and  $\mathbf{W}_{\mathbf{q}_{\perp}}^{-}(z, z')$  corresponds to  $\mathbf{W}_{\mathbf{q}_{\perp}}(z, z')$  at  $z < z'$ . Unknown functions  $C_{\sigma}^{(1)}(z')$  and  $C_{\sigma}^{(2)}(z')$  can be found by substituting of Eq. (2.25) into Eq. (2.21) and integrating the resulting equation with respect to  $z$  over the interval  $[z' - \varepsilon, z' + \varepsilon]$  where  $\varepsilon \rightarrow +0$ . As a result, we obtain the following algebraic vector equation for the functions  $C_{\sigma}^{(1)}(z')$  and  $C_{\sigma}^{(2)}(z')$ :

$$\mathbf{W}_{\mathbf{q}_{\perp}}^{+}(z', z') - \mathbf{W}_{\mathbf{q}_{\perp}}^{-}(z', z') = -\mathbf{D}. \quad (2.26)$$

The solution of this equation can easily be found in the following form:

$$\left( C_{+}^{(1)}, C_{+}^{(2)}, C_{-}^{(1)}, C_{-}^{(2)} \right)^T = -\hat{S}^{-1} e^{(\frac{L}{2}-z')\hat{H}} \mathbf{D}. \quad (2.27)$$

Here,  $\hat{S}^{-1}$  is the matrix inverse to the matrix  $\hat{S}$  consisting of the following columns:

$$\hat{S} = \left( \mathbf{w}^{(1)}, \mathbf{w}^{(+)}, -e^{-L\hat{H}} \mathbf{w}^{(1)}, -e^{-L\hat{H}} \mathbf{w}^{(-)} \right). \quad (2.28)$$

The functions  $C_{\sigma}^{(1)}(z')$  and  $C_{\sigma}^{(2)}(z')$ , found in Eq. (2.27), can be substituted into Eq. (2.25). The desired the correlation function  $g_{\mathbf{q}_{\perp}}(z, z')$  is given by the first component of the found four-dimensional vector  $\mathbf{W}_{\mathbf{q}_{\perp}}(z, z')$ .

### 3. Light scattering by c-director fluctuations

Light scattering in Sm-C\* occurs with fluctuations of the permittivity, which are connected with the fluctuations of c-director. In the lowest approximation with respect to the angle  $\varphi$ , we have:

$$\delta \tilde{\varepsilon}_{\alpha\beta} = \tilde{\varepsilon}_{\alpha} \left( \frac{\partial n_{\alpha}}{\partial \varphi} n_{\beta} + n_{\alpha} \frac{\partial n_{\beta}}{\partial \varphi} \right) \varphi. \quad (3.1)$$

Here,  $\tilde{\varepsilon}_a$  is the anisotropy of the permittivity at optical frequencies. In the Born approximation, the intensity of the scattered light can be represented as [12-14]:

$$I = \frac{VI_0k_0^4}{(4\pi R)^2} e_\alpha^{(s)} e_\beta^{(s)} W_{\alpha\nu\beta\mu}(\mathbf{q}_{sc}) e_\nu^{(i)} e_\mu^{(i)}, \quad (3.2)$$

where  $I$  is the intensity of the scattered light,  $I_0$  is the intensity of the incident beam,  $V$  is the scattering volume,  $k_0$  is the wave number of the incident and scattered beams,  $R$  is the distance from the film to the observation point,  $\mathbf{e}^{(i)}$  and  $\mathbf{e}^{(s)}$  are the polarization vectors in the incident and scattered rays,  $\mathbf{q}_{sc} = \mathbf{k}_s - \mathbf{k}_i$  is the scattering vector,  $\mathbf{k}_i$  and  $\mathbf{k}_s$  are the wave vectors of the incident and scattered rays. The function  $W_{\alpha\nu\beta\mu}(\mathbf{q}_{sc})$  is the Fourier transform of the correlation function for permittivity fluctuations at optical frequencies, namely:

$$W_{\alpha\nu\beta\mu}(\mathbf{q}) = \frac{1}{L} \int_{-\frac{L}{2}}^{\frac{L}{2}} dz \int_{-\frac{L}{2}}^{\frac{L}{2}} dz' e^{-iq_z(z-z')} \int d\mathbf{r}_\perp e^{-i\mathbf{q}_\perp \cdot \mathbf{r}_\perp} \langle \delta\tilde{\varepsilon}_{\alpha\nu}(\mathbf{r}_\perp, z) \delta\tilde{\varepsilon}_{\beta\mu}(\mathbf{0}, z') \rangle. \quad (3.3)$$

Here, for the wave vector used, the notation  $\mathbf{q} = (\mathbf{q}_\perp, q_z)$ . After substituting Eqs. (3.1) and (3.3) into Eq. (3.2), and taking into account the definition (2.14), we obtain the following expression for the intensity of light scattering:

$$I \sim \tilde{\varepsilon}_a^2 \left[ e_\alpha^{(s)} \left( \frac{\partial n_\alpha}{\partial \varphi} n_\beta + n_\alpha \frac{\partial n_\beta}{\partial \varphi} \right) e_\beta^{(i)} \right]^2 G_{\mathbf{q}_{sc}}, \quad (3.4)$$

Where:

$$G_{\mathbf{q}} = \frac{1}{L} \int_{-\frac{L}{2}}^{\frac{L}{2}} dz \int_{-\frac{L}{2}}^{\frac{L}{2}} dz' e^{-iq_z(z-z')} g_{\mathbf{q}_\perp}(z, z'). \quad (3.5)$$

The numerical calculations were performed for the beam incident on the film surface at the angle  $\theta_i$  relative to the  $z$  axis in the  $xz$  plane. Fig. 2 shows the geometry of the optical experiment for the case of incidence of the beam normal to the Sm-C\* film.

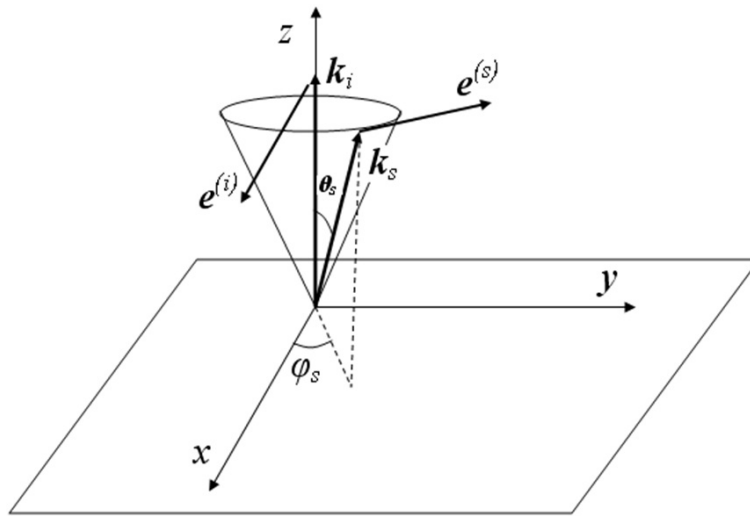


FIG. 2. Direction of the wave vectors of the incident and scattered rays in an optical experiment,  $\mathbf{k}_i$  and  $\mathbf{k}_s$ , respectively. Also shown are the direction of the polarization vectors in the incident and scattered rays:  $\mathbf{e}^{(i)}$  and  $\mathbf{e}^{(s)}$

The wave vectors of the incident and scattered rays and the polarization vectors in this geometry are given by:

$$\begin{aligned} \mathbf{k}_i &= k_0(\sin \theta_i, 0, \cos \theta_i), \\ \mathbf{k}_s &= k_0(\sin \theta_s \cos \varphi_s, \sin \theta_s \sin \varphi_s, \cos \theta_s), \\ \mathbf{e}^{(i)} &= (1, 0, 0), \\ \mathbf{e}^{(s)} &= (-\sin \varphi_s, \cos \varphi_s, 0). \end{aligned} \quad (3.6)$$

Here,  $\theta_i$  and  $\theta_s$  polar angles of the incident and scattered rays,  $\varphi_s$  is the azimuth angle of the scattered beam. In this case, we obtain from Eq. (3.4) the following angular dependence of the scattered light intensity:

$$I \sim \tilde{\varepsilon}_a^2 \sin^4 \theta \cos^2 \varphi_s G_{\mathbf{q}_{sc}}. \quad (3.7)$$

It should be noted that the angular dependence of the intensity is determined entirely by the last two factors in Eq. (3.7), while the first two factors are material constants.

The numerical calculations were performed via Eq. (3.7) for the free standing Sm-C\* film with the following parameters:  $L = 10^{-4}$  cm,  $\theta = 15^\circ$ ,  $\tilde{\varepsilon}_a = 5$ ,  $k_0 = 10^5$  cm $^{-1}$ ,  $E = 0.3$  statvolt/cm = 8994 V/m,  $K_{11} = 0.7 \cdot 10^{-6}$  dyn =  $0.7 \cdot 10^{-11}$  N,  $K_{22} = 0.4 \cdot 10^{-6}$  dyn =  $0.4 \cdot 10^{-11}$  N,  $K_{33} = 1.7 \cdot 10^{-6}$  dyn =  $1.7 \cdot 10^{-11}$  N. For spontaneous polarization, different values were used, namely,  $P = 10, 15, 20$  statcoulomb/cm $^2 = 3.34 \cdot 10^4, 5.01 \cdot 10^4, 6.67 \cdot 10^4$  nC/m $^2$ .

In Figs. 3 and 4 are shown the angular dependences for the scattered light intensity in the case where the  $xz$  plane is the scattering plane. Since in this case  $\varphi_s = 0$ , it follows from the Eq. (3.7) that precisely the same angular dependence has the correlation function of the  $\mathbf{c}$ -director fluctuations  $G_{\mathbf{q}_{sc}}$ .

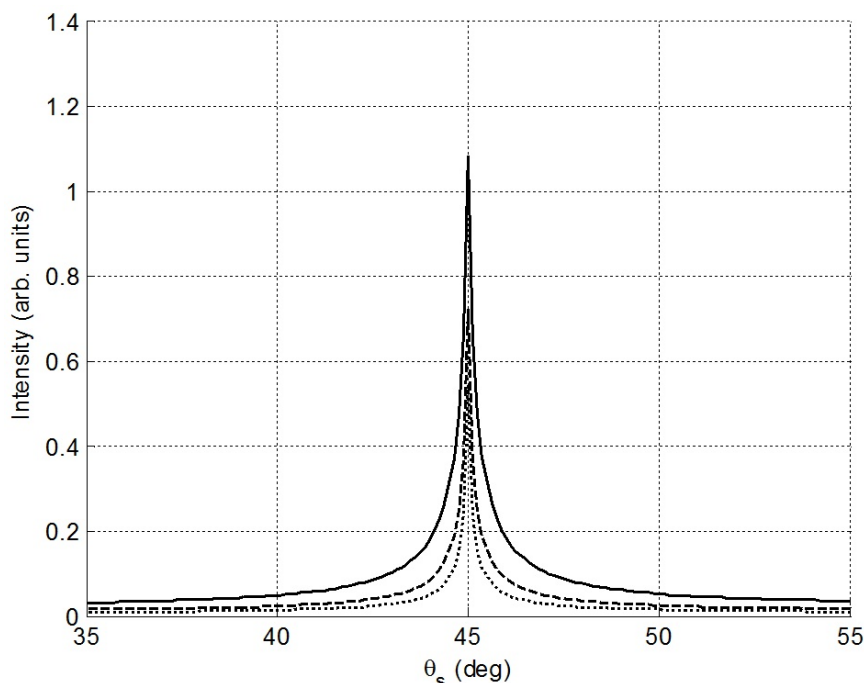


FIG. 3. The angular dependence of the scattered light intensity is shown for different spontaneous polarization values. For solid, dashed and dotted lines, the spontaneous polarization values are respectively: 10, 15, 20 statcoulomb/cm $^2$ . The beam of light falls on the film at an angle of  $45^\circ$  to the normal. The scattering plane coincides with the  $xz$  plane

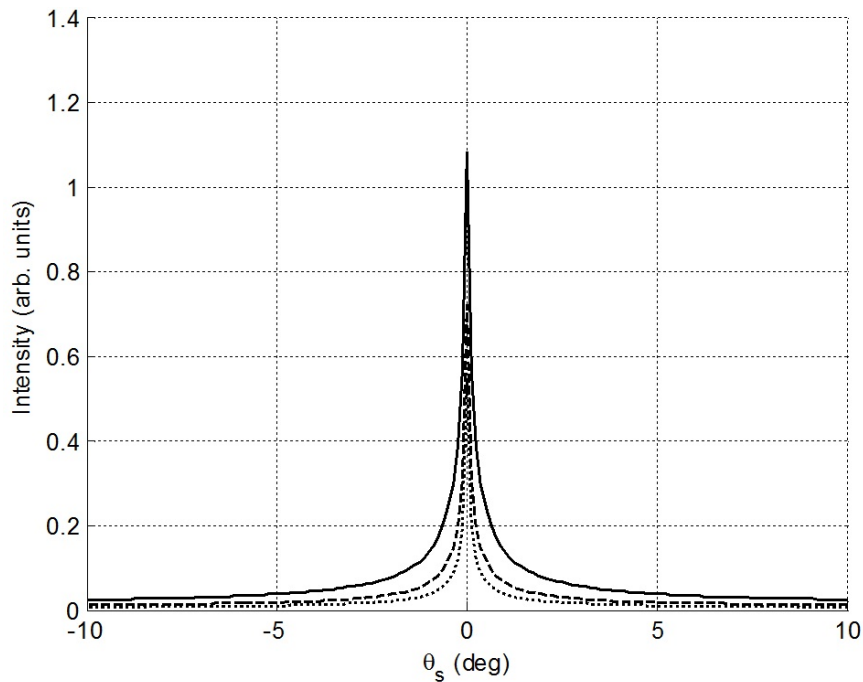


FIG. 4. The same as in Fig. 3, but in this instance, the light beam's angle of incidence is perpendicular to the film's surface. Positive values of  $\theta_s$  correspond to  $\varphi_s = 0^\circ$ , and negative to  $\varphi_s = 180^\circ$

As can be seen from Figs. 3, 4, the correlation function of  $\mathbf{c}$ -director fluctuations  $G_{\mathbf{q}}$  and the scattered light intensity are significantly dependent on the spontaneous polarization  $P$ . These dependences are mainly determined by the electrostatic interaction of the polarization charges. With increased spontaneous polarization  $P$ , the correlation function  $G_{\mathbf{q}_{sc}}$  and the scattered light intensity are reduced. Hence, the  $\mathbf{c}$ -director fluctuations are suppressed with increasing  $P$ ; i.e., the system becomes more rigid in orientation, as was noted in [4-9, 15].

In Figs. 5 and 6 are shown respectively the dependences of the scattered light intensity and the correlation function  $G_{\mathbf{q}_{sc}}$  on the azimuthal angle  $\varphi_s$  at normal incidence of light on the film. The incident beam is polarized in the direction of the  $x$  axis, perpendicular to the external electric field. The scattered beam propagates at an angle of  $10^\circ$  relative to the normal to the smectic layers and is polarized in the  $xy$  plane. Fig. 5 shows that the correlation function  $G_{\mathbf{q}_{sc}}$  significantly depends on the value of the spontaneous polarization  $P$  and the azimuthal angle  $\varphi_s$ . The function  $G_{\mathbf{q}_{sc}}$  reaches a maximum when  $\mathbf{q}_{sc}$  is within the  $xy$  plane, and minimal, if  $\mathbf{q}_{sc} \in xz$ . Fig. 6 shows that in accordance with Eq. (3.7), the effects associated with the geometry of the experiment are added to the above relationships in the intensity of the scattered light. If the direction of the wave vector and the polarization vector in the incident and scattered rays are given by Eq. (3.6), the maximum intensity should be observed in the scattering plane  $xz$ , and the minimum occurs in the  $xy$  plane.

#### 4. Conclusion

A number of works have suggested that the electrostatic interaction between the polarization charges may be very important in the study of Sm- $C^*$  [4-8, 16-19]. Systems with a large spontaneous polarization have been shown to increase the effective rigidity of the orientation and increase the effective orientation viscosity [4-9, 15]. We have studied

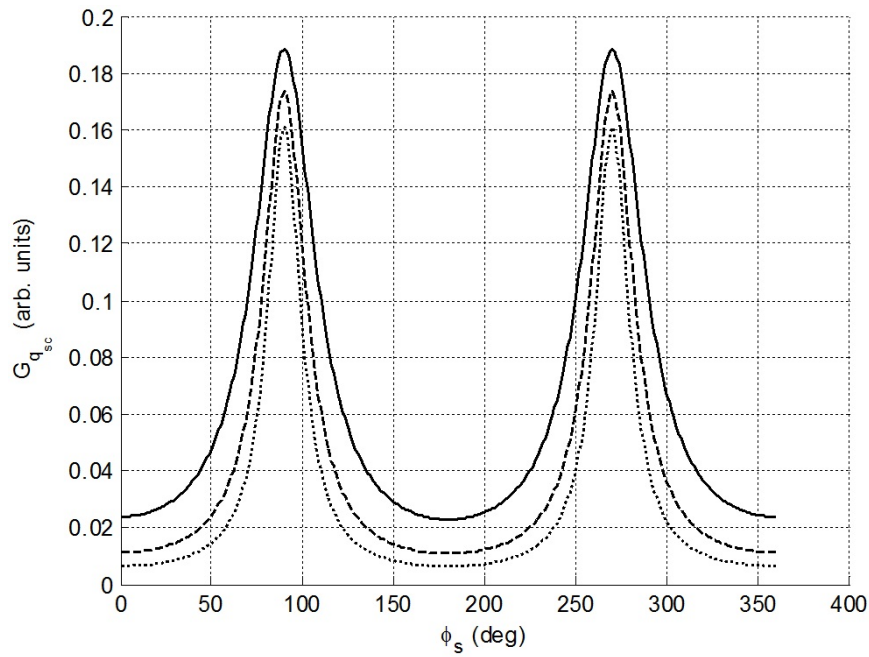


FIG. 5. The dependence of the correlation function  $G_{\mathbf{q}_{sc}}$  on the azimuthal angle  $\varphi_s$  is shown for the same spontaneous polarization values as in Fig. 3. A beam of light falls perpendicular to the surface of the film. The value  $\theta_s = 10^\circ$  remains constant

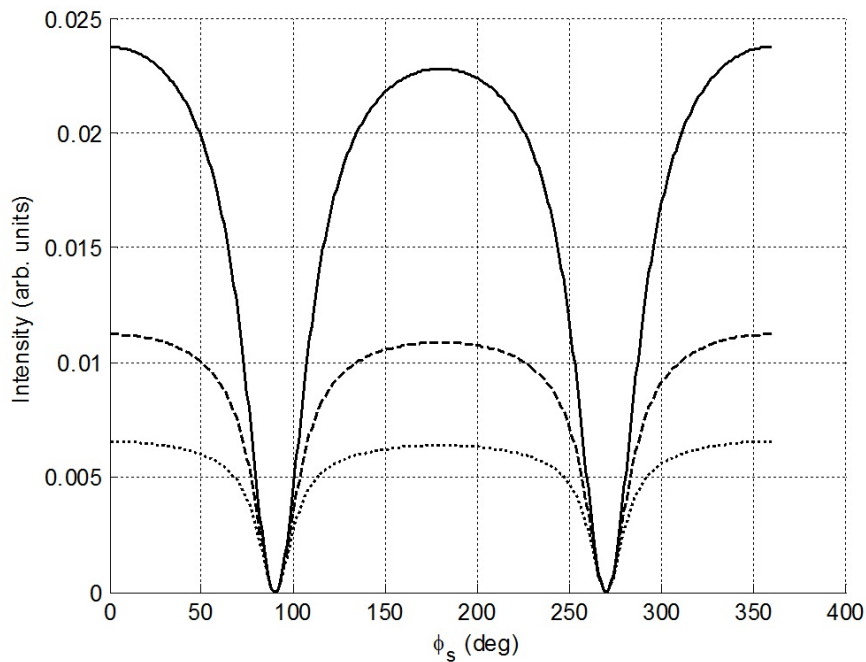


FIG. 6. The dependence of the scattered light intensity on the azimuthal angle  $\varphi_s$  is shown for the same conditions used in Fig. 5

the role of the Coulomb interaction between the polarization charges in the formation of the correlation function of director fluctuations in freely standing Sm-C\* films of finite thickness. The film considered was in an external electric field directed along the layers. At equilibrium, the  $\mathbf{c}$ -director helicoid was unwound. The obtained correlation function permitted the calculation of the angular dependence for the scattered light intensity. As a result of the calculations, the correlation function for the orientation fluctuations and the scattered light intensity were found to significantly depend on the magnitude of the spontaneous polarization. These relationships are caused by the Coulomb interaction between the polarization charges occurring due to orientation fluctuations. Increasing the magnitude of polarization was shown to significantly reduce the correlation function of the orientation fluctuations as well as the scattered light intensity, indicating that the suppression of the director fluctuations occurs as a result of the electrostatic interaction between the polarization charges. This can be regarded as a definite increase in the orientation rigidity of the system.

## Acknowledgments

The authors acknowledge Saint Petersburg State University for research Grants No. 11.37.145.2014 and No. 11.37.161.2014, and the Russian Foundation for Basic Research for Grant No. 13-02-01255-a.

## References

- [1] De Gennes P.G., Prost J. *The Physics of Liquid Crystals*. Clarendon, Oxford, UK, 1993, 597 p.
- [2] Demus D., Goodby J., Gray G.W., Spiess H.-W., Vill V. *Handbook of Liquid Crystals*. Wiley-VCH, Weinheim, 1998, Vol. 2B., 491-1009.
- [3] Takezoe H., Gorecka E., Cepic M. Antiferroelectric liquid crystals: Interplay of simplicity and complexity. *Rev. Mod. Phys.*, 2010, **82**(1), P. 897–938.
- [4] Young C.Y., Pindak R., Clark N.A., Meyer R.B. Light-Scattering Study of Two-Dimensional Molecular-Orientation Fluctuations in a Freely Suspended Ferroelectric Liquid-Crystal Film. *Phys. Rev. Lett.*, 1978, **40**, P. 773–776.
- [5] Rosenblatt C., Pindak R., Clark N.A., Meyer R.B. Freely Suspended Ferroelectric Liquid-Crystal Films: Absolute Measurements of Polarization, Elastic Constants, and Viscosities. *Phys. Rev. Lett.*, 1979, **42**, P. 1220–1223.
- [6] Rosenblatt C., Meyer R.B., Pindak R., Clark N.A. Temperature behavior of ferroelectric liquid-crystal thin films: A classical XY system. *Phys. Rev. A*, 1980, **21**, P. 140-147.
- [7] Lu M.H., Crandall K.A., Rosenblatt C. Polarization-induced renormalization of the B1 elastic modulus in a ferroelectric liquid crystal. *Phys. Rev. Lett.*, 1992, **68**, P. 3575–3578.
- [8] Lu M.H., Rosenblatt C., Petschek R.G. Ion-director coupling in a ferroelectric liquid crystal. *Phys. Rev. E*, 1993, **47**, P. 1139–1143.
- [9] Lee J.B., Pelcovits R.A., Meyer R.B. Role of electrostatics in the texture of islands in free-standing ferroelectric liquid crystal films. *Phys. Rev. E*, 2007, **75**, P. 051701(5).
- [10] Shalaginov A.N. Light Scattering by Fluctuations in a ferroelectric Liquid-Crystal Cell. *Optics and spectroscopy*, 1998, **85**(1), P. 99–105.
- [11] Romanov V.P., Ulyanov S.V. Anisotropy of electrostatic interaction in smectic-C\* liquid crystals. *Phys. Rev. E*, 2014, **90**(5), P. 052502(6).
- [12] Lax M., Nelson D.F. Adventures in Green's Land: Light Scattering in Anisotropic Media. In Proceedings of the Third Rochester Conference on Coherence and Quantum Optics. Plenum, New York, 1973, P. 415–445.
- [13] Langevin D., Bouchiat M.-A. Anisotropy of the turbidity of an oriented nematic liquid crystal. *J. Phys. (Paris)*, 1975, Colloq. 36, C1-197-C1-202.
- [14] Val'kov A.Yu., Romanov V.P. Characteristics of propagation and scattering of light in nematic liquid crystals. *Sov. Phys. JETP*, 1986, **63**(4), P. 737–743.

- [15] Link D.R., Chattham N., MacLennan J.E., Clark N.A. Effect of high spontaneous polarization on defect structures and orientational dynamics of tilted chiral smectic freely suspended films. *Phys. Rev. E*, 2005, **71**(2), P. 021704(9).
- [16] Dolganov P.V., Dolganov V.K., Cluzeau P. The Effect of Spontaneous Polarization on Two-Dimensional Elasticity of Smectic Liquid Crystals. *J. Exp. Theor. Phys.*, 2013, **116**(6), P. 1043–1049.
- [17] Pattanaporkratana A., Park C.S., MacLennan J.E., Clark N.A. Direct Measurement of Interaction Forces Between Islands on Freely Suspended Smectic C Films Using Multiple Optical Tweezers. *Ferroelectrics*, 2006, **344**, P. 71–80.
- [18] Vijay Kumar M., Krishna Prasad S. Composites of single walled carbon nanotubes and liquid crystals as switchable conductor. *Nanosystems: Physisc, Chemistry, Mathematics*, 2013, **4**(3), P. 425-429.
- [19] Bogdanov A.A., Denisov S.P., Karetnikov A.A., Kovshik A.P., Romanov V.P., Brukkel D. The effect of the cell phone radiation on a freely suspended liquid-crystal film. *Nanosystems: Physisc, Chemistry, Mathematics*, 2014, **5**(6), P. 782–788.
- [20] Ulyanov S.V., Romanov V.P., Uzdin V.M. X-ray scattering from layered nanosystems with rough interfaces. *Nanosystems: Physisc, Chemistry, Mathematics*, 2012, **3**(3), P. 110–122.

# Exact classical stochastic representations of the many-body quantum dynamics

E. A. Polyakov<sup>1</sup>, P. N. Vorontsov-Velyaminov<sup>1</sup>

<sup>1</sup>Saint Petersburg State University,  
Dept. of molecular biophysics and polymer physics, Faculty of Physics,  
198504, Saint Petersburg, Russia

e.a.polyakov@gmail.com, voron.wgroup@gmail.com

PACS 05.30.Ch, 05.10.Gg, 02.70.-c, 02.70.Ss

DOI 10.17586/2220-8054-2015-6-4-501-512

In this work we investigate the exact classical stochastic representations of many-body quantum dynamics. We focus on the representations in which the quantum states and the observables are linearly mapped onto classical quasiprobability distributions and functions in a certain (abstract) phase space. We demonstrate that when such representations have regular mathematical properties, they are reduced to the expansions of the density operator over a certain overcomplete operator basis. Our conclusions are supported by the fact that all the stochastic representations currently known in the literature (quantum mechanics in generalized phase space and, as it recently has been shown by us, the stochastic wave-function methods) have the mathematical structure of the above-mentioned type. We illustrate our considerations by presenting the recently derived operator mappings for the stochastic wave-function method.

**Keywords:** quantum ensemble theory, quantum noise, stochastic equations.

*Received: 20 June 2015*

## 1. Introduction

At the theoretical department of Physical Faculty at Saint Petersburg State University, there is a scientific school with long-standing experience in various fields of stochastic systems, stochastic dynamics, and their applications to the physics of condensed matter. V. P. Romanov, to whose memory is devoted the current issue, contributed to this school by his works on stochastic aspects of light propagation in fluctuating nematic liquid crystals [1-3].

Over the past few decades, increasing efforts have been undertaken to devise and carry out the exact stochastic (Monte Carlo) simulations of many-body quantum dynamics. The field of research, which is the subject of such an activity, is truly interdisciplinary: quantum optics [4], ultracold atoms in traps [5-7], quantum phase transitions [8], open quantum systems [9], and the measurement theory [10]. The motivation behind such studies range from purely practical (to provide exact data in order to verify a theory, or in order to interpret an experiment) to fundamental (to characterize the relationship between the classical and quantum computational complexity).

In order to devise a Monte Carlo simulation algorithm for quantum dynamics, we need to represent the quantum dynamics as an equivalent (with respect to average observable properties) probabilistic model. Such a model is called a stochastic representation. In this work, we focus only on classical diffusive stochastic representations of the reversible dynamics for quantum systems with pairwise interactions. Here, the adjective “classical” means that

the quantum dynamics is mapped onto a classical stochastic process, rather than onto some quantum non-commutative extension of stochastic calculus [11].

Despite the fact that more than thirty years have passed since the fundamental work of Drummond *et al.* [4], where the first exact classical stochastic representation was introduced, this field of research still remains at an early stage of development. This is reflected in the fragmentedness of the literature on this subject: novel stochastic methods are constantly being invented [12-20], but based on entirely different and unrelated principles.

The classical stochastic representations of reversible quantum dynamics can be divided into two major groups: quantum dynamics in the generalized phase space, and stochastic wave-function methods. In our recent paper [21], we have demonstrated that the latter group of methods actually has the mathematical structure of the former, i. e. these two groups can be united into one common group.

In this work, we make an attempt to summarize various approaches in the literature [12-20] by defining the most general formulation for the classical stochastic representation of quantum dynamics. In Sec. 2, we define the notion of the classical stochastic representation. In such a representation, the mappings, which associate the classical quasiprobability distributions and functions with the quantum states and observables, appear as linear operators. In Sec. 3 we discuss (at the physical level of rigor) the general implications of the proposed definition of the classical stochastic representation. In particular, we demonstrate that, provided the mathematical properties of the representation are sufficiently regular, the representation reduces to an expansion of the density operator over a certain overcomplete operator basis. In Sec. 4, we illustrate our definitions by providing a concrete implementation of the classical stochastic representation: we present the recently derived [21] ordered operator correspondences for the stochastic wave-function method of Carusotto *et al.* [22].

## 2. The classical stochastic representation

Suppose that we are given a many-body quantum system with a Hamiltonian  $\hat{H}$ :

$$\hat{H} = \sum_{r,s} h_{rs} \hat{a}_r^\dagger \hat{a}_s + \frac{1}{2} \sum_{r,s} V_{rs} \hat{a}_r^\dagger \hat{a}_s^\dagger \hat{a}_s \hat{a}_r, \quad (1)$$

containing a two-body interaction. Here, we assume that discretization of the continuous system was carried out [21], and the annihilation  $\hat{a}_r$  and creation  $\hat{a}_s^\dagger$  operators adhere to the bosonic commutation relations:

$$[\hat{a}_r, \hat{a}_s^\dagger] = \delta_{rs}, \quad (2)$$

where  $r$  and  $s$  are the (multi-)indices of the discretization lattice sites [21]. The exact quantum evolution is governed by the full many-body quantum Liouville equation:

$$\frac{\partial}{\partial t} \hat{\rho} = \frac{1}{i\hbar} [\hat{H}, \hat{\rho}(t)], \quad (3)$$

where the density operator  $\hat{\rho}(t)$  determines the state of the system at time  $t$ .

Summarizing various classical stochastic representations which are presented in the literature [12-20, 23, 24], we arrive at a general formulation for what we call here the “classical stochastic representation”. We select a certain convex set  $P_+$  of physical density operators which are characteristic to our system. That is, if we take an arbitrary density operator  $\hat{\rho}_0 \in P_+$  as the initial condition for Eq. (3) at  $t = 0$ , then, at any later time  $t$ , the solution  $\hat{\rho}(t)$  of Eq. (3) still belongs to the set  $P_+$ .

In a classical stochastic representation of quantum dynamics, the quantum state should be represented by a quasiprobability distribution in a certain (abstract) space  $L$ . The

prefix 'quasi' means that such distributions do not correspond to any physical probabilities, and such distributions do not even satisfy the Kolmogorov axioms, since the elements  $\lambda$  of the space  $L$  cannot be interpreted as elementary events (usually, the Dirac distributions corresponding to the elements  $\lambda$  do not correspond to any physical state). The space  $L$  is usually called the generalized phase space [23-26], due to its intrinsic analogy to the phase space in the deformation quantization [27]. We suppose that the stochastic representation provides us with a methodology for how to assign a positive quasiprobability distribution  $\mathcal{P}(\lambda)$  to any  $\hat{\rho} \in P_+$ . Such a procedure is given by the (possibly nonlinear) mapping  $C_\rho$ :

$$C_\rho[\hat{\rho}] = \mathcal{P}(\lambda), \quad \text{where } \mathcal{P}(\lambda) \geq 0 \text{ for every } \lambda \in L. \tag{4}$$

In a classical stochastic representation, the average value for the observable  $\langle \hat{o} \rangle$  should be represented by a classical expectation over the quasiprobability. Therefore, we need a second mapping,  $C_o$ :

$$C_o \hat{o} = \mathcal{O}(\lambda), \tag{5}$$

which defines how the quantum observables in our stochastic representation are delineated by classical functions  $\mathcal{O}(\lambda)$  in the space  $L$ . Then, we have the expression for the expected value  $\langle \hat{o} \rangle$ :

$$\langle \hat{o} \rangle = \text{Tr} \hat{o} \hat{\rho} = \int d\lambda \mathcal{O}(\lambda) \mathcal{P}(\lambda), \tag{6}$$

which is required to be valid for every classical representation of the observable  $\mathcal{O}(\lambda)$  and for every quasiprobability  $\mathcal{P}(\lambda)$  from the image  $\text{im } C_\rho$ . We assume that the mapping  $C_o$  is a linear operator.

We are not only interested in the expected values of the observables, but also in their evolution over time. We want the time evolution in our representation to be represented in such a way, that it could be simulated by Monte Carlo methods. Thus, we need a third mapping,  $C_s$ :

$$C_s \left\{ \left[ \hat{H}, \cdot \right] / i\hbar \right\} = \mathcal{H}. \tag{7}$$

This defines how the quantum Liouville superoperator  $\left[ \hat{H}, \cdot \right] / i\hbar$  is being represented by such integro-differential operator  $\mathcal{H} : D \rightarrow D$ , that the quantum Liouville equation (3) is now represented by the differential Chapman-Kolmogorov master equation:

$$\frac{\partial}{\partial t} \mathcal{P} = \mathcal{H} \mathcal{P}. \tag{8}$$

For example, if we are interested in a diffusive stochastic representation, we may look for such a stochastic representation which possesses such a mapping  $C_s$  that  $\mathcal{H}$  is a Fokker-Planck operator (in the Ito form [28]):

$$\mathcal{H} = - \sum_i \frac{\partial}{\partial \lambda_i} \mathcal{A}_i(\lambda) + \frac{1}{2} \sum_{i,j} \frac{\partial^2}{\partial \lambda_i \partial \lambda_j} \mathcal{D}(\lambda), \tag{9}$$

where  $\lambda_i$  is a component of the vector  $\lambda$  (if the space  $L$  is multidimensional). In this case, we can simulate the quantum dynamics by numerically integrating the stochastic differential equation

$$d\lambda_i = \mathcal{A}_i(\lambda) dt + \sum_j \mathcal{B}_{ij}(\lambda) dW_j, \tag{10}$$

where the Wiener increments have the standard statistical properties,  $E[dW_i] = 0$  and  $E[dW_i dW_j] = \delta_{ij} dt$ ;  $\mathcal{D} = \mathcal{B} \mathcal{B}^T$  [28]. We assume that the mapping  $C_s$  is a linear operator.

The practical Monte Carlo simulation involves the following stages. First, we represent the initial condition  $\hat{\rho}(t=0)$  as a positive quasiprobability distribution  $\mathcal{P}(\lambda, t=0)$  using the mapping  $C_\rho$ . Then, we sample the initial conditions  $\lambda(t=0)$  for the stochastic process (10) from the initial probability  $\mathcal{P}(\lambda, t=0)$  using the importance sampling method [29]. Each sampled initial condition  $\lambda(t=0)$  is propagated in time by the numerical integration of the stochastic differential equation (10). The average value of the observable  $\langle \hat{o} \rangle(t)$  at a time  $t$  is evaluated as the classical expectation  $\langle \hat{o} \rangle(t) = \mathbb{E}[\mathcal{O}(\lambda(t))]$  over an ensemble of trajectories  $\lambda(t)$ .

### 3. Some properties of the stochastic representations

#### 3.1. The mapping for observables $C_o$

Our classical stochastic model, as defined in the previous section by the tuple  $(P_+, L, C_\rho, C_o, C_s)$ , should bear a physical meaning. Let us examine what consequences can be drawn from this statement. The state of a physical system is completely defined by its observable properties. In the quantum case, the latter statement is true, since the density operator  $\hat{\rho}$  is completely defined by all the moments of the canonically conjugate variables [30-32]. Therefore, the most important ingredient of our otherwise completely abstract model is the mapping  $C_o$  for the observables. Let us write the trace formula (6) as a dot product:

$$\langle \hat{o} \rangle = \text{Tr} \hat{o} \hat{\rho} = \langle \mathcal{O}^*, \mathcal{P} \rangle_{S_+}. \quad (11)$$

Suppose that all the observable operators  $\hat{o}$  belong to some operator space  $O_+$ , and all their possible classical representations  $\mathcal{O}$  belong to some space  $S_+$ . Then, the mapping  $C_o$  is acting between the spaces  $O_+$  and  $S_+$ ,

$$C_o : O_+ \rightarrow S_+. \quad (12)$$

Suppose that  $S_+$  is chosen to be the minimal possible space, i.e.  $S_+ = \text{im } C_o$ . Note that the spaces  $O_+$  and  $S_+$  are real. Since the physical consistency requires that different  $\hat{o}$  should be mapped onto different  $\mathcal{O}$ , we conclude that  $C_o$  is a bijection. Now, since the average values of the observables are computed according to the dot-product formula (11), we see that one can actually introduce a space of quasiprobabilities  $D$ , for which the dot product (11) is well-defined for any  $\mathcal{O} \in S_+$ . We require that the space  $D$  is such that one can introduce a dot-product  $\langle \cdot, \cdot \rangle_D$  in it. Further, we call  $D$  “the space of admissible quasiprobability distributions”. From Eq. (11), it is seen that the space  $D$  is split into two subspaces:

$$D = R \oplus Z, \quad (13)$$

where the subspace  $Z$  consists of all such quasiprobabilities  $\mathcal{Z}(\lambda)$  which are orthogonal to every  $\mathcal{O}^*(\lambda) \in S_+$ :  $\langle \mathcal{O}^*, \mathcal{Z} \rangle_{S_+} = 0$ . The space  $R$  is the orthogonal complement to  $Z$  in the space  $D$  (in the sense of the dot-product  $\langle \cdot, \cdot \rangle_D$ ). If we add any element  $\mathcal{Z} \in Z$  to the quasiprobability  $\mathcal{P}$ , then the observable properties of the state  $\mathcal{P} + \mathcal{Z}$  are the same as those of  $\mathcal{P}$ . Therefore, if our model is physically consistent, the quasiprobabilities  $\mathcal{P}$  and  $\mathcal{P} + \mathcal{Z}$  should correspond to the same density operator  $\hat{\rho}$ . Hence, if the space  $Z$  is not trivial, it contributes to the non-uniqueness of the quasiprobability representation. The opposite is also true: every element  $\mathcal{Z}$  such that it can be added to any  $\mathcal{P}$  without changing the corresponding physical state  $\hat{\rho}$ , should belong to  $Z$ . We call the space  $R$  the “minimal representation space”, because (i) for every density operator  $\hat{\rho}$ , there is a unique quasiprobability  $\mathcal{R} \in R$  such that it has the same observable properties as  $\hat{\rho}$ , and (ii) the quasiprobability representation  $\mathcal{R}$  of a given density operator  $\hat{\rho}$  has the lowest possible norm  $\|\mathcal{R}\|_D = \sqrt{\langle \mathcal{R}, \mathcal{R} \rangle_D}$  among all the possible quasiprobability representations of  $\hat{\rho}$ . We call the space  $Z$  the ‘zero representation space’, since it contains all the quasiprobabilities which correspond to  $\hat{\rho} = 0$ .

Note that we can extend the definition of the mapping  $C_o$  from the real space  $O_+$  of Hermitian operators to the complex space  $O = O_+ \oplus iO_+$  of non-Hermitian operators. Indeed, an arbitrary operator  $\hat{o}$  can be decomposed into Hermitian  $\hat{o}^+$  and skew-Hermitian  $\hat{o}^-$  parts:

$$\hat{o} = \hat{o}^+ + \hat{o}^- . \tag{14}$$

However,  $i\hat{o}^-$  is a hermitian operator. Therefore, we can map  $\hat{o}$  as:

$$C_o \hat{o} = C_o \{ \hat{o}^+ + \hat{o}^- \} = C_o \hat{o}^+ - i C_o \{ i\hat{o}^- \} . \tag{15}$$

Now, if we extend the real space  $S_+$  to the complex space  $S = S_+ \oplus iS_+$ , the mapping  $C_o$  becomes a bijection between  $O$  and  $S$ . For example, if the stochastic representation is sufficiently well-defined, we can map the nondiagonal projections  $|n\rangle \langle m|$  of some orthonormal basis  $\{|n\rangle\}$ , onto

$$C_o \{|n\rangle \langle m|\} = \mathcal{O}_{nm}(\lambda) . \tag{16}$$

Next, we should determine whether the trace formula (11) is valid for non-hermitian  $\hat{o}$ ? This is indeed the case: since the relation (11) is linear with respect to  $\hat{o}$  and with respect to  $\mathcal{O}(\lambda)$ , we can split  $\hat{o}$  into hermitian and skew-hermitian parts, and perform the same operation as in Eq. (15).

### 3.2. Expansion over overcomplete basis

One important consequence of the arguments in the preceding section is that, using the map  $C_o$ , we can define the inverse mapping for the density operators:

$$\langle m | \hat{\rho} | n \rangle = \text{Tr} ( |n\rangle \langle m| ) \hat{\rho} = \int d\lambda \mathcal{O}_{nm}(\lambda) \mathcal{P}(\lambda) . \tag{17}$$

Introducing the operator  $\hat{\Lambda}(\lambda)$  defined by its matrix elements:

$$\langle m | \hat{\Lambda}(\lambda) | n \rangle = C_o \{|n\rangle \langle m|\} = \mathcal{O}_{nm}(\lambda) , \tag{18}$$

we obtain the expansion of density operators over the operator basis  $\hat{\Lambda}(\lambda)$ :

$$\hat{\rho} = \int d\lambda \hat{\Lambda}(\lambda) \mathcal{P}(\lambda) . \tag{19}$$

This equation defines the mapping from the space of admissible quasiprobability distributions  $D$  to a certain space  $P$  of operators, which contains the convex set of physical density operators  $P_+$ :  $P_+ \subset P$ . Note that since the matrix elements of  $\hat{\Lambda}(\lambda)$  belong to the space  $S$ , the operator basis  $\hat{\Lambda}(\lambda)$  is overcomplete (if the space  $\mathcal{Z}$  is non-trivial):

$$\int d\lambda \hat{\Lambda}(\lambda) \mathcal{Z}(\lambda) = 0 \text{ for any } \mathcal{Z} \in Z . \tag{20}$$

Now, by substitution of the density operator expansion (19) into the trace formula (11), we obtain the trace representation of the map  $C_o$ :

$$C_o \hat{o} = \mathcal{O}(\lambda) = \text{Tr} \hat{o} \hat{\Lambda}(\lambda) . \tag{21}$$

Since every operator can be expanded over the projections  $|n\rangle \langle m|$ , and  $C_o$  is a bijection, we conclude that  $\mathcal{O}_{nm}(\lambda)$  is a basis in the space  $S$ .

### 3.3. The mapping for density operators $C_\rho$

In this section, we will connect the properties of the mapping  $C_\rho$  with those of  $C_o$ . Let us denote by  $C_\rho^{(R)}$  the inverse of the mapping defined by the expansion (19),  $\mathcal{R} = C_\rho^{(R)}\hat{\rho}$ , and  $C_\rho^{(R)} : P \rightarrow \mathcal{R}$  is a bijection. Then, the physical and mathematical consistency of our model requires that  $C_\rho\hat{\rho} - C_\rho^{(R)}\hat{\rho} \in Z$  for any  $\hat{\rho}$ . This means that we have a (non)linear operator  $C_\rho - C_\rho^{(R)}$  which for every density operator  $\hat{\rho}$ , associates a certain quasiprobability  $\mathcal{Z} \in Z$ . As long as the density operators  $\hat{\rho}$  and the quasiprobabilities  $\mathcal{R}(\lambda)$  are in a one-to-one correspondence, we may write:

$$C_\rho\hat{\rho} = \mathcal{R}(\lambda) + \alpha[\mathcal{R}](\lambda), \quad (22)$$

where  $\mathcal{R} = C_\rho^{(R)}\hat{\rho}$ , and  $\alpha$  is a certain (non)linear mapping,  $\alpha : R \rightarrow Z$ . Therefore, the existence of the mapping  $C_\rho$  guarantees that we can choose at least one such mapping  $\alpha$ , that the quasiprobabilities in Eq. (22) become real and positive.

### 3.4. The mapping for the Liouville superoperator $C_s$

Consider the action of the quantum Liouville superoperator:

$$\hat{\rho}' = [\hat{H}, \hat{\rho}] / i\hbar, \quad (23)$$

which is a linear operator  $P \rightarrow P$  (assuming that  $\hat{\rho}' \in P$ ). Substituting  $\hat{\rho}' = (C_\rho^{(R)})^{-1}\mathcal{R}'$  and  $\hat{\rho} = (C_\rho^{(R)})^{-1}\mathcal{R}$  into Eq. (23), we obtain the operator  $\mathcal{H}^{(R)} : R \rightarrow R$  defined as:

$$\mathcal{R}'(\lambda) = \mathcal{H}^{(R)}[\mathcal{R}](\lambda) = \frac{1}{i\hbar}C_\rho^{(R)} \left\{ \int d\lambda' [\hat{H}, \hat{\Lambda}(\lambda')] \mathcal{R}(\lambda') \right\} (\lambda). \quad (24)$$

Here, we assume that the space  $D$  of admissible quasiprobabilities is such that we can move the linear operators through the integration whenever necessary. In this manner, we obtain the stochastic representation for the Liouville superoperator. Note that the definition of  $\mathcal{H}^{(R)}$  [Eq. (24)] can be extended to the whole space  $D$  in a consistent manner: we have  $\mathcal{H}^{(R)}[\mathcal{R} + \mathcal{Z}] = \mathcal{H}^{(R)}[\mathcal{R}]$  for any quasiprobability  $\mathcal{Z} \in Z$  due to the basis overcompleteness (20). Now, suppose that there exists another linear operator  $\mathcal{H} : D \rightarrow D$ , which differs from  $\mathcal{H}^{(R)}$ , but which also represents the superoperator (23). Then, the physical and mathematical consistency of our model requires that  $(\mathcal{H} - \mathcal{H}^{(R)})\mathcal{P} \in Z$  for any  $\mathcal{P} \in D$ . Introducing the space  $A$  of linear operators  $\alpha : D \rightarrow Z$ , we obtain the general form of all possible representations of the superoperator (23):

$$\mathcal{P}'(\lambda) = \mathcal{H}[\mathcal{P}](\lambda) = \mathcal{H}^{(R)}[\mathcal{P}](\lambda) + \alpha[\mathcal{P}](\lambda) \quad (25)$$

for arbitrary  $\alpha \in A$ . The existence of the mapping  $C_s$ , which is postulated in Eq. (7), guarantees that we can always choose such  $\alpha \in A$  that  $\mathcal{H}$  becomes a generator of a stochastic process.

We see that the mapping  $C_o$  [Eq. (5)] together with the trace formula (6) are the most important components of the stochastic representation: they completely define the mathematical structure of our stochastic representation, which is given by Eqs. (19), (21), (22) and (25).

### 3.5. Quasiprobability master equation

Having described the general form for all the ingredients in our stochastic representation, let us now discuss under what conditions we can obtain the master equation (8), and when it represents indeed the exact quantum dynamics given by the quantum Liouville equation (3). We have discussed the representation of the right hand side of Eq. (3) in the previous section, and there, we have assumed that the space  $D$  is selected so that such a representation is valid. Then, the general form of the master equation is:

$$\frac{\partial}{\partial t} \mathcal{P} = \mathcal{H} \mathcal{P} + \alpha [\mathcal{P}], \quad (26)$$

for arbitrary  $\alpha \in A$ . The necessary condition for Eq. (26) to be valid for a given initial condition  $\mathcal{P}(\lambda, t=0) \in D$  is that the  $\alpha$  should be such that at any later time the solution  $\mathcal{P}(\lambda, t)$  should belong to the space  $D$ . Further restrictions come from the left-hand side of Eq. (26): to arrive at the term  $\partial \mathcal{P} / \partial t$ , we differentiate by  $t$  the expansion (19), and we need to move the time derivative through the (usually) improper integral. Therefore, an additional constraint is imposed on the solution of Eq. (26): for each time moment  $t$ , there should exist an arbitrary small but finite interval  $[t - \epsilon, t + \epsilon]$  such that the improper integral in the expansion (19) is converging uniformly with respect to  $t \in [t - \epsilon, t + \epsilon]$ . If these conditions are violated, then the results of Monte Carlo simulations would show systematic errors with respect to the exact quantum dynamics Eq. (3), and phenomena like the so-called “spiking behavior” and “unaccounted boundary terms” would be observed [11, 23, 33].

### 3.6. Annihilators of the overcomplete basis

In the previous section, we have seen that the space  $A$  of operators  $\alpha : D \rightarrow Z$  plays an important role in the stochastic representation. First, these operators  $\alpha$  allow us to transform the representation  $\mathcal{H}$  [Eq. (25)] of the quantum Liouville superoperator into the form which admits the stochastic interpretation; second, the operators  $\alpha$  allow us to adjust the quasiprobability master equation [Eq. (26)] so that it is valid and that it possesses no systematic errors with respect to the exact quantum dynamics [Eq. (3)].

Here, we obtain the characterization of the space  $A$  which is more useful in practice [21]. Suppose that the space of admissible quasiprobability distributions  $D$  is such that for the operators  $\alpha \in A$  there exist their adjoints with respect to the dot product  $\langle \cdot, \cdot \rangle_S$ :

$$\langle \mathcal{O}^*, \alpha \mathcal{P} \rangle_S = \langle (\alpha^T \mathcal{O})^*, \mathcal{P} \rangle_S. \quad (27)$$

Here, by superscript  $T$  we have denoted the transposition operation, which is defined as the composition of Hermitian conjugation and the complex conjugation,  $\alpha^T = (\alpha^\dagger)^*$ ; the domains are  $\alpha^T : S \rightarrow S$ ; here  $\mathcal{O} \in S$  and  $\mathcal{P} \in D$ . As far as  $\alpha \mathcal{P} \in Z$ , we have:  $\langle (\alpha^T \mathcal{O})^*, \mathcal{P} \rangle_S = 0$  for any  $\mathcal{P} \in D$ . Therefore,  $\alpha^T \mathcal{O}$  is an observable which is zero for every state, and we conclude that  $\alpha^T \mathcal{O} = 0$ . In particular, since  $\langle m | \hat{\Lambda}(\lambda) | n \rangle \in S$ , we have:

$$\alpha^T \hat{\Lambda} = 0 \quad \text{for any } \alpha \in A. \quad (28)$$

According to mathematical convention, we call the operators  $\alpha^T$  “the annihilators of the basis  $\hat{\Lambda}(\lambda)$ ”.

The definition (28) has practical benefits due to the way in which one usually constructs the stochastic representations [12, 17, 20, 22, 34]. Suppose that we are given a concrete physical system. Then, at the first stage, one usually starts from an appropriate self-consistent field model, which takes into account all the major features of this system on a qualitative level. As a rule, this corresponds to the assumption that the density operator

$\hat{\rho}$  can be well approximated by a certain operator ansatz  $\hat{\Lambda}(\lambda)$ . At the second stage, one is looking for a way to incorporate the noise into this self-consistent field model, so that the resulting stochastic representation is equivalent to the exact quantum dynamics. Therefore, the common situation is that we are given a certain operator ansatz  $\hat{\Lambda}(\lambda)$ , and we need to investigate the possibilities that it provides for the stochastic representations. Then, it is much easier to find the differential identities of the form (28), to transpose them, and to add them into the master equation (26), than to find the spaces  $Z$ ,  $D$ , and  $A$ .

#### 4. Example of a stochastic representation: the stochastic wave-function method

In our recent work [21], we have studied the stochastic wave-function method of Carusotto *et al.* [22]. In this method, one selects the  $N$ -particle Hartree-Fock state projections:

$$\hat{\Lambda}(\phi, \phi^{+*}) = |N : \phi\rangle \langle N : \phi^+|, \quad (29)$$

as the operator ansatz for the density operator  $\hat{\rho}$ . Here, the Fock state is defined as  $|N : \phi\rangle = \left[ \sum_k \phi_k \hat{a}_k^\dagger \right]^N |0\rangle / \sqrt{N!}$ . Therefore, the space  $L$  consists of all the vectors  $\lambda = (\phi, \phi^*, \phi^+, \phi^{+*})$ . Now, in order to define the stochastic representation, we need to find all the necessary mappings for operators and superoperators.

##### 4.1. Operator correspondences for the density operator

In [21], the mapping  $C_\rho$  is constructed in the following way. Suppose that we have presented the density operator  $\hat{\rho}$  as an antinormally ordered operator series,

$$\hat{\rho} = c_0 + \sum_{m=1}^N \prod_{j=1}^m \left\{ \sum_{k_j=1}^{\mathcal{N}} \hat{a}_{k_j} \right\} \prod_{j=1}^m \left\{ \sum_{k'_j=1}^{\mathcal{N}} \hat{a}_{k'_j}^\dagger \right\} h(\mathbf{x}_{k_1}, \dots, \mathbf{x}_{k_m} | \mathbf{x}_{k'_1}, \dots, \mathbf{x}_{k'_m}), \quad (30)$$

where  $\mathcal{N}$  is the size of the discretization lattice. Then, the corresponding quasiprobability  $\mathcal{P}(\lambda) = C_\rho \hat{\rho}$  is found within two steps. First, we perform the replacements  $\hat{a}_{k_j} \rightarrow \phi_{k_j}^*$ ,  $\hat{a}_{k'_j}^\dagger \rightarrow \phi_{k'_j}$  in Eq. (30), and multiply each monomial by a normalization factor:

$$\mathcal{P}(\lambda) = \left\{ \frac{1}{\Gamma_{\mathcal{N}}(N) N!} c_0 + \frac{1}{\Gamma(m+N) N!} \sum_{m=1}^{\infty} \prod_{j=1}^m \left\{ \sum_{k_j=1}^{\mathcal{N}} \phi_{k_j}^* \right\} \prod_{j=1}^m \left\{ \sum_{k'_j=1}^{\mathcal{N}} \phi_{k'_j} \right\} \right. \\ \left. \times h(\mathbf{x}_{k_1}, \dots, \mathbf{x}_{k_m} | \mathbf{x}_{k'_1}, \dots, \mathbf{x}_{k'_m}) \right\} \delta_S(\|\phi\| - 1) \delta(\phi^+ - \phi), \quad (31)$$

where the normalization factor is

$$\Gamma_{\mathcal{N}}(p) = S_{2\mathcal{N}-1} \frac{(\mathcal{N}-1)!}{(\mathcal{N}-1+p)!}, \quad (32)$$

and  $S_{2\mathcal{N}-1}$  is the volume of the unit sphere in  $\mathbb{C}^{\mathcal{N}}$ . However, the quasiprobability  $\mathcal{P}(\lambda)$  which is obtained in Eq. (31), is not positive in general. We make it positive within the second step, by employing the method of Carusotto *et al.* [22, 35]; we write the density operator expansion for the basis (29),

$$\hat{\rho} = \int \prod_{k=1}^{\mathcal{N}} d\phi_k d\phi_k^* \prod_{k=1}^{\mathcal{N}} d\phi_k^+ d\phi_k^{+*} \mathcal{P}(\phi, \phi^*, \phi^+, \phi^{+*}) |N : \phi\rangle \langle N : \phi^+|. \quad (33)$$

Then we separate the phase of  $\mathcal{P}(\lambda)$ :

$$\mathcal{P}(\lambda) = |\mathcal{P}(\lambda)| e^{i\xi(\lambda)}. \quad (34)$$

Next, we absorb the phase into  $|N : \phi\rangle \langle N : \phi^+|$ :

$$\hat{\rho} = \int \prod_{k=1}^{\mathcal{N}} d\phi_k d\phi_k^* \prod_{k=1}^{\mathcal{N}} d\phi_k^+ d\phi_k^{+*} |\mathcal{P}(\lambda)| |N : \phi e^{i\xi(\lambda)/2N}\rangle \langle N : \phi^+ e^{-i\xi(\lambda)/2N}|. \quad (35)$$

If we change the variables as  $\phi e^{i\xi(\lambda)/2N} \rightarrow \phi$ ,  $\phi^+ e^{-i\xi(\lambda)/2N} \rightarrow \phi^+$ , and calculate the Jacobian determinant, we can return to form (33), where  $\mathcal{P}$  is now real and positive. However from the point of view of the stochastic simulations, one may stop at (35); we sample the initial conditions with the probability distribution  $|\mathcal{P}(\lambda)|$ , and each time we multiply the sampled wave functions by the phase factor  $e^{\pm i\xi(\lambda)/2N}$ .

## 4.2. Operator correspondences for the observables

The mapping  $C_o$  is constructed in the following way. Suppose that we have presented the observable operator  $\hat{O}$  as a normally ordered operator series:

$$\hat{O} = c_0 + \sum_{m=1}^{\mathcal{N}} \prod_{j=1}^m \left\{ \sum_{k_j=1}^{\mathcal{N}} \hat{a}_{k_j}^\dagger \right\} \prod_{j=1}^m \left\{ \sum_{k'_j=1}^{\mathcal{N}} \hat{a}_{k'_j} \right\} h(\mathbf{x}_{k_1}, \dots, \mathbf{x}_{k_m} | \mathbf{x}_{k'_1}, \dots, \mathbf{x}_{k'_m}). \quad (36)$$

Due to the linearity of the mapping  $C_o$ , it is sufficient to consider the terms

$$\hat{O} = \hat{a}_{k_1}^\dagger \dots \hat{a}_{k_l}^\dagger \hat{a}_{k'_1} \dots \hat{a}_{k'_m}. \quad (37)$$

Then, we employ the trace representation (21):

$$\begin{aligned} C_o \hat{a}_{k_1}^\dagger \dots \hat{a}_{k_l}^\dagger \hat{a}_{k'_1} \dots \hat{a}_{k'_m} &= \text{Tr} \hat{a}_{k_1}^\dagger \dots \hat{a}_{k_l}^\dagger \hat{a}_{k'_1} \dots \hat{a}_{k'_m} |N : \phi\rangle \langle N : \phi^+| \\ &= \phi_{k_1}^{+*} \dots \phi_{k_l}^{+*} \phi_{k'_1} \dots \phi_{k'_m} \delta_{lm} \frac{N!^2}{(N-m)!} \langle \phi^+ | \phi \rangle^{N-m}. \end{aligned} \quad (38)$$

## 4.3. Operator correspondences of the star-product type

In order to find the mapping  $C_s$  for the quantum Liouville superoperator, we proceed in a constructive way [21]. We note that for a Hamiltonian of the form (1), the action of the Liouville superoperator  $[\hat{H}, \cdot] / i\hbar$  is constructed from the multiplications by  $\hat{a}_s$  and  $\hat{a}_s^\dagger$  from the left and from the right. Since such multiplications, e. g.,  $\hat{a}_s \times \cdot$  and  $\cdot \times \hat{a}_s$ , are also superoperators, we find the mapping  $C_s$  for the left multiplication by a number-conserving normally-ordered product of creation and annihilation operators [21]:

$$C_s \left[ \hat{a}_{k_1}^\dagger \dots \hat{a}_{k_l}^\dagger \hat{a}_{k'_1} \dots \hat{a}_{k'_l} \times \cdot \right] = (-1)^l \frac{\partial}{\partial \phi_{k_1}} \dots \frac{\partial}{\partial \phi_{k_l}} \phi_{k'_1} \dots \phi_{k'_l}, \quad (39)$$

and for the right multiplication,

$$C_s \left[ \cdot \times \hat{a}_{k_1}^\dagger \dots \hat{a}_{k_l}^\dagger \hat{a}_{k'_1} \dots \hat{a}_{k'_l} \right] = (-1)^l \frac{\partial}{\partial \phi_{k'_1}^{+*}} \dots \frac{\partial}{\partial \phi_{k'_l}^{+*}} \phi_{k_1}^{+*} \dots \phi_{k_l}^{+*}. \quad (40)$$

Using these relations, we can evaluate the operator  $\mathcal{H}$ :

$$\begin{aligned} \mathcal{H} = C_s \left[ \widehat{H}, \cdot \right] / i\hbar = & - \sum_r \frac{\partial}{\partial \phi_r} \mathcal{A}_r [\phi] - \sum_r \frac{\partial}{\partial \phi_r^{+*}} (\mathcal{A}_r [\phi^+])^* \\ & + \frac{1}{2} \sum_{r,s} \frac{\partial}{\partial \phi_r} \frac{\partial}{\partial \phi_s} V_{rs} \frac{\phi_r \phi_s}{i\hbar} + \frac{1}{2} \sum_{r,s} \frac{\partial}{\partial \phi_r^{+*}} \frac{\partial}{\partial \phi_s^{+*}} \left( V_{rs} \frac{\phi_r^+ \phi_s^+}{i\hbar} \right)^*. \end{aligned} \quad (41)$$

We see that the operator  $\mathcal{H}$  does not have the required form of the genuine Fokker-Planck operator in complex variables [21]. In particular, the drift terms lack their complex conjugates, and the diffusion matrix is not Hermitian. Nevertheless, we can solve this issue by adding the annihilator  $\alpha$  to the master equation (41).

#### 4.4. Annihilators of the overcomplete basis

As was described in Sec. 3.6, the properties of the stochastic representation are most conveniently described in terms of the differential identities of form (28). In work [21], we find the following differential identities for the Hartree-Fock state projections (29): (i) the analyticity of the basis  $\widehat{\Lambda}(\phi, \phi^{+*})$  with respect to its variables;

$$\frac{\partial}{\partial \phi_k^*} \widehat{\Lambda}(\phi, \phi^{+*}) = 0, \quad \frac{\partial}{\partial \phi_k^+} \widehat{\Lambda}(\phi, \phi^{+*}) = 0; \quad (42)$$

(ii) the homogeneity of the Hartree-Fock state,

$$\left[ N - \sum_k \phi_k \frac{\partial}{\partial \phi_k} \right] \widehat{\Lambda}(\phi, \phi^{+*}) = 0, \quad (43)$$

$$\left[ N - \sum_k \phi_k^{+*} \frac{\partial}{\partial \phi_k^{+*}} \right] \widehat{\Lambda}(\phi, \phi^{+*}) = 0. \quad (44)$$

From expressions (42)-(44), we conclude that the operator  $\alpha$ , in the general form (26) of the master equation, has the form:

$$\alpha = \sum_k \frac{\partial}{\partial \phi_k^*} l_k^* + \sum_k \frac{\partial}{\partial \phi_k^+} l_k^+ + \left[ N + \sum_k \frac{\partial}{\partial \phi_k} \phi_k \right] d + \left[ N + \sum_k \frac{\partial}{\partial \phi_k^{+*}} \phi_k^{+*} \right] d^{+*}. \quad (45)$$

Here,  $l_k, l_k^+, d, d^+$  are some linear operators  $D \rightarrow D$ .

In work [21] it is discussed in detail how we can choose such parameters  $l_k, l_k^+, d, d^+$  that the master equation (26) with  $\mathcal{H}$  [Eq. (41)] becomes the Fokker-Planck equation, and satisfies the validity conditions discussed in Sec. 3.5.

## 5. Conclusion

In this work we have considered the most general definition of the classical stochastic representation of the many-body quantum dynamics. Such representation should provide several mappings: for density operators  $C_\rho$ , for observables  $C_o$ , and for superoperators  $C_s$ . The most important postulated property of the stochastic representation is the classical representation of the trace formula for average values of the observables.

The main result of this work is that when the mathematical properties of the stochastic representation are regular enough, and it is physically consistent, then the stochastic representation is reduced to the expansion of the density operator over a certain overcomplete operator basis  $\widehat{\Lambda}(\lambda)$ . This operator basis  $\widehat{\Lambda}(\lambda)$  defines all the properties of the stochastic representation: the general form of all the mappings. Moreover, the overcompleteness of the

basis leads to the existence of equivalent transformations of quasiprobability master equations, which allows us to perform their stochastic unraveling. Such a structure is already known to occur in the representations of quantum mechanics in generalized phase spaces [23-26]. We also demonstrate that the stochastic wave-function methods [8, 12-20, 36] also fall into this category of stochastic representations.

## Acknowledgements

This work is supported by the Russian Foundation for Basic Research (grant 14-02-31109).

## References

- [1] Aksenova E. V., Kuz'min V. L., Romanov V. P. Coherent backscattering of light in nematic liquid crystals. *J. Exp. Theor. Phys.*, 2009, **108**, P. 516.
- [2] Aksenova E. V., Kokorin D. I., Romanov V. P. Simulation of coherent backscattering of light in nematic liquid crystals. *J. Exp. Theor. Phys.*, 2012, **115**, P. 337.
- [3] Aksenova E. V., Kokorin D. I., Romanov V. P. Simulation of radiation transfer and coherent backscattering in nematic liquid crystals. *Phys. Rev. E.*, 2014, **89**, P. 052506.
- [4] Drummond P. D., Gardiner C. W. Generalized p-representations in quantum optics. *J. Phys. A: Math. Gen.*, 1980, **13**, P. 2353.
- [5] Deuar P., Drummond P. D. First-principles quantum dynamics in interacting bose gases: I. the positive p representation. *J. Phys. A: Math. Gen.*, 2006, **39**, P. 1163.
- [6] Savage C. M., Schwenn P. E., Kheruntsyan K. V. First-principles quantum simulation of dissociation of molecular condensates: Atom correlations in momentum space. *Phys. Rev. A.*, 2006, **74**, P. 033620.
- [7] Deuar P., Drummond P. D. Correlations in a bec collision: First-principles quantum dynamics with 150 000 atoms. *Phys. Rev. Lett.*, 2007, **98**, P. 120402.
- [8] Juillet O., Gulminelli F. Exact pairing correlations for one-dimensionally trapped fermions with stochastic mean-field wave functions. *Phys. Rev. Lett.*, 2004, **92**, P. 160401.
- [9] Biele R., D'Agosta R. A stochastic approach to open quantum systems. *J. Phys.: Condens. Matter.*, 2012, **24**, P. 273201.
- [10] Lee M. D., Ruostekoski J. Classical stochastic measurement trajectories: Bosonic atomic gases in an optical cavity and quantum measurement backaction. *Phys. Rev. A.*, 2014, **90**, P. 023628.
- [11] Gardiner C. W., Zoller P. *Quantum Noise: a Handbook of Markovian and Non-Markovian Quantum Stochastic Methods with Applications to Quantum Optics. Springer Series in Synergetics.* Berlin, Germany, Springer, 2004. ISBN: 3540223010, 9783540223016.
- [12] Carusotto I., Castin Y. An exact reformulation of the bose-hubbard model in terms of a stochastic gutzwiller ansatz. *New. J. Phys.*, 2003, **5**, P. 91.
- [13] Wilkie J. Variational principle for stochastic wave and density equations. *Phys. Rev. E.*, 2003, **67**, P. 017102.
- [14] Tessieri L., Wilkie J., etinba M. Exact norm-preserving stochastic time-dependent hartree-fock. *J. Phys. A: Math. Gen.*, 2005, **38**, P. 943.
- [15] Montina A., Castin Y. Exact bcs stochastic schemes for a time-dependent many-body fermionic system. *Phys. Rev. A.*, **73**, P. 013618.
- [16] Wilkie J., Wong Y. M., Ng R. Survey of exact n-body decompositions of stochastic scalar-jastrow-hartree form. *Chem. Phys.*, 2010, **369**, P. 43.
- [17] Lacroix D. Stochastic schroedinger equation from optimal observable evolution. *Ann. Phys.*, 2007, **322**, P. 2055.
- [18] Lacroix D. Optimizing stochastic trajectories in exact quantum-jump approaches of interacting systems. *Phys. Rev. A.*, 2005, **72**, P. 013805.
- [19] Breuer H.-P. Exact quantum jump approach to open systems in bosonic and spin baths. *Phys. Rev. A.*, 2004, **69**, P. 022115.
- [20] Lacroix D., Ayik S. Stochastic quantum dynamics beyond mean field. *Eur. Phys. J. A.*, 2014, **50**, P. 95.
- [21] Polyakov E. A., Vorontsov-Velyaminov P. N. Quasiprobability distributions in stochastic wave-function methods. *Phys. Rev. A.*, 2015, **91**, P. 042107.

- [22] Carusotto I., Castin Y., Dalibard J. N-boson time-dependent problem: A reformulation with stochastic wave functions. *Phys. Rev. A.*, 2001, **63**, P. 023606.
- [23] Deuar P., Drummond P. D. Gauge p representations for quantum-dynamical problems: Removal of boundary terms. *Phys. Rev. A.*, 2002, **66**, P. 033812.
- [24] Corney J. F., Drummond P. D. Gaussian quantum operator representation for bosons. *Phys. Rev. A.*, 2003, **68**, P. 063822.
- [25] Corney J. F., Drummond P. D. Gaussian phase-space representations for fermions. *Phys. Rev. B.*, 2006, **73**, P. 125112.
- [26] Quantum dynamics in ultracold atomic physics / Qiong-Yi He, Margaret D. Reid, Bogdan Opanchuk et al. *Front. Phys.*, 2012, **7**, P. 16.
- [27] Błaszak M., Domański Z. Phase space quantum mechanics. *Ann. Phys. (N. Y.)*, 2012, **327**, P. 167–211.
- [28] Gardiner C. *Stochastic Methods: A Handbook for the Natural and Social Sciences. Springer Series in Synergetics*, Berlin, Germany, Springer, 2009. ISBN: 3540707123, 9783540707127.
- [29] Frenkel D., Smit B. *Understanding Molecular Simulation*. New York : Academic Press, 2001. ISBN: 0122673514, 9780122673511.
- [30] Cahill K. E., Glauber R. J. Ordered expansions in boson amplitude operators. *Phys. Rev.*, 1969, **177**, P. 1857.
- [31] Cahill K. E., Glauber R. J. Density operators and quasiprobability distributions. *Phys. Rev.*, 1969, **177**, P. 1882.
- [32] Cahill K. E., Glauber R. J. Density operators for fermions. 1999, **59**, P. 1538.
- [33] Gilchrist A., Gardiner C. W., Drummond P. D. Positive p representation: Application and validity. *Phys. Rev. A.*, 1997, **55**, P. 3014.
- [34] Juillet O., Chomaz P. Exact stochastic mean-field approach to the fermionic many-body problem. *Phys. Rev. Lett.*, 2002, **88**, P. 142503.
- [35] Carusotto I., Castin Y. Exact reformulation of the bosonic many-body problem in terms of stochastic wave functions: an elementary derivation. *Ann. Henri Poincaré*, 2003, **4**, P. S783.
- [36] Breuer H.-P. The non-markovian quantum behaviour of open systems: An exact monte carlo method employing stochastic product states. *Eur. Phys. J. D.*, 2004, **29**, P. 105.

# Entropic sampling of star-shaped polymers with different number of arms: temperature dependencies of structural properties

I. A. Silanteva<sup>1</sup>, P. N. Vorontsov-Velyaminov<sup>1</sup>

<sup>1</sup>Saint Petersburg State University, Dept. of molecular biophysics and polymer physics,  
Faculty of Physics, 198504, Saint Petersburg, Russia  
sila3@yandex.ru, voron.wgroup@gmail.com

PACS 02.70.-c, 02.70.Uu, 05.10.Ln, 05.70.-a, 05.70.Fh, 07.05.Tp, 36.20.-r, 36.20.Hb, 64.60.-i, 64.70.Nd, 64.70.km, 64.70.pj, 65.40.Ba, 65.80.+n, 81.07.Nb, 82.20.Wt, 82.35.Lr, 87.10.Rt, 87.15.ak, 87.16.aj, 87.53.Wz, 87.55.K

DOI 10.17586/2220-8054-2015-6-4-513-523

The lattice model for a star-shaped polymer with a total number of up to 72 segments is considered. The number of arms varied, ranging from 2 to 6. Entropic sampling Monte Carlo simulation is used to obtain the equilibrium, thermal and structural properties of the considered systems over a wide range of temperatures. The coil-globule transition is observed and the transition temperature is shown to shift toward lower temperatures with an increase in the number of arms. This study demonstrates how the structure of the star-shaped polymer affects its equilibrium properties.

**Keywords:** star-shape polymer, lattice model, entropic sampling, Wang-Landau algorithm, phase transition.

*Received: 20 June 2015*

## 1. Introduction

Over the last couple of decades, there has been an increased interest in studying nano-objects of various types including the polymer molecules. Modern facilities are now able to synthesize macromolecules with complicated architecture, such as stars, brushes, nets or dendrimers. In this paper, we restrict ourselves to the simulation study of star-shaped molecules. Due to their specific structural features, these polymers have essentially new characteristics in comparison to linear chains. As a result, their average size is considerably smaller than that of the linear polymers with the same number of segments. Consequently, they have greater concentration of monomers that leads to greater volume effects. Star-like molecules can be considered as unique objects, combining properties of linear polymers and colloid particles as was also pointed out in [1, 2]. It was correctly mentioned in [3] that the star polymer with a small number of arms is close in its behavior and properties to that of a linear polymer, while with an increased number of arms, it becomes closer to a rigid spherical particle. The main aim of this paper is to observe how initial structural characteristics, such as the number of its arms, influence its equilibrium structural properties, including features of the coil-globule transition. This problem is also discussed in a number of papers [4, 5] so it would be desirable to compare our data with that of [4]. It is known that in the star-like polymers, there can be observed transitions of two types: liquid-crystal (1st order) and the coil-globule (2nd order), wherein the second order transition is very sensitive to the polymer's topology.

It should also be stressed that studies of star-like polymers are important because of their possible application for the transport of DNA and drug substances into cells [6–8].

The considered model is presented in section 2. The results for the athermal and thermal cases are discussed in sections 3 and 4 correspondingly. Conclusions are given in section 5.

## 2. Model

In this work, we consider the model of a regular neutral polymer star on a simple cubic (SC) lattice. Lattice models have been widely used for a long time in the study of polymers [9]. These models are still useful now [10–14], since such an approach allows one to obtain reasonable results with minimal computational requirements.

Star-like polymers (for convenience, we refer to as "star") can be represented as  $f$  chains fixed by their single ends to a common center. We consider cases of  $f \leq 6$  where  $f=1$  and  $f=2$  correspond to linear chains. Each arm is a chain of  $N_{\text{arm}}$  bonds (segments) and  $N_{\text{arm}} + 1$  monomers (knots). The total number of segments in a star is  $N = fN_{\text{arm}}$ . Each  $i$ -th monomer has coordinates  $(x_i, y_i, z_i)$ . The segments are being generated with the aid of semi-phantom random walks along the lattice with reverse steps being forbidden [15], contrary to the case of free (or phantom) walks. In order to change the configuration of the star, an arm and its  $k_0$ -th monomer are randomly chosen and a new piece of this arm, starting from  $k_0$  up to the end of the arm, is newly generated.

In our work, we use the entropic sampling simulations [16, 17] within Wang-Landau algorithm [18]. This method was successfully applied in our previous works [13, 15, 19–21] as well as by other authors [4, 12, 22–24] in polymer studies. An important attractive feature of this method is in its ability to obtain statistics for very rare events with relative ease. Hence, this method provides a means for calculating the equilibrium characteristics of the studied system over a wide range of temperatures, including the phase transition area. The calculation time required was about a few hours on a standard 4-core processor in most instances.

## 3. Athermal case

In the athermal case, the interaction between monomers is reduced to the exclusion of intersections. In order to learn how strongly the fixation of all arms' ends at the same point (in the center of the star) restricts their freedom, it is worth considering their excess entropy. The complete number of conformations for a semi-phantom star with  $f \leq z$  arms is  $z!(z-1)^{N-f}/(z-f)!$  [21]. So, the entropy can be expressed as:

$$S = \ln \left( \frac{z!(z-1)^{N-f}}{(z-f)!} \Omega_0 \right), \quad (1)$$

where  $z=6$  is the coordinate number of our SC lattice and  $\Omega_0$  is the ratio of the self-avoiding conformations which we obtain in the same way as in our preceding paper [21]. Values of  $\Omega_0$  were calculated for stars with the total number of segments  $N \leq 800$ . The error does not exceed 15%. The entropy of the phantom chain (star) is  $\ln(z^N)$ . So the specific excess entropy of our system (relative to this basic system) is:

$$\frac{\Delta S}{N} = \frac{1}{N} \ln \left( \frac{z!(z-1)^{N-f}}{(z-f)!} \Omega_0 \right) - \ln z. \quad (2)$$

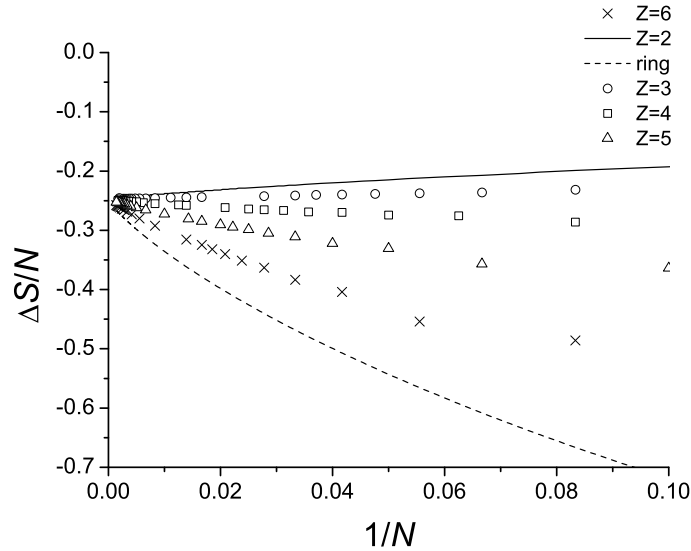


FIG. 1. Specific excess entropy (relative to the phantom chain) as a function of the inverse number of segments for stars with different numbers of arms ( $3 \div 6$ ), for a chain, and for ring [15].

The dependence of  $\Delta S/N$  on  $1/N$  is presented in Fig. 1. It is seen that for the 3-arm star, the curve in this scale is rising and is rather close to that of the single chain. But for  $f=4$ , the dependency already begins to decrease; and with an increased number of arms, this tendency becomes more pronounced. This picture demonstrates that increasing the number of arms results in increased configurational restrictions. For comparison, Fig. 1 presents the appropriate curve for ring chains [15] and it is seen that restrictions caused by closure of the chain are even greater than in the case of when the 6 arms were affixed to the center of the star.

#### 4. Thermal case

In the thermal case, we account also for interactions of non-bonded monomers if they occur in contact with each other (i.e. at a distance of the lattice constant). In this case, an energy ( $\epsilon > 0$  or  $\epsilon < 0$ ) is attributed to each such contact. The value of  $\epsilon$  can characterize the solvent quality of the real polymer solutions. In this work, we present only the most interesting case — attraction ( $\epsilon < 0$ ). The energy in the given conformation is  $E = \epsilon m$ , where  $m$  is the number of contacts,  $m \in [0, m_{\max}]$ . As a result of the simulation for a given star, we obtain a distribution of conformations over the number of contacts  $\Omega_m$  for a given star. Knowledge of  $\Omega_m$  allows calculation of equilibrium properties over a wide temperature range, according to the canonical expression:

$$\langle F \rangle (T) = \frac{\sum_{m=0}^{m_{\max}} F_m e^{-E_m/k_B T} \Omega_m}{\sum_{m=0}^{m_{\max}} e^{-E_m/k_B T} \Omega_m}, \quad (3)$$

where  $F$  is a certain physical quantity and  $F_m$  is its distribution over the number of contacts which is also determined during simulation. In this paper, we obtained such distributions for

the module of the radius-vector of the center of mass, mean square of the radius of gyration and its orthogonal components. In the limit  $T \rightarrow \infty$ , equation (3) yields the athermal values.

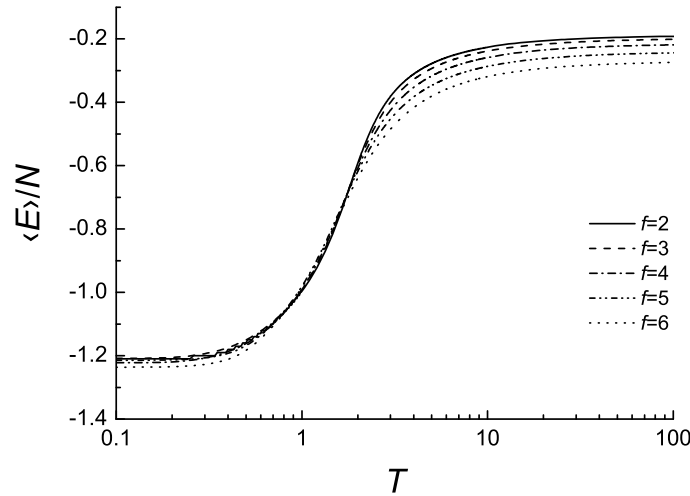


FIG. 2. Specific configuration energy as a function of temperature for stars with different numbers of arms (3 ÷ 6) and for a chain. Total number of segments  $N=70$  for  $f=5$  and  $N=72$  for all the rest.

We have studied stars with different numbers of arms (from 3 to 6) and approximately equal total number of segments:  $f=3$ ,  $N_{\text{arm}}=24$ ;  $f=4$ ,  $N_{\text{arm}}=18$ ;  $f=5$ ,  $N_{\text{arm}}=14$ ;  $f=6$ ,  $N_{\text{arm}}=12$ . Also, for comparison, the chain (i.e.  $f=2$ ,  $N_{\text{arm}}=36$ ) has been considered. The case with a fixed number of arms ( $f=6$ ) was studied earlier in [19–21]. Fig. 2 presents temperature dependencies of the specific configuration energy according to (3) with  $F_m = \epsilon m$ . Here and subsequently, the temperature is given in  $|\epsilon|$ -units,  $k_B T / |\epsilon|$ . A monotonic growth of the energy was observed, with the curves being close to each other and a very small difference between them is only noticeable at higher temperatures.

In order to observe structural transitions, it is also useful to calculate the heat capacity:

$$C(T) = \frac{\partial E}{\partial T} = \frac{\langle E^2 \rangle (T) - (\langle E \rangle (T))^2}{T^2}. \quad (4)$$

The temperature dependence of the specific heat capacity is presented in Fig. 3. It was observed that for all the considered cases, there exists a maximum which becomes wider and is shifted to lower temperatures with an increased number of arms. The latter provides the increase of the total monomer density, such that it hinders the collapse of the coil-globule transition. Similar results were obtained in [4], where the fluctuating bond model was used.

Additionally, we present several structural characteristics for our models. In order to observe the coil-globule structure transition, we calculated the mean square radius of gyration for a star. For each conformation, the radius of gyration was determined and was ultimately averaged separately for each number of contacts using the following equation:

$$\langle R_g^2 \rangle_m = \frac{1}{2N^2} \left\langle \sum_{i=1}^N \sum_{j=1}^N |r_{ij}|^2 \right\rangle_m = \frac{1}{N} \left\langle \sum_{i=1}^N (r_i - R_c)^2 \right\rangle_m. \quad (5)$$

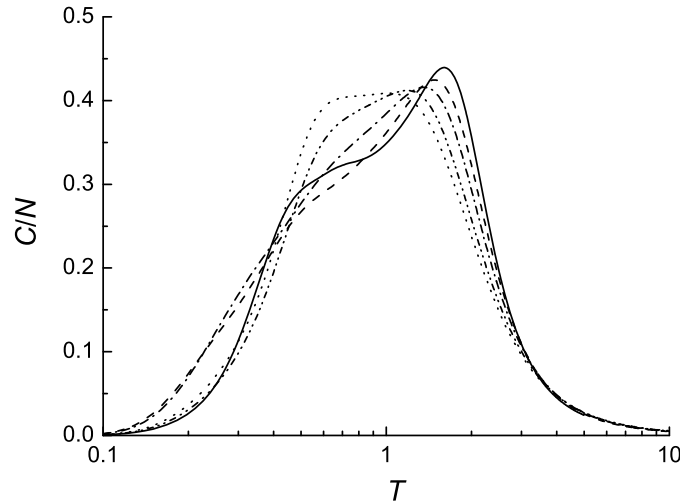


FIG. 3. Specific heat capacity as a function of temperature for stars with different numbers of arms ( $3 \div 6$ ) and for a chain.  $N=70$  for  $f=5$  and  $N=72$  for all the rest. Legend, see in Fig. 2.

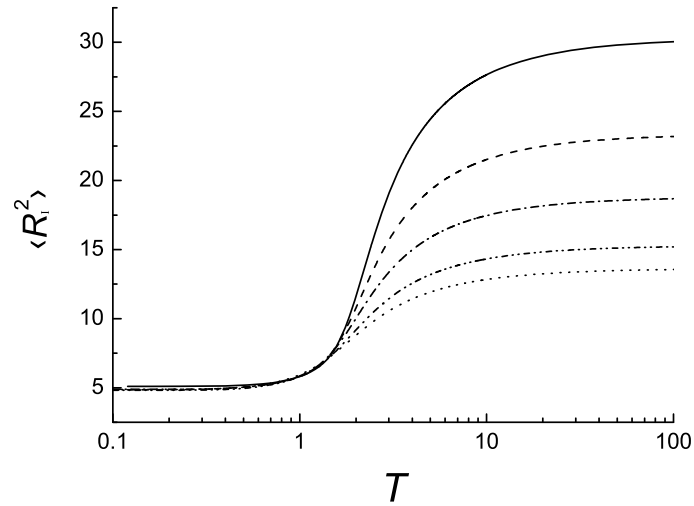
Here,  $r_{ij}$  is the distance between monomers and the sum is taken over all monomeric pairs,  $R_c$  is the center of mass vector. The obtained data is canonically averaged according to formula (3). The dependence of the mean square radius of gyration on temperature is shown in Fig. 4a. In Fig. 4b data is presented for the  $T$ -dependence of the factor  $g = \langle R_I^2 \rangle_{\text{star}} / \langle R_I^2 \rangle_{\text{chain}}$ . The latter is shown to be non-monotonic and there exists a temperature at which the star attains the most extended state in comparison with that of the corresponding chain. At higher temperatures, for increasing  $f$ , the difference between the size of the star and the size of the chain becomes larger. For decreasing temperatures, the size of the stars lessens and a transition from the coiled state to that of the globule occurs. The size of the globule does not depend on the number of arms and is determined only by the total number of segments.

Limiting values of  $g$  at  $T \rightarrow \infty$  are presented in Table 1. Also, there are presented values of  $g_{\text{ph}}$  for the phantom (ideal) star model [9], according to the expression  $g_{\text{ph}} = (3f - 2)/f^2$ , together with the results of our simulation. For the latter purpose, the distribution of the conformations  $\Omega_n$  and the square radius of gyration  $R_{I_n}^2$  over the number of intersections  $n$  and the corresponding average was determined according to the expression:

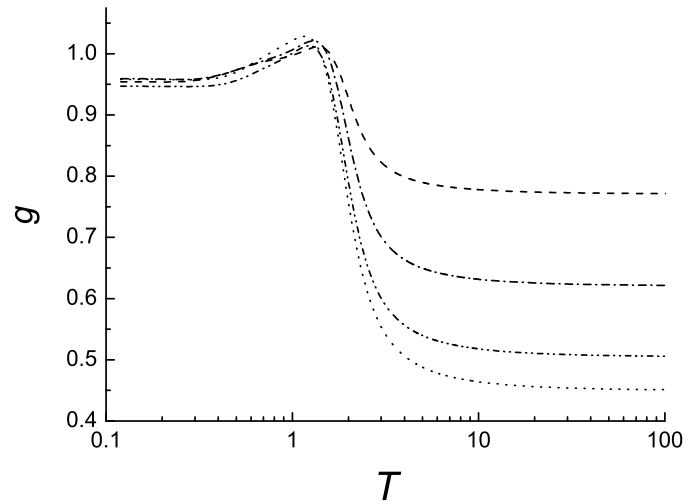
$$\langle R_I^2 \rangle_{\text{ph}} = \frac{\sum_{n=0}^{n_{\text{max}}} R_{I_n}^2 \Omega_n}{\sum_{n=0}^{n_{\text{max}}} \Omega_n}. \quad (6)$$

It is interesting to note that  $g$ -values for the athermal case with intersection avoidance appear to be in sufficiently fair agreement with those of phantom random progression cases. It could be affirmed that for stars with small number of arms ( $f \leq 6$ ) the volume effects do not differ much from those of chains with the same total number of segments.

Fig. 5 presents temperature dependencies for the reduced modulus of the center of mass radius-vector  $R_c/N_{\text{arm}}$ . Its location was determined relative to the position of the star center, and was fixed as the coordinate's origin. For the chain ( $f=2$ ), the dependency was



a



b

FIG. 4. Mean square radius of gyration (a) and  $g$ -factor (b) as functions of temperature for stars with different numbers of arms ( $3 \div 6$ ).  $N=70$  for  $f=5$  and  $N=72$  for all the rest. Legend, see in Fig. 2.

TABLE 1. Limiting values of the mean square radius of gyration  $\langle R_I^2 \rangle$ , and factor  $g$  for stars under athermal and ideal conditions.

$f$	$\lim_{T \rightarrow \infty} \langle R_I^2 \rangle$	$g$	$\langle R_I^2 \rangle_{\text{ph}}$	$g_{\text{ph}}$	$g$ , ideal star [9]
2	29.1	1	13.4673	1	1
3	23.3474	0.8023	10.6939	0.7940	0.7778
4	18.7997	0.6460	8.7705	0.6512	0.625
5	15.2897	0.5254	7.2798	0.5406	0.52
6	13.6292	0.4684	6.5164	0.4839	0.4444

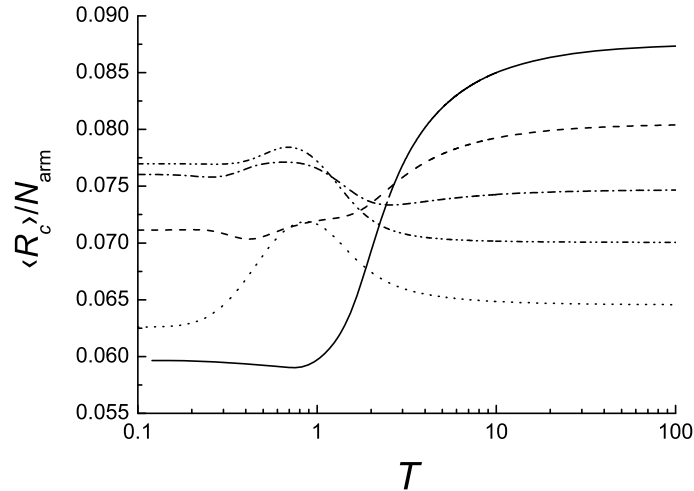


FIG. 5. Temperature dependence of the reduced modulus of the center of mass radius-vector  $R_c/N_{\text{arm}}$  for stars with different number of arms ( $3 \div 6$ ).  $N=70$  for  $f=5$  and  $N=72$  for all the rest. Legend, see in Fig. 2.

shown to increase. For stars with  $f=4, 5, 6$ , there exists a maximum that becomes more pronounced with an increased number of arms  $f$ . This might lead one to suppose that in the region of transition to the compact conformation, the internal state of the star is unstable, with its form essentially deviating from a symmetric one.

In order to analyze a star's form, it is necessary to calculate the orthogonal components of the square radius of gyration [23, 25]. First, all the components were obtained and then, matrix diagonalization was performed, such that the three nonzero components  $L_1^2 < L_2^2 < L_3^2$ , and that  $R_1^2 = L_1^2 + L_2^2 + L_3^2$ . These were initially averaged for each value of energy and finally, the canonical averages according to the relation (3) were obtained. All three components have different values, so we can state that the simulated stars have an average form of the three-axis ellipsoid. Knowledge of these components makes it possible to calculate the asphericity parameter of the star [11]:

$$\delta = 1 - 3(sf_1sf_2 + sf_2sf_3 + sf_3sf_1), \quad (7)$$

where the reduced components are  $sf_1 = L_1^2/R_1^2$ ,  $sf_2 = L_2^2/R_1^2$ ,  $sf_3 = L_3^2/R_1^2$ . The asphericity parameter ranges from 0 (absolute symmetry, sphere) up to 1 (the form of a rod). In the globular state, the star with any number of arms has a form similar to that of a sphere (Fig. 6a), and with elevated temperature, the asphericity increases. For the chain, this rising  $\delta(T)$  is monotonous and for stars, this dependency has a maximum, which becomes more distinct with increased  $f$ . The maximum is slightly shifted to lower temperatures with increased  $f$ . Such a tendency can be explained in the following way: the greater the monomer density inside the star, the greater the relative asymmetry the star requires to attain a globular state. It is also clear from the figures that the greater the number of arms, the smaller the deviation of the star's form from an ideal sphere.

We have also considered the parameter that allows us to distinguish between the oblate and the elongated forms [11]

$$S^* = (3sf_1 - 1)(3sf_2 - 1)(3sf_3 - 1). \quad (8)$$

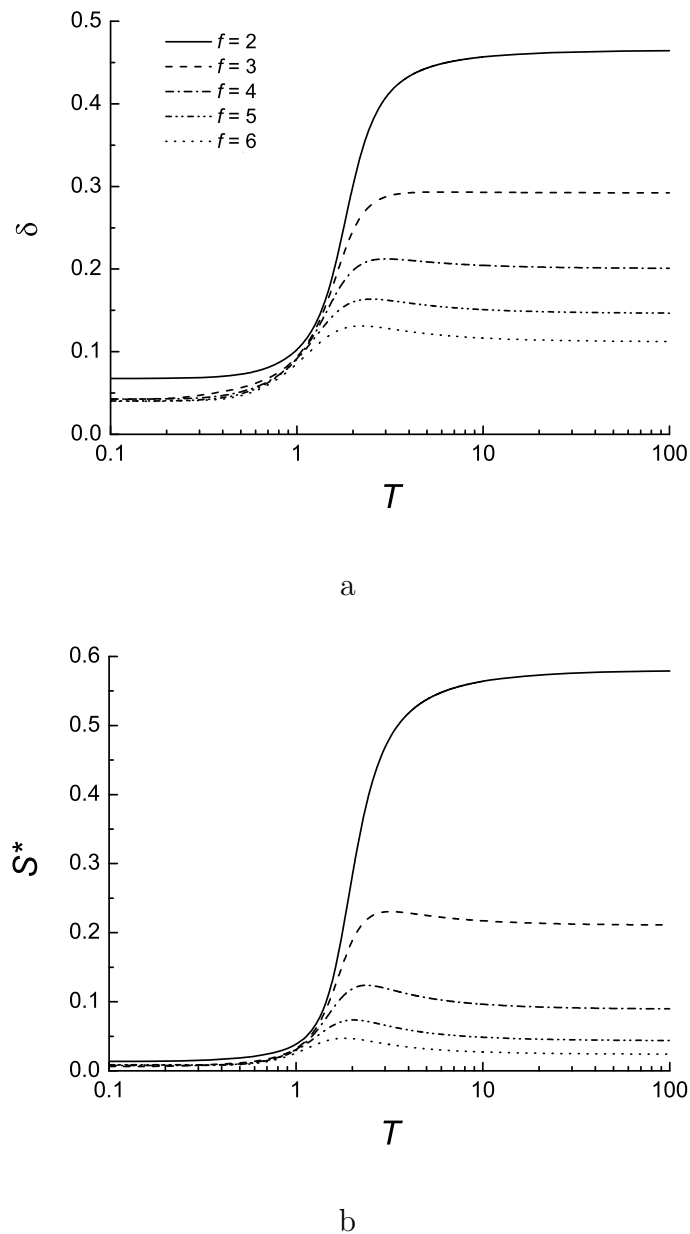


FIG. 6. Temperature dependence of the asphericity  $\delta$  (a) and of the parameter  $S^*$  characterizing the form (b), for stars with different number of arms ( $3 \div 6$ ).  $N=70$  for  $f=5$  and  $N=72$  for all the rest.

This parameter ranges over the interval  $[-0.25, 2]$ , so it can be both negative (oblate form) and positive (elongated form). The temperature dependency of  $S^*$  is presented in Fig. 6b. It is seen that  $S^* > 0$  over the entire temperature range, and hence, the star has the average form of a slightly elongated sphere. It is also worth noting that there is a temperature for which the elongation for stars has a slight maximum while for a chain, the dependency  $S^*(T)$  is monotonous. With the transition to the globular state ( $T < 1$ ), the elongation vanishes.

Fig. 7 presents the dependencies  $\delta(T)$ ,  $S^*(T)$  for 6-arm stars with different arm lengths. Increasing the arms' length was shown to shift the maxima of  $\delta$  and  $S^*$  to higher temperatures and make it slightly more narrow.

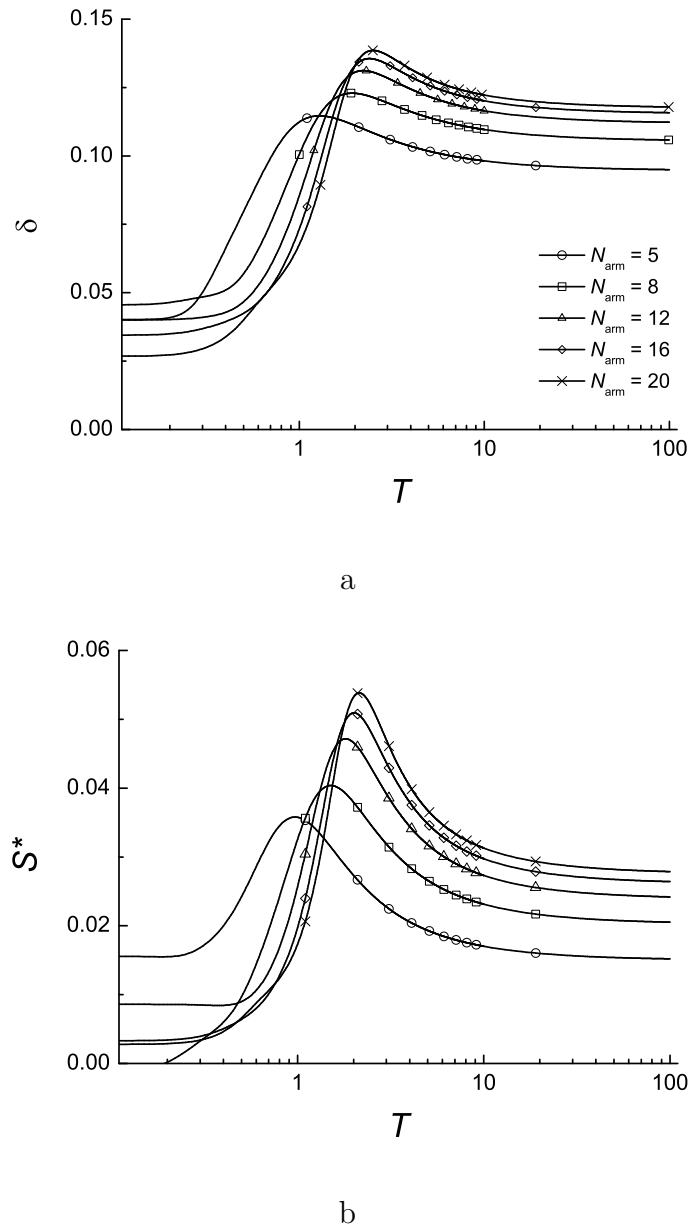


FIG. 7. Temperature dependencies of the asphericity  $\delta$  (a) and of the parameter  $S^*$  characterizing the form (b), for five 6-arm stars with varying arm lengths ( $N_{\text{arm}}=5, 8, 12, 16, 20$ ). Symbols in lines are used for marking different lines.

## 5. Conclusion

In this paper, we have studied a lattice model of regular, non-charged star polymer with the attractive interactions between segments and with varying number of arms. The effect of these characteristics upon temperature behavior of structural characteristics for star polymers is demonstrated. Using the entropic sampling method [18], we could calculate structural properties for stars over a wide temperature range and show that at certain temperatures, a transition of the coil-globule type occurs. This transition shifts to lower temperatures with an increased number of the arms, since it is more difficult to collapse

stars with greater number of arms into a compact globule. In the area of this transition, the form of the star becomes most asymmetric i. e. an elongated ellipsoid.

The number of segments in the considered stars was not very large, however the applied method provides an opportunity to increase this value. Moreover, the next step of this work can imply simulation of star polymers where electrostatic interactions are considered.

## References

- [1] Rud O. V., Mercurieva A. A., Leermakers F. A. M., and Birshtein T. M. Collapse of polyelectrolyte star. Theory and modeling. *Macromolecules*, 2012, **45**, P. 2145–2160.
- [2] Muzafarov A., Vasilenko N., Tatarinova E., Ignateva G., Myakushev V., Obrezkova M., Meshkov I., Voronina N., Novozhilova O. Macromolecular nanoobjects — promising area of polymer chemistry. *Macromolecular compounds C.*, 2011, **53**(7), P. 1217–1230 (in Russian).
- [3] Likos C. N. Soft matter with soft particles. *Soft Matter.*, 2006, **2**, P. 478–498.
- [4] Wang Z., He X. Phase transition of a single star polymer: a Wang-Landau sampling study. *J. Chem. Phys.*, 2011, **135**, P. 094902.
- [5] Polotsky A. A., Zhulina E. B., Birshtein T. M. Effect of the ionic strength on collapse transition in star-like polyelectrolytes. *Macromol. Symp.*, 2009, **278**, P. 24–31.
- [6] Alhoranta A. M., Lehtinen J. K., Urtti A. O., Butcher S. J., Aseyev V. O., Tenhu H. J. Cationic amphiphilic star and linear block copolymers: synthesis, self-assembly, and in vitro gene transfection. *Biomacromolecules*, 2011, **12**, P. 3213–3222.
- [7] Aryal S., Prabakaran M., Pilla S., Gong S. Biodegradable and biocompatible multi-arm star amphiphilic block copolymer as a carrier for hydrophobic drug delivery. *International Journal of Biomacromolecules*, 2009, **44**, P. 346.
- [8] Cameron D., Shaver M. Aliphatic polyester polymer stars: synthesis, properties and applications in biomedicine and nanotechnology. *Chemical Society Reviews*, 2011, **40**, P. 1761–1776.
- [9] Grossberg A. Y., Khokhlov A. R. *Statistical physics of macromolecules*. Moscow, Nauka, 1989 (in Russian).
- [10] Clisby N. Efficient implementation of the pivot algorithm for self-avoiding walks. *J. Stat. Phys.*, 2010, **140**, P. 349–392.
- [11] Zifferer G., Eggerstorfer D. Monte Carlo simulation studies of the size and shape of linear and star-branched copolymers embedded in a tetrahedral lattice. *Macromol. Theory. Simul.*, 2010, **19**, P. 458–482.
- [12] Wüst T., Lee Yu., Landau D. Unraveling the beautiful complexity of simple lattice model polymers and proteins using Wang-Landau sampling. *J. Stat. Phys.*, 2011, **144**, P. 638–651.
- [13] Yurchenko A. A., Antyukhova M. A., Vorontsov-Velyaminov P. N. Investigation of the interaction of the polymer with the surface by entropic modeling. *J. Structure Chemistry.*, 2011, **52**(6), P. 1216–1223 (in Russian).
- [14] Vogel T., Bachmann M., and Janke W. Freezing and collapse of flexible polymers on regular lattices in three dimensions. *Phys. Rev. E.*, 2007, **76**, P. 061803.
- [15] Volkov N. A., Yurchenko A. A., Lyubartsev A. P., Vorontsov-Velyaminov P. N. Entropic sampling of free and ring polymer chains. *Macromol. Theory Simul.*, 2005, **14**, P. 491–504.
- [16] Berg B. A., Neuhaus T. Multicanonical ensemble: a new approach to simulate first-order phase transitions. *Phys. Rev. Lett.*, 1992, **68**, P. 9–12.
- [17] Lee J. New Monte Carlo algorithm: entropic sampling. *Phys. Rev. Lett.*, 1993, **71**, P. 211–214.
- [18] Wang F., Landau D. P. Efficient, multiple-range random walk algorithm to calculate the density of states. *Phys. Rev. Lett.*, 2001, **86**, P. 2050–2035.
- [19] Vorontsov-Velyaminov P. N., Yurchenko A. A., Antyukhova M. A., Silantyeva I. A., Antipina A. Yu. Entropic sampling of polymers: A chain near a wall, polyelectrolytes, star-shaped polymers. *Polymer Science C*, 2013, **55**(1), P. 112–124.
- [20] Silantyeva I. A., Vorontsov-Velyaminov P. N. Thermodynamic properties of star shaped polymers investigated with Wang-Landau Monte Carlo simulations. *Macromol. Symp.*, 2012, **317-318**, P. 267–275.
- [21] Silantyeva I. A., Vorontsov-Velyaminov P. N. The calculation of the density of states and the thermal properties of the polymer chains and stars on a lattice by Monte Carlo method using the Wang-Landau algorithm. *Numerical Methods and Programming*, 2011, **12**, P. 397–408 (in Russian).
- [22] Seaton D. T., Wüst T., Landau D. P. Collapse transition in a flexible homopolymer chain: application of the Wang-Landau algorithm. *Phys. Rev. E.*, 2010, **81**, P. 011802.

- [23] Martemyanova J. A., Stukan M. R., Ivanov V. A., Müller M., Paul W., Binder K. Dense orientationally ordered states of a single semiflexible macromolecule: An expanded ensemble Monte Carlo simulation. *J. Chem. Phys.*, 2005, **122**, P. 174907.
- [24] 24. Wang Z., Wang L., Chen Y., He X. Phase transition behaviours of a single dendritic polymer. *Soft Matter.*, 2014, **10**, P. 4142–4150.
- [25] 25. Arkin H., Janke W. Ground-State properties of a polymer chain in attractive sphere. *J. Phys. Chem. B.*, 2012, **116**, P. 10379–10386.

# Boundary effect on multiple scattering of elastic waves in a half-space

A. Yu. Val'kov<sup>1,2</sup>, V. L. Kuzmin<sup>1,2</sup>, V. P. Romanov<sup>1</sup>, M. A. Nikitina<sup>1</sup>, V. Meglinskii<sup>3,4</sup>

<sup>1</sup> Department of Physics, St. Petersburg State University, St. Petersburg, Russia

<sup>2</sup> Department of Mathematics, St. Petersburg State University of Commerce and Economics, St. Petersburg, Russia

<sup>3</sup> Department of Physics, University of Otago, Dunedin, New Zealand

<sup>4</sup> Faculty of Physics, Saratov State University, Saratov, Russia

alexvalk@mail.ru, kuzmin\_vl@mail.ru

**PACS** 43.35.Cg, 43.20.Gp, 43.20.Bi, 43.40.Ph

**DOI** 10.17586/2220-8054-2015-6-4-524-536

*Received: 20 June 2015*

The scattering of elastic waves is studied in the vicinity of a vacuum-medium boundary. The Green's function for a half-space is re-derived within the mixed 2D-Fourier representation, which is convenient for studying layered media. Monte-Carlo simulations of elastic wave scattering from random inhomogeneities within a simplified scalar model are performed, accounting for a boundary-induced term in the Green's function. The multiply scattered elastic waves' radiation is shown to decay with distance from the source much slower in vicinity of boundary than in an infinite medium, due to the boundary condition requirements.

**Keywords:** Elastic waves, Boundary effect, Half-space, Multiple scattering, Monte-Carlo simulation.

## 1. Introduction

We consider the problem of scattering for radiation generated by a point-like source of harmonic oscillations in an elastic half-space. The field of the point-source, known as the Green's function of the wave equation, is fundamental for the theory of the single-, as well as multiple- scattering in random media ([1]).

The problem of the displacement field generated by a point-like source in an elastic bounded medium has been considered for more than 150 years, beginning with [2], and [3]. This problem is nevertheless still relevant today ([4–6]).

There is considerable interest in coda waves, which were interpreted in [7] as scattering from lithospheric heterogeneities (see, e.g., [8–11]). Great attention has been paid in the last few decades to the multiple scattering of waves of different physical natures in random media ([12]). In particular, remarkable progress has been achieved in multiple light scattering (see, i.g., [13]). Subsequent methods elaborated for light scattering in random media were applied to the investigation of elastic field scattering, mainly for seismic issues ([14–20]).

Previously, the multiple scattering of elastic waves were studied using the Monte Carlo method ([14, 21, 22]) for a one-mode scalar model. Such a one-mode model can be justified with the elastic waves transfer equation ([23]), which assumes the shear mode to be dominant. Realistically accounting for the mode conversions allowed the authors ([18]) to show that the shear mode becomes dominant very rapidly in the coda. Detailed Monte Carlo simulations were performed in ([24]), taking into account mode conversions and considering multiple scattering in an infinite space.

In the case of an electromagnetic field, the larger share of the wave refracting at the boundary with vacuum escapes from the medium due to small reflectivity; the reflected share of radiation is on the order of several percent for most dielectric materials. In contrast, for elastic wave radiation, there occurs a total reflection at the boundary of an elastic medium with a vacuum, requiring that the radiation incident upon the boundary should be completely returned back to the medium. Thus, while the corrections to the Green's function caused by the boundary can be neglected for the light scattering, for acoustic radiation, the specific boundary contributions to the acoustic Green's function should turn out to be quite important.

In earlier simulations of multiple light scattering, we developed the semi-analytic Monte-Carlo approach ([25]) for a scalar model based upon the Bethe-Salpeter equation, successively describing a number of correlation and coherent phenomena in random media optics. Here, we generalize this approach for the multiple scattering of elastic waves, also in the scalar one-mode approximation. We perform the elastic wave multiple scattering simulation, describing radiation transfer in the framework of a simplified Bethe-Salpeter equation, within the one-mode approximation. A crucial distinction of the present approach is that calculating the iterative expansion terms for the Bethe-Salpeter equation in scattering demands we use the exact form of the scalar Green's function for the half-space geometry, thus explicitly accounting for boundary conditions at the vacuum-elastic medium boundary. To the best of our knowledge, such an approach to the boundary effect problem in multiple scattering has not been applied before. We perform the Monte Carlo simulation for multiple scattering of waves propagated from a point-like radiation source to a point-like receiver. For comparison, we present the simulation results obtained using Green's function for an unbounded space. We found that using the exact Green's function for a half-space and the Green's function for an infinite space gave rather different results. The simulations have shown that multiply scattered radiation, obtained with proper accounting for the boundary, propagates in the vicinity of vacuum-medium boundary for much longer distances than would be the case for a simplified approach, wherein one neglects the boundary effect on the Green's function.

The paper is organized as follows: section 2 contains general equations of elastic wave theory; section 3 presents the Green's function for a half-space within the 2D-Fourier representation; in the fourth section the Monte Carlo procedure accounting for boundary effect is described; section 5 contains results of simulations, and section 6 contains conclusions.

## 2. Generals

The elastic field, described as displacement vector  $\mathbf{u}(\mathbf{r}, t)$  dependent on space  $\mathbf{r}$  and time  $t$  ([26]), in an homogeneous medium satisfies the wave equation:

$$\partial^2 \mathbf{u} / \partial t^2 - c_t^2 \Delta \mathbf{u} + (c_l^2 - c_t^2) \text{grad div } \mathbf{u} = \mathbf{0}, \quad (1)$$

where  $c_t = \sqrt{\mu/\rho}$  and  $c_l = \sqrt{(K + 4\mu/3)/\rho}$  are the velocities of transverse and longitudinal elastic waves, respectively;  $\rho$  is the density,  $\mu$  and  $K$  are the shear and the compression moduli. The boundary conditions at the vacuum-medium interface  $B$  are defined as:

$$\boldsymbol{\sigma} \mathbf{n}|_B = \mathbf{0}, \quad (2)$$

where  $\mathbf{n}$  is the normal vector to surface  $B$ , and  $\boldsymbol{\sigma}(\mathbf{r}, t)$  is the stress tensor, with components

$$\sigma_{ij} = (K - 2\mu/3) \delta_{ij} \text{div } \mathbf{u} + \mu \left( \frac{\partial u_i}{\partial r_j} + \frac{\partial u_j}{\partial r_i} \right). \quad (3)$$

We consider harmonic fields with the temporal dependence of the form  $\propto \exp(-i\omega t)$ , where  $\omega$  is the frequency. For the harmonic point-source with frequency  $\omega$ , the displacement field is described by the tensor Green's function  $\mathbf{G}(\mathbf{r}, \mathbf{r}'; \omega)$  which satisfies the equation:

$$\rho [(c_t^2 - c_l^2) \nabla \otimes \nabla - \mathbf{l} (\omega^2 + c_t^2 \Delta)] \mathbf{G}(\mathbf{r}, \mathbf{r}', \omega) = \mathbf{l} \delta(\mathbf{r} - \mathbf{r}'), \quad (4)$$

where  $\mathbf{l}$  is the identity tensor,  $\otimes$  denotes the tensor product,  $\mathbf{r}'$  and  $\mathbf{r}$  are the source and receiver positions. Further, for brevity, we omit the argument  $\omega \geq 0$ .

For an infinite homogeneous medium, the Green's function  $\mathbf{G}(\mathbf{r}, \mathbf{r}') = \mathbf{G}_0(\mathbf{R})$  with  $\mathbf{R} = \mathbf{r} - \mathbf{r}'$  due to translational invariance. This Green's function in the  $(\mathbf{r}, \omega)$ -representation is known to be (see, i.g. [4], Eq. (4.43)):

$$\begin{aligned} \mathbf{G}_0(\mathbf{R}) = \frac{1}{\rho c_t^2} \frac{e^{ik_t R}}{4\pi R} \left[ \left( \mathbf{l} - \frac{\mathbf{R} \otimes \mathbf{R}}{R^2} \right) + \left( \frac{i}{k_t R} - \frac{1}{k_t^2 R^2} \right) \left( \mathbf{l} - 3 \frac{\mathbf{R} \otimes \mathbf{R}}{R^2} \right) \right] + \\ + \frac{1}{\rho c_l^2} \frac{e^{ik_l R}}{4\pi R} \left[ \frac{\mathbf{R} \otimes \mathbf{R}}{R^2} - \left( \frac{i}{k_l R} - \frac{1}{k_l^2 R^2} \right) \left( \mathbf{l} - 3 \frac{\mathbf{R} \otimes \mathbf{R}}{R^2} \right) \right], \quad (5) \end{aligned}$$

where  $k_l = \omega/c_l$  and  $k_t = \omega/c_t$  are the longitudinal and transverse wave numbers respectively. The radiation condition adds to  $k_{t,l}$  infinitesimal damping  $\text{Im}(k_{t,l}) = +i0$ . Forbidding waves to propagate from infinity to the source requires that the Green's function should satisfy the Sommerfeld radiation condition. As can easily be seen, the near-field asymptotics  $\mathbf{G}_0(\mathbf{R}) \propto R^{-1}$ , whereas terms of the form  $R^{-3}$  and  $R^{-2}$  cancel each other out in the short distance limit,  $R \rightarrow 0$ , in contrast with the electromagnetic field, containing ([27]) asymptotic term  $R^{-3}$ .

For a half-space medium, the 2D Fourier transform over transversal variables  $x, y$  turns to be an effective method for solution of the wave equation due to its cylindrical symmetry ([4,28]). Thus, in this  $(\mathbf{q}_\perp, z)$ -representation, the wave equation (1) for temporally harmonic displacement takes the form:

$$(\mathbf{K}_2 \partial^2 / \partial z^2 + i\mathbf{K}_1 \partial / \partial z + \mathbf{K}_0) \mathbf{u}(\mathbf{q}_\perp, z) = \mathbf{0}, \quad (6)$$

where  $\mathbf{K}_2, \mathbf{K}_1 = \mathbf{K}_1(\mathbf{q}_\perp)$  and  $\mathbf{K}_0 = \mathbf{K}_0(\mathbf{q}_\perp)$  are the  $3 \times 3$ -matrices,

$$\begin{aligned} \mathbf{K}_0 = (\omega^2 - c_t^2 q_\perp^2) \mathbf{l} - (c_l^2 - c_t^2) \mathbf{Q} \otimes \mathbf{Q}, \quad \mathbf{K}_1 = (c_l^2 - c_t^2) (\mathbf{Q} \otimes \mathbf{n} + \mathbf{n} \otimes \mathbf{Q}), \\ \mathbf{K}_2 = c_l^2 \mathbf{l} + (c_l^2 - c_t^2) \mathbf{n} \otimes \mathbf{n}, \end{aligned} \quad (7)$$

and the transversal vector  $\mathbf{q}_\perp$  is presented formally as the 3D-vector  $\mathbf{Q} = (\mathbf{q}_\perp, 0)$ .

There are six independent solutions of Eq. (6):

$$\mathbf{e}_j^\pm(\mathbf{q}_\perp, z) = \mathbf{e}_j^\pm(\mathbf{q}_\perp) e^{\pm i\kappa_j(q_\perp)z}, \quad j = 1, 2, 3, \quad (8)$$

where  $\kappa_{1,2}(q_\perp) = \kappa_t(q_\perp)$ ,  $\kappa_3(q_\perp) = \kappa_l(q_\perp)$ ,

$$\kappa_t = \sqrt{k_t^2 - q_\perp^2}, \quad \kappa_l = \sqrt{k_l^2 - q_\perp^2}, \quad (9)$$

are the eigenvalues and

$$\begin{aligned} \mathbf{e}_1^\pm(\mathbf{q}_\perp) = \mathbf{q}_\perp \times \mathbf{n} / q_\perp, \quad \mathbf{e}_3^\pm(\mathbf{q}_\perp) = \mathbf{q}_l^\pm (q_\perp^2 + |\kappa_l|^2)^{-1/2}, \\ \mathbf{e}_2^\pm(\mathbf{q}_\perp) = (\pm \kappa_t(q_\perp) \mathbf{q}_\perp / q_\perp - q_\perp \mathbf{n}) (q_\perp^2 + |\kappa_t|^2)^{-1/2} \end{aligned} \quad (10)$$

— eigenvectors of the second order matrix differential operator in Eq. (6), with

$$\mathbf{q}_l^\pm = (\mathbf{q}_\perp, \pm \kappa_l(q_\perp)) \quad (11)$$

being the 3D wave vector. The waves with superscripts “ $\pm$ ” propagate along axis  $z$  in directions  $z \rightarrow \pm\infty$ , respectively. These normal waves have simple physical interpretation:  $\mathbf{u}_{1,2}^\pm(\mathbf{q}_\perp, z)$  are the transverse waves with wave vectors  $\mathbf{q}_t^\pm$  and  $\mathbf{u}_3^\pm(\mathbf{q}_\perp, z)$  are the longitudinal waves with wave vectors  $\mathbf{q}_t^\pm$ . Unit vectors  $\mathbf{e}_j^\pm$  are the polarizations of these waves.

It should be noted that due to the equality  $\varkappa_1 = \varkappa_2$ , one can take as a set of eigenvectors  $\mathbf{e}_{1,2}^\pm$  any pair of linear independent vector satisfying to the orthogonality condition  $\mathbf{e}_{1,2}^\pm \perp \mathbf{q}_t^\pm$ . We have fixed the choice requiring supplementarily the orthogonality relations  $\mathbf{e}_1^\pm \perp \mathbf{n}$ ,  $\mathbf{e}_1^\pm \perp \mathbf{q}_\perp$  and  $\mathbf{e}_1^\pm \perp \mathbf{e}_2^\pm$  should be fulfilled. Then, the subscript  $j = 1$  corresponds to SH-wave,  $j = 2$  — to SV-wave, and  $j = 3$  — to the P-wave.

### 3. The Green’s function in a Half-Space

Let an elastic medium occupy the half-space  $z > 0$ . There have been several derivations beside the classic ones for the Greens function in an elastic half-space; our approach is quite close to that used by Johnson. The Green’s function within the  $(\mathbf{q}_\perp, z)$ -representation with the  $\delta$ -form source obeys the equation:

$$\rho (K_2 \partial^2 / \partial z^2 + iK_1 \partial / \partial z + K_0) \mathbf{G}(\mathbf{q}_\perp; z, z') = l\delta(z - z'). \quad (12)$$

The solution of Eq. (12) supplemented with boundary conditions at  $z = 0$  can be sought as a sum of two terms

$$\mathbf{G}(\mathbf{q}_\perp; z, z') = \mathbf{G}_0(\mathbf{q}_\perp; z - z') + \mathbf{G}_B(\mathbf{q}_\perp; z, z'), \quad (13)$$

where  $\mathbf{G}_0$  is the Green’s function for the infinite homogenous medium and  $\mathbf{G}_B$ , being the solution of the homogeneous wave equation

$$(K_2 \partial^2 / \partial z^2 + iK_1 \partial / \partial z + K_0) \mathbf{G}_B(\mathbf{q}_\perp; z, z') = \mathbf{0}, \quad (14)$$

satisfies to the boundary condition.

The first term, the Green’s function for an infinite homogeneous medium (5), can be written in the form:

$$\mathbf{G}_0(\mathbf{q}_\perp, z - z') = i (2\varkappa_i \rho \omega^2)^{-1} \left[ \varkappa_i^{-1} e^{i\varkappa_i |z - z'|} (k_t^2 l - \mathbf{q}_t^\pm \otimes \mathbf{q}_t^\pm) + \varkappa_i^{-1} e^{i\varkappa_i |z - z'|} \mathbf{q}_t^\pm \otimes \mathbf{q}_t^\pm \right], \quad (15)$$

where superscripts “+” must be chosen for  $z - z' > 0$  and “-” for  $z - z' < 0$  in  $\mathbf{q}_{t,l}^\pm$ .

Since components of the tensor Green’s function can be interpreted as matter displacements, induced by the point source, the boundary conditions (2) give:

$$(\mathbf{B}_1 \partial / \partial z + i\mathbf{B}_0) \mathbf{G}(\mathbf{q}_\perp; z, z')|_{z=0} = \mathbf{0}, \quad (16)$$

where  $z'$  is an arbitrary point inside the medium,  $z' > 0$ ,

$$\mathbf{B}_0 = \mu \mathbf{Q} \otimes \mathbf{n} + (K - 2\mu/3) \mathbf{n} \otimes \mathbf{Q}, \quad \mathbf{B}_1 = \mu l + (K + \mu/3) \mathbf{n} \otimes \mathbf{n}. \quad (17)$$

Additionally, one should require there should be no wave propagation from infinity,  $+\infty$ , to the source. Since, for the body term  $\mathbf{G}_0(\mathbf{q}_\perp; z, z')$ , this requirement is fulfilled, it should also be fulfilled for the term  $\mathbf{G}_B(\mathbf{q}_\perp; z, z')$ .

The solution for matrix equation (14), containing no wave propagation from infinity, can be written as:

$$\mathbf{G}_B(\mathbf{q}_\perp; z, z') = \sum_{j,m=1}^3 C_{jm} \mathbf{u}_m^+(\mathbf{q}_\perp; z) \otimes \mathbf{u}_j^-(\mathbf{q}_\perp; -z'), \quad (18)$$

where  $C_{jm} = C_{jm}(\mathbf{q}_\perp)$  are the coefficients determined by the set of boundary conditions (16),

$$(\mathbf{B}_1 \partial / \partial z + i\mathbf{B}_0) \mathbf{G}_B(\mathbf{q}_\perp; z, z')|_{z=0} = - (\mathbf{B}_1 \partial / \partial z + i\mathbf{B}_0) \mathbf{G}_0(\mathbf{q}_\perp; z, z')|_{z=0}. \quad (19)$$

Physically, the  $(j, m)$  term describes wave  $\mathbf{u}_j^-$  incident upon the boundary and reflected as wave  $\mathbf{u}_m^+$ , propagating from boundary to receiver. We schematically illustrate in Fig. 1 the propagation of waves, constituting the Green's function  $\mathbf{G}(\mathbf{r}', \mathbf{r})$ , in a half space with boundary  $B$ , from the source to receiver.

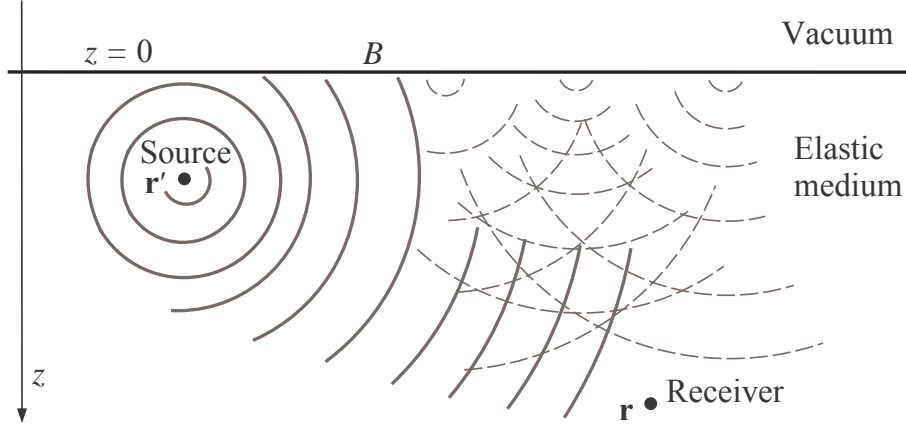


FIG. 1. Schematic source and receiver arrangement in the half-space geometry. The solid and dash circular arcs represent waves  $\mathbf{G}_0$  and  $\mathbf{G}_B$ , respectively, and  $B$  is the boundary of the medium-vacuum.

Substituting Eqs. (18) and (15) into (19), we obtain a set of algebraic equations for nine coefficients  $C_{jm}$  with solution in the form:

$$C_{jm} = -ia_{mj} (2\rho c_j^2 \varkappa_j D)^{-1}, \quad (20)$$

where  $j, m = 1-3$ ;  $c_{1,2} = c_t$ ,  $c_3 = c_l$ , and

$$\begin{aligned} a_{11} &= D, \quad D = 4\varkappa_t \varkappa_l q_\perp^2 + E^2, \quad E = k_t^2 - 2q_\perp^2, \quad a_{22} = a_{33} = D - 2E^2, \\ a_{23} &= -4c_l c_t^{-1} \varkappa_l q_\perp E, \quad a_{32} = -a_{23} c_t^2 c_l^{-2} \varkappa_t \varkappa_l^{-1}, \quad a_{1j} = a_{j1} = 0 \quad (j = 2, 3). \end{aligned} \quad (21)$$

Performing the inverse Fourier transform we present the boundary induced term  $\mathbf{G}_B$  in the physical space as follows:

$$\mathbf{G}_B(\mathbf{R}_\perp; z, z') = -\frac{i}{2\rho} \sum_{j,m=1}^3 c_j^{-2} \int \frac{d\mathbf{q}_\perp}{(2\pi)^2} \frac{a_{mj}}{D \varkappa_j} e^{i\mathbf{q}_\perp \cdot \mathbf{R}_\perp} e^{i(\varkappa_m z + \varkappa_j z')} \mathbf{e}_m^+(\mathbf{q}_\perp) \otimes \mathbf{e}_j^-(\mathbf{q}_\perp). \quad (22)$$

The 2D-integrals are expressed through 1D-integrals for the Bessel functions. The  $(j, m)$ -term in this sum can be described as an input for the transformation of the  $j$ -mode incident wave into the  $m$ -mode generated wave. The zero values for coefficients  $a_{12}$ ,  $a_{21}$ ,  $a_{13}$ ,  $a_{31}$  correspond to the well-known selection rules ([4]).

Various contributions to integrals (22) over  $\mathbf{q}_\perp$  reproduce the known types of elastic waves of different physical nature. The vicinity of stationary phases in exponentials of Eq. (22) yields the known formulas of geometrical acoustics describing all pairs of different modes of incident and reflected waves. The pole singularity due to the zero of determinant  $D(q_\perp)$  in the integrand, gives rise to surface Rayleigh waves. The zeros of  $\varkappa_j$  at  $q_\perp = k_{t,l}$ , being the branch points of the integrands, give rise to head waves.

In the far-field zone,  $q_\perp R_\perp + z \varkappa_m + z' \varkappa_j \gg 1$ , the integrands in Eq. (22) contain rapidly oscillating exponents and the method of stationary phase can be applied. The relevant

contribution to each integral comes from the range of the stationary point  $\mathbf{q}_{\text{st}}^{jm} = q_{jm}\mathbf{R}_{\perp}/R_{\perp}$ , ( $0 \leq q_{jm} < k_{t,l}$ ), which can be found as the root of equation:

$$z'q_{jm}\varkappa_j^{-1}(q_{jm}) + zq_{jm}\varkappa_m^{-1}(q_{jm}) = R_{\perp}. \quad (23)$$

As a result, this contribution can be presented as follows:

$$\mathbf{G}_B^{\text{st}}(\mathbf{R}_{\perp}; z, z') \sim - \sum_{j,m=1}^3 \frac{1}{\rho c_j^2} F_{jm}(q_{jm}) \frac{e^{i\Phi_{jm}(q_{jm})}}{4\pi R_{jm}(q_{jm})} \mathbf{e}_m^+(\mathbf{q}_{\text{st}}^{jm}) \otimes \mathbf{e}_j^-(\mathbf{q}_{\text{st}}^{jm}), \quad (24)$$

where

$$R_{jm} = \sqrt{(R_{\text{in}}^j k_j + R_{\text{ref}}^m k_m \varkappa_j^2 \varkappa_m^{-2}) R_{\perp} q_{jm}^{-1}}, \quad (25)$$

and  $R_{\text{in}}^j(q_{jm})$  and  $R_{\text{ref}}^m(q_{jm})$  can be interpreted as the geometric acoustic path of an elastic wave traveling from the source to the boundary in the form of the  $j$ -th mode and reflected from the boundary to the receiver as the  $m$ -th mode, and:

$$\Phi_{jm} = q_{jm}R_{\perp} + \varkappa_m(q_{jm})z + \varkappa_j(q_{jm})z' \quad (26)$$

is the total phase, and  $F_{jm}(q_{jm}) = a_{mj}(q_{jm})/D(q_{jm})$  are the generalized reflection coefficients. Coefficient  $F_{jm}$  describes conversion of the  $j$ -th incident mode into the  $m$ -th reflected mode at the medium-vacuum boundary. It also accounts for phase shifts and the solid angle transformation occurring at reflection of spherical waves (see Sec. 6 in [4], cf. in optics [29, 30]).

It should be noted that the terms of asymptotic formula (24) can be interpreted as five spherical waves generated by three imaginary sources.

The near-field zone asymptotics of the Green's function, described by (22), as well as the Rayleigh wave contribution, were considered within the approach outlined in [31].

There have been several derivations for the Green's function in an elastic half-space, however, our approach is quite similar to that used in ([28]).

#### 4. Multiple scattering in a half-space

In addition to the coherent wave propagating from a source in a heterogeneous elastic medium, scattered waves also appear. The radiation is scattered from fluctuations of density  $\rho^{(\text{fl})}(\mathbf{r})$  as well as material parameters, which are generally described with the fourth rank tensor  $\mathbf{C}^{(\text{fl})}(\mathbf{r})$ . For a locally-isotropic medium, it can be written as:

$$C_{\alpha\beta\gamma\zeta}^{(\text{fl})}(\mathbf{r}) = K^{(\text{fl})}(\mathbf{r})\delta_{\alpha\beta}\delta_{\gamma\zeta} + \mu^{(\text{fl})}(\mathbf{r}) \left( \delta_{\alpha\gamma}\delta_{\beta\zeta} + \delta_{\alpha\zeta}\delta_{\gamma\beta} - \frac{2}{3}\delta_{\alpha\beta}\delta_{\gamma\zeta} \right), \quad (27)$$

where  $K^{(\text{fl})}(\mathbf{r})$  and  $\mu^{(\text{fl})}(\mathbf{r})$  are the random, or fluctuating compression and shear modules.

We present the material parameters as

$$\rho^{(\text{fl})}(\mathbf{r}) = \rho + \delta\rho(\mathbf{r}), \quad \mathbf{C}^{(\text{fl})}(\mathbf{r}) = \mathbf{C} + \delta\mathbf{C}(\mathbf{r}), \quad (28)$$

where  $\delta\rho(\mathbf{r})$  and  $\delta\mathbf{C}(\mathbf{r})$  are random fluctuations with respect to the average values for  $\rho$  and  $\mathbf{C}$ .

The wave equation for the Green's function  $\mathbf{G}^{(\text{fl})}$  in a random medium in the  $(\mathbf{r}, \omega)$ -representation can be written as:

$$\left[ \rho^{(\text{fl})}(\mathbf{r})\delta_{\alpha\gamma}\omega^2 + \frac{\partial}{\partial r_{\beta}} \left( C_{\alpha\beta\gamma\zeta}^{(\text{fl})}(\mathbf{r}) \frac{\partial}{\partial r_{\zeta}} \right) \right] G_{\gamma\eta}^{(\text{fl})}(\mathbf{r}, \mathbf{r}') = -\delta_{\alpha\eta}\delta(\mathbf{r} - \mathbf{r}'). \quad (29)$$

For an homogeneous non-fluctuating medium, it returns to (4). The differential equation (29) can be written in the form of an integral equation (see [32]):

$$\begin{aligned} \mathbf{G}^{(\text{fl})}(\mathbf{r}, \mathbf{r}') = & \mathbf{G}(\mathbf{r}, \mathbf{r}') + \omega^2 \int \mathbf{G}(\mathbf{r}, \mathbf{r}_1) \delta\rho(\mathbf{r}_1) \mathbf{G}^{(\text{fl})}(\mathbf{r}_1, \mathbf{r}') d\mathbf{r}_1 - \\ & - \int \frac{\partial \mathbf{G}(\mathbf{r}, \mathbf{r}_1)}{\partial \mathbf{r}_1} \delta\mathbf{C}(\mathbf{r}_1) \frac{\partial \mathbf{G}^{(\text{fl})}(\mathbf{r}_1, \mathbf{r}')}{\partial \mathbf{r}_1} d\mathbf{r}_1. \end{aligned} \quad (30)$$

Here,  $\mathbf{G}(\mathbf{r}, \mathbf{r}')$  is the Green's function of an homogeneous medium occupying the half-space.

Our aim is to study the effect of the boundary on multiple scattering. Multiple scattering has been studied in detail for the case of an electromagnetic field for some time. However, the boundary conditions turn to be quite different for elastic or electromagnetic fields. Namely, for the case of elastic waves and a medium-vacuum boundary, the scattered radiation remains in the medium, in contrast with the electromagnetic field, which permits us to disregard a reflection at the dielectric-vacuum boundary.

In order to illustrate the influence of boundaries on the multiple scattering of elastic waves we introduce a number of simplifying assumptions.

First, we will neglect the tensorial character of the wave equation (30). Then, the Green's function for a half-space takes the form of sum of two spherical scalar waves:

$$G(\mathbf{r}, \mathbf{r}') = G_0(\mathbf{r} - \mathbf{r}') + G_B(\mathbf{r}; \mathbf{r}'); \quad (31)$$

here, the first term is the field of the point-source in an infinite medium:

$$G_0(\mathbf{r} - \mathbf{r}') = 1/(4\pi\rho c^2) |\mathbf{r} - \mathbf{r}'|^{-1} \exp(ik|\mathbf{r} - \mathbf{r}'|), \quad (32)$$

and the second one:

$$G_B(\mathbf{r}; \mathbf{r}') = -G_0(\mathbf{r} - \mathbf{r}'_M) \quad (33)$$

can be interpreted as the field of the source's mirror image, located at point  $\mathbf{r}'_M = (x', y', -z')$  where  $\mathbf{r}' = (x', y', z')$  and  $c$  is the velocity of the considered wave mode. (Formally the tensor equations (13), (5) and (24) are reduced to scalar ones, (31)–(33), if  $c_l = c_t = c$ ; this condition is non-physical for an elastic medium, but simplifies greatly the mathematical aspects of multiple scattering analysis and simulation.) The wave number  $k = k' + ik''$  contains both the real part,  $k' = \omega/c$ , as well as the imaginary part,  $k'' = 1/(2l)$ , where  $l$  is the extinction length; the extinction is contributed by elastic scattering and adsorption, namely  $l^{-1} = l_a^{-1} + l_s^{-1}$  where  $l_s$  is the scattering mean free path and  $l_a$  is adsorption length. A similar scalar model has been used in a number of Monte-Carlo simulations for seismic problems (see, e.g., [22, 33]).

Secondly, we will neglect fluctuations of elastic moduli as compared with the density fluctuations. This approach corresponds to the widely-known assumption that the fluctuations of thermodynamic variable derivatives are to be smaller than those of the variables themselves; thus we neglect the second integral term in (30).

As a result, we arrive at the one-mode scalar approximation for the considered wave-scattering problem. In particular, we neglect the difference in reflection for the specific modes of different types and do not consider the non-trivial transformation of the longitudinal and transverse waves under scattering. These effects are significant, and thus, require special consideration. Note also that with these simplifications, the simulation of the elastic field transfer turns to be exactly the same as simulations of light radiation in a random medium in the scalar field approach framework ([25]). Additionally, to make the boundary conditions as distinct as possible from that of light scattering, we presently add a term accounting for the contribution of reflected radiation for every scattering event.

The intensity of scattered radiation,  $I_{sc}(\mathbf{r}, \mathbf{r}')$ , transferred from the source in point  $\mathbf{r}'$  to receiver located in  $\mathbf{r}$ , is proportional to the square of the Green's function modulus:

$$I_{sc}(\mathbf{r}, \mathbf{r}') \propto |G^{(H)}(\mathbf{r}, \mathbf{r}')|^2. \quad (34)$$

Iterating the integral equation (30) and multiplying it by its complex conjugate, one presents the quadratic form (34) as a series in orders of scattering.

For problems dealing with multiple scattering, all the contributions wherein the phase shift between the pair of complex-conjugated fields is not compensated are known to be neglected due to the random configuration of the medium's inhomogeneities. As a result, one can restrict oneself only with ladder contributions, wherein paths traveled by a pair of complex-conjugated fields coincide. Thus, the multiple scattering intensity can be presented as the series:

$$I_{sc}(\mathbf{r}, \mathbf{r}') \propto \sum_{\sigma_{0,1}} \int \Lambda(\mathbf{r}, \mathbf{r}_1^{\sigma_1}) B(\mathbf{k}_{(s)1}^{\sigma_1} - \mathbf{k}_{(i)0}^{\sigma_0}) \Lambda(\mathbf{r}_1, \mathbf{r}'^{\sigma_0}) d\mathbf{r}_1 + \\ + \sum_{\sigma_{0,1,2}} \int \Lambda(\mathbf{r}, \mathbf{r}_2^{\sigma_2}) B(\mathbf{k}_{(s)2}^{\sigma_2} - \mathbf{k}_{(i)1}^{\sigma_1}) \Lambda(\mathbf{r}_2, \mathbf{r}_1^{\sigma_1}) B(\mathbf{k}_{(s)1}^{\sigma_1} - \mathbf{k}_{(i)0}^{\sigma_0}) \Lambda(\mathbf{r}_1, \mathbf{r}'^{\sigma_0}) d\mathbf{r}_1 d\mathbf{r}_2 + \dots, \quad (35)$$

where the propagator in an infinite medium  $\Lambda(\mathbf{R}, \mathbf{R}')$  describing the radiation transfer between two successive scattering events occurring at points  $\mathbf{r}_{j+1}$  and  $\mathbf{r}_j$  is formed by the product of pair of the Green's function (31)

$$\Lambda(\mathbf{r}_{j+1}, \mathbf{r}_j^\sigma) = |G_0(\mathbf{r}_{j+1} - \mathbf{r}_j^\sigma)|^2. \quad (36)$$

The cross-terms  $G_0 G_B^*$ ,  $G_0^* G_B$  are omitted due to chaotic randomization of phase shifts over the inhomogeneities.

Subscripts  $j = 1, 2, \dots, n$  enumerate the scattering events, therewith indices  $j = 0$  and  $j = n + 1$  refer to the source and receiver,  $\mathbf{r}_0 = \mathbf{r}'$ ,  $\mathbf{r}_{n+1} = \mathbf{r}$ , respectively, (Fig. 2a);

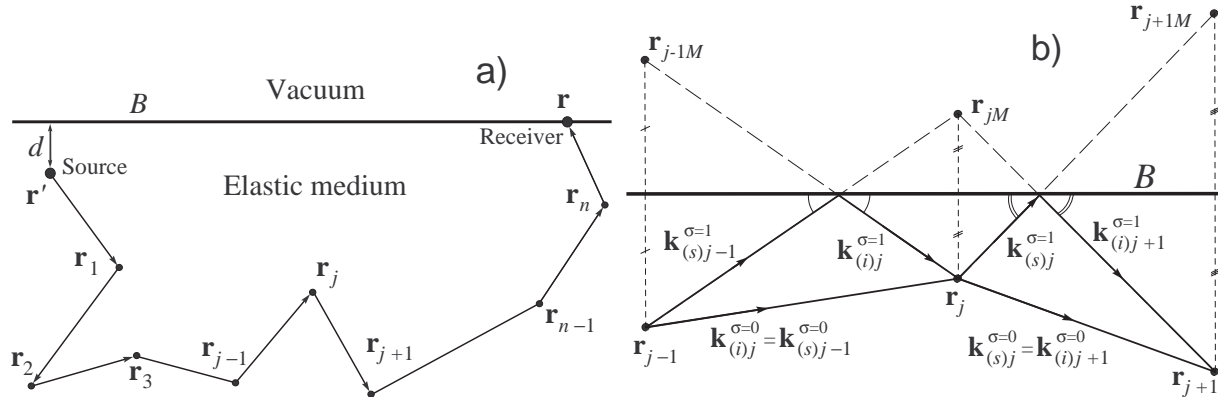


FIG. 2. a) The stochastic trajectory presented as the path traveled by a “phonon packet” undergoing a sequence of  $n$  scattering events. b) Wave vectors of incident,  $\mathbf{k}_{(i)j}^\sigma$ , and scattered,  $\mathbf{k}_{(s)j}^\sigma$ , elastic waves involved in the  $j$ -th scattering event. Superscripts  $\sigma = 0$  and  $\sigma = 1$  correspond to the direct propagation of the beam and to propagation with intermediate reflection, respectively.

$$\mathbf{r}_j^\sigma = \begin{cases} \mathbf{r}_j, & \sigma = 0, \\ \mathbf{r}_{jM}, & \sigma = 1, \end{cases} \quad (37)$$

points  $\mathbf{r}_j$  and  $\mathbf{r}_{jM}$  are the positions of the  $j$ -th scatterer and its mirror image,  $\mathbf{r}_{0M}$   $\mathbf{r}_{n+1,M}$  are the mirror images of the source and the receiver (Fig. 2b). Wave vectors of incident,  $\mathbf{k}_{(i)j}^\sigma$ , and scattered,  $\mathbf{k}_{(s)j}^\sigma$ , elastic waves in  $j$ -th scattering event are

$$\mathbf{k}_{(i)j}^\sigma = k' (\mathbf{r}_j - \mathbf{r}_{j-1}^\sigma) / |\mathbf{r}_j - \mathbf{r}_{j-1}^\sigma|, \quad \mathbf{k}_{(s)j}^\sigma = k' (\mathbf{r}_{j+1}^\sigma - \mathbf{r}_j) / |\mathbf{r}_{j+1}^\sigma - \mathbf{r}_j|. \quad (38)$$

Summing over  $\sigma_0, \sigma_1, \dots$  in Eq. (35), we account for reflections of incident and scattered beams of all scattering orders. Thus, accounting for the boundary effect doubles the number of terms of Eq. (35) with the scattering order increasing per unit.

The phase function  $B(\mathbf{q})$  is the Fourier transform of the density correlation function

$$B(\mathbf{q}) = \int \langle \delta\rho(\mathbf{R})\delta\rho(\mathbf{R}') \rangle e^{-i\mathbf{q}(\mathbf{R}-\mathbf{R}')} d\mathbf{R},$$

where  $\mathbf{q}$  is the momentum transfer  $\mathbf{q} = \mathbf{k}_{(s)} - \mathbf{k}_{(i)}$ . For the isotropic scattering phase function,  $B(q)$  is constant; for anisotropic scattering, it depends on the scattering angle  $\theta$  through wave vectors of incidence  $\mathbf{k}_{(i)}$  and  $\mathbf{k}_{(s)}$ ,  $q = 2k' \sin(\theta/2)$ .

Accounting for the explicit form of the Green's function of a scalar field for a half-space (31), (32), the propagator, describing the radiation transfer between two successive events of scattering in Eq. (35), can be written as follows:

$$\Lambda(\mathbf{r}_{j+1}, \mathbf{r}_j^\sigma) = (4\pi\rho c^2 |\mathbf{r}_{j+1} - \mathbf{r}_j^\sigma|)^{-2} \exp(-|\mathbf{r}_{j+1} - \mathbf{r}_j^\sigma|/l). \quad (39)$$

The exponential decay factor comes from the imaginary part of the wave number in Eq. (32).

Within the Monte-Carlo method, one simulates a stochastic trajectory (Fig. 2). The average over these trajectories gives the scattered radiation intensity.

A random trajectory is constructed recurrently. Let  $\mathbf{r}_j$  be the position of the  $j$ -th scattering event. We define the position of the next scattering event as  $\mathbf{r}_{j+1} = \mathbf{r}_j + \mathbf{r}$ . Let  $U_1$ ,  $U_2$ , and  $U_3$  be three independent random variables uniformly distributed within the interval  $(0; 1)$ ; one determines spherical coordinates of vector  $\mathbf{r}$  with  $\mathbf{r}_j$  as polar axis, namely the distance  $r = |\mathbf{r}|$ , and polar and azimuthal angles,  $\theta$  and  $\phi$ , via these random variables, as follows.

The distance  $r = |\mathbf{r}_{j+1} - \mathbf{r}_j^\sigma|$  is generated using the substitution  $r = -l \ln U_1$ . In this way, the inverse transform sampling method is realized (see, i.g., [34]) which takes into account the exponential decay in Eq. (39).

The azimuthal  $\phi$  is distributed uniformly,  $\phi = 2\pi U_2$ .

The angle  $\theta$  in the own coordinate frame for vector  $\mathbf{r}_j$  is generated using the substitution  $\theta = F^{-1}(U_3)$ , where  $F^{-1}$  is the inverse transform of function:

$$F(x) = \left( \int_0^\pi B(2k' \sin(\theta/2)) d\theta \right)^{-1} \int_0^{\pi x} B(2k' \sin(\theta/2)) d\theta.$$

The  $(j+1)$ -th scatterer position  $\mathbf{r}_{j+1}$  and superscript  $\sigma_j$  are defined as follows. If the point  $\mathbf{r}_j + \mathbf{r}\mathbf{n}$  is located inside the elastic half space (i.e.  $r_{jz} + rn_z \geq 0$ ) then  $\mathbf{r}_{j+1} = \mathbf{r}_j + \mathbf{r}\mathbf{n}$  and we take  $\sigma_j = 0$ . Otherwise, the point  $\mathbf{r}_j + \mathbf{r}\mathbf{n}$  is reflected:  $\mathbf{r}_{j+1} = (\mathbf{r}_j + \mathbf{r}\mathbf{n})_M$  and we take  $\sigma_j = 1$ .

The number of scattering events,  $n_{\max}$ , are determined with the requirement that the numerical data become stable. In our simulations  $n_{\max}$  did not exceed several hundreds.

## 5. Results of simulation

We performed the Monte-Carlo simulation for elastic radiation transfer in the vicinity of a boundary with vacuum for a scalar scattering model for distances far exceeding the characteristic extinction. The approach based on the radiative transfer theory requires that the wavelength should be small, as compared to the extinction length. Performing calculations, we take the sound velocity as  $c = 2.5 \times 10^3$  m/s, and the radiation frequency as  $f = 10^2$  Hz, which produces the wavelength of  $\lambda = 25$  m. We then take the extinction length, range as  $l = 200$  m to  $l = 1000$  m.

To account for scattering anisotropy, we apply the Henyey-Greenstein phase function

$$B(2k' \sin(\theta/2)) \propto (1 - g^2)(1 + g^2 - 2g \cos \theta)^{-3/2}. \quad (40)$$

containing the unique parameter, the mean cosine of scattering angle,  $g = \langle \cos \theta \rangle$ . This function, widely used in many radiation transfer problems ([1]), is a particular realization of the von Kármán phase function (see for example [35]):

$$B(q) \propto (1 + q^2 a^2)^{-3/2 - \varkappa}, \quad (41)$$

well-known in geophysics, with the Hurst exponent  $\varkappa = 0$  and characteristic size of inhomogeneities  $a$  being specified as  $a = k^{-1} \sqrt{g}/(1 - g)$ .

We have also used the optical theorem (see, e.g., [36,37]) which relates the extinction length  $l$  and phase function  $B(q)$ .

We have shown the intensity of multiply scattered radiation as a function of the distance between the source and receiver. We present results for two positions of the source, either at the surface, or at one kilometer deep  $d$  in the medium; the receiver is placed at the boundary.

In Figs. 3a and 3b, the presented results for scattered intensity calculations were shown to be dependent on the distance between the source and the receiver. In Fig. 3a results are presented for isotropic scattering,  $g = 0$ , and in Fig. 3b — for anisotropic scattering,  $g = 0.8$ .

For isotropic scattering, the plots of intensity for multiply-scattered radiation, shown in the same units as function of the source-receiver distance, turn out to be quite close for both geometries. For small distances it can be explained by equal values for the ballistic “phonon” inputs which are dominant at this spatial range, while with increased distances, the depth of the source positions becomes negligible in comparison to the distance along the surface.

For anisotropic scattering, the picture is different. The intensity of multiply scattered radiation turns to be noticeably smaller for the geometry with an imbedded source, as compared to the surface-based source. For comparison, we show the simulation results obtained for the model wherein the boundary of the medium is accounted for only in the spatial integrals over half-space in the series over the scattering orders obtained by iterations of integral equations like the Bethe-Salpeter equation Eq. (30). Such an approach was specifically used in [14,15]. The principal distinction of our approach is that we not only account for the boundedness of the scattering medium by performing the spatial integrations, but also the fact that the integrand itself, being the pair product of Green’s functions, varies approaching the boundary range. For both geometries, the radiation intensity is seen to be smaller for isotropic as well as anisotropic scattering, and decays with distance much faster. Physically, this can be explained by the loss of “phonons” at the boundary due to the neglect of reflection.

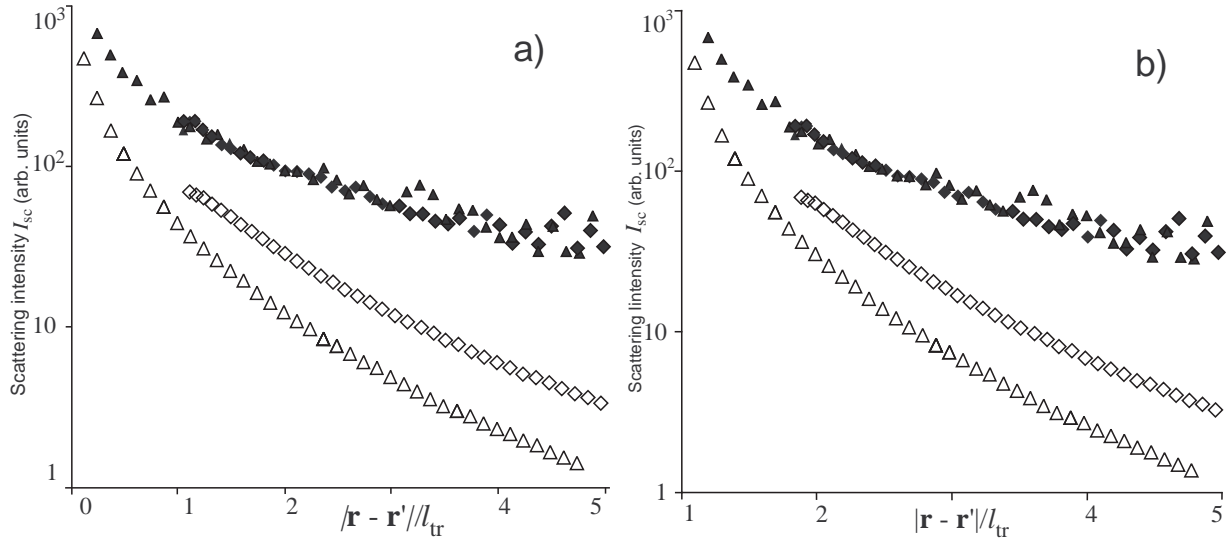


FIG. 3. Intensity of multiply scattered radiation via distance between source and receiver. The sampling volume  $N = 2 \times 10^6$ . The receiver moves along the surface, and the source is located:  $\blacktriangle$  and  $\triangle$  — at the surface,  $\blacklozenge$  and  $\diamond$  — at the depth of 1 km; For both plots:  $\triangle$  — and  $\diamond$  — the reflection of radiation at the boundary is neglected thoroughly, for  $\blacktriangle$  and  $\blacklozenge$  the total reflection at the boundary is supposed. a) isotropic scattering,  $g = 0$ , scattering mean free path  $l_s = 1000$  m. b) anisotropic scattering,  $g = 0.8$ , scattering mean free path  $l_s = 200$  m, adsorption length  $l_a = 10000$  km for both figures.

In media with an anisotropic scattering indicatrix, the transport length  $l_{tr} = l_s(1 - \langle \cos \theta \rangle)^{-1}$ , is known ([1]) to take part of the universal spatial scale for multiple scattering instead of the scattering mean free path  $l_s$ . Thus, we plot the distance between source and receiver in units of  $l_{tr}$ . This permits us to compare results for simulations of acoustic as well as optical models with quite different spatial dimensions.

This effect is especially pronounced within the boundary region, when the source and receiver are both near the surface. It should be noted that the curves, plotted in terms of transport length, would appear to be quite non-sensitive to anisotropy of the scattering cross-section. This verifies the widely acknowledged assumption regarding the validity of the diffusion mechanism for radiation transfer independently of the physical nature of radiation.

## 6. Conclusion

Thus, numerical simulations performed for a quite simplified model of an elastic medium exhibit the important role boundary conditions play in the description of multiple scattering; we have shown that proper accounting for the boundary requires that the form of the Green's function itself should be modified due to the boundary conditions.

Simulating the elastic random wave transfer, we have used a previously-developed approach for the study of multiple scattering of light in random media. However, the boundary conditions for elastic waves highlight a fundamental distinction from that of light scattering. The boundary brings about reflected and refracted waves; for dielectric media, the reflected light radiation, in most cases, can be neglected, since it leads to small radiation amount dependent on the reflectivity mismatch. In contrast, for an elastic medium at the boundary with a vacuum, the total radiation is returned back; thus the boundary effect turns out to be much stronger for an elastic waves as compared with optics.

The results obtained permit us to conclude that under similar conditions, multiply scattered elastic waves travel much longer on an acoustic path, than the light waves, over relevant extinction scales.

For the scalar model considered presently the effect of boundary is simply accounted for due to the fact that the boundary-induced term of the Green's function long-range asymptotics takes the form of a spherical wave generated by a single virtual mirror image source. For a more sophisticated problem of elastic wave multiple scattering, one is to take into account the tensorial character of the Green's function. The boundary-induced term specifically describes, in the far field zone, non-trivial transformations at the vacuum-medium boundary of three incident elastic wave modes into three reflected ones as inputs of different mirror image sources for different types of incident-reflected modes pairs. Near the boundary, above all, the Rayleigh surface waves' input must also be taken into account. We hope that the simulations performed here can be generalized, accounting for all elastic wave modes.

## Acknowledgments

This work was supported partially by the Russian Foundation for Basic Research (Grant No. 13-02-01255).

## References

- [1] Ishimaru A. *Wave Propagation and Scattering in Random Media*. IEEE Press Series on Electromagnetic Wave Theory. Wiley, New York, 1999.
- [2] Sir W. Thomson. Note on the integration of the equations of equilibrium of an elastic solid. *Cambridge and Dublin Mathematical Journal*, 1848, **3**, P. 87–89.
- [3] Sir G. G. Stokes. On the theories of the internal friction of fluids in motion, and of the equilibrium and motion of elastic solids. *Trans. Cambridge Phil. Soc.*, 1849, **8**, P. 287–319.
- [4] Aki K. and Richards P. G.. *Quantitative Seismology: Theory and Methods*. University Science Books, Sausalito, CA, 2nd edition, 2002.
- [5] Felsen L. B. and Marcuvitz N. *Radiation and Scattering of Waves*. IEEE Press Series on Electromagnetic Wave Theory. John Wiley & Sons, New York, 2003.
- [6] Kachanov M. L., Shafiro B., and Tsukrov I. *Handbook of Elasticity Solutions*. Kluwer Academic Publisher, Dordrecht, 2003.
- [7] Aki K. Analysis of the seismic coda of local earthquakes as scattered waves. *Journal of Geophysical Research*, 1969, **74**(2), P. 615–631.
- [8] Herraiz M. and Espinosa A. F. Coda waves: A review. *Pure and Applied Geophysics*, 1987, **125**(4), P. 499–577.
- [9] Snieder R. Coda wave interferometry and the equilibration of energy in elastic media. *Phys. Rev. E*, 2002, **66**, P. 046615.
- [10] Snieder R. Extracting the green's function from the correlation of coda waves: A derivation based on stationary phase. *Phys. Rev. E*, 2004, **69**, P. 046610.
- [11] Anache-Ménier D., van Tiggelen B. A., and Margerin L. Phase statistics of seismic coda waves. *Phys. Rev. Lett.*, 2009, **102**, P. 248501.
- [12] van Tiggelen B. A. and Skipetrov S. E., editors. *Wave Scattering in Complex Media: From Theory to Applications*, volume **107** of *NATO Science Series II: Mathematics, Physics and Chemistry*, Kluwer Academic Publisher, London, 2003.
- [13] van Rossum M. C. W. and Nieuwenhuizen Th. M. Multiple scattering of classical waves: microscopy, mesoscopy, and diffusion. *Rev. Mod. Phys.*, 1999, **71**, P. 313–371.
- [14] Abubakirov I. R. and Gusev A. A. Estimation of scattering properties of lithosphere of kamchatka based on monte-carlo simulation of record envelope of a near earthquake. *Physics of the Earth and Planetary Interiors*, 1990, **64**(1), P. 52–67.
- [15] Sato H. Multiple isotropic scattering model including p-s conversions for the seismogram envelope formation. *Geophysical Journal International*, 1994, **117**(2), P. 487–494.

- [16] Shapiro S. A. and Treitel S. Multiple scattering of seismic waves in multilayered structures. *Physics of the Earth and Planetary Interiors*, 1997, **104**(1–3), P. 147–159.
- [17] Trégourès N. P., Hennino R., Lacombe C., Shapiro N. M., Margerin L., Campillo M., and van Tiggelen B. A. Multiple scattering of seismic waves. *Ultrasonics*, 2002, **40**(1–8), P. 269–274.
- [18] Malcolm A. E., Scales J. A., and van Tiggelen B. A. Extracting the green function from diffuse, equipartitioned waves. *Phys. Rev. E*, 2004, **70**, P. 015601.
- [19] Trujillo L., Peniche F., and Jia X. *Waves in Fluids and Solids*, chapter 5. Multiple Scattering of Elastic Waves in Granular Media: Theory and Experiments, pages 127–152. Intech, Chanhai, China, 2011.
- [20] Margerin L. Diffusion approximation with polarization and resonance effects for the modelling of seismic waves in strongly scattering small-scale media. *Geophysical Journal International*, 2013, **192**(1), P. 326–345.
- [21] Hoshiya M. Simulation of multiple-scattered coda wave excitation based on the energy conservation law. *Physics of the Earth and Planetary Interiors*, 1991, **67**(12), P. 123–136.
- [22] Gusev A. A. and Abubakirov I. R. Vertical profile of effective turbidity reconstructed from broadening of incoherent body-wave pulses — I. General approach and the inversion procedure. *Geophysical Journal International*, 1999, **136**(2), P. 295–308.
- [23] Ryzhik L., Papanicolaou G., and Keller J. B.. Transport equations for elastic and other waves in random media. *Wave Motion*, 1996, **24**(4), P. 327–370.
- [24] Margerin L., Campillo M., and van Tiggelen B. A. Monte carlo simulation of multiple scattering of elastic waves. *Journal of Geophysical Research*, 2000, **105**(B4), P. 7873–7892.
- [25] Meglinski I. V., Kuzmin V. L., Churmakov D. Y., and Greenhalgh D. A. Monte carlo simulation of coherent effects in multiple scattering. *Proceeding of the Royal Society A*, 2005, **461**(2053), P. 43–53.
- [26] Landau L. D. and Lifshitz E. M. *Theory of Elasticity*. Butterworth-Heinemann, Oxford, 3rd edition, 2007.
- [27] Jackson J. D. *Classical Electrodynamics*. Wiley, New York, 3rd. edition, 1998.
- [28] Johnson L. R.. Green's function for Lamb's problem. *Geophysical Journal of the Royal Astronomical Society*, 1974, **37**(1), P. 99–131.
- [29] Lax M. and Nelson D. F.. Adventures in Green's land: Light scattering in. anisotropic media. In L. Mandel and Emil E. Wolf, editors, *Proceedings of the Third Rochester Conference on Coherence and Quantum Optics*, Plenum Press, New York, 1973, P. 415–445.
- [30] Lax M. and Nelson D. F. Light scattering in crystals with surface corrections. In B. Bendow, V. M. Agranovich, and J. L. Birman, editors, *Theory of Light Scattering in Condensed Media, Proc. of the First Joint USA-USSR Symp.*, Plenum Press, New York, 1976, P. 371–90.
- [31] Val'kov A., Kuzmin V., Romanov V., Nikitina M., Kozhevnikov S., and Meglinski I. Field of a point source in a semi-infinite elastic medium. *Waves in Random and Complex Media*, 2012, **22**(3), P. 423–434.
- [32] Snieder R. *Scattering: scattering and inverse scattering in pure and applied science*, volume 1 of *Scattering: Scattering and Inverse Scattering in Pure and Applied Science*, chapter 1.7.1 — General Theory of Elastic Wave Scattering, Academic Press, London, 2002, P. 528–542.
- [33] Maeda T., Sato H., and Nishimura T. Synthesis of coda wave envelopes in randomly inhomogeneous elastic media in a half-space: single scattering model including rayleigh waves. *Geophysical Journal International*, 2008, **172**(1), P. 130–154.
- [34] Devroye L. *Non-Uniform Random Variate Generation*. Springer, New York, 1986.
- [35] Sato H., Fehler M. C., and Maeda T. *Seismic Wave Propagation and Scattering in the Heterogeneous Earth*. Springer, Berlin, 2nd edition, 2012.
- [36] Marston P. L. Generalized optical theorem for scatterers having inversion symmetry: Applications to acoustic backscattering. *J. Acoust. Soc. Am.*, 2001, **109**(4), P. 1291–1295.
- [37] Margerin L. and Sato H. Generalized optical theorems for the reconstruction of green's function of an inhomogeneous elastic medium. *The Journal of the Acoustical Society of America*, 2001, **130**(6), P. 3674–3690.

# On construction of evolutionary operator for rectangular linear optical multiport

M. M. Lipovich, I. S. Lobanov

ITMO University, Kronverkskiy pr. 49, St. Petersburg, 197101, Russia

mariel.21@yandex.ru, lobanov.igor@gmail.com

PACS 42.50.-p, 42.50.Ex

DOI 10.17586/2220-8054-2015-6-4-537-546

The work of Knill et. al. (2001) established the possibility of nondeterministic realization of certain quantum logic operations using linear optical elements, ancilla photons and postselection techniques. It was also shown that any discrete unitary operator acting on  $N$  optical modes can be implemented by a triangular multiport device constructed from a series of beam splitters and phase shifters (see work of Reck, Zeilinger et. al., 1994). Here, we consider the rectangular linear optical multiport that is used for the probabilistic realization of unitary transformations on  $n$  qubits. This kind of linear optical scheme is suitable for probabilistic realization of unitary operators using ancilla photons and projective measurements. Qubits are encoded into the bosonic states of optical modes in two possible polarizations, and a number of ancilla photons and photodetectors are used for postselection of the qubits' state, based on the output of the detectors. We derive a procedure of evolutionary operator calculation for schemes of the considered type and present algorithms for their efficient computation on symmetric state space. We also provide complexities for different algorithms for the computation of evolutionary operator and estimate demands of resources in each case. A destructive Toffoli gate, acting on three qubits, using one ancilla photon and a photodetector, is implemented using schemes of the presented type.

**Keywords:** Quantum computing with linear optics, Projective measurements, Postselection, Photon detectors, Realization of unitary operator, Toffoli gate.

*Received: 30 January 2015*

*Revised: 21 March 2015*

## 1. Introduction

The usage of photons and linear optical elements, such as beam splitters, phase shifters, mirrors, presents the possibility of realizing controllable and scalable quantum computing [1]. Photons demonstrate easily observable, obvious quantum effects and are also able to maintain their coherent states for a long time. Construction of optical devices is comparably easy [1,2]. For instance, these devices do not require low temperatures (except for realization of single-photon sources). In 2001, E. Knill and R. Laffame published the work [2] which established the possibility of constructing quantum logic gates based on linear optics. Projective measurements and ancilla photons were used to introduce the interaction between photons in order to implement non-deterministic realizations of certain quantum operations, like CNOT [3–5].

The experimental realization of unitary operators  $U(N)$  transforming  $N$  optical modes using beam splitters and phase shifters was proposed in paper [6]. Here we present another type of optical multiport that transforms states of photon qubits and performs quantum teleportation by means of a number of ancilla photons and the detectors provided. The problem is to experimentally realize multiqubit unitary operators using this type of optical schemes. The main result, presented in this paper, is a procedure for calculating the evolutionary operator corresponding to mentioned optical schemes and efficient computational algorithms. This result

introduces a step towards creating a method for the automatic construction of non-deterministic linear optical multiports corresponding to a given quantum circuit.

This paper has five sections. In section 2, we derive the evolutionary operator corresponding to a rectangular optical lattice having two-mode linear optical elements in its nodes. This can be implemented using beam splitters coupled by single-mode optical fibers. For the described network, we learn how to compute the corresponding single-particle evolutionary operator. In sections 3 and 5, we show how to efficiently compute multiparticle evolutionary operator. On the basis of the optical network considered in section 2 and inspired by CNOT gate, presented in [7], we propose a destructive Toffoli gate acting on three qubits (see Sec. 4).

### 2. Constructing evolutionary operator for rectangle linear optical multiport

Consider the rectangular grid having  $n$  rows and  $m$  columns (see Fig. 1) in which the nodes are polarizing beam splitters with no phase shift. Here, we compute the single-particle evolutionary operator for this optical grid. Taking into account only the transmitted and reflected modes, an evolutionary operator for this scheme can be implemented by scattering matrix that transforms the amplitudes of the  $2(n + m)$ -mode state. Each beam splitter is associated with a unitary transformation on four optical modes:

$$\begin{pmatrix} H'_a \\ V'_a \\ H'_b \\ V'_b \end{pmatrix} = \begin{pmatrix} \cos(\theta) & -\sin(\theta) & 0 & 0 \\ \sin(\theta) & \cos(\theta) & 0 & 0 \\ 0 & 0 & \cos(\theta) & -\sin(\theta) \\ 0 & 0 & \sin(\theta) & \cos(\theta) \end{pmatrix} \begin{pmatrix} H'_c \\ V'_d \\ H'_d \\ V'_c \end{pmatrix}, \tag{1}$$

where  $(a, b)$  and  $(c, d)$  denote input and output spatial modes,  $H$  and  $V$  denote two possible polarizations and parameter  $\theta$  describes reflectivity and transmittance of the beam splitter [6, 8].

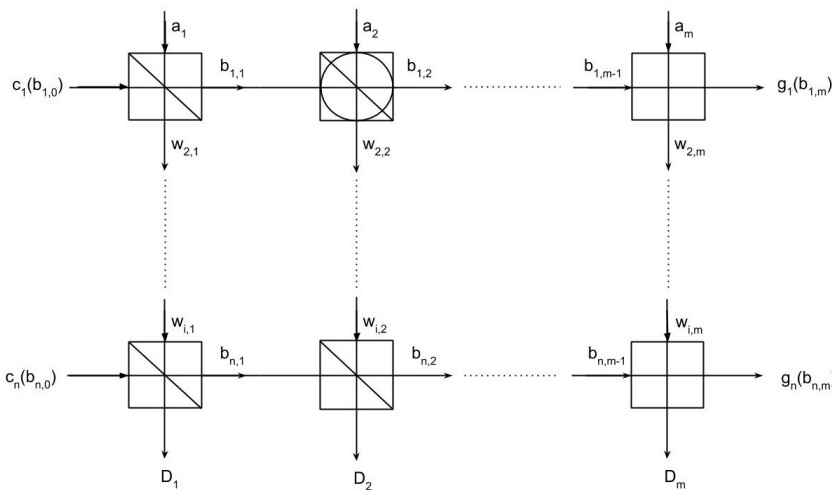


FIG. 1. Grid network with input ports  $c_1 \dots c_n$ ,  $a_1 \dots a_m$  and outputs  $g_1 \dots g_n$ ,  $D_1 \dots D_m$ , for convenience of further calculations some ports are labeled twice

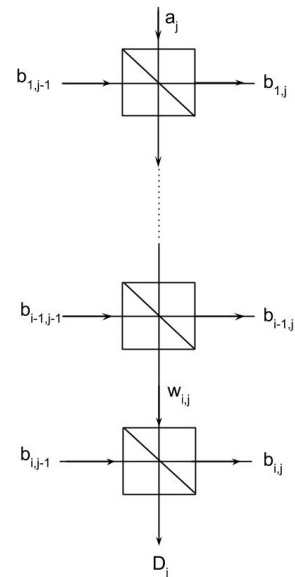


FIG. 2. Subscheme  $N(1 \dots i, j)$

First, we consider separately  $j$ -th column of length  $i$  (see Fig. 2). We denote this subscheme as  $N(1 \dots i, j)$  and find out how it affects the state of the photon. We imply that initially photon

is in the modes  $(Ha_j, Va_j; Hc_{1,j}, Vc_{1,j}, \dots Hc_{i,j}, Vc_{i,j})$ , so the input state for  $N(1 \dots i, j)$  is the following  $2(i + 1)$ -mode state (order of basis elements is preserved):

$$|\varphi_{1\dots i,j}\rangle_{in} = \varphi_{Ha_j} |Ha_j\rangle + \varphi_{Va_j} |Va_j\rangle + \varphi_{Hb_{1,j}} |Hb_{1,j}\rangle + \varphi_{Vb_{1,j}} |Vb_{1,j}\rangle + \dots + \varphi_{Hb_{i,j-1}} |Hb_{i,j-1}\rangle + \varphi_{Vb_{i,j-1}} |Vb_{i,j-1}\rangle,$$

which is transformed into an output state of the form:

$$|\varphi_{1\dots i,j}\rangle_{out} = \varphi_{HD_j} |HD_j\rangle + \varphi_{VD_j} |VD_j\rangle + \varphi_{Hb_{1,j}} |Hb_{1,j}\rangle + \varphi_{Vb_{1,j}} |Vb_{1,j}\rangle + \dots + \varphi_{Hb_{i,j}} |Hb_{i,j}\rangle + \varphi_{Vb_{i,j}} |Vb_{i,j}\rangle,$$

assuming that finally the photon can be found in the modes  $(HD_j, VD_j; Hb_{1,j}, Vb_{1,j} \dots Hb_{i,j}, Vb_{i,j})$ . Input and output states of the particle corresponding to the transformation on  $2i$  modes given by the subscheme  $N(1 \dots i - 1, j)$  are respectively of the following form:

$$\begin{aligned} |\varphi_{1\dots i-1,j}\rangle_{in} &= \varphi_{Ha_j} |Ha_j\rangle + \varphi_{Va_j} |Va_j\rangle + \varphi_{Hb_{1,j-1}} |Hb_{1,j-1}\rangle + \varphi_{Vb_{1,j}} |Vb_{1,j}\rangle + \dots + \\ &\quad \varphi_{Hb_{i-1,j-1}} |Hb_{i-1,j-1}\rangle + \varphi_{Vb_{i-1,j-1}} |Vb_{i-1,j-1}\rangle, \\ |\varphi_{1\dots i-1,j}\rangle_{out} &= \varphi_{Hw_{i,j}} |Hw_{i,j}\rangle + \varphi_{Vw_{i,j}} |Vw_{i,j}\rangle + \varphi_{Hb_{1,j}} |Hb_{1,j}\rangle + \varphi_{Vb_{1,j}} |Vb_{1,j}\rangle + \dots + \\ &\quad \varphi_{Hb_{i-1,j}} |Hb_{i-1,j}\rangle + \varphi_{Vb_{i-1,j}} |Vb_{i-1,j}\rangle. \end{aligned}$$

For each subscheme, we write a transition matrix, that changes the basis of the input states to the basis of the output states and matches the corresponding scattering matrix. Let then  $U^{(i-1,j)}$  be matrix of size  $2(i-1) \times 2(i-1)$  corresponding to scattering operator of  $N(1 \dots i-1, j)$  so  $|\psi_{1\dots i-1,j}\rangle = U^{(i-1,j)} |\varphi_{1\dots i-1,j}\rangle$ . If we compare the  $|\varphi_{1\dots i,j}\rangle_{in}$  and  $|\varphi_{1\dots i-1,j}\rangle_{in}$  states, then the latter doesn't have a spatial mode  $b_{i,j-1}$  and has  $w_{i,j}$  instead of  $D_j$ . Using this remark and assuming that element in the node  $(i, j)$  is associated with scattering matrix  $T^{(i,j)}$  (see (1)) with matrix elements  $\|t_{k,l}\|_{k,l=1}^4$ , we get the following system:

$$\begin{pmatrix} \varphi_{Hw_{i,j}} \\ \varphi_{Vw_{i,j}} \\ \varphi_{Hb_{1,j}} \\ \varphi_{Vb_{1,j}} \\ \vdots \\ \varphi_{Hb_{i-1,j}} \\ \varphi_{Vb_{i-1,j}} \end{pmatrix} = U^{(i-1,j)} \begin{pmatrix} \varphi_{Ha_j} \\ \varphi_{Va_j} \\ \varphi_{Hb_{1,j-1}} \\ \varphi_{Vb_{1,j-1}} \\ \vdots \\ \varphi_{Hc_{i-1,j-1}} \\ \varphi_{Vc_{i-1,j-1}} \end{pmatrix}, \quad \begin{pmatrix} \varphi_{HD_j} \\ \varphi_{VD_j} \\ \varphi_{Hb_{i,j}} \\ \varphi_{Vb_{i,j}} \end{pmatrix} = T^{(i,j)} \begin{pmatrix} \varphi_{Hw_{i,j}} \\ \varphi_{Vw_{i,j}} \\ \varphi_{Hb_{i,j-1}} \\ \varphi_{Vb_{i,j-1}} \end{pmatrix},$$

from which the recurrent relation for the scattering matrix  $U^{(i,j)}$  of size  $2(i + 1) \times 2(i + 1)$ , that transforms  $|\varphi_{1\dots i,j}\rangle_{in}$  into  $|\varphi_{1\dots i,j}\rangle_{out}$  is:

$$U^{(i,j)} = \begin{pmatrix} t_{1,1} & t_{1,2} & 0 & \dots & 0 & t_{1,3} & t_{1,4} \\ t_{2,1} & t_{2,2} & 0 & \dots & 0 & t_{2,3} & t_{2,4} \\ 0 & 0 & 1 & & \mathbf{0} & 0 & 0 \\ \vdots & \vdots & & \ddots & & \vdots & \vdots \\ 0 & 0 & \mathbf{0} & & 1 & 0 & 0 \\ t_{3,1} & t_{3,2} & 0 & \dots & 0 & t_{3,3} & t_{3,4} \\ t_{4,1} & t_{4,2} & 0 & \dots & 0 & t_{4,3} & t_{4,4} \end{pmatrix} \left( \begin{array}{ccc|cc} & & & 0 & 0 \\ & & & \vdots & \vdots \\ & & & 0 & 0 \\ \hline 0 & \dots & 0 & 1 & 0 \\ 0 & \dots & 0 & 0 & 1 \end{array} \right), \quad (2)$$

where  $U^{(1,j)} = T^{(1,j)}$ . Obviously, each factor of expression (2) can be transformed to block-diagonal form, where each block is unitary. Then, we conclude that  $U^{(i,j)}$  is also unitary, as expected.

To finish the construction of the grid scattering matrix, we consider a rectangular sub-scheme having  $i$  rows and  $j$  columns with top-left angle matching the one of the large scheme. Let it be denoted as  $N(1 \dots i, 1 \dots j)$  (see Fig. 1). The corresponding input and output states are respectively of the form:

$$\begin{aligned} |\varphi_{1 \dots i, 1 \dots j}\rangle_{in} &= \varphi_{Ha_j} |Ha_j\rangle + \varphi_{Va_j} |Va_j\rangle + \dots + \varphi_{Ha_1} |Ha_1\rangle + \varphi_{Va_1} |Va_1\rangle + \varphi_{Hc_1} |Hc_1\rangle + \varphi_{Vc_1} |Vc_1\rangle + \\ &\quad \dots + \varphi_{Hc_i} |Hc_i\rangle + \varphi_{Vc_i} |Vc_i\rangle, \\ |\varphi_{1 \dots i, 1 \dots j}\rangle_{out} &= \varphi_{HD_j} |HD_j\rangle + \varphi_{VD_j} |VD_j\rangle + \dots + \varphi_{VD_1} |VD_1\rangle + \varphi_{Hb_{1,j}} |Hb_{1,j}\rangle + \\ &\quad \varphi_{Vb_{1,j}} |Vb_{1,j}\rangle + \dots + \varphi_{Hb_{i,j}} |Hb_{i,j}\rangle + \varphi_{Vb_{i,j}} |Vb_{i,j}\rangle. \end{aligned}$$

If  $Y^{(i,j-1)}$  is the matrix of the operator corresponding to  $N(1 \dots i, 1 \dots j-1)$ , then using the recurrence for calculating  $U^{(i,j)}$ , we get the following system:

$$\begin{pmatrix} \varphi_{HD_{j-1}} \\ \varphi_{VD_{j-1}} \\ \dots \\ \varphi_{HD_1} \\ \varphi_{VD_1} \\ \varphi_{Hb_{1,j-1}} \\ \varphi_{Vb_{1,j-1}} \\ \dots \\ \varphi_{Hb_{i,j-1}} \\ \varphi_{Vb_{i,j-1}} \end{pmatrix} = Y^{(i,j-1)} \begin{pmatrix} \varphi_{Ha_{j-1}} \\ \varphi_{Va_{j-1}} \\ \dots \\ \varphi_{Va_1} \\ \varphi_{Hc_1} \\ \varphi_{Vc_1} \\ \dots \\ \varphi_{Hc_i} \\ \varphi_{Vc_i} \end{pmatrix}, \quad \begin{pmatrix} \varphi_{HD_j} \\ \varphi_{VD_j} \\ \varphi_{Hb_{1,j}} \\ \varphi_{Vb_{1,j}} \\ \vdots \\ \varphi_{Hb_{i,j}} \\ \varphi_{Vb_{i,j}} \end{pmatrix} = U^{(i,j)} \begin{pmatrix} \varphi_{Ha_j} \\ \varphi_{Va_j} \\ \varphi_{Hb_{1,j-1}} \\ \varphi_{Vb_{1,j-1}} \\ \vdots \\ \varphi_{Hb_{i,j-1}} \\ \varphi_{Vb_{i,j-1}} \end{pmatrix}$$

from which, we eventually derive the following recurrent relation for matrix of operator  $Y^{(i,j)}$  of size  $2(i+j) \times 2(i+j)$ :

$$Y^{(i,j)} = \left( \begin{array}{c|cc|c} \mathbf{O} & 1 & \mathbf{0} & \mathbf{O} \\ & \ddots & & \\ \hline & \mathbf{0} & 1 & \\ \hline U_1^{(i,j)} & \mathbf{O} & U_2^{(i,j)} & \end{array} \right) \left( \begin{array}{c|c} 1 & 0 \\ 0 & 1 \\ \hline \mathbf{O} & Y^{(i,j-1)} \end{array} \right), \quad (4)$$

where  $U_1^{(i,j)} = U^{(i,j)}[1 \dots 2(i+1); 1, 2]$  and  $U_2^{(i,j)} = U^{(i,j)}[1 \dots 2(i+1); 3 \dots 2(i+1)]$  (here we denote submatrix of matrix  $M$  with rows  $r_1, \dots, r_n$  and columns  $c_1, \dots, c_m$  by  $[r_1, \dots, r_n; c_1, \dots, c_m]$ ). Following the same reasoning as for  $U^{(i,j)}$ , it is also obvious that  $Y^{(i,j)}$  is unitary. Hereby, for scattering matrix of the large scheme (see Fig. 1), it is enough to compute  $Y(m, n)$ .

### 3. Multiparticle systems

Consider the scheme on Fig. 1 and an arbitrary state of  $n$  photons incident to ports  $c_1, \dots, c_n$ :

$$|\varphi_0\rangle = \sum_{\rho \in \Pi_n} \varphi(\rho) |\rho_{c_1}^1 \dots \rho_{c_n}^n\rangle, \quad \sum_{\rho \in \Pi_n} |\varphi(\rho)|^2 = 1, \\ \Pi_k = \{H, V\}^{\times k}. \quad (5)$$

which is a state of  $n$  qubits encoded into photon polarization modes  $H$  and  $V$ . Suppose we define a state of  $m$  ancilla photons incident to ports  $a_1, \dots, a_m$  as:

$$|\varphi_A\rangle = \bigotimes_1^m \varphi_{H_{a_j}} |H_{a_j}\rangle + \varphi_{V_{a_j}} |V_{a_j}\rangle,$$

and input state as  $|\varphi_{in}\rangle = \text{Sym}(\varphi_0 \otimes \varphi_A)$ . Then, we can write the output in the following form (see (5)) :

$$|\psi_{out}\rangle = \sum_{\substack{\tau \in T_{m'} \\ P \in \Pi_{m'}}} \left( \mu(\tau) |P^1 \dots P^{m'}\rangle_{\tau} \sum_{\rho \in \Pi_{n'}} \psi(\rho, P, \tau) |\rho^1 \dots \rho^{n'}\rangle \right) + c_{\perp} |\psi_{\perp}\rangle, \\ T_k = \{ \{D_{s_i}\}_1^k \mid s_i \in 1, \dots, k; s_{i+1} \geq s_i \} \quad (6)$$

where  $|\psi_{\perp}\rangle$  is a state orthogonal to those having only one photon in each of modes  $g_1, \dots, g_{n'}$ . The product of state vectors is defined as their symmetrization:

$$|P^1 \dots P^{m'}\rangle_{\tau} |\rho^1 \dots \rho^{n'}\rangle = \frac{\sum_{\sigma \in \Sigma_{\rho, P, \tau}} |\sigma_1\rangle \dots |\sigma_{n'+m'}\rangle}{\sqrt{|\sigma|!}}, \\ \Sigma_{\rho, P, \tau} = \{ \pi(P_{D_{\tau_1}}^1, \dots, P_{D_{\tau_{m'}}}^{m'}, \rho_{g_1}^1, \dots, \rho_{g_{n'}}^{n'}) \}.$$

Evolutions generated by linear optical elements preserve the photon total number so  $n' = n + m - m'$ . Suppose that we detect photons in modes  $D_1, \dots, D_{m'}$ . As seen from (6), with the appropriate choice of ancilla photon states and postselection based on polarization and quantity of photons on each detector, we can project the output in modes  $g_1, \dots, g_{n'}$  into the state having  $\sum_{\rho \in \Pi_{n'}} |\psi(\rho)|^2 = 1$ , thus meaning that we received a state of  $n'$  qubits. The scheme is considered non-destructive in case  $n = n'$  and destructive if  $n' < n$  as we collapsed the state of one or more qubits.

Let scheme with evolutionary operator  $U$  transform state of  $q = n + m$  input photons. In order to obtain the transformation for bosonic states, we compute the restriction of the multiparticle evolutionary operator  $U^{\otimes q}$  on its invariant subspace  $Sp_i$ . Then, the input state space is given by:

$$Sp_0 = \text{span} (\{ |X1_{m_1}\rangle \otimes |X2_{m_2}\rangle \otimes \dots \otimes |Xq_{m_q}\rangle \mid Xi \in \{H, V\}, \\ s_j \in \{c_1, \dots, c_n, a_1, \dots, a_m\}, i, j = 1 \dots q \}), \quad (7.1)$$

where  $c_j$  are spatial modes corresponding to input ports of the scheme. The restriction operator can be computed as follows, assuming that matrix of  $U^{\otimes q}$  is of size  $2^q \times 2^q$  and  $\dim(Sp_i) = k$ :

$$U_i^{\otimes q} = R_i^{\dagger} U^{\otimes n} R_i, \quad (7.2)$$

where  $R_i$  is a  $2^q \times k$  matrix which columns represent basis vectors of  $Sp_i$ . It can also easily be shown that for invariant subspaces, the restriction operator is unitary.

#### 4. Constructing Toffoli gate using linear optics

Inspired by non-destructive CNOT gate presented in work [7] and with use of algorithms given in section 5, it became possible to construct a scheme implementing quantum Toffoli transformation. Although it is known that at least five two-qubit gates are necessary for a non-destructive Toffoli gate [9]. It turns out that for the destructive Toffoli gate on three bosonic qubits only eight polarization modes are needed (see Fig. 3). We use an ancilla photon in equal superposition state and an arbitrary three-qubit state on left input ports of the following scheme:

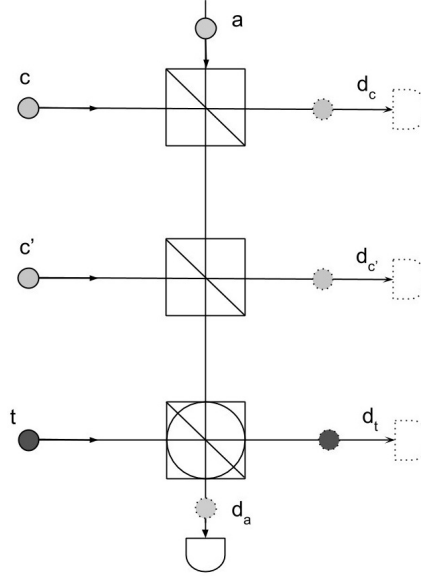


FIG. 3. Destructive Toffoli gate

$$|\psi_a\rangle = \frac{1}{\sqrt{2}} |H_a\rangle + \frac{1}{\sqrt{2}} |V_a\rangle,$$

$$|\psi_0\rangle = \alpha_1 |H_c H_{c'} H_t\rangle + \alpha_2 |H_c H_{c'} V_t\rangle + \dots + \alpha_8 |V_c V_{c'} V_t\rangle.$$

The initial state  $|\psi_{in}\rangle = \text{Sym}(\psi_0 \otimes \psi_A)$  is transformed into the output state, which can be written in the form of equation 6 (see section 3):

$$\begin{aligned} |\psi_{out}\rangle = & \frac{1}{2\sqrt{2}} |H_{d_a}\rangle (\alpha_1 |H_{d_c} H_{d_{c'}} H_{d_t}\rangle + \alpha_2 |H_{d_c} H_{d_{c'}} V_{d_t}\rangle) + \\ & \frac{1}{2\sqrt{2}} |V_{d_a}\rangle (\alpha_3 |H_{d_c} V_{d_c} H_{d_t}\rangle + \alpha_4 |H_{d_c} V_{d_c} V_{d_t}\rangle) + \\ & \frac{1}{2\sqrt{2}} |H_{d_a}\rangle (\alpha_5 |H_{d_{c'}} V_{d_{c'}} H_{d_t}\rangle + \alpha_6 |H_{d_{c'}} V_{d_{c'}} V_{d_t}\rangle) + \\ & \frac{1}{2\sqrt{2}} |H_{d_a}\rangle (\alpha_7 |V_{d_c} V_{d_{c'}} V_{d_t}\rangle + \alpha_8 |V_{d_c} V_{d_{c'}} H_{d_t}\rangle) + \frac{\sqrt{2}}{2} |\psi_{\perp}\rangle. \end{aligned}$$

In the output state, the probability amplitudes of vectors from the following sets are equal to 0 :

$$S_1 = \{|H_{d_c} V_{d_{c'}} H_{d_t}\rangle, |H_{d_c} V_{d_{c'}} V_{d_t}\rangle, |V_{d_c} H_{d_{c'}} V_{d_t}\rangle, |V_{d_c} H_{d_{c'}} H_{d_t}\rangle\},$$

$$S_2 = \{|V_{d_c} H_{d_c} H_{d_t}\rangle, |V_{d_c} H_{d_c} V_{d_t}\rangle, |V_{d_c} V_{d_c} H_{d_t}\rangle, |V_{d_c} V_{d_c} V_{d_t}\rangle, |H_{d_{c'}} H_{d_c} H_{d_t}\rangle, |H_{d_{c'}} H_{d_c} V_{d_t}\rangle\},$$

$$S_3 = \{|V_{d_{c'}} H_{d_{c'}} H_{d_t}\rangle, |V_{d_{c'}} H_{d_{c'}} V_{d_t}\rangle, |V_{d_{c'}} V_{d_{c'}} H_{d_t}\rangle, |V_{d_{c'}} V_{d_{c'}} V_{d_t}\rangle, |H_{d_c} H_{d_{c'}} H_{d_t}\rangle, |H_{d_c} H_{d_{c'}} V_{d_t}\rangle\},$$

therefore, when the following events occur:

- $A_1 = \{\text{Each spatial mode has only one photon, photodetector registers single } H\text{-polarized photon}\}$ ,  $P(A_1) = \frac{1}{4}$ ,
- $A_2 = \{2 \text{ photons in mode } d_c, \text{ photodetector registers single } V\text{-polarized photon}\}$ ,  $P(A_2) = \frac{1}{8}$ ,
- $A_3 = \{2 \text{ photons in mode } d_c', \text{ photodetector registers single } H\text{-polarized photon}\}$ ,  $P(A_3) = \frac{1}{8}$ ,

we get a quantum Toffoli transformation preserving the state of the controlled qubit, which succeeds with probability  $P(A_1) + P(A_2) + P(A_3) = \frac{1}{2}$ . The main difficulty concerning implementation of this scheme lies in necessity to count photons using photodetectors, although such devices seem to be available now.

## 5. Algorithm realization

We present an algorithm for efficient calculation of the evolutionary operator corresponding to a system of  $p$  particles and rectangle linear optical multiport considered in section 2 (see Supplementary Materials). This is an optimization of the straightforward algorithm achieved by means of sparse matrices and lazy tensor product calculation. It should be noted that when running procedure 2 (see Supplementary Materials) in parallel, due to the fact that first three nested loops are independent, it becomes possible to obtain a linear performance increase that is proportional to the number of processors in use, whereas number of threads can grow up to  $Size(Sp)^2(p!)$ .

## 6. Conclusion

In this paper, a rectangular linear optical grid was considered. Similar to the triangular multiport presented in work [6], in order to implement unitary transformation of  $N$  optical modes a number of beam splitters proportional to  $N^2$  is required. However, the optical networks considered in the current paper are comparably easy to construct and permit the usage of a sufficient number of ancilla photons and detectors to realize quantum teleportation. The formal procedure of evolutionary operator calculation, corresponding to a given rectangular optical network, introduces a step towards the efficient experimental realization of an arbitrary unitary operator. At present, there are also several other problems of interest: construction of quantum logic gates based on linear optics, the problem of simulation of quantum optical gates with noise and implementation flaws being taken into account. Substantial problems that prevent these schemes from being used in practice are qubit phase drifts and photon loss, which is why effective correcting codes for qubit states are necessary. Unsolved technical problems are the construction of an extremely sensitive and low-latency photodetector and reliable single-photon sources.

## 7. APPENDIX

Here we present procedures for calculation of evolutionary operator corresponding to system of  $p$  particles and rectangle linear optical multiport (see alg. 1, 2, 3).

- `@Transition_Matrix_Spased` (see alg. 1) calculates matrix  $R_i$  and stores it in a sparse matrix.
- `@Kron_And_Mult_Spased` (see alg. 2) calculates  $U_i^{\otimes n}$  (see article, eq. 7.2).
- `@Lazy_kron` (see alg. 3) is an auxiliary function for `@Kron_And_Mult_Spased` that calculates tensor product matrix elements.

Complexities of simple and optimized procedures for calculation of evolutionary operator are summarized in table 1. In table 2 dimentions of most important subspaces of  $Sp_0$  (see article, eq. (7.1)) are given. In table 3 we present mean time and space resource demands for calculation of evolutionary operator on symmetric subspace.

TABLE 1. Complexity of procedures depending on subspace size  $Size(Sp)$  and number of particles  $p$

Procedure	Time	Space
Transition_Matrix_Spased	$O(Size(Sp)(p+1)!)$	$O(3(2p)^p)$
Transition_Matrix_Simple	$O\left(Size(Sp)\left(1+(p+1)!\frac{(1-(2p)^p)}{1-2p}+p!(2p)^p\right)\right)$	$O(Size(Sp)(2p)^p)$
Kron_And_Mult_Spased	$O(Size(Sp)^2(p!)^2p)$	$O(Size(Sp)^2)$
Kron_And_Mult_Simple	$O\left(\frac{1-(2p)^{2p}}{1-(2p)^2}+Size(Sp)^4(2p)^{2p}\right)$	$O((2p)^{2p}+Size(Sp)(2p)^p)$

TABLE 2. Subspaces of  $Sp_0$ .

Subspace (Sp)	Size (Size(Sp))
Full	$(2p)^p$
Asym	$\binom{2p}{p}$
Sym	$\binom{3p-1}{p}$
Coinc	$2^p$

TABLE 3. Mean time and space for evolutionary operator calculation on symmetric subspace using an approx. 50 GFLOPS processor

p	Time (s)		Space (MB)	
	simple	spased	simple	spased
3	0.46	0.034	0.224	0.014
4	$2 \cdot 10^4$	25.09	69.16	0.4623
5	$1.6 \cdot 10^{10}$	$2.9 \cdot 10^4$	$38.9 \cdot 10^3$	16.43
6	$2.09 \cdot 10^{16}$	$4.8 \cdot 10^7$	$34.15 \cdot 10^6$	618.45

**Algorithm 1** Transition\_Matrix\_Sparsed

---

**Require:**  $p \geq 3$ ,  $Sp$  {args:  $p$  for number of particles, matrix  $Sp$  which rows represent basis vectors of a given subspace. In MATLAB environment function that generates  $Sp$  for symmetric subspace may look like <sup>a</sup>

```

Sp = combinator(2 * p, p, 'c', 'r').
}
idx, jdx, vals ← array((2p)p)
cnt ← 0
for i = 1 to len(Sp) do
  Perms ← uniqueperms(Sp(i))
  for j = 1 to len(Perms) do
    pos ← 1
    for k = 1 to p do
      pos ← l * (pos - 1) + Perms(j, k)
    end for
    cnt ← cnt + 1
    idx(cnt) ← i
    jdx(cnt) ← pos
    vals(cnt) ← 1/sqrt(len(Perms))
  end for
end for
T = make_sparse_matrix(idx, jdx, vals)

```

---

<sup>a</sup><http://www.mathworks.com/matlabcentral/fileexchange/24325-combinator-combinations-and-permutations>

**Algorithm 2** Kron\_And\_Mult\_Sparsed

---

**Require:**  $p \geq 3$ ,  $U$ ,  $Sp$  {args:  $p$  for number of particles,  $U$  for single particle evolutionary operator (see article, eq. 4), and matrix  $Sp$  for basis vectors of given subspace (see 1)}

```

T ← Transition_Matrix_Sparsed(Sp, p)
m ← len(Sp)
Ur ← matrix(m, m)
for i = 1 to m do
  tmp_norm_i ← T(i, 1)
  for j = 1 to m do
    tmp_norm_j ← T(j, 1)
    for r = 1 to len(T(i)) do
      crj ← 0
      for r = 1 to len(T(j)) do
        up_elem ← Lazy_kron(T(i, r),
          T(j, l), p, U)
        crj ← crj + up_elem * tmp_norm
      end for
      Ur(i, j) = Ur(i, j) + tmp_norm_j *
        crj
    end for
  end for
end for
return Ur

```

---

**Algorithm 3** Lazy\_kron

---

**Require:**  $1 \leq i, j \leq (2p)^p, p \geq 3$ ,  $U$  {args:  $i, j$  for row and column of element to be calculates,  $p$  for tensor product order and  $U$  for single-particle evolutionary operator (see article, eq. 4)}

```

res ← 1
while p > 0 do
  ic, jc ← i % rows(U), j % cols(U)
  if ic is 0 then
    ic ← rows(U)
  end if
  if jc is 0 then
    jc ← cols(U)
  end if
  res ← res * U(ic, jc)
  i ← ceil(i/rows(U))
  j ← ceil(j/cols(U))
  p ← p - 1;
end while
return res

```

---

## Acknowledgements

This work was partially financially supported by the Government of the Russian Federation (grant 074-U01), by the Ministry of Science and Education of the Russian Federation (GOSZADANIE 2014/190, Project 14.Z50.31.0031), by grant MK-5001.2015.1 of the President of the Russian Federation.

## References

- [1] Kok P., Munro W., et al. Linear optical quantum computing. *Rev. Mod. Phys.*, 2008, **79** (135), P. 1-3.
- [2] Knill E., Laflamme R., Milburn R.J. A scheme for efficient quantum computation with linear optics. *Nature*, 2001, **409**, P. 46-52.
- [3] Pittman T.B., Fitch M.J., Franson J.D. Demonstration of nondeterministic quantum logic operations using linear optical elements. *Phys. Rev. Lett.*, 2002, **88**, P. 257902/4.
- [4] Pittman T.B., Fitch M.J., Franson J.D. Probabilistic quantum logic operations using polarizing beam splitters. *Phys. Rev. A*, 2001, **64**, P. 062311/9.
- [5] Trifanov A.I., Miroshnichenko G.P. Reduced conditional dynamic of quantum system under indirect quantum measurement. *Nanosystems: physics, chemistry, mathematics*, 2013, **4** (5), P. 635-647.
- [6] Reck M., Zeilinger A., Berstein H.J., Bertrani P. Experimental realization of discrete unitary operator. *Phys. Rev. Lett.*, 1994, **73** (1), P. 58-61.
- [7] Pittman T.B., Fitch M.J., Jacobs B., Franson J.D. Experimental controlled-not logic gate for single photons in the coincidence basis. *Phys. Rev. A*, 2003, **68**, P. 032316/4.
- [8] Weihs G., Zeilinger A. *Photon statistics at beam-splitters: an essential tool in quantum information and teleportation*. Perina J. (Ed.), Wiley, 2001, p. 10.
- [9] Yu N., Duan R., Ying M. Five two-qubit gates are necessary for implementing Toffoli gate. *Phys. Rev. A*, 2007, **88**, P. 010304(R)/5.

# Estimation of the contact area of solids by electrothermal analogy

E. D. Eidelman<sup>1,2</sup>

<sup>1</sup>Ioffe Physico-Technical Institute of the Russian Academy of Sciences,  
Polytechnicheskaya 26, Saint Petersburg, 194021, Russia

<sup>2</sup>Saint Petersburg Chemical-Pharmaceutical Academy, Popova street 14,  
Saint Petersburg, 197376, Russia

eidelman@mail.ioffe.ru

DOI 10.17586/2220-8054-2015-6-4-547-550

A method of thermal measurements has been proposed for determining the real surface contact area. Measurement of the true contact area is somewhat difficult. We propose here a method of contact area measurement, which is, in essence, an idealization of the well-known probe method employed in surface studies. In this study, to determine (estimate!) the fraction of the contact surface area projected onto the plane of a geometrical area of the section of the surface, it is proposed to use the electrothermal analogy. Considered in terms of this analogy, electrical conductance is assumed to correlate with heat transfer. As a result, the real contact area is found to be millions of times smaller than the area of the plane surface.

**Keywords:** tribology, contact area, Landauer's relation, electrothermal analogy.

*Received: 29 April 2015 Revised: 5 May 2015*

## 1. Introduction

Calculation of the true contact area between solid bodies, if it is to be made with due allowance for the processes involved, is an intricate problem of tribology, as well as that of engineering and materials sciences [1]. The space between the areas in contact is usually filled by an intermediate phase and products of destruction. This space is naturally pervaded by electric fields generated by atoms and molecules of the surface. Any attempt at modeling the real contact area should lean upon surface shape measurements made before contact [2], but the assumptions made in simulation about the shape of the overlaying contact surfaces largely depreciate these measurements [1].

The measurement of the true contact area is met with some difficulty. Indeed, measurements conducted by traditional methods involving contact with a painted surface will obviously yield an overestimate because of squeezing and adhesion, which, in the absence of a color layer, may be completely absent. The method based on measuring the electrical resistance of contacts does not actually permit operation without the application of pressure and the unavoidable fracture in the contact areas. The techniques involved in nondestructive testing depend markedly on the thickness of the layer within which radiation interacts with matter.

It is difficult to correctly estimate the effects of the potentials generated by surface atoms in these methods (for more details cf. [3, 4] and references therein).

We are proposing here a method of contact area measurement, which is, in essence, an idealization of the well-known probe method employed in surface studies. In this approach, the point probe is actually an atomically sized part of the surface of the body brought in contact with an atomically sized region of the body under study.

## 2. Formulation of the problem

First, we let heat (phonons) and electric current (electrons) be transported only within small areas  $S_i$  ( $i = 1, 2, 3 \dots$ ), within which the distance between atoms of the bodies brought in contact is on the order of the lattice constant of these bodies, or on the order of interatomic distances in amorphous bodies. In this study, to determine (estimate!) the fraction of the contact surface area  $\sum_i S_{i\perp} = S_r$  projected onto the plane of a geometrical area  $S$  of this section of the surface, we propose to use the electrothermal analogy.

Considered in terms of this analogy, electrical conductance  $G$  is assumed to correlate with heat transfer, which in common notation (see, e.g., [5]), is written as  $\alpha S_r$ , where  $\alpha$  is the heat transfer coefficient. The inverse quantity,  $1/\alpha$ , is usually termed thermal resistance or the Kapitza resistance. The use of the heat transfer coefficient at the boundaries of solids is fully justified. Indeed, contact between solids, except for very small areas, is actually that between the liquid mixtures covering these surfaces [5].

Let a certain amount of heat cross the boundary per unit time and unit area. Then, the heat conductance flux in the first body, which has the temperature  $T_1$  far from the point of contact and  $T'_1$  at the boundary, the heat transfer flux between the boundaries with temperatures  $T'_1$  and  $T''_1$ , and, finally, the heat conductance flux in the second body with the temperatures  $T''_2$  at the boundary and  $T''$  far from it, are equal. These fluxes can be cast as

$$\frac{\lambda_1}{\delta_1}(T_1 - T'_1) = \alpha(T'_1 - T''_1) = \frac{\lambda_2}{\delta_2}(T''_2 - T''),$$

where  $\lambda_j$  and  $\delta_j$  are, accordingly, the thermal conductivities and the characteristic dimensions of temperature variation for each of the bodies, with  $j = 1, 2$ . Obviously enough, at the boundary, there is a temperature jump  $\delta T = T'_1 - T''_1$ .

The main assumption maintained in this work is that a solid can be considered as an array of quasi-one-dimensional linear filaments. We will limit ourselves to a purely mechanical model of connection [6-7], neglecting all rheological effects, adhesion, structure change as a result of contact, and all electric and quantum potentials of interactions. This should not qualitatively change the estimates, to which we are going to adhere in what follows.

The conductivity of a quantum point contact between two one-dimensional conductors, one of which is located in body 1, and the other, in body 2, can be calculated in the quantum one-dimensional filament approximation using Landauer's relation [8, 9]:

$$G = G_0 \sum t_i(n_{i1} - n_{i2}), \quad (1)$$

where  $t_i$  is the normalized squared amplitude of transit of an electron with charge  $e$  in contact numbered  $i$ ,  $n_{ij}$  is the number of such electrons specified in accordance with the Fermi-Dirac distribution for each of the conductors with the number  $j = 1, 2$ ,  $G_0 = e^2/(\pi\hbar)$  is the conductance quantum, and, as usual,  $\hbar$  is Planck's constant.

By electrothermal analogy, for the heat transfer quantum we have  $\hbar\omega d\omega/(\pi\hbar\delta T)$ , where  $\omega$  is the phonon frequency, and  $\delta T$  is the temperature jump at the boundary. The frequency  $\omega$  must naturally be smaller than the lowest of the Debye frequencies  $\omega^*$  characteristic of bodies in contact.

Thus, Eq. (1) for heat transfer can be recast as:

$$\alpha S_r = \frac{1}{\pi} \int_0^{\omega^*} \hbar\omega d\omega \frac{n_1 - n_2}{\delta T} t, \quad (2)$$

where  $t$  is the normalized squared amplitude of transfer, i.e., the transfer coefficient of a phonon of frequency  $\hbar\omega$ , and

$$n_j = \frac{1}{\exp\left(\frac{\hbar\omega}{kT_j}\right) - 1}$$

is the number of such phonons specified in accordance with the Bose-Einstein distribution for each of the contacting bodies numbered  $j = 1, 2$ , and  $k$  is the Boltzmann constant.

### 3. Estimation of the projection of contact area

Obviously, at high enough temperatures  $(n_1 - n_2)/\delta T \cong k/(\hbar\omega)$ .

The square of the amplitude  $t$  of phonon transfer (vibration) over two semi-infinite one-dimensional chains coupled elastically at the boundary was calculated for frequencies lower than the lowest of the Debye frequencies for the corresponding contacting bodies [5]. It was shown [5] that  $t$  may be considered frequency independent and equal to:

$$t = \frac{4\rho_1 c_1 \rho_2 c_2}{(\rho_1 c_1 + \rho_2 c_2)^2},$$

where  $\rho_j$  and  $c_j$  are, accordingly, the densities and sound velocities in the bodies in contact.

In this approximation, the integral in Eq. (2) can readily be taken to yield:

$$\alpha S_r = \frac{k^2 \Theta_*}{\pi \hbar} \frac{4a}{(1+a)^2},$$

where  $\Theta_*$  is the lowest of the Debye temperatures for the materials in contact, and the parameter

$$a = \frac{\rho_1 c_1}{\rho_2 c_2},$$

is the relative characteristic of the contacting materials. It is usually a quantity on the order of unity.

In an experiment, one usually studies the amount of heat  $P$  crossing a “geometric” surface per unit time. It is known that  $P = \alpha S \delta T$ . Thus, we come to the relation suitable for the subsequent estimation:

$$\frac{S_r}{S} = \frac{k^2 \Theta_*}{\pi \hbar} \frac{4a}{(1+a)^2} \frac{\delta T}{P} \quad (3)$$

The temperature jump at the boundary is usually [1] on the order of  $\delta T \cong 10K$ , already at milliwatt-scale power, so that the real contact area turns out to be millions of times smaller than the area of the plane surface. Taking into due account the various rheological phenomena, adhesion and interaction potentials may significantly alter this estimate.

The relation operating with a temperature difference between the contacting bodies offset from the points of contact,  $\Delta T = T' - T''$ , would probably be more suitable for practical measurements than Eq. (3). We thus come to the following equation:

$$\frac{S_r}{S} = \frac{k^2 \Theta_*}{\pi \hbar} \frac{4a}{(1+a)^2} \left[ \frac{\Delta T}{P} - \frac{1}{S} \left( \frac{\delta_1}{\lambda_1} + \frac{\delta_2}{\lambda_2} \right) \right].$$

### 4. Conclusion

A method of thermal measurement has been proposed for determining the real surface contact area. This method can be employed both directly for a preliminary evaluation of the contact area and in the method of mechanical or atomic force sensing to refine the contact area of the probe with a sample surface.

## Acknowledgments

The author expresses gratitude to A. P. Meilakhs for a discussion of Landauer's relation, as well as to S. A. Chizhik and M. L. Heifets for having made acquaintance with the state of the art of the problem. I am grateful to A. Ya. Vul' for interest in the work.

Support of the RAS Presidium programs "Fundamentals of nanostructure technologies and nanomaterial" and "Quantum mesoscopic and disordered systems", as well as of RFBR (Grants 14-08-90011 Bel-a) is gratefully acknowledged.

## References

- [1] Kaufman D. M. *Coupled Principles for Computational Frictional Contact Mechanics*. New Brunswick, New Jersey, 2009, 160p.
- [2] Chizhik S.A., Wierzcholski K., Trushko A.V., Zhytkova M.A., Miszczak A. Properties of Cartilage on Micro- and Nanolevel. *Advances in Tribology*, 2010, **2010**, Article ID 243150, 8 pages.
- [3] Koval'chyk Yu. I., Shyrokov V. V., Modeling of Temperature Flashes under the Conditions of Periodic Contact of Friction Surfaces. *Materials Science* 3-2005, **41**(2), P. 192–201.
- [4] Koval'chyk Yu. I., Simulation of Wave Processes under Conditions of Friction of Rough Surfaces (Review). *Materials Science*, 2003, **39**(4), P. 584–595.
- [5] Faghri A., Zhang Y., Howell J., *Advanced Heat and Mass Transfer*. Columbia, MO: Global Digital Press., 2010, 550 p.
- [6] Zhang U.L, Keblinski P., Wang J-S., Li B. L. Interfacial thermal transport in atomic junctions. *Phys.Rev.B.*, 2011, **83**, P. 064303-1-8.
- [7] Meilakhs A. P., Eidelman E. D. New model of heat transport across the metal-insulator interface by the example of boundaries in a diamond-copper composite. *JETP Letters*, 2013, **97**(1), P. 38–40.
- [8] Landauer R. Spatial variation of currents and fields due to localized scatterers in metallic conduction. *IBM Journal of Research and Development*, 1957, **1**, P. 223–231.
- [9] Buttiker M., Imry Y., Landauer R., Pinhas S. Generalized-channel conductance formula with application to small rings. *Phys. Rev. B.*, 1995, **31**, P. 6207–6219.

# The kinetics of formation and morphological memory of polymeric nanostructures

I. V. Melikhov<sup>1</sup>, O. V. Alekseeva<sup>2</sup>, V. N. Rudin<sup>1</sup>, E. D. Kozlovskaya<sup>1</sup>, A. V. Noskov<sup>2</sup>

<sup>1</sup>M. V. Lomonosov Moscow State University, Moscow, Russia

<sup>2</sup>G. A. Krestov Institute of Solution Chemistry of RAS, Ivanovo, Russia  
melikhov@radio.chem.msu.ru, ova@isc-ras.ru

PACS 81.05.Lg

DOI 10.17586/2220-8054-2015-6-4-551-561

The mesokinetic model of the polymeric body formation was formulated, describing the nucleation, growth and aggregation of macromolecules followed by the aggregates' assembly into the nanostructured body. According to this model, the near-surface nanostructure of the polymeric body retains the information on how it was formed, and this information can be extracted from the morphological characteristics of the microrelief of the body while maintaining its integrity, that is, body has the morphological memory. The mesokinetic model was used to study film formation by the evaporation of an *o*-xylene or toluene solution of polystyrene, which provided an opportunity to identify the kinetics of nanostructure formation found in the surface area of the film after completion of the process. It turned out that at the beginning of evaporation, a number of the primary macromolecules in the form of spheroidal nanoparticles were formed, and then, the primary aggregates coalesced into the secondary aggregates forming the ordered chains of nanoparticles.

**Keywords:** polystyrene, microrelief, primary (nanoparticles) and secondary (microparticle) units.

*Received:* 9 April 2015

## 1. Introduction

According to the electron micrographs of polymers (films, granules, membranes, etc.) published in the literature, many of these substances have nanostructured microrelief. We observed such microrelief on the surface of polystyrene granules purchased from “Aldrich” (Germany), as indicated by Fig. 1, which shows that the near-surface areas of the studied granules have a multilevel hierarchical nanostructure. They consist of aggregates of polystyrene molecules in the form of spheroidal nanoparticles, aggregated into the chains, combined into microparticles, which form a granule. Fig. 1 leads to the question, whether the microrelief of the polymeric body retains information about how it was formed. Is it possible, focusing on electron microscopic images of the microrelief, to determine the speed of the elementary processes that lead to this microrelief? As it is known, the exact answer to this question may be provided by studying the kinetics of elementary processes for monomer integration into oligomer and polymer molecules, the formation of aggregates from polymer molecules (associates, floccules, colloidal particles) and aggregates association in a polymeric body (solidification, crystallization) [1-8]. Methods of studying of these elementary processes have been developed and are widely used [3-11]. In this case, the design of experiments and interpretation of the results is based on kinetic models that enable the successful description of many experimental results [11-15], but do not allow their quantitative prediction, as each model inevitably contains arbitrary assumptions that reduce its predictive ability. With this in mind, this article attempts to formulate a mesokinetic model in which the only arbitrary assumption is the crucial role of binary collisions of particles in the system, and other assumptions are included in the unknown frequency functions and are available for

experimental determination. The proposed model was used to study the microrelief of the films formed by evaporation of a polystyrene solution (Fig. 2), which led to the concept of morphological film memory. The study of the microrelief of granules from Aldrich (Fig. 1) as well as the study of the electron-microscopic images of many polymeric bodies described in the literature has led to the same conclusion. This enabled us to assert that many polymeric bodies possess morphological memory which is different from the shape memory and other types of polymer memory [16-18] with the memory carrier being localized at the body surface, rather than within its volume.

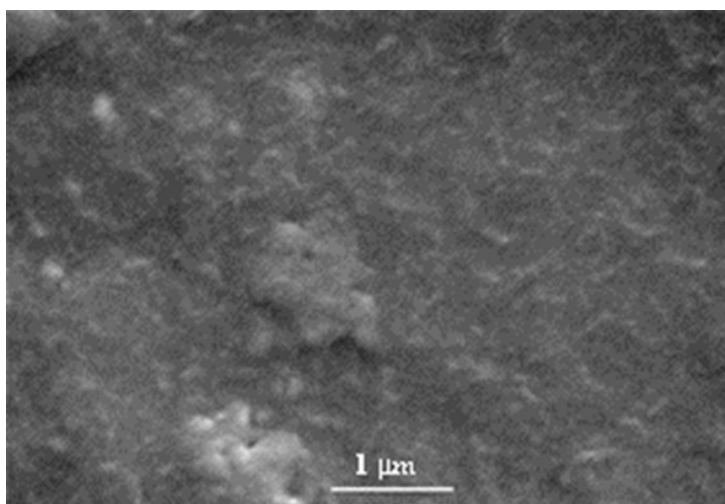


FIG. 1. Electron micrograph of the surface area of a typical polystyrene granules from “Aldrich” (Germany). Microscope CamScan, a sample was prepared by the standard method

## 2. Model of nanostructure formation

The processes in a homogeneous solution of a monomer A which evaporates at a predetermined speed are studied. At the time  $t = 0$  the polymerization initiator B is added into the solution, which leads to the formation of polymeric molecules which combine together to form ordered aggregates. Upon evaporation of the solution, its volume decreases, leading to an increase in the concentration of molecules and aggregates, which do not evaporate. During the evaporation, an increasing number of the molecules and aggregates is brought into contact with each other, and at the moment  $t_F$  of the complete removal of the solvent they form a polymer body with the following hierarchical structure, its nanolevel consisting of polymer molecules, microlevel – by the aggregates, and macrolevel – by the body itself.

At  $0 < t < t_F$  the solution contains monomer molecules ( $j = 0$ ), polymer molecules ( $j = 1$ ) and aggregates ( $j = 2, 3\dots$ ).

The state of each particle is characterized by parameters  $\vec{X} = \{n_1 \dots n_i \dots n_m, v, X_1 \dots X_i \dots X_p\}$ , where  $n_i$  is the number of A molecules, which have formed one of the  $m$  of polymer molecules of the particle, with a total number of the A molecules equal to  $n = \sum_{i=1}^m n_i$ ;  $v$  is a particle volume;  $X_i$  is a parameter of shape, composition or structure of the particle. The condition for the conservation of the number of atoms introduced into the

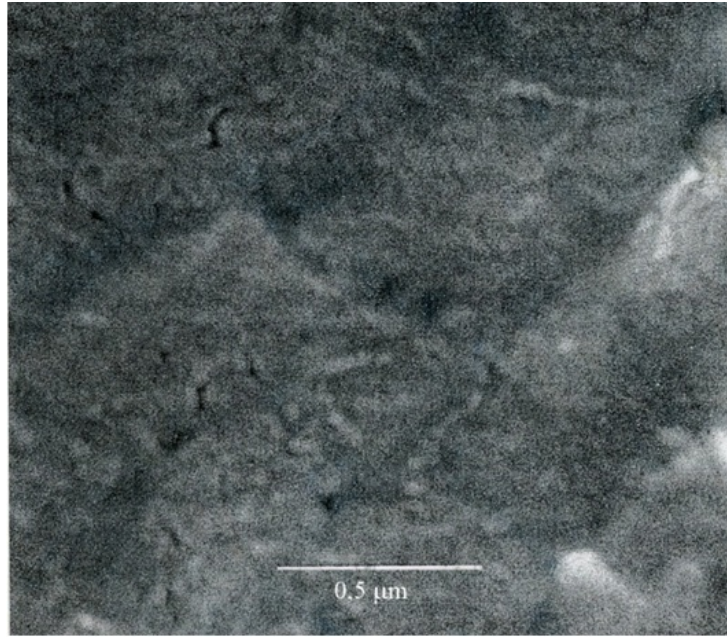


FIG. 2. Microrelief of the film obtained by removing the solvent from the *o*-xylene solution of polystyrene. The conditions of film formation:  $V_0 = 36,5 \text{ cm}^3$ ,  $T = 293\text{K}$ , initial concentration of polystyrene in the solution  $M_0 = 0.15 \text{ g/cm}^3$ ,  $S = 1200 \text{ cm}^2$ . Microscope CamScan

system in the molecules A is fulfilled:

$$C_{A0}V_0 = \int_V \left[ C_A(1 - \varepsilon) + \sum_j \sum_n nN_{jn}(t) \right] dV, \quad (1)$$

where  $C_{A0}$  and  $C_A$  are the initial and the current concentration of the A molecules in the solution;  $V_0$  and  $V$  are the initial and the current volume of the system;  $\varepsilon$  is the share of the system volume occupied by the polymer molecules and aggregates;  $N_{jn}(t)$  is the concentration of macromolecules and aggregates, including  $n$  molecules of A by the time  $t$ .

The volume  $V$  is equal to:

$$V = V_0 \int_0^t v_L S \omega_S dt, \quad (2)$$

where  $v_L$  is the volume change after the evaporation of one of the solvent molecules;  $S$  is the area of the evaporation surface;  $\omega_S$  is the flow of solvent molecules in the vapor at the moment  $t$ .

At  $0 < t < t_F$  the concentration  $N_{jn}(t)$  in each system area changes due to the associations of the particles, because of the binary collisions and fragmentation of molecules and aggregates under the influence of thermal motion and mechanical effects. Therefore:

$$\Delta N_{jn}(t) = \left( \Omega_{j+} - \Omega_{j-} - \text{div} \vec{J}_{jn} \right) \Delta t, \quad (3)$$

where  $\Delta N_{jn}(t)$  is the change of the  $N_{jn}(t)$  between the time moments of  $t$  and  $t + \Delta t$ ;  $\Omega_{j+}$  and  $\Omega_{j-}$  are the frequency functions that characterize the processes that lead to an increase and decrease of  $n$  of the particles of  $j^{\text{th}}$  type;  $\vec{J}_{jn}$  is the flow of the particles in the condition  $(j, n)$  through the given area.

Therein:

$$\Omega_{j+} = \alpha_{jn-1}N_{jn-1}C_A + \alpha_{j-1,n-a}N_{j-1,n-a}N_{j-1,a} + \sum_{k \geq j} \beta_{k,n+b}N_{k,n+b}, \quad (4)$$

$$\Omega_{j-} = \alpha_{jn}N_{jn}C_A + \sum_{k > j} \alpha_{jn}N_{jn}N_{k,a} + \beta_{jn}N_{jn}, \quad (5)$$

where  $N_{jn} = N_{jn}(t)$ ;  $\alpha_{jn}$  and  $\beta_{jn}$  are functions that characterize the frequency of association and fragmentation of particles;  $a$  and  $b$  are the characteristic changes of  $n$  during a single act of unification and fragmentation.

With the known frequency functions  $\alpha_{jn}(n, t)$  and  $\beta_{jn}(n, t)$ , equations (1)–(5) allow one to calculate the volume fraction of the area filled with the particles of  $j^{\text{th}}$  type:

$$\varepsilon_j(t) = \sum_n v_{Aj}nN_{jn}(t), \quad (6)$$

where  $v_{Aj}$  is the volume per single A molecule after its transition into the polymer molecule of the  $j^{\text{th}}$  type particle.

From relations (4)–(6), it follows that moving from the concentration  $N_{jn}(t)$  to the distribution function  $\varphi_{jn} = \partial N_{jn}/\partial n$  and expanding  $\alpha_{jn}\varphi_{jn}$  and  $\beta_{jn}\varphi_{jn}$  in Taylor series limiting to three terms of the expansion, equation (3) can be written as:

$$\frac{\partial \varphi_{jn}}{\partial t} = \frac{\partial^2 (D_{jn}\varphi_{jn})}{\partial n^2} - \frac{\partial (G_{jn}\varphi_{jn})}{\partial n} + W_{jk} - \text{div} \vec{J}_{jn}, \quad (7)$$

where  $D_{jn} = \frac{1}{2}(a^2\alpha_{jn}C_A + b^2\beta_{jn})$ ;  $G_{jn} = a\alpha_{jn}C_A - b\beta_{jn}$ .  $W_{jk}$  is the function of the transition of the particles of  $j^{\text{th}}$  type in the groups of particles of other  $k^{\text{th}}$  types, related by the frequency functions in accordance with the conditions (4) and (5).

Therein:

$$\varepsilon_j(t) = \int_{n > n_{j0}} v_{Aj}n\varphi_{jn}(t)dn, \quad (8)$$

where  $n_{j0}$  is a number of molecules A, forming a particle of minimum size, to which the speed of enlargement  $G_{jn}$  can be attributed.

The solution of equation (7) with the corresponding boundary conditions can provide the ability to search the particle distribution function for a status parameter  $\vec{X}$ , which can be expressed as  $\varphi_j(\vec{X}, t) = \varphi_{jn}(t)f_j(v)_n f_j(X_1)_n \dots f_j(X_i)_{nv} \dots f_j(X_p)_{nv}$ , where  $f_j(v)_n$  and  $f_j(X_i)_{nv}$  are the distribution density on  $v$  of the particles with the given  $n$  and the distribution density on  $X_i$  of the particles with the given  $n$  and  $v$ .

### 3. Morphological body memory model

Within the framework of the considered model, the microrelief of the body at time  $t$  is represented by a set of ordered aggregates, among which the molecules are located, with the degree of filling of the volume of the body's surface area by particles of:

$$\varepsilon_S = \int_{n > n_{j0}} v_{Aj}n\varphi_{jn}(t_F)_S dn, \quad (9)$$

where  $\varphi_{jn}(t_F)_S$  is the distribution on  $n$  of particles of the  $j^{\text{th}}$  type on the body's surface area at the moment  $t_F$ . Distribution  $\varphi_{jn}(t_F)_S$ , as well as any distribution on any area of the system, is an integral of equation (7) and is determined by which of the frequency functions  $\alpha_{jn}(n, t_F)$  and  $\beta_{jn}(n, t_F)$  occurred at  $t \rightarrow t_F$ . Consequently, the information about the functions  $\alpha_{jn}(n, t_F)$  and  $\beta_{jn}(n, t_F)$ , included in this integral, can be extracted from the

distribution  $\varphi_{jn}(t_F)_S$ . Taking this into account, functions  $\varphi_{jn}(t_F)_S$  can be considered as carriers of the body morphological memory of the process which during the time  $t_F$  has led its microrelief into the state represented by the equation (9). According to equations (1)–(8), the frequency functions depend on the system properties  $\vec{y} = \{C_{A0}, V_0, S, \omega_S\}$ , accordingly the microrelief saves the information about the conditions in which the body was formed.

The distribution  $\varphi_{jn}(t_F)_S$  can be variable. For the formation of macromolecules not prone to aggregation in a homogeneous system under the condition of independence of  $\alpha_{jn}$  and  $\beta_{jn}$ , this distribution on  $n$  is determined by integrating the equation (7) in the form:

$$\frac{\partial \varphi_{jn}}{\partial t} = D_{1n} \frac{\partial^2 \varphi_{1n}}{\partial n^2} - G_{1n} \frac{\partial \varphi_{1n}}{\partial n}. \tag{10}$$

If the conditions  $\vec{y}$  are such that  $\alpha_{1n} C_A \gg \beta_{1n}$ , integration leads [19,20] to the formula

$$\varphi_{1n}(t_F)_S = C_{B0} \left[ (\pi Ap)^{-1/2} \exp(-X_-^2) - \frac{1}{2p} \exp\left(\frac{n - n_{10}}{p}\right) \operatorname{erfc}(X_+) \right], \tag{11}$$

where  $C_{B0}$  is the initiator concentration in the initial solution:

$$A = \int_0^t G_{1n} dt; p = D_{1n}/G_{1n}; X_{\pm} = (n - n_{0j} \pm A) / (4\pi Ap)^{1/2}; \operatorname{erfc}(X_+) = \frac{2}{\sqrt{\pi}} \int_{X_+}^{\infty} e^{-X^2} dX.$$

Equation (11) describes the molecular weight distribution of the polymer molecules forming the microrelief of the body, provided that the body was formed according to the model (1)–(8) in the independence of  $D_{1n}$  and  $G_{1n}$  on  $n$ . Given this, we can assume that in systems where the experimental data on the microrelief is described by relation (11), this condition is realized, and the information about it is accumulated by the distribution  $\varphi_{1n}(t_F)_S$ .

When  $t > t_F$ , the distribution  $\varphi_{1n}(t_F)_S$  can change under the influence of various factors, so that going from  $n$  to  $\vec{X}$ :

$$\varphi_j(\vec{X}, \tau)_S = \varphi_{jn}(t_F)_S P_j(\vec{X}, t_F, \tau), \tag{12}$$

where  $\varphi_j(\vec{X}, \tau)_S$  is the distribution function on  $\vec{X}$  of the near-surface particles of the  $j^{\text{th}}$  type after influences on the body over time  $\tau$ ;  $P_j(n, t_F, \tau)$  is the indicator of the microrelief stability to external influences.

Function  $P_j(\vec{X}, t_F, \tau)$ , which characterizes the degree of preservation of the body's morphological memory after its use, can be defined in the framework of our model after detailing of the respective frequency functions.

From the above, it follows that if after the formation and use of the body the microrelief remains on its surface, allowing one to experimentally determine the distribution functions of the structural elements of the microrelief on morphological parameters of the state and to present them as a solution of the equation (7), it can be argued that the body has morphological memory. According to the electron micrographs published in the literature, there are several polymeric bodies exhibiting morphological memory. Such a memory is also possessed by many inorganic nanostructured materials, although their nanoparticles, after aggregation, often become indistinguishable.

#### 4. Experimental study of polystyrene film formation. Methods and results

In conducting this research, we used a previously-described technique [21,22]. The polystyrene granules from Aldrich were dissolved in a solvent capable of rapid evaporation under normal conditions. A portion of the solution with a predetermined polystyrene content was introduced into a flat glass cuvette, which was then placed in the thermostatic chamber of a scale for continuous weighing, so that the weight change of the cuvette with the solution during the evaporation of the solvent was observed. Evaporation was carried out so that only the molecules of the solvent evaporated, making it possible to determine the rate at which the concentration of the polystyrene solution increased by measuring the rate at which the mass of the cuvette decreased. When the mass of the cuvette stopped changing, the formed polymer film was removed from the cuvette, its near-surface areas were studied using a scanning electron microscope, and the distribution functions of particle images of its microrelief on size were determined:  $\theta_k(\ell) = B_k(\ell)/B_{k0}$ , where  $B_k(\ell)$  is the number of measured particles of  $k^{\text{th}}$  type, that are smaller than  $\ell = s^{1/2}$  at the area of the image of  $s$ ;  $B_{k0}$  is the total number of particles measured. The particles which had homogeneous images were taken for primary nanoparticles ( $k = 1$ ), the ordered clusters of primary particles were taken for the aggregates (microparticles,  $k = 2$ ), and the groups of orderly contacted assemblies were taken for the secondary aggregates ( $k = 3$ ). In some experiments, a solution of  $C_{60}$  was added to the initial solution of polystyrene, and then the action was taken as described above.

The experiments have shown that the rate of the solvent removal from the cuvette was varied in two steps, as can be seen in Fig. 3, which shows the data on weight changes of the toluene solution of polystyrene in the cuvette. Therein the condition was fulfilled:

$$J = J_0\Delta + J_1 \exp[-\omega(t - t_1)](1 - \Delta), \quad (13)$$

where  $J_0$  and  $J_1$  are flows of evaporated solvent molecules from the surface of the cuvette at  $t < t_1$  and  $t = t_1$ ;  $\Delta = 1$  at  $t < t_1$  and  $\Delta = 0$  at  $t > t_1$ ;  $J_0 = 2,06 \cdot 10^{-3} \text{ mol}/(\text{m}^2 \cdot \text{s})$ ;  $J_1 = 2,53 \cdot 10^{-3} \text{ mol}/(\text{m}^2 \cdot \text{s})$ ;  $\omega = (2,3 \pm 0,5) \cdot 10^{-3} \text{ c}^{-1}$  is the empirical parameter.

By the end of the second step, when the evaporation was almost complete, a polymer film was formed in the cuvette which had properties that did not alter after transferring it to an electron microscope. Microrelief of the film was created by the microparticles, single or combined into the chains spheroidal nanoparticles were found on their surface and between them (Fig. 2). For the microparticles and their constituent nanoparticles the functions  $\theta_k(\ell)$  are presented as functions of  $Z$ , shown in Fig. 4, where  $Z = (\ell - l_{k0})/(l_{kM} - l_{k0})$ ,  $l_{k0}$  is the minimum size of measured particles of  $k^{\text{th}}$  type;  $l_{kM}$  is the size corresponding to the condition  $\theta_k(l_{kM}) = 0,5$  (Table 1). The corresponding differential distribution functions  $\psi_k(\ell) = \frac{\partial \theta_k(\ell)}{\partial \ell}$  are described by the formula:

$$\psi_k(\ell) = \left[ (\pi A_k p_k)^{-1/2} \exp(-X_-^2) - \frac{1}{2p_k} \exp\left(\frac{\ell - l_{k0}}{p_k}\right) \text{erfc}(X_+) \right], \quad (14)$$

where  $A_k$ ,  $p_k$ ,  $l_{k0}$  are empirical parameters, some of which are listed in the Table 2;  $X_{\pm} = (\ell - l_{k0} \pm A_k) / (4\pi A_k p_k)^{1/2}$ .

Functions  $\theta_1(\ell)$  of nanoparticles, included in the microparticles of different sizes, were similar. They changed when fullerene was introduced into the system (Fig. 4). In particular, during the formation of the film using an *o*-xylene solution of polystyrene at  $V_0 = 36,5 \text{ cm}^3$ ,  $M_0 = 0,15 \text{ g/cm}^3$  and initial fullerene concentration of  $M_C = 10^{-5} - 10^{-4} \text{ g/cm}^3$ , the function  $\theta_1(\ell)$  shifted toward larger units provided the following:

$$l_{1M} = l_{M0} (1 + 5,1 \cdot 10^2 M_C/M_0), \quad (15)$$

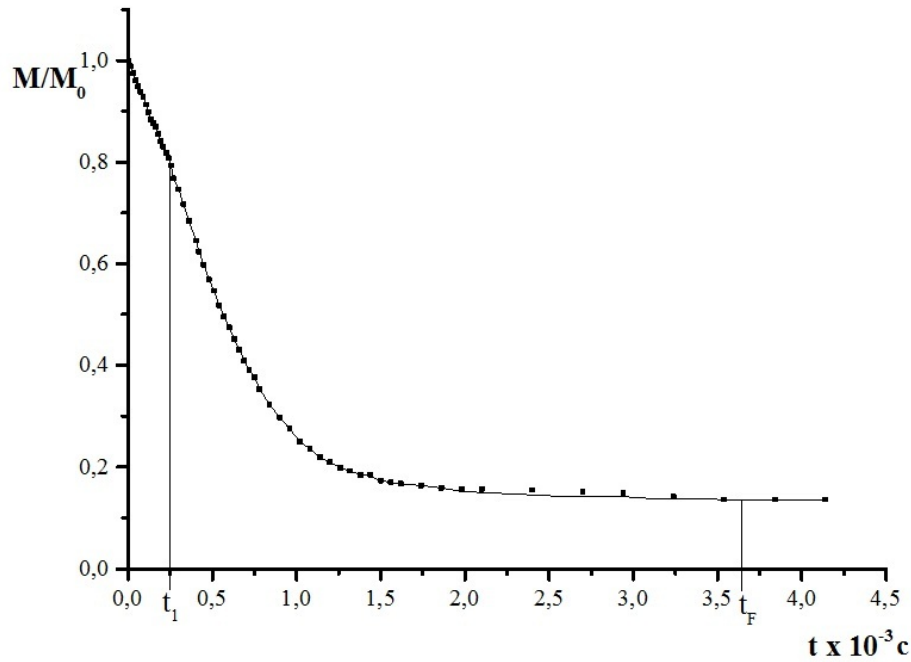


FIG. 3. Change of mass  $M$  of the polystyrene solution in toluene. The experimental conditions: solvent: toluene,  $T = 293$  K,  $V_0 = 0.463$  cm<sup>3</sup>, initial solution weight  $M_0 = 0.439$  g,  $S = 15.2$  cm<sup>2</sup>

TABLE 1. The characteristic size of the film nanostructure elements

Nanoparticle type	$M_C/M_0$	$l_{ko}$ , nm	$l_{kM}$ , nm
nano	0	$21 \pm 2$	$45 \pm 1$
micro	0	$280 \pm 20$	$750 \pm 20$
nano	$3 \cdot 10^{-4}$	$24 \pm 2$	$53 \pm 2$
nano	$1 \cdot 10^{-3}$	$26 \pm 2$	$65 \pm 2$

TABLE 2. The parameters of the differential distribution functions of nanoparticles microrelief on size

Body type	$l_{ko}$ , nm	$A_k$ , nm	$p_k$ , nm	$n_{10}$
film nanoparticle	$21 \pm 2$	$43 \pm 1$	$2,0 \pm 0,2$	$(3,1 \pm 0,1) \cdot 10^8$
film microparticle	$280 \pm 40$	$690 \pm 10$	$30 \pm 3$	$(7,4 \pm 0,5) \cdot 10^9$

where  $l_{M_0}$  is the size in the absence of fullerene.

## 5. Discussion

The obtained data characterize the near-surface area of the system, which at the beginning of the process was the initial solution, and in the end, was an ordered layer of microparticles that are shown in Fig. 2. The change in the properties of the near-surface area occurred in two stages, as indicated by Fig. 3 and equation (13). According to equation (13), processes in the subsurface solution did not affect the flow  $J$  of evaporated solvent molecules at  $t < t_1$  and reduced the flow to the  $J_1 = 0$  for  $t > t_1$ , and the function  $J(t)$  underwent the change at  $t = t_1$ , similar to the changes that take place at the border in supersaturated

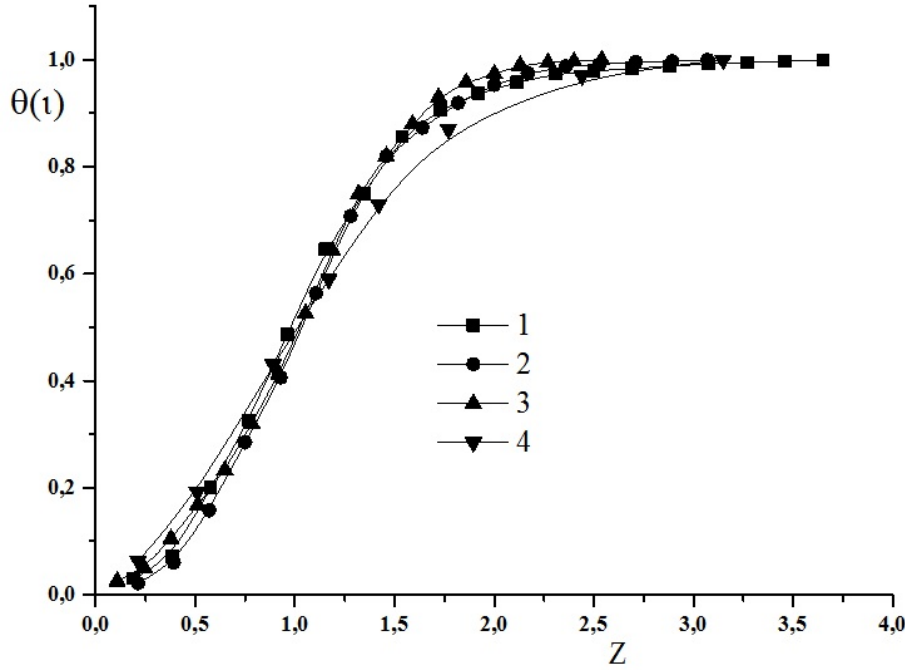


FIG. 4. Integral distribution functions of the structural elements of the films microrelief on size. 1 - nanoparticles; 2 - nanoparticles with fullerene content  $3 \cdot 10^{-4}$ ; 3 - nanoparticles with fullerene content  $1 \cdot 10^{-3}$ ; 4 - microparticles

metastable environments. Given these facts, we can assume that in the first stage ( $t < t_1$ ), the formation of the nanoparticles and their aggregation onto the microparticles took place, and in the second stage ( $t > t_1$ ), the enlargement of microparticles and their association in the aggregates dominated, forming the nanostructure which is shown in Fig. 2. This conclusion needs to be made to explain the proximity of the  $\theta_1(l)$  functions of nanoparticles within the microparticles of different sizes (Figure 4). This closeness indicates that the microparticles were formed surrounded by nanoparticles which have acquired a stable  $\theta_1(l)$  function prior to their significant association in the microparticles, i.e. in the first stage of the process. With this in mind, the data in Fig. 4 can be regarded as an appearance of the film's morphological memory, which preserves the information about the two-step process. The presence of morphological memory is also witnessed by formula (15), which allows one to determine the quantity of the fullerene in the system during film formation using the data on the  $\theta_1(l)$  functions. Information on the kinetics of nano- and micro-particle formation can be extracted from formula (14). This formula is a solution of the equation:

$$\frac{\partial \psi_k(l)}{\partial t} = D_{kl} \frac{\partial^2 \psi_k(l)}{\partial l^2} - G_{kl} \frac{\partial \psi_k}{\partial l}, \quad (16)$$

at the boundary condition:

$$\left[ G_{kl} \psi_k(l) - D_{kl} \frac{\partial \psi_k(l)}{\partial l} \right]_{l \rightarrow l_{0k}} = \delta(t), \quad (17)$$

where  $G_{kl}$  and  $D_{kl}$  are the parameters satisfying the conditions  $\int_0^t G_{kl} dt = A_k$  and  $D_{kl}/G_{kl} = p_k$ ;  $\delta(t)$  is the Dirac function. Equation (16) can be obtained using the relations (3)–(6), similar to the equation (7), assuming that  $W_{jk} = 0$ ,  $\text{div} \vec{J}_{jn} = 0$ ,  $n = \pi l^3/6v_{A_j}$ , and

$$G_{kl} = a_k \alpha_{kl} - b_k \beta_{kl} \quad (18)$$

$$D_{kl} = 1/2(a_k^2\alpha_{kl} + b_k^2\beta_{kl}) \tag{19}$$

Here,  $a_k$  and  $b_k$  are the effective changes of  $l$  at the single acts of integration and disintegration of the particles;  $\alpha_{kl}$  and  $\beta_{kl}$  are the repetition frequency of these acts, independent on  $l$ , so that:

$$p_k = \frac{a_k}{Z_k} (1 + q_k^2 Z_k) / (1 - q_k Z_k) \tag{20}$$

at  $Z_k = \beta_{kl}/\alpha_{kl}$  and  $q = b_k/a_k$ .

These facts allow us to assume that the groups of nanoparticles in the first stage and the microparticles in the second stage were formed according to the same accretion mechanism (i.e. attaching of small particles to larger particles). This is indicated by the fact that the distribution of nanoparticles as well as microparticles is described by equation (14), characterizing a plurality of particles, each of them is coarsened by attaching the fragments significantly smaller than the particle itself. According to relations (14), (15) and (17), the nanoparticle nuclei were in the initial solution or were formed after the start of evaporation during the time much smaller than  $t_1$ . Their parameter,  $n_{10}$ , can be estimated, assuming that  $n_{10} = \frac{\pi}{6} l_{10}^3 / v_{Ak}$ , where  $v_{Ak}$  is the volume of the styrene molecule in its crystal. Doing so gives a figure of  $n_{10} = (3.1 - 3.2) \cdot 10^8$  styrene molecules.

Based on equations (7), (14), (16)–(20), the nanoparticles on the first stage and the microparticles on the second stage undergo accretion independently ( $W_{jk} = 0$ ) at homogenization of the near-surface solution areas at  $t > t_1$  ( $div \vec{J}_{jn} = 0$ ). This finding is consistent with formula (13). Additionally, relations (7), (14) and (16) indicate that the rate of integration of nano- and microparticles does not depend on their size. According to formulas (3)–(7), the independence of  $D_{kl}$  and  $G_{kl}$  from  $l$  may be due to the fact that the nano- and microparticles had constant number of active centers, to which the macromolecules attached. As such centers, the nanoparticles could contain the ends of macromolecule chains, from which they consisted of, collected in the groups responsible for the independence of the parameters  $a_k$  and  $b_k$  on  $l$  and for the formation of chains of nanoparticles, from which the microparticles were composed.

According to the model ((1)–(7)), the independence of  $D_{kl}$  and  $G_{kl}$  on  $l$  does not exclude their dependence on evaporation time. This dependence is reflected by the parameters  $A_k$  and  $p_k$  in equation (14). Equation (14) is a solution of equation (16) for an arbitrary function  $A_k(t)$  and a constant parameter  $p_k$ . According to the formulas (17)–(20), the constancy of the parameter  $p_k$  may be due to the fact that the frequency functions  $\alpha_{kl}(l, t)$  and  $\beta_{kl}(l, t)$  are such that the values  $Z_k$  and  $q_k$  are constant or  $Z_k q_k \ll 1$ . More detailed information on the frequency functions in the model ((3)–(20)) cannot be extracted from the data on microrelief. However, it can be assumed that the function  $\Psi_1(l)$  characterizes the primary aggregates of macromolecules ( $j = 2$ ), as indicated by the value  $n_{10}$ , and the function  $\Psi_2(l)$  refers to the ordered groups of aggregates (secondary aggregates  $j = 3$ ). Given this, one can proceed from the function  $\Psi_1(l)$  to the distribution  $\varphi_2(n, t)_s$ , using the condition:

$$\int_{l>l_{10}} \Psi_1(l) dl = \frac{1}{N_2} \int_{n>n_{10}} \varphi_2(n, t_F)_s dn, \tag{21}$$

where  $N_2$  is number of primary aggregates per unit volume of the near-surface layer of the film at  $t = t_F$ . A similar relation leads to a transition from the function  $\Psi_2(l)$  to the distribution  $\varphi_3(n, t)_s$ . At the transition from  $\varphi_3(n, t)_s$  to  $\varphi_3(\vec{X}, \tau)_s$  it can be taken that  $P_3(\vec{X}, t_F, \tau) = 1$ .

## 6. Conclusions

It has been established that by evaporation of *o*-xylene and toluene solutions of polystyrene, polymeric bodies are formed which have a two-tier hierarchical nanostructure microrelief, and each level of the nanostructure has a stable distribution function of its structural elements on size. The results of these functions' determination coincide with the solution of the kinetic equations for the model of polymer body formation by evaporation of the polymer solution, beginning with the primary aggregates of macromolecules (nanoparticles), continued with the association of nanoparticles into the secondary aggregates of macromolecules (microparticles) and completed with the association of microparticles in the polymer bodies.

This model is based on the conservation of the number of atoms in the system and on the consolidation of nano- and microparticles as a result of binary collisions, and does not contain arbitrary assumptions. Therefore, the fit of the model to the experimental data can be considered as an indication of the fact that these processes actually took place during evaporation of the solution of polystyrene, and nano- and microparticles retained the information on how they were being consolidated, and this information can be obtained without destroying the film, defining the distribution function of the structural elements of the microrelief on size. Research methods used in this paper are not specific to the polystyrene. There are a wide range of polymers which have electron micrographs published in the literature that show microrelief, thus making them prime candidates for study using the above-described model.

## Acknowledgment

The work was supported by Russia Foundation for Basic Research (grant N 15-43-03034-a).

## References

- [1] Entelis S.G., Evreinov V.V., Kuzaev F.I. *Reactive oligomers*, M.: Chemistry, 1985, 304 p.
- [2] Matyjaszewski K., *Controlled/Living Radical Polymerization*. Oxford University Press, Oxford, 2000, 416 p.
- [3] Nalwa H.S. (Ed) *Handbook of Nanostructured Materials and Nanotechnology*. Organic, Polymer and Biological Compounds. Boston: Acad Press. 2000, **5**, P. 577-583.
- [4] Osada Y, Khokhlov A.R. (Eds) *Polymer Gels and Network*. Marcel Dekker, New York Basel, 2002, 309 p.
- [5] Volynsky A.A., Bakeev N.F. *Structural self-organization of amorphous polymers*. Moscow, FIZMATLIT, 2005, 232 p.
- [6] Caruso F.(Ed.), *Colloids and Colloid Assemblies*. Wiley-VCH, Weinheim, 2004, 603 p.
- [7] Kabanov V.A., *Selected Works*. M.:Nauka, 2010, 432 p.
- [8] Korolev G.V., Mogilevich M.M. *Three-dimensional radical polymerization. Mesh and hyperbranched polymers*. Chemistry: St. Petersburg. 2006, 334 p.
- [9] Mezhevikovsky S.M. *Physical-chemical reactivity of oligomers*. M.:Nauka, 1998, 233 p.
- [10] Grosberg A.Y., Khokhlov A.R. *Polymers and biopolymers from the point of view of physics*. Intellect Publishing House, Dolgoprudny, 2010, 303 p.
- [11] Zaitsev S.Yu., Zaitseva V.V. *Supramolekulyarnye momomernye sistemy na osnove stirola I ikh komplksno-radikalnaya sopolimerizatsiya* (Styrene-Based Supramolecular Monomer-Polymer System and Their Complex-Radical (Copolymerization), Krasand, Moscow, 2012, 312 p.
- [12] Acadsky A.A., Kondrashchenko V.I. *Computational materials science of polymers*. M: Nauchny mir, 1999, 544 p.

- [13] Zherenkova L.V., Khalatur P.G., Khokhlov A.R. On the theory of polymer-containing dispersed systems. Aggregation of dispersed particles at the adsorption of macromolecules and the formation of ordered structures. *Russ. Colloid Journal*. 1997, **59**(5), P. 634–645.
- [14] Moor R.B, Martin C.R. *Anal.Chem.* 1986, **58**, P. 2568–2580.
- [15] Tobita H., Fundamental Molecular Weight Distribution of RAFT Polymers. *Macromol. React. Eng.* 2008, **2**(5), P. 371–381.
- [16] Liu C., Qin H., Mather P.T. Review of progress in shape-memory polymers. *J. Mater. Chem.* 2007, **17**(16), P. 1543–1558.
- [17] Xie T. Tunable polymer multi-shape memory effect. *Nature*, 2010, **464**, P. 267–270.
- [18] Jinlian Hu, Yong Zhu, Huahua Huang, Jing Lu. Recent advances in shape-memory polymers: Structure, mechanism, functionality, modeling and applications. *Progress in Polymer Science*, 2012, **37**, P. 1720–1763.
- [19] Melikhov I.V., Berliner L.B. Kinetics of periodic crystallization in the presence of crystals growing with fluctuating rates. *Teor.Osn.Khim.Tekhnol.* 1985, **19**(2), P. 158–165.
- [20] Melikhov I.V. *Physico-chemical evolution of solid matter*. M: Binom, 2006, 309 p.
- [21] Alekseeva O.V., Bagrovskaya N.A., Kuzmin S.M., Noskov A.V., Melikhov I.V., Rudin V.N. The Influence of Fullerene Additives on the Structure of Polystyrene Films. *Russ.J. Phys. Chem. A*, 2009, **83**(7), P. 1170–1175.
- [22] Kratschmer W., Huffman D.R. Production and Discovery of Fullerene: New Forms of Crystalline Carbon. *Phil. Trans. Poy. Soc.(London) A*, 1993, **343**(1667), P.33–38.
- [23] Melikhov I.V., Berliner B.L. Simulation of Batch Crystallization, *Chem. Engineering Sci.*, 1981, **36**, P. 1021–1024.
- [24] Melikhov I.V. An evolutionary approach to the creation of nanostructures. *Nanosystems: physics, chemistry, mathematics*. 2010, **1**(1), P.148–155.

# Stimulated emission of an atomic system under coherent excitation

A. G. Petrashen, N. V. Sytenko

ITMO University, 197101, St. Petersburg, Russia

apetrashen@mail.ru

PACS 32.60.+i, 32.10.Dk, 32.80.-t

DOI 10.17586/2220-8054-2015-6-4-562-569

The stimulated emission of a coherently excited atomic system was studied in the presence of a strong magnetic field.

**Keywords:** coherent excitation, density matrix, Liouville equation.

*Received:* 25 April 2015

*Revised:* 30 April 2015

## 1. Introduction

The possibility of collective spontaneous emission was first indicated by Dicke [1]. Later, these effects were detected in cesium atomic beams [2], as well as in ensembles of rubidium atoms [3,4]. The ideas of Dicke were subsequently developed in numerous publications (see for instance [5,6]), which included mostly bi-level systems with different ways of population inversion, possibly leading to superradiance - high intensity pulses, followed by a certain delay in relation to the inverse state formation time. It should be emphasized that generally speaking, population inversion is not a necessary condition for the creation of superradiance. This phenomenon can occur if a dipole moment is induced on the upper state [7,9]. This is known as induced superradiance. The present work is not directly related to superradiance as such. Below, within the framework of the ideas used for superradiance, we will investigate the collective polarization emission of a complex atomic system which has been placed in a strong magnetic field, the lower state of which, is populated by axially symmetric interactions.

## 2. Statement of the problem

In this paper, we consider the time dependence of the  $3^3S_1$  state of the *He* atom, the excitation of which is performed by a  $2^3P$  multiplet of this atom. It is assumed that the system has been placed in a magnetic field strong enough to break the thin bond of the P-multiplet under consideration. We will also assume that the  $2^3P$  state is populated from the ground state of this atom by a proton or electron impact or other axially symmetric excitation sufficient to break the fine bond, and its symmetry axis makes an angle  $\theta$  with the axis *OZ* of the laboratory frame of reference. As a result of this excitation, the ordering of the angular moments of the  $T_0^0$  population and the longitudinal alignment of  $T_0^2$  will be induced on the  $2^3P$ -levels in the frame of reference associated with the anisotropy axis. Then, by introducing a parameter  $\alpha = T_0^2/T_0^0$ , which may be called the anisotropy parameter for the population efficiencies of the  $2^3P_j$  state magnetic sublevels in the laboratory frame of reference *XYZ*, one can write:

$$\sigma_{j,m;j',m'} = \frac{1}{2j+1} A^{(0)}(j,j',l,s) + \alpha \sum_q (-1)^{j'+m'} \begin{bmatrix} j & j' & 2 \\ m & -m' & q \end{bmatrix} D_{0,q}^{(2)}(\theta) A^{(2)}(j,j',l,s), \quad (1)$$

where  $l$  and  $s$  are the orbital and the spin moments,  $D_{m,m'}^2(\theta)$  elements of three-dimensional rotation [10], and  $A_j^{(k)}$  depends on coefficients of vector moment addition:

$$A^{(k)}(j, j', l, s) = (-1)^{j'+s+k+l} \sqrt{(2j+1)(2j'+1)} \begin{Bmatrix} l & l & k \\ j & j' & s \end{Bmatrix}. \quad (2)$$

The Hamiltonian operator of the atomic system placed in a strong magnetic field of strength  $\mathcal{H}$  is defined by the orbital  $\hat{L}$  angular momenta and  $\hat{S}$  – the spin moments:

$$\hat{H} = \hat{H}_0 + \mu_0 \mathcal{H}(\hat{L} + 2\hat{S}) + \hat{V}, \quad (3)$$

where  $\mu_0$  – is the Bohr's magneton, and operator  $\hat{V}$  describes the excitation of  $3^3S_1$  state, from the lower  $2^3P$  ones (hereinafter referred to as the state of 'b' and 'a', respectively) by electromagnetic field polarization. This polarization makes an angle  $\chi$  with the  $OZ$  axis of the laboratory frame of reference as follows:

$$(V_{ab})_{m_a, m_b} = \langle j_a m_a | d_z | j_b m_b \rangle = \hbar \tilde{\Omega} (W_{ab})_{m_a, m_b}, \quad (4)$$

where  $\tilde{\Omega}(t) = E(t)\langle r \rangle / \hbar$  is the Rabi frequency, which depends on the value of electric field strength  $\vec{E}(t)$  and  $\langle r \rangle$  – reducible matrix element of operator  $\hat{r}$ . The elements of the  $W_{a,b}$  matrix are defined by the regulations of the vector additions:

$$(W_{ab})_{m_a, m_b} = \hbar \Omega_R (-1)^{l_a+s+j_b l_b+1} \sqrt{(2l_b+1)(2j_b+1)} \begin{bmatrix} j_b & 1 & j_a \\ m_b & 0 & m_a \end{bmatrix} \begin{Bmatrix} l_b & l_a & 1 \\ j_a & j_b & s \end{Bmatrix} \begin{bmatrix} l_b & 1 & l_a \\ 0 & 0 & 0 \end{bmatrix}. \quad (5)$$

The excitatory electric field  $E(t)$  leads to the polarization of the medium, which is characterized by a polarization vector  $\vec{P}$ . The value of this vector is proportional to the mean value of the operator of dipole moment  $\hat{d}$ , evaluated on the correlation density matrix:

$$\vec{P} = -n_0 \mathfrak{S} \left[ \text{Sp} \left( \rho_{ab} \hat{d} \right) \right]. \quad (6)$$

From the last relation, one can see that the polarization of the environment by the excitation process is defined by the correlation density matrix and hence, depends on its variation. In turn, the right hand side of the Liouville equation, which describes the variation of the density matrix, contains the Rabi frequency, which depends on the electric field strength. So, the mutual variation of the density matrix and the electric field is described by a system of self-consistent equations:

$$\begin{aligned} \frac{d}{dt} \tilde{\rho}_{aa}(t) &= \Gamma \tilde{\rho}_{bb}(t) - \frac{i}{\hbar} (V_{ab}(t) \tilde{\rho}_{ba}(t) - \tilde{\rho}_{ab}(t) V_{ba}(t)), \\ \frac{d}{dt} \tilde{\rho}_{bb}(t) &= -\Gamma \tilde{\rho}_{bb}(t) - \frac{i}{\hbar} (V_{ba}(t) \tilde{\rho}_{ab}(t) - \tilde{\rho}_{ba}(t) V_{ab}(t)), \\ \frac{d}{dt} \tilde{\rho}_{ab}(t) &= -\frac{\Gamma}{2} \tilde{\rho}_{ab}(t) - \frac{i}{\hbar} (E_a - E_b) \tilde{\rho}_{ab}(t) - \frac{i}{\hbar} (V_{ab}(t) \tilde{\rho}_{bb}(t) - \tilde{\rho}_{aa}(t) V_{ab}(t)), \\ \tilde{\rho}_{ba}(t) &= \tilde{\rho}_{ab}^\dagger(t), \\ \nabla^2 E - \frac{1}{c^2} \frac{\partial^2}{\partial t^2} E &= \frac{4\pi}{c^2} \frac{\partial^2}{\partial t^2} P, \end{aligned} \quad (7)$$

where  $E_a$  and  $E_b$  are stationary energy levels of the lower and upper states and matrix  $\Gamma$  describes the relaxation process. It should be mentioned that the  $2^3P$  state of the helium atom consists of three levels, one of which with  $j = 2$  is metastable [11]. Since the lifetime of the upper  $3^3S_1$  state is approximately one-third the size of the lower  $2^3P_j$  state, this system of two multiplets can be considered self-contained, which means that the total population of levels ‘a’ ‘b’ is conserved.

In order to simplify the main calculation it is necessary to move the squared momentum and its projection from the base of the eigenfunction to the diagonalized base (M-base), which describes the integration with the strong magnetic field. Diagonalization was performed analytically using the Mathematica software package. As a result, two sets of orthogonal eigenvectors were obtained, each of which corresponds to the eigenvalues of the state ‘b’  $(\varepsilon)_{M_b} = \mu_0 \mathcal{H} M_b$ , ( $M_b = \pm 2.0$ ) and the state ‘a’  $(\varepsilon)_{M_a} = \mu_0 \mathcal{H} M_a$ , ( $M_a = \pm 3, \pm 2, \pm 1.0$ ). In the latter case, the states with  $M_a = \pm 1$  are doubly degenerate. Then, in light of the information above, the eigenvalues of the Hamiltonian operator in a strong magnetic field takes the form:  $(E_a)_{M_0} = E_a + (\varepsilon_a)_{M_0}$ ,  $(E_b)_M = E_b + (\varepsilon_b)_M$ .

In order to reduce the system (7) to a more convenient form for numerical computation, it is first necessary to introduce dimensionless time  $\tau = t/\tau_0$ , where  $\tau_0 = 36 \cdot 10^{-9}$  sec [11] – the lifetime of the excited  $3^3S_1$  state, and secondly, to introduce the density matrix  $\rho_{i,j}(t)$  ( $i, j = a, b$ ), connected with the analogous matrix used previously with the relations  $(\rho_{ii}(\tau))_{M,M_1} = (\tilde{\rho}_{ii}(\tau))_{M,M_1}$  ( $i = a, b$ ),  $(\rho_{ba}(\tau))_{M,M_1} = (\tilde{\rho}_{ba}(\tau))_{M,M_1} \exp[-i\tau((E_b)_M - (E_a)_{M_1})]$ ,  $(\rho_{i,j}(\tau) = (\rho_{j,i}(\tau))^\dagger)$ . Additionally, it is assumed that the system is situated in a circular resonator, the eigenfrequency of which coincides with the transition frequency between the upper and lower multiplets. In order to eliminate rapidly oscillating terms in the system (7), the solution of the last equation of this system may be searched in the form of a progressive wave  $E(t) = -\mathcal{E}(t)e^{i\omega t}$ , and the response of the system in the form of a superposition of such waves  $P(t) = \Re(\mathcal{P}(t))e^{i\omega t} + i\Im(\mathcal{P}(t))e^{i\omega t}$ . Then, assuming that the field and polarization vector amplitudes are slowly varying, and that their values are independent of the space variables (mean field assumption), then system (7) takes the following form:

$$\begin{aligned} \frac{d}{d\tau} \rho_{aa}(\tau) &= \Gamma_a \rho_{bb}(\tau) + \frac{i\Omega_R}{2} \left[ \rho_{ab}(\tau) (W_{ba})_I - (W_{ab})_I \rho_{ba}(\tau) \right], \\ \frac{d}{d\tau} \rho_{bb}(\tau) &= -\Gamma \rho_{bb}(\tau) - \frac{i\Omega_R}{2} \left[ (W_{ba})_I \rho_{ab}(\tau) + \frac{i}{2\hbar} \rho_{ba}(\tau) (W_{ab})_I \right], \\ \frac{d}{d\tau} \rho_{ab}(\tau) &= -\frac{\Gamma}{2} \rho_{ab}(\tau) + \frac{i\Omega_R}{2} \left[ \rho_{aa}(\tau) (W_{ab})_I - \frac{i}{2\hbar} (W_{ab})_I \rho_{bb}(\tau) \right], \\ \frac{d}{d\tau} \rho_{ba}(\tau) &= -\frac{\Gamma}{2} \rho_{ba}(\tau) - \frac{i\Omega_R}{2} \left[ (W_{ba})_I \rho_{aa}(\tau) + \frac{i}{2\hbar} \rho_{bb}(\tau) (W_{ba})_I \right], \\ \frac{\partial}{\partial t} \mathcal{E} &= -4\pi\omega n_0 \Im \mathcal{P}, \end{aligned} \quad (8)$$

where  $\mathcal{P} = \text{Sp}(\rho_{ab}r/a_0)$  and  $n_0$  are the density of the particles. In order the last equation contains dimensionless values one can introduce the dimensionless Rabi frequency  $\Omega_R = \tau_0 \mathcal{E} \langle r \rangle / \hbar$ . Than the last equation of the system (6) takes the form:

$$\frac{d}{d\tau} \Omega_R = -\Omega_M^2 \text{Sp} \left( \rho_{ab} \frac{r}{a_0} \right), \quad (9)$$

where the introduced denotation

$$\Omega_M = \sqrt{4\pi n_0 \left(\frac{ea_0}{\hbar}\right)^2 \hbar\omega \frac{\langle r \rangle}{a_0}},$$

which depends on  $\langle r \rangle$  – the dimensionless mean value of operator  $\hat{r}$  in the state  $3^3S_1$ .

### 3. The results of numerical calculation. Discussion

Before considering the results of numerical calculations, it should be mentioned that the fine splitting for the  $2^3P_j$  state is relatively small and that this splitting is due to the strong magnetic field, compared to the energy difference of the ‘centers of gravity’ of  $2^3P_j$  and  $3^3S_1$  multiplets, the radiation of the system under consideration should be similar to that of the bi-level system considered in detail in [8]. The emissions of such a system are harmonic oscillations, known as nutations. After this, the system was integrated using initial conditions  $\Omega_R(0) = 0$  and the density matrix values that were obtained in the previous step. The process of integration was accomplished via the series expansion method that was described in detail in our previous articles [12, 13]. The results of our calculations are represented on the Fig. 1 – Fig. 5.

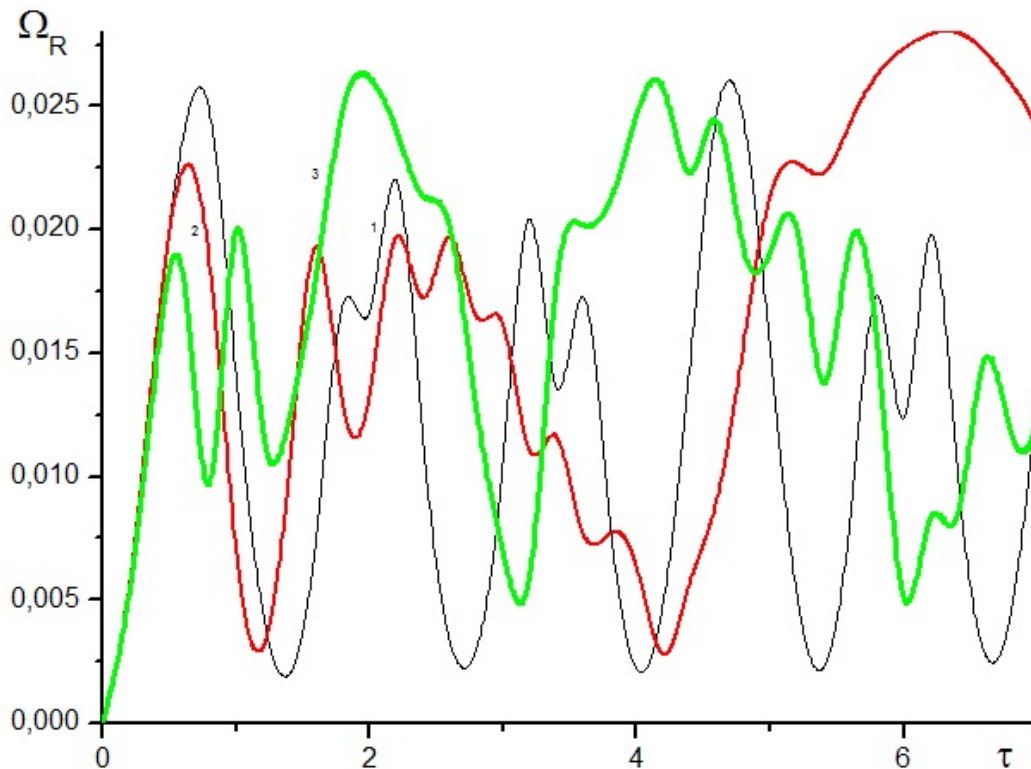


FIG. 1. The dependence of the induced Rabi frequency on dimensionless time for two values of particle density  $n_0 = 10^{11}$  and  $n_0 = 10^{13} \text{ cm}^{-3}$

In Fig. 1, the dependence of the induced Rabi frequency on dimensionless time is shown for two values of frequency  $\Omega_M$  (two values of particles density  $n_0$ ). From this figure, one can see that the nutation frequency increases with increasing  $\Omega_M$ . Also, one can see that the nutations take place relative to some curve that shifts up the abscissa axis with increasing  $\Omega_M$ .

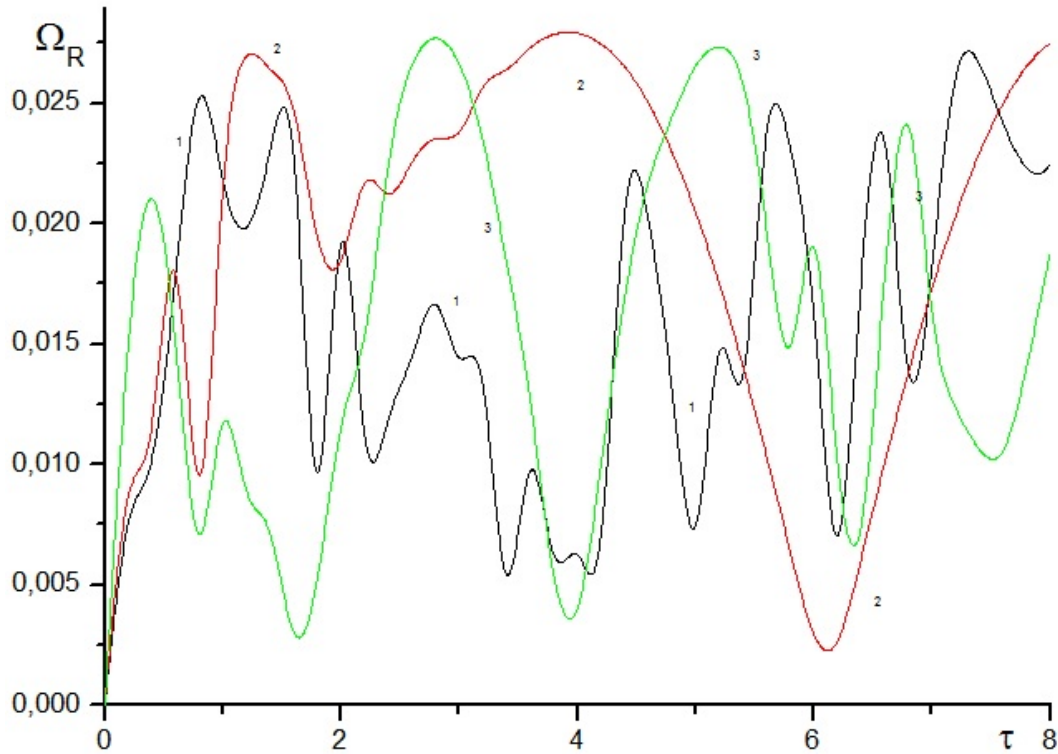


FIG. 2. The dependence of the induced Rabi frequency on dimensionless time for two laser detuning frequency values  $\delta = 0, 0.5, 1$

The dependence of the induced Rabi frequency upon time for some laser detuning frequency values is represented in Fig. 2. From this plot, one can see that at zero detuning, the dependence is represented by a sequence of rather short impulses. With increased signal cleaning, the widths of the impulses first rapidly increase, however, with additional increased detuning, the width of the impulses begins to decrease.

The dependence of induced Rabi frequency upon time for some values angle  $\chi$  (the angle between the direction of the magnetic field and the  $OZ$  axis of the laboratory frame of reference) is illustrated in Fig. 3. From this figure, one can see that over the range of angle  $0 < \chi < \pi/3$  the emission signal increases and for  $\chi > \pi/3$  rapidly decreases, with the signal vanishing at  $\chi = \pi/2$ . A similar dependence for systems under coherent excitation was reportedly fixed in our works [12, 13]. It should be mentioned that such a dependence follows from the fact that at  $\chi = \pi/2$ , the system is in a state of coherent population trapping. In other words, the population at the state  $3^3S_1$  is zero, and thus, the system did not absorb the electromagnetic radiation. The situation under consideration is illustrated on the Fig. 4, where the dependence of the  $3^3S_1$  state's population for some values of angle  $\chi$  is represented.

The problem is also illustrated here, in the frame of the approximate solution for system (9) in the framework of perturbation theory over the Rabi frequency. By restricting to first order perturbation theory over the Rabi frequency, one can write:

$$\begin{aligned} \frac{d}{d\tau} \rho_{ab}(\tau) &= \Omega_R \rho_{aa}(0) (W_{ab})_I(\tau), \\ \frac{d}{d\tau} \Omega_R(\tau) &= -\Omega_m^2 \mathfrak{S} \left[ \text{Sp} \left( \rho_{ab} \frac{r_{ba}}{a_0} \right) \right]. \end{aligned} \quad (10)$$

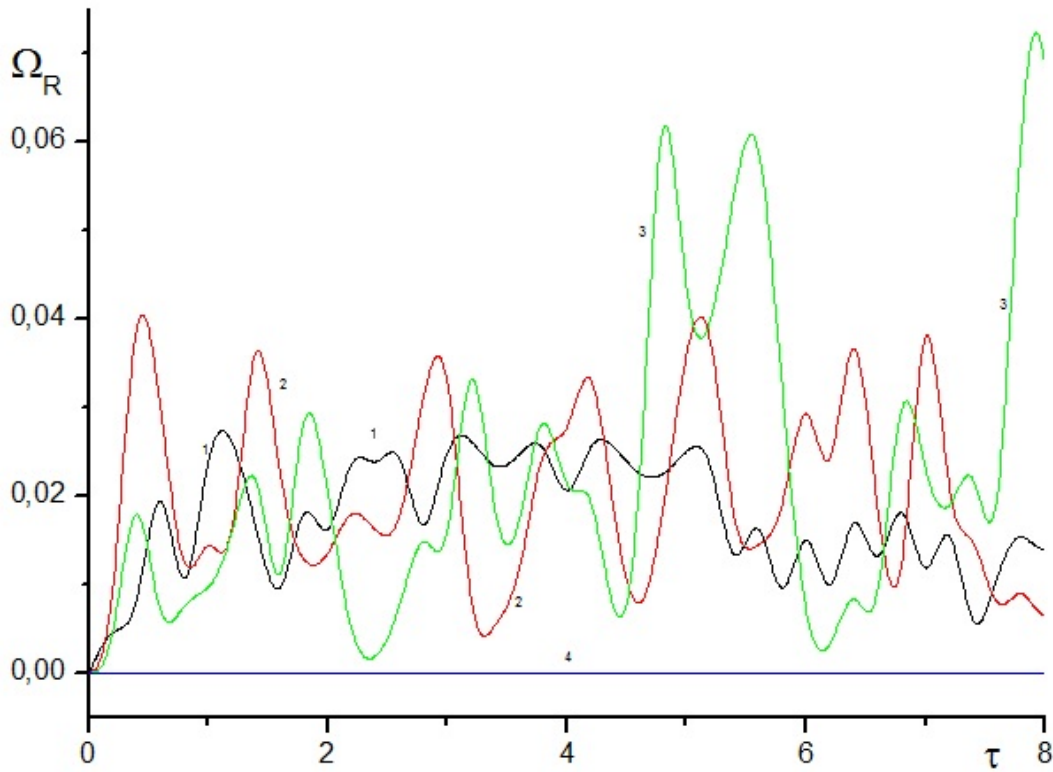


FIG. 3. The dependence of the induced Rabi frequency on dimensionless time for two angle  $\chi = 0, \pi/6, \pi/3, \pi/2$ . Curves 1 – 4

From these relations, it follows that:

$$\frac{d^2}{d\tau^2}\Omega_R(\tau) = -\Omega_R \left\{ \Omega_m^2 \Im \left[ \text{Sp} \left( \rho_{aa}(0) (W_{ab})_I(\tau) \frac{r_{ba}}{a_0} \right) \right] \right\}. \quad (11)$$

The right hand part of this relation can be calculated with help of Mathematica. The resulting rather enormous relation takes a rather compact form in some cases. For instance, in the case when  $\chi = \pi/4$  or  $\chi = \pi/2$ , one can write:

$$\begin{aligned} \frac{d^2}{d\tau^2}\Omega_R(\tau) + \frac{1}{144}\Omega_M^2 \left( 11 + 8 \cos \left[ \frac{\Omega_L}{\hbar}\tau \right] \right) \Omega_R(\tau) &= 0, & \chi = \pi/4; \\ \frac{d^2}{d\tau^2}\Omega_R(\tau) + \frac{7}{72}\Omega_M^2 \cos \left[ \frac{\Omega_L}{\hbar}\tau \right] \Omega_R(\tau) &= 0, & \chi = \pi/2. \end{aligned} \quad (12)$$

Because of the assumption that only the induced emission was considered before, we are therefore suggesting that in the system at  $\tau < 0$ , the dipole moment was induced. So, equations should be solved for the initial conditions  $\Omega_R(0) = 0.01$ ,  $\frac{d}{d\tau}\Omega_R(0) = 1$ . The results are represented in Fig. 5, from which, one can see that induced emission at  $\chi = \pi/2$  is significantly lower than at  $\chi = \pi/4$ .

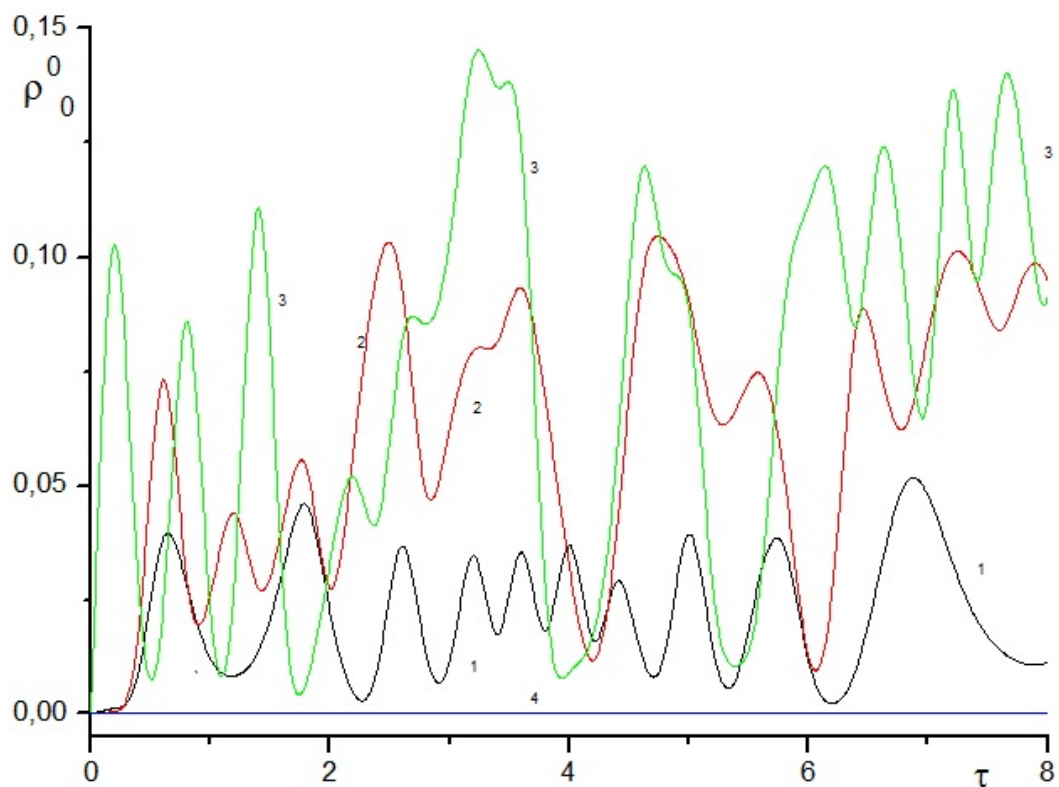


FIG. 4. The dependence of the  $3^3S_1$  population for  $\chi = 0, \pi/6, \pi/3$  and  $\pi/2$ . Curves 1 – 4

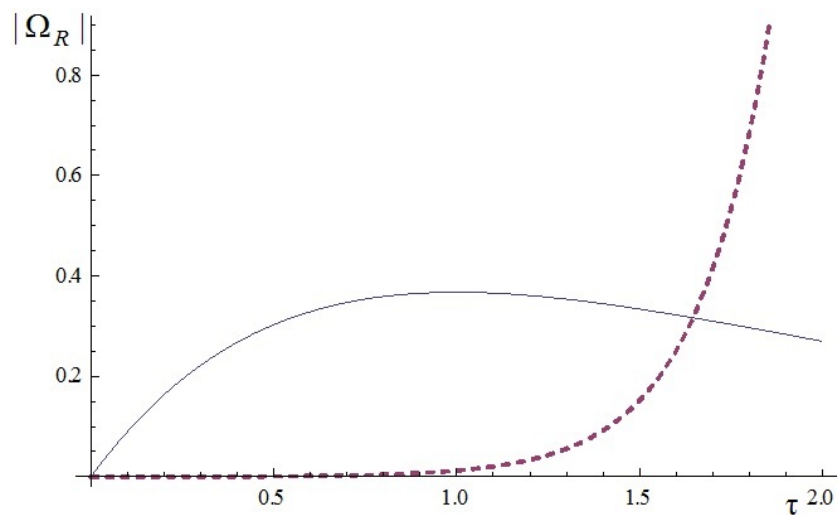


FIG. 5. The dependance on dimensionless time of of Rabi frequencies obtained in the frame of perturbation theory  $\chi = \pi/2$  (lower curve),  $\chi = \pi/4$  (upper curve)

#### 4. Conclusion

In this work, the induced emission of a complex atomic system in the presence of the strong magnetic field was considered. The dependence of the induced emission on the atom's density and laser's detuning was examined. In the case when the direction of the magnetic field is orthogonal to the direction of the polarization of exiting radiation the induced emission vanishes.

#### Acknowledgements

This work was partially financially supported by the Government of the Russian Federation (grant 074-U01), by Ministry of Science and Education of the Russian Federation (GOSZADANIE 2014/190, Projects No. 14.Z50.31.0031 and No. 1.754.2014/K), by grant MK-5001.2015.1 of the President of the Russian Federation.

#### References

- [1] R.H. Dicke Coherence in spontaneous radiation processes. *Phys. Rev.*, 1954, **93**, P. 99–105.
- [2] H.M. Gibbs, Q.H. Vreken, H.M. Hikspoors. Single-pulse superfluorescence in Cesium. *Phys. Rev. Lett.*, 1977, **39**, P. 547–550.
- [3] E. Paradis, B. Barret et al. Observation of superfluorescent emissions from laser-cooled atoms. *Phys. Rev. A*, 2008, **77**, P. 043419.
- [4] G.O. Ariunbold, M.M. Kash, et al. Observation of picosecond superfluorescent pulses in rubidium atomic vapor pumped by 100-fs laser pulses. *Phys. Rev. A*, 2010, **82**, P. 043421.
- [5] R. Bonifacio, L.A. Lugiato. Cooperative radiation processes in two-level systems: Superfluorescence. II. *Phys. Rev. A*, 1975, **12** (2), P. 587–592.
- [6] J.H. Brownell, Y. Lu, S.R. Hartmann. Yoked superfluorescence. *Phys. Rev. Lett.*, 1995, **75**, P. 3265–3268.
- [7] R.F. Malikov, E.D. Trifonov. Induced superradiance in activated crystals. *Opt. Comm.*, 1984, **52** (1), P. 74–76.
- [8] L. Allen, J. Eberly. *Optical resonances and two-level atoms*. New-York, London, 1975.
- [9] A.I. Zaishev, V.A. Malyshev, I.V. Ryzhov, E.D. Trifonov. Inversion-free superfluorescence of the ensemble three-level in the high-Q resonator. *JETP*, 1999, **115**, P. 505–520 [In Russian].
- [10] A. Jucys, A. Bandzaitis. *Momentum theory in quantum mechanics*. Vilnius, 1965, 462 p.
- [11] A. Radzig, B.M. Smirnov. *Reference data on atoms, molecules and ions*. Springer-Verlag, Berlin, 1985.
- [12] A.G. Petrashen, N.V. Sytenko. Polarization characteristics of emission of an ensemble of atoms on coherent excitation in the presence of a strong magnetic field with allowance for the Doppler profile width. *Optics and Spectroscopy*, 2015, **118** (6), P. 851–856.
- [13] A.G. Petrashen, N.V. Sytenko. The polarization characteristics of the radiation of atomic ensemble under the coherent excitation in the presence of the strong magnetic field. *Nanosystems: Phys., Chem., Math.*, 2015, **6** (1), P. 122–132.

## Dielectric relaxation of fulleroid materials filled PA6 composites and the study of its mechanical performance

Alex N. Sinitsin<sup>1</sup>, Vjacheslav V. Zuev<sup>1,2</sup>

<sup>1</sup>ITMO University, Kronverkskiy pr., 49, 197101 St. Petersburg, Russia

<sup>2</sup>Institute of Macromolecular Compounds of the Russian Academy of Sciences,  
Bolshoi pr. 31, 199004 St. Petersburg, Russia  
lyubomirov85@mail.ru, zuev@hq.macro.ru

PACS 81.07.Lb

DOI 10.17586/2220-8054-2015-6-4-570-582

The effect of fulleroid materials (fullerene C<sub>60</sub> and fullerene soot which is used for fullerenes production) on the mechanical properties of polymer nanocomposites based on polyamide 6 (PA6) was investigated. Composites were synthesized by direct mixing in an extruder. Dielectric spectroscopy was used to investigate the influence of nanoparticles on relaxation processes in the polymer matrix. It is found that the segmental relaxation processes becomes faster with the addition of fullerene C<sub>60</sub>. In contrast, the secondary processes of PA6/fullerene C<sub>60</sub> nanocomposites were observed to slow down with the addition of fullerene C<sub>60</sub>. This means that the local ‘molecular stiffness’ is increased, and a phenomenological link between the secondary relaxation times and the mechanical properties explains the increase in the Young’s modulus of the nanocomposites upon the addition of C<sub>60</sub>. These observations suggest that nanoparticles can have a qualitatively different effect on the matrix polymer dynamics at different length scales, and caution must be taken in comparing the changes in the dynamics associated with different relaxation processes.

**Keywords:** composites; manufacturing; mechanical properties; fullerene C<sub>60</sub>; fullerene soot; dielectric spectroscopy.

*Received:* 2 March 2015

*Revised:* 18 April 2015

### 1. Introduction

Reinforcing thermoplastic polymers with nanoparticles to form nanocomposites is one means to increase the usage of polymeric materials. A number of polymers can be considered as competitive materials for tribological applications because of their low friction coefficients against steel counterparts, good damping properties, and self-lubricating ability. Among thermoplastic polymers, PA6 has become a strong competitor matrix owing to its good thermal stability, low dielectric constant and high tensile strength. PA6 has been reported to have a superior wear resistance sliding against a steel counterface relative to other polymers. In order to meet the special needs of tribological applications, polymer composites can be designed by selecting the correct composition and choosing an appropriate manufacturing process. The improvement of mechanical and/or tribological properties of polymers by incorporation of particulate filler materials has been widely studied [1]. Under extreme friction conditions, however, conventional polymer composites usually are not effective for antiwear and friction reduction; for example, under heavy load. Nanoparticle-reinforced polymer composites are the most rapidly growing class of materials due to a good combination of high strength and modulus at very low level of loading [2]. Nanocomposites are compatible with conventional polymer processing, thus avoiding the costly lay up required for the fabrication of conventional fiber-reinforced composites. When the fillers’ sizes are on the order of nanometers, even small a concentration can

lead to enhancements in properties unprecedented in conventional composites [3]. The unique properties of polymer nanocomposites are attributed to the high filler surface area-to-volume ratio, which results in significant interfacial contact areas between the polymer and the particles. The large interfacial contact areas enable a substantial fraction of polymer segments to interact directly with the filler particles, even at low particle concentrations.

Polymer/ fullerene C<sub>60</sub> blends are an ideal system to study polymer-nanoparticles interactions since fullerene C<sub>60</sub> is monodisperse, available in high purity, and dispersible in many polymer and block copolymers [4]. The most challenging problem in the fabrication of polymer nanocomposites is dispersing the nanofillers in the polymer matrix [5]. Nanofillers strongly self-associate into ropes and other high-ordered structures which are extremely difficult to disperse in polymers. As result, the mechanical properties of polymer nanocomposites can be very far from that which was predicted [6]. Here, we use broadband dielectric spectroscopy (BDS) to directly measure the influence of fullerene C<sub>60</sub> on the polymer relaxations corresponding to different lengths and time scales. BDS is one of the most efficient tools for studying the molecular relaxations of polymers. It covers a broad frequency range, allowing measurement of different relaxation processes simultaneously, and even entire chain relaxation processes under favorable circumstances [7].

We studied the influence of fullerene C<sub>60</sub> or fullerene C<sub>60</sub> containing materials on the mechanical properties of PA6 based composites. In this paper, we report the data obtained from BDS measurements.

## 2. Experimental

### 2.1. Material and manufacturing

Fullerene C<sub>60</sub> (purity 99.9%), and fullerene soot, containing about 10.5% fullerenes, which was supplied by ZAO ILIP (Russia), were used as fillers. The fullerene soot used is an ultra dispersed carbon formed by a voltaic arc of graphite in an inert gas atmosphere during fullerene production, with particle diameters of 0.5 – 2.0 μm. Plasticizer ARMOSIL E® (AKZO NOBEL, (amide of oleic acid)) was added to the 1% C<sub>60</sub> samples to aid the C<sub>60</sub> dispersion.

The granules of PA6 (Volgamid® 32, OAO Kuibishevasot, Russia, here after B32, density 1.14 g/cm<sup>3</sup>) were used for the preparation of nanocomposites. We used a C<sub>60</sub> solution in o-xylene as the means for impregnating the granules with a calculated amount of fullerene. The fullerene soot was premixed with calculated amounts of PA6 granules for 5 min in a high-speed powder mixer. After that, the granules were dried for 5 h at 80 °C. The composite preparation was carried out in a single screw extruder (Haake Rheocord, Germany) at a screw speed of 50 rpm. Plasticizer ARMOSIL E® (AKZO NOBEL, (amide of oleic acid)) was added to the PA6 granules with 1% C<sub>60</sub> to aid the best C<sub>60</sub> dispersion. The temperature setting from the hopper to the die was 220/225/230/235 °C. During melt extrusion, ventilation was kept on to remove trapped air in materials. After pelletizing, the nanocomposite granules were dried for 5 h at 80 °C. Dried pellets were injected-molded (KM-160E injecting molding machine, KraussMaffei, Germany) into standard test species. The temperature profile setting from hopper to nozzle ranged from 200 – 215 °C and the mold temperature was kept at 25 °C. The holding pressure and screw rotation speed were 300 bar and 100 rpm respectively with throughput of 50 cm<sup>3</sup>/s. As a reference, neat PA6 was also similarly extruded and injected-molded. For dielectric measurements, nanocomposite pellets were placed and melted in a parallel-plate capacitor with 20 mm diameter; a pair of glass fiber with 80 μm diameter was used as the spacer between electrodes.

## 2.2. Mechanical properties

Tensile properties were measured in the accordance with ISO 527. Tests were conducted using  $6 \times 6 \times 40$  mm<sup>3</sup> specimens for tensile strength and Young's modulus estimation on a UTS 10 devise (UTS Test System, Germany) at an elongation rate of 2 mm/min. No less than 5 specimens were taken for each sample to obtain an average value. Shore *D* hardness test of composites were performed according to the ASTM 2240 using a Zwick/Roell Test stand 7206.200 machine. To increase the accuracy of measurement, all samples' surfaces were well polished using high-grade sandpaper prior to test. An average hardness was calculated by 10 indentation measurements.

## 2.3. Microscopy

An optical microscope, Micromed Met 400 (Micromed Met, Russia), with magnification up to  $400\times$ , was used to analyze the worn surfaces of the composites. Scanning electron microscopy (SEM) images were obtained with Zeiss ULTRAplus FEG-SEM instrument with magnification  $2.000 - 30.000\times$ .

## 2.4. Thermal properties

Differential scanning calorimetry (DSC) measurements were performed using a Netzsch DSC 204F1 instrument at a scan rate 10 K/min. The thermal gravimetric analysis (TGA) measurements were performed in an inert N<sub>2</sub> atmosphere and an oxygenated atmosphere on a NTZSCH TG 209 F1 instrument with Al<sub>2</sub>O<sub>3</sub> pan using 2 – 3 mg of nanocomposite as probe. The samples were heated 30 – 800 °C and the temperature was raised at the rate of 10 K/min.

## 2.5. Dielectric spectroscopy

Measurements were performed with an Alpha Analyzer combined with a Quatro Temperature Control system unit that provides temperature stability of 0.1 °C, both by Novocontrol. Complex dielectric permittivity  $\varepsilon^*(f) = \varepsilon'(f) - i\varepsilon''(f)$  was measured isothermally in steps of 5 °C over the temperature interval  $-150$  to  $+200$  °C and frequency range from  $10^{-2}$  to  $10^6$  Hz. Nanocomposite films were placed and melt in parallel-plate copper capacitor with 20 mm diameter, and a pair of glass fiber with 50  $\mu$ m diameter was used as the spacers between electrodes.

## 3. Results and discussion

### 3.1. Preparation of nanocomposites

The reinforcement effect in nanocomposites is very sensitive to the quality of the nanoparticle dispersion [5]. Fabrication methods are overwhelmingly focused on improving nanofiller dispersion because better filler distribution in the polymer matrices has been found to improve the nanocomposites' properties. In-situ polymerization is generally more effective than other potential methods in dispersing nanofillers in a polymer matrix due to the high viscosities of polymeric solutions and melts. Furthermore, in-situ polymerization methods enable covalent bonding between the nanofillers and the polymer matrix by using various reactions to promote compatibilization as was shown by us previously [8]. Conversely, mixing in an extruder is a more acceptable industrial method for the preparation of polymer composites. This stimulated us to use this method as a fabrication technique for the synthesis of PA6/fulleroid material nanocomposites.

As an initial level of analysis, the dispersion state of fullerene C<sub>60</sub> can be evaluated by the polymer nanocomposite's color. It is well known, that if fullerene C<sub>60</sub> is semicrystalline

or aggregated in a polymer matrix, the nanocomposite has a brownish color, while when it is well dispersed in polystyrene the color is purple, or orange when in polymethylmethacrylate (PMMA) [9]. We used a fullerene  $C_{60}$  solution in *o*-xylene as the means of impregnating the granules with a calculated amount of the fullerene  $C_{60}$  because this pathway gives much better results than pulverization [10]. As a result, the samples containing 0.01 wt.% of fullerene  $C_{60}$  after injecting molding were light cream colored. In the SEM images of these samples, one can not find any aggregates of fullerene  $C_{60}$ . However, it is well known that the results of the scattering methods regarding dispersion of nanofillers in polymers are difficult to interpret because of the low contrast, and because the precise rigid-rod behavior ( $I \propto Q^{-1}$ ) is not equivalent to good dispersion at all length scales [11]. Hence, the light cream color of the nanocomposites may give evidence that the fullerene  $C_{60}$  dispersion is not on the molecular level.

A similar way of preparing nanocomposites with 1 wt.% of fullerene  $C_{60}$  leads to aggregation of nanofillers in the polymer matrix, as seen from the SEM images. To solve this problem, we have added a plasticizer (ARMOSIL E, at 0.05 wt.%) to the composition. The decrease in viscosity of the polymer melt allows for better dispersion of the filler and the resulting nanocomposite after injection molding was light cream colored (similar to the composite with 0.01 wt.% of fullerene  $C_{60}$ ). The SEM images of these samples also did not show any aggregates of fullerene  $C_{60}$  (Fig. 1).

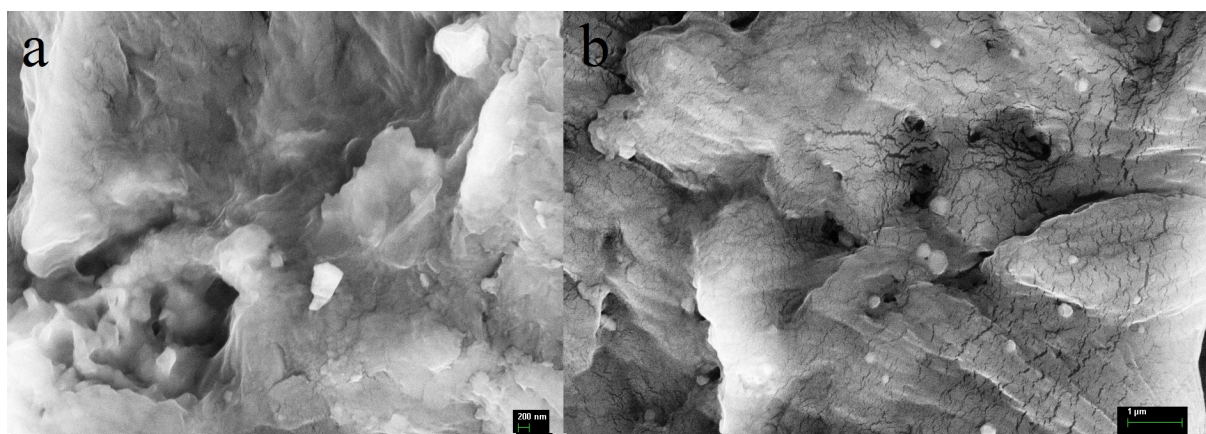


FIG. 1. SEM micrographs ( $\times 30$  k) of polymer nanocomposites: (a) with 1 wt.% of fullerene  $C_{60}$  and 0.05 wt.% of ARMOSIL E; (b) with 1 wt.% of fullerene soot

The similarity of the quality of fullerene  $C_{60}$  dispersion in both composites (with 0.01 and 1 wt.% of fullerene  $C_{60}$ ) is supported by DSC measurements. The melting temperatures of neat PA6 and the composites are nearly identical (Table 1).

To estimate the crystallinity of the samples, a value of 190.6 J/g was used for the melting enthalpy of 100% crystalline PA6 [12]. The degree of crystallinity,  $\chi$ , was calculated from the areas of the corresponding DSC melting peaks according to  $\chi = H_m / \Delta H_{100}$ , where  $\chi$  is degree of crystallinity,  $\Delta H_m$  is the peak area of the consideration, and  $\Delta H_{100}$  is the heat of fusion of 100% crystalline PA6. We have found that the crystallinity of nanocomposites is increased in comparison with neat PA6 (from 22% to 26 – 27%), independently of the fullerene  $C_{60}$  content (for nanocomposite with 1 wt.% of fullerene  $C_{60}$  this amount should be subtracted from the total mass of the composite), allowing us to neglect any differences in the fullerene  $C_{60}$  dispersion quality in both nanocomposites. A micrograph of the PA6 nanocomposite surface filled with fullerene soot (Fig. 1) demonstrates that no segregation of soot particles is observed and that

TABLE 1. Molten behavior of neat PA6 and nanocomposites

Loading, wt.%	$T_m$ (°C)	$\Delta H$ , J/g	Crystallinity, %
B32	221	42.3	22
Fullerene	$C_{60}$		
0.01	221	51.0	27
1 <sup>a</sup>	220	48.1	25
Fullerene	Soot		
1	221	45.4	24

<sup>a</sup>0.05 wt.% of ARMOSIL E (AKZO NOBEL)

they are randomly distributed in the polymer matrix. This is favorable for achieving greater matrix stiffness and consequently increases the toughening efficiency.

Thus, we see that our method for preparing the PA6/fulleroid materials is free from filler aggregation, thus allowing us to investigate the influence of pristine fulleroid filler (with no ropes and other high-ordered structures) on the properties of nanocomposites.

### 3.2. Mechanical properties

The main improvement in mechanical properties of nanocomposites relates to the large increase in modulus. Usually, an increase in the modulus of approximately 10% per wt.% filler has been observed in both in situ polymerized and melt processed PA6 nanocomposites [13]. Such an increase is too small for nanofillers which are used with much lower loadings. In our previous work, both the tensile modulus and tensile strength of in situ-polymerized PA6 composites were improved by up to 15% with a loading of 0.01 wt.% fullerene  $C_{60}$ . The tensile mechanical properties of composites under study are summarized in Table 2.

TABLE 2. Effect of loading on the mechanical properties of the polymer nanocomposites

Loading, wt.%	Young's modulus (E), GPa	Tensile strength $\sigma$ , MPa	Elongation $\varepsilon$ , %	Hardness Shore D (H)	Rigidity ( $E/H$ ) $\times 10^{-3}$	Resistance to plastic deformation ( $H^3/E^2$ ) $\times 10^5$
B32	0.693 $\pm$ 0.017	63 $\pm$ 1	290 $\pm$ 6	72.18	9.60	7.83
Fullerene	$C_{60}$					
0.01	0.714 $\pm$ 0.022	65 $\pm$ 1	301 $\pm$ 6	73.35	9.73	7.74
1 <sup>a</sup>	0.265 $\pm$ 0.037	11 $\pm$ 1	287 $\pm$ 2	48.93	5.42	1.65
Fullerene	Soot					
1	0.622 $\pm$ 0.045	62 $\pm$ 1	286 $\pm$ 14	73.06	8.51	10.15

<sup>a</sup> 0.05 wt.% of ARMOSIL E (AKZO NOBEL)

Table 2 shows that the Young's modulus, the tensile strength and elongation of the melt processed nanocomposite increase slightly at this filler loading. Furthermore, all of these parameters decrease significantly with an increase in the filler concentration. This is mainly attributed to the carbon particles aggregating easily as the filler concentration is increased. Additionally, the sample with 1% of fullerene  $C_{60}$  also contained ARMOSILIP E (0.05%) which acted as a plasticizer. The difference in the properties of neat PA6 synthesized by us [8] and commercial 32 used as the choice of polymer for extrusion can be related to effect of reprocessing [14].

The possibility of degradation is of clear importance here, since two mixing cycles are needed to produce these materials. For nanocomposites, besides the possible degradation processes associated with the matrix, additional degradation processes due to the presence of nanoparticles can occur. These processes can lead to additional degradation of the matrix induced by the presence of nanoparticles, as the latter can act as a catalyst; degradation by modification of the polymer/filler interface or degradation by collapsing and agglomeration of the nanoparticles. If any of the above processes take place to a significant extent, they would influence the mechanical properties. In our case the first two possibilities are excluded because the fullerene  $C_{60}$  prevents all free-radical degradation processes of polymers, including mechanodestruction. This was supported by the data of TGA measurements (Fig. 2). As one can see, the TGA curves for neat B32 and all nanocomposites are identical.

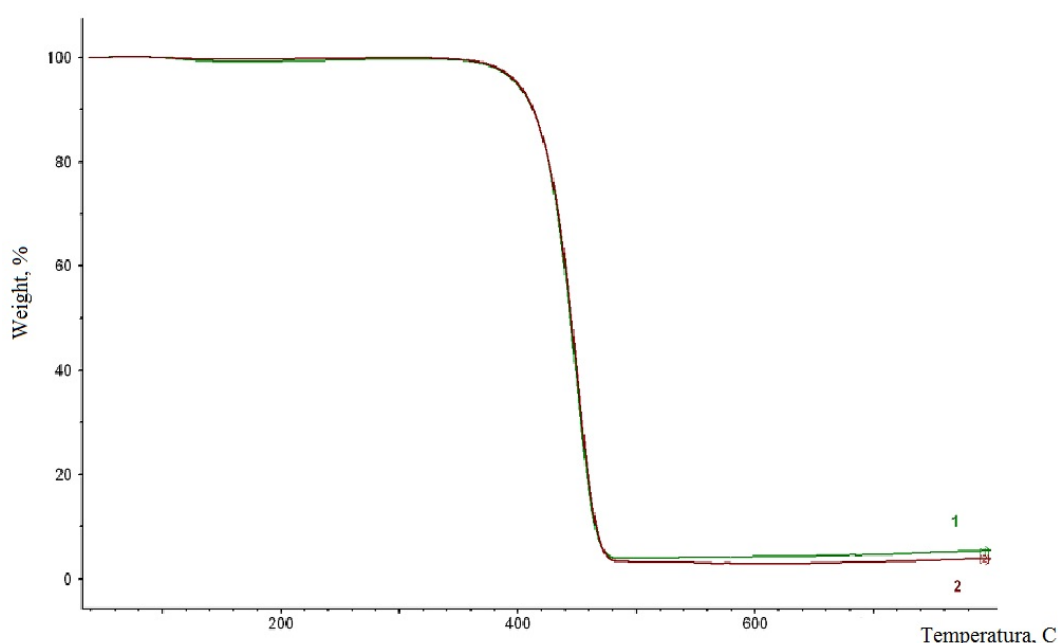


FIG. 2. TGA curve of neat PA6 (1); and with 1 wt.% of fullerene soot (2)

As can be seen from Table 2, the hardness of nanocomposites (without adding the plasticizer) increased slightly in comparison to neat PA6, which can be connected with increased crystallinity. According to conventional fracture mechanics theory, the ratio of the Young's modulus and hardness ( $E/H$  ratio) represents the rigidity of a material and the ratio  $H^3/E^2$  represents the resistance to plastic deformation. Hence, the nanocomposite with 0.01 wt.% of fullerene  $C_{60}$  added was found to be highly rigid and tough. Such spectacular increase of the overall stiffness is generally reported upon the addition of very low fractions of nanofillers (e.g., clay or phyllosilicates [15]). This remarkable improvement in mechanical properties in regard to the neat PA6, compared to conventional polymer composites with similar filler content, is attributed to the high specific area of the nanoparticles, and therefore, to the strong interactions with polymer macromolecules [16]. PA6 is a crystalline thermoplastic polymer and its crystalline structure can involve different forms which coexist in different amounts depending on the processing conditions and additives. PA6 usually crystallizes into two forms:  $\alpha$  and  $\gamma$  [17]. Although the  $\alpha$  and  $\gamma$ -forms are thermally stable, the addition of nanoparticles can induce a crystal transformation from the  $\alpha$ -form to the  $\gamma$ -form and inversely, that has

been well documented using DSC, FTIR, XRD, and NMR measurements [18]. The PA6  $\alpha$ -phase crystals were reported to exhibit a higher modulus than those of the  $\gamma$ -phase [19]. This could be one of the reasons for the enhanced properties observed in PA6 composites reinforced with various materials. The fullerene  $C_{60}$  [8] or fullerene  $C_{60}$ -like inorganic fillers [13] have an  $\alpha$ -nucleation effect on the PA6-matrix upon in situ polymerization. It was manifested as ground for reinforcing mechanism of such types of nanocomposites [20]. The thermal properties of the composites were investigated by DSC. However, fullerene  $C_{60}$  does not change the crystallization behavior of PA6 nanocomposites prepared by the extrusion method. Only the  $\alpha$ -form crystalline phase was found in B32 and the nanocomposites prepared by us. Therefore, there should be other reinforcing mechanisms. Essentially these mechanisms should involve active interactions between the fullerene  $C_{60}$  and PA6 chains.

Here, we use BDS to measure directly the influence of fullerene  $C_{60}$  on the polymer relaxations corresponding to different lengths and time scales.

### 3.3. Dielectric spectroscopy

Complex dielectric permittivity  $\varepsilon^*$  was measured over wide frequency and temperature ranges. Fig. 3 is an isochronal graph of the dielectric loss of the B32 and nanocomposites as a function of temperature.

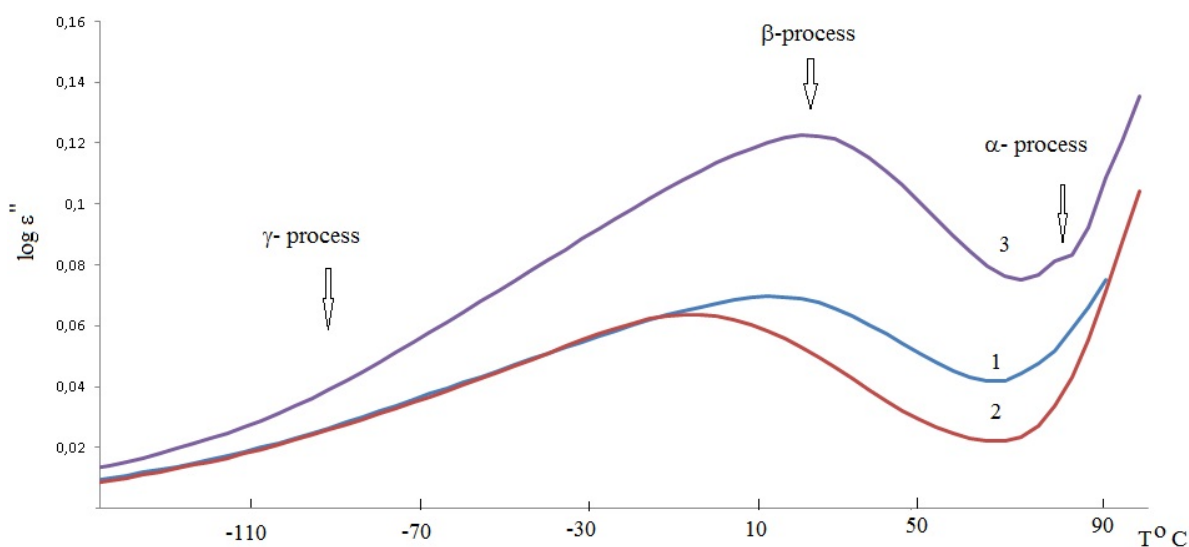


FIG. 3. Temperature dependence of imaginary part of the dielectric permittivity for neat PA6 (1); with 0.01 wt.% of fullerene  $C_{60}$  (2); with 1 wt.% of fullerene soot (3) at 1 Hz

Three relaxations can be identified in all samples. They were identified and reported for the pure PA6 [21–24]. In the present work, the effect of water on the relaxation processes is considered to be negligible, due to the initial drying of the materials prior to testing. If any small amounts of water remained in the samples, it was firmly bound water. Additionally, similar amounts of bound water should be present in all tested samples, thereby making direct comparison of the results possible.

The main characteristic of each relaxation process is the most probable relaxation time,  $\tau_{\max}$ , determined according to [25] as:

$$\tau_{\max} = \tau_{HN} \left( \frac{\sin\left(\frac{\pi\alpha\beta}{2(\beta+1)}\right)}{\sin\left(\frac{\pi\alpha}{2(\beta+1)}\right)} \right)^{\frac{1}{\alpha}} \quad (1)$$

Based on the previous experience, a model function has been fitted to the dielectric data, with the Havriliak – Negami (N-H) phenomenological relation [26]:

$$\varepsilon^*(\omega) = \varepsilon_{\infty} + \frac{\Delta\varepsilon}{(1 + (i\omega\tau_{NH})^{1-\alpha})^{\beta}}, \quad (2)$$

being the most general form. In this expression,  $\varepsilon^* = \varepsilon' - i\varepsilon''$ , is the complex dielectric function,  $\omega = 2\pi f$ ,  $f$  is the field frequency,  $\Delta\varepsilon$  is the intensity of the dielectric process,  $\tau_{NH} = 1/2\pi f_{NH}$  and  $f_{NH}$  is the position of the relaxation process on the frequency scale,  $\varepsilon_{\infty}$  is  $\varepsilon'(f)$  for  $f \gg f_{NH}$ ,  $\alpha$  and  $\beta$  are shape parameters representing the symmetrical and asymmetrical broadening of the relaxation with respect to the Debye peak. Fig. 4 displays the fits obtained when one NH term is used to fit the relaxation spectrum obtained for the nanocomposite with 0.01 wt.% of fullerene C<sub>60</sub> at 223 K. The quality of the fit is quite good and the characteristic relaxation time for each relaxation process (Fig. 4a shows  $\gamma$ -relaxation and  $\beta$ -relaxation) can be extracted.

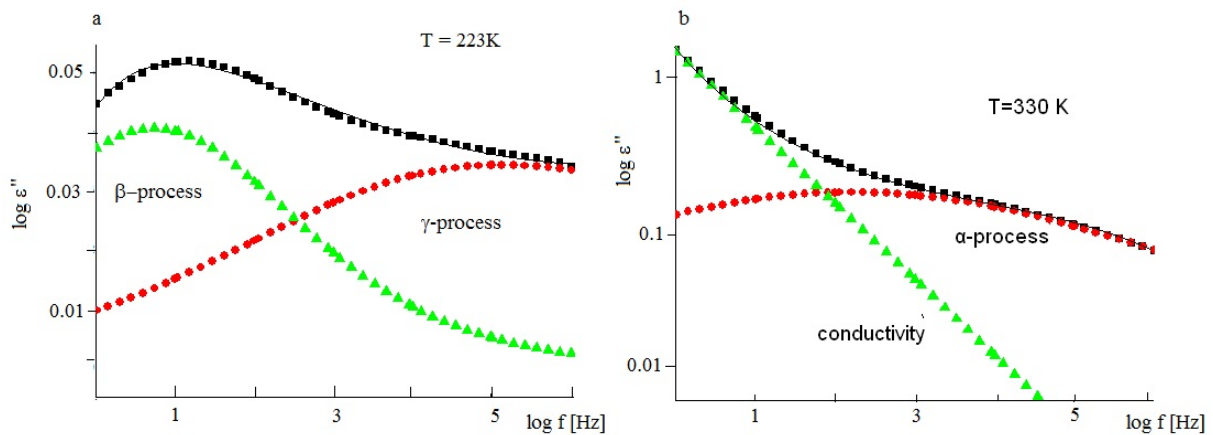


FIG. 4. Decomposition in N-H distributions of the isothermal runs of imaginary part of the dielectric permittivity for nanocomposite with 0.01 wt.% of fullerene C<sub>60</sub> sample (a) and with 1 wt.% and of fullerene C<sub>60</sub> and 0.05 wt.% of ARMOSIL E (b): (■) is experimental points; solid line is sum of calculated profiles

The  $\gamma$ - and  $\beta$ -relaxations are due to relatively shorter chain motions. The dependences of  $-\log \tau_{\max}$  on the inverse temperature are linear for all nanocomposites and neat B32 in the regions of  $\gamma$  and  $\beta$  processes (Fig. 5). As a result, the temperature dependence of these relaxations can be modeled by an Arrhenius type expression (Eq. 3) [27]:

$$\tau(T)_{\max} = \tau_0 \exp\left(\frac{E_a}{RT}\right). \quad (3)$$

Here,  $\tau_0 = \tau_{\max}$  at  $T \rightarrow \infty$ ,  $E_a$  is the activation energy. Values of  $\tau_0$  and  $E_a$  are given in Table 3.

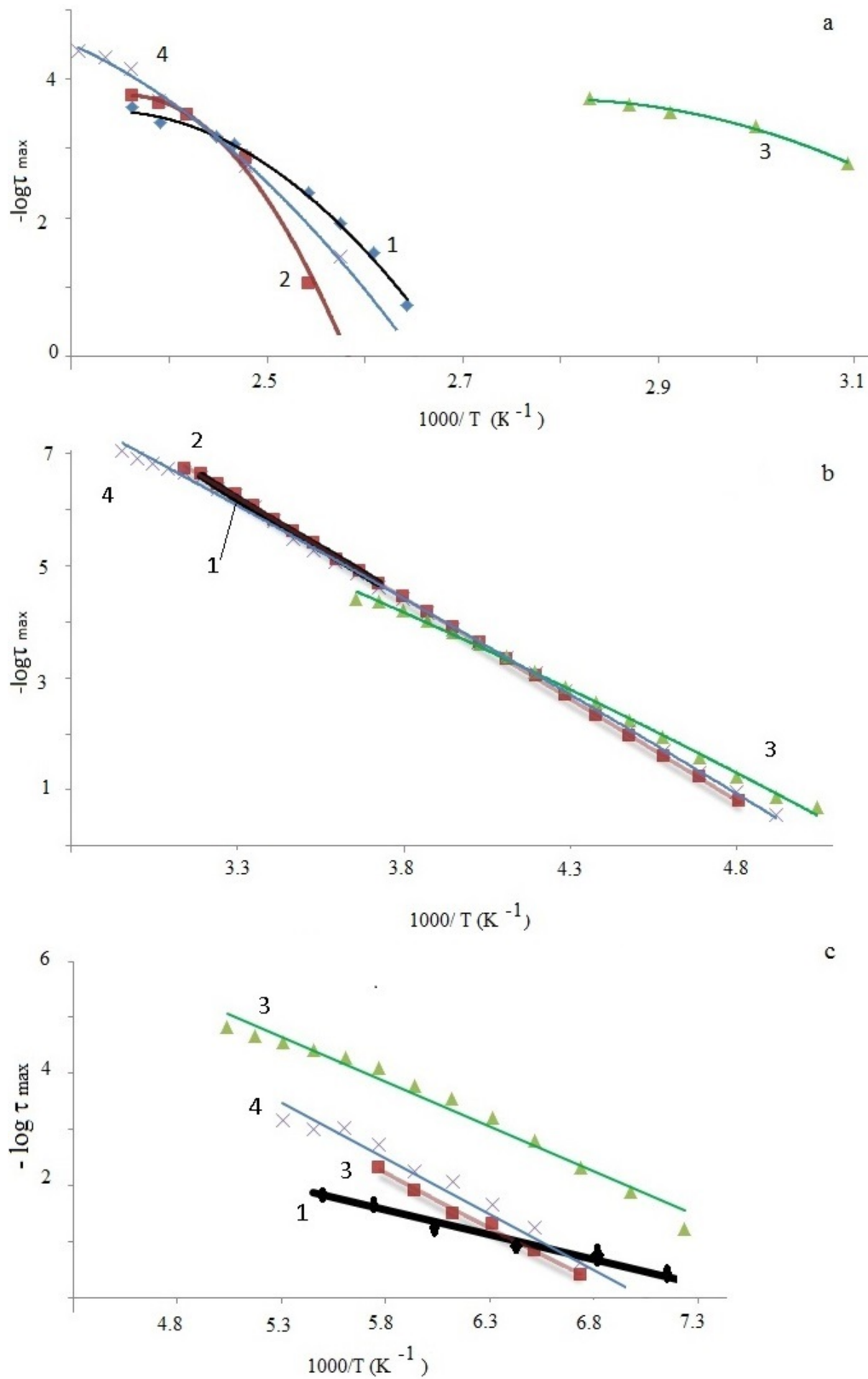


FIG. 5. Dependences of  $-\log \tau_{\max}$  on reciprocal temperature for neat PA6 (1) and nanocomposites with 0.01 wt.% of fullerene C<sub>60</sub> (2); with 1 wt.% and of fullerene C<sub>60</sub> and 0.05 wt.% of ARMOSIL E (3); with 1 wt.% of fullerene soot (4); a:  $\alpha$ -relaxation process; b:  $\beta$ -relaxation process; c:  $\gamma$ -relaxation process

TABLE 3.  $T_g$  and parameters of  $\gamma$ ,  $\beta$  and  $\alpha$  (from VFT fit) relaxation processes of neat PA6 and nanocomposites

Loading, wt.%	$E_a$ , kcal/mol	$\tau_0$ , s	$E_{VFT}$ , kcal/mol	$D$	$T_0$ , K	$T_g$ , K
B32						
$\gamma$ -mode	6.43	$1 \times 10^{-11}$	2.58			
$\beta$ -mode	15.65	$1 \times 10^{-17}$				
$\alpha$ -mode		$1.9 \times 10^{-7}$		1.18	260	360
Fullerene	0.01% C <sub>60</sub>					
$\gamma$ -mode	8.79	$1 \times 10^{-13}$				
$\beta$ -mode	16.59	$1 \times 10^{-18}$				
$\alpha$ -mode		$5.9 \times 10^{-6}$	2.59	1.14	260	360
	1% <sup>a</sup>					
$\gamma$ -mode	7.39	$1 \times 10^{-13}$				
$\beta$ -mode	13.25	$1 \times 10^{-15}$				
$\alpha$ -mode		$4.5 \times 10^{-5}$	3.42	1.55	261	335
Fullerene	Soot 1%					
$\gamma$ -mode	9.19	$1 \times 10^{-14}$				
$\beta$ -mode	15.63	$1 \times 10^{-17}$				
$\alpha$ -mode		$7.6 \times 10^{-9}$	2.65	5.02	260	360

<sup>a</sup> 0.05 wt.% of ARMOSIL E (AKZO NOBEL)

The  $\beta$ -relaxation is phenomenologically linked to the mechanical properties of polymeric materials [28,29]. From Table 3, one can see that symbatic changes of  $E_a$  and Young's modulus for the composites shows that the presence of fullerene hampers the molecular motions in the composites, leading to hardening of the polymer chains and impeding secondary relaxation processes. This explains the increase in Young's modulus for the nanocomposites. Assignment of molecular motions associated with the  $\beta$ -relaxation is complicated and a number of varying opinions exist in the literature [21–24]. However, these motions should be connected with the motion of amide groups together with neighboring methylene groups, and size of this moving unit is comparable to the size of the fullerene C<sub>60</sub> molecule. This can explain the hampering of  $\beta$ -relaxation upon introduction of such fillers.

The low temperature  $\gamma$ -relaxation involves the motion of short sequences of CH<sub>2</sub> groups connected with an amide group which provides the dielectric activity. As a result, the dependence of  $E_a$  of the  $\gamma$ -relaxation on the amount of nanofiller is quite. The tightly bound fullerene molecules create inter-chain bonds between the neighboring carbonyl groups, thus increasing the energy necessary to reorient the dipolar entities whose motion causes the  $\gamma$  process. The introduction of the plasticizer slightly blurs this dependence.

It is well known that the  $\beta$  process is related to the toughness of the polymer [25]. The nanocomposite with 1 wt.% of fullerene soot was found to be both rigid and tough (Table 2). There was a demonstrated decrease in the activation energy of the  $\beta$  process compared to that of the nanocomposite with 0.01 wt.% of fullerene C<sub>60</sub>. This indicated that carbon nanoparticles can significantly improve the energy dissipation process in the polyamide matrix. This process can lead to domination of the plastic deformation mechanism in the composite that effectively blunts

the crack trip. Hence, the suggested mechanism could be a major reason for the higher values of the resistance to plastic deformation. This mechanism is applicable to both semicrystalline and amorphous systems and is typically absent in conventional polymer composites. The decrease in the activation energy of the  $\beta$  relaxation process indicates that the mobility of polymer matrix is a pre-condition for this mechanism to be effective. In other words, the increase in toughness is proportional to the increase in the local mobility of the polymer chains, which in turn determines the nanoparticle mobility.

The  $\alpha$ -relaxation (the highest temperature relaxation in Fig. 3) is connected with onset of large-scale motions of chain segments in the vicinity of  $T_g$ . At higher temperatures near the  $\alpha$  relaxation process, heating is accompanied by creation of carriers due to ionization of impurities and the breaking of chemical bonds (e.g., the N-H bonds, etc.). Hence, it is necessary to add an additional term connected with conductivity in Eq. (2):

$$\varepsilon^*(\omega) = \varepsilon_\infty + \frac{\Delta\varepsilon}{(1 + (i\omega\tau_{NH})^{1-\alpha})^\beta} - i \left( \frac{\sigma_0}{\omega\varepsilon_0} \right). \quad (4)$$

In this equation,  $\sigma_0$  is dc conductivity and  $\varepsilon_0$  is the permittivity of free space (8.854 pF/m). Fig. 4b displays the fits obtained when two such N-H terms are used to fit relaxation spectrum obtained for the nanocomposite with 0.01 wt.% of fullerene C<sub>60</sub> at 330 K. The fitting procedure is complicated because of the presence of very often incomplete peaks, in spite of the frequency window extending over more than 8 decades. As the temperature increases, the relaxation peaks shift to higher frequencies and sweep the frequency window with different speeds characteristic of the relaxation energy of each mode. The fit is quite good and the characteristic relaxation time for the  $\alpha$ -relaxation process can be extracted. The temperature dependence of the characteristic relaxation times can then be described using the Vogel-Fulcher-Tammann equation [30]:

$$\tau = \tau_0 \exp \left( \frac{DT_0}{T - T_0} \right), \quad (5)$$

where  $\tau_0$  is the relaxation time at infinite high temperature,  $T_0$  is so-called Vogel temperature at which the relaxation time goes to infinity, and  $D$  is the parameter related to the *fragility* of material [31]. A smaller value of  $D$  implies steeper temperature dependence of the relaxation time or a more ‘fragile’ behavior. The changes in the  $D$  values for the nanocomposites show that additives such as fullerene C<sub>60</sub> enhance the fragility of glass formation related to the molecular packing efficiency of polymer materials, which is indicated physically by softening of the material in the glass state.  $E_{VTF}$  is the characteristic energy for the Vogel-Tammann-Fulcher (VTF) relaxation times and can be found as  $E_{VTF} = DT_0$ . The relaxation diagrams  $-\log \tau_{\max}$  vs.  $1/T$  are curved for the VTF dependences (Fig. 5).

The VFT energies increase with the addition of fullerene C<sub>60</sub>, but the glass transition temperature does not change. This effect is opposite to the typical result for nanofiller addition, well documented as the ‘antiplasticization’ phenomenon. In a typical antiplasticization effect, the additives will cause a decrease in the second relaxation time and an increase in the  $\alpha$  relaxation time [32]. The addition of fullerene C<sub>60</sub>, as reported in literature, can either increase or decrease the glass transition temperature of the polymer matrix [33]. In our opinion, this effect is related to the way in which fullerene C<sub>60</sub> is incorporated in the polymer matrix (for example, with formation of inclusion complexes in which the C<sub>60</sub> molecules are encapsulated within the polymer chain cavity [34]), and the quality of the filler dispersion. In the case of poor dispersion, the aggregates have act as macrofillers, leading to a decrease in the glass transition temperature of the polymer matrix.

Finally, it is clear that the complex character of the nanoparticle-polymer matrix interactions and better understanding of how nanoparticles can modify the basic polymer properties are of obvious practical, as well as scientific interest. Although the immobilization is a reasonable reinforcing mechanism and its molecular origin is well documented [27–29], a precise prediction or simulation of its extent for various composite systems still represents an intriguing unresolved problem.

#### 4. Conclusions

The following conclusions can be drawn from the present study. Fullerene C<sub>60</sub>, as a filler, improves the mechanical performance of PA6 based composite at low loading. Dielectric spectroscopy was used to investigate the influence of nanoparticles on relaxation processes in polymer matrix. The segmental relaxation processes become faster with the fullerene C<sub>60</sub> addition. In contrast, the secondary processes in PA6/ fullerene C<sub>60</sub> nanocomposites were observed to slow down with fullerene C<sub>60</sub> addition. This indicates an increase in the local ‘molecular stiffness’. Therefore, the local ‘molecular stiffness’ is increased, and the second relaxation times are phenomenologically linked to the mechanical properties, which may explain the increased Young’s moduli of nanocomposites with fullerene C<sub>60</sub> additives. These observations suggest that nanoparticles can have a qualitatively different effect on matrix polymer dynamics at different length scales, and caution must be taken when comparing changes in the dynamics associated with different relaxation processes.

#### References

- [1] Bijwe J., Logani C.M., Tewari U.S. Influence of fillers and fiber reinforcement on abrasive wear resistance of some polymeric composites. *Wear*, 1990, **138**, P. 77–92.
- [2] Treacy M.M.J., Ebesen T.W., Gibson J.M. Nanoparticles as reinforced agents. *Nature*, 1996, **381**, P. 678–680.
- [3] Strobl G. *The Physics of Polymers*. Springer, Berlin, 2007, 450 p.
- [4] Prato M. [60] Fullerene chemistry for material science applications. *J. Mater. Chem.*, 1997, **7**, P. 1097–1109.
- [5] Schaefer D.W., Justice R.S. How nano are nanocomposites. *Macromolecules*, 2007, **40**, P. 8501–8517.
- [6] Spitalsky Z., Tasis D., Papagelis K., Galiotis K. Carbon nanotube–polymer composites: Chemistry, processing, mechanical and electrical properties. *Prog. Polym. Sci.*, 2010, **35**, P. 357–401.
- [7] Adachi K., Kotaka T. Dielectric normal mode relaxation. *Progr. Polym. Sci.*, 1993, **18**, P. 585–622.
- [8] Zuev V.V., Ivanova Y.G. Mechanical and electrical properties of polyamide-6 based nanocomposites reinforced by fulleroid fillers. *Polym. Eng. Sci.*, 2012, **52**, P. 1206–1211.
- [9] Kawauchi M., Kawauchi T., Takeichi T. Solubilization of [60]Fullerene Owing to Inclusion Complex Formation between Syndiotactic Poly(methyl methacrylate) and the Fullerenes in Polar Solvents. *Macromolecules*, 2009, **42**, P. 6136–6142.
- [10] Zuev V.V., Shlikov A.V. Polyamide 12/ fullerene C<sub>60</sub> composites: investigation on their mechanical and dielectric properties. *J. Polym. Research*, 2012, **19**, P. 1–6 (9925).
- [11] Moniruzzaman M., Winey K.I. Polymer nanocomposites containing carbon nanotubes. *Macromolecules*, 2006, **39**, P. 5194–5205.
- [12] Russo P., Acierno D., Di Maio L., Demma G. Thermal and mechanical characterization of films from nylon 6/EVOH blends. *Eur. Polym. J.*, 1999, **35** (7), P. 1261–1268.
- [13] Naffakh M., Diaz-Pascual A.M., et al. Opportunities and challenges in the use of inorganic fullerene-like nanoparticles to produce advanced polymer nanocomposites. *Prog. Polym. Sci.*, 2013, **38**, P. 1163–1231.
- [14] Goitisolo I., Eguiazabal J.I., Nazabal J. Effects of reprocessing on the structure and properties of polyamide 6 nanocomposites. *Polym. Deg. Stab.*, 2008, **93**, P. 1747–1752.
- [15] Lincoln D.M., Vaia R.A., Wang Z.-G., Hsiao B.S. Secondary structure and elevated temperature crystallite morphology of nylon-6/ layered silicate nanocomposites. *Polymer*, 2001, **42**, P. 1621–1629.
- [16] Liu H., Brinson L.C. Reinforcing efficiency of nanoparticles: a simple comparison for nanocomposites. *Compos. Sci. Tech.*, 2008, **68**, P. 1502–1512.
- [17] Liu T., Phang I.Y., et al. Morphology and mechanical properties of multiwalled carbon nanotubes reinforced nylon-6 composites. *Macromolecules*, 2004, **37**, P. 7214–7222.

- [18] Wu T.M., Liao C.S. Polymorphism in nylon 6/clay nanocomposites. *Macromo. Chem. Phys.*, 2000, **201**, P. 2820–25.
- [19] Ito M., Mitsuuchi K., Kanamoto T. Effects of crystalline forms on the deformation behaviour of nylon-6. *Polymer*, 1998, **39**, P. 4593–4598.
- [20] Mesbah A., Zari F., et al. Experimental characterization and modeling stiffness of polymer/clay nanocomposites within a hierarchical multiscale framework. *J. Appl. Polym. Sci.*, 2009, **114**, P. 3274–91.
- [21] Avakian P., Matheson R.R., Starkweather H.W. Implications of dielectric response for the mechanism of changes in oxygen transport due to traces of moisture in amorphous nylons. *Macromolecules*, 1991, **24**, P. 4698–4700.
- [22] Laredo E., Grimau M., Sanchez F., Bello A. Water Absorption Effect on the Dynamic Properties of Nylon-6 by Dielectric Spectroscopy. *Macromolecules*, 2003, **36**, P. 9840–9850.
- [23] Laredo E., Hernandez M.C. Moisture effect on the low- and high-temperature dielectric relaxations in nylon-6. *J. Polym. Sci. B*, 1997, **35**, P. 2879–2888.
- [24] Frank B., Frubing P., Pissis P. Water sorption and thermally stimulated depolarization currents in nylon-6. *J. Polym. Sci. B*, 1996, **34**, P. 1853–1860.
- [25] Havriliak S., Negami S.. A complex plane analysis of  $\alpha$ -dispersions in some polymer systems. *J. Polym. Sci. C*, 1966, **14**, P. 99–117.
- [26] Havriliak S., Negami S. A complex plane representation of dielectric and mechanical relaxation processes in some polymers. *Polymer*, 1967, **8**, P. 161–210.
- [27] Allegra G., Raos G., Vacatello M. Theories and simulations of polymer based nanocomposites: from chain statistics to reinforcement. *Prog. Polym. Sci.*, 2008, **33**, P. 683–731.
- [28] Reynaud E., Jouen T., et al. Nanofillers in polymeric matrix: a study on silica reinforced PA6. *Polymer*, 2001, **42**, P. 8759–8768.
- [29] P. Ramasundaram S., Kim K.J. In-situ synthesis and characterization of polyamide 6/POSS nanocomposites. *Macromol. Symp.*, 2007, **249–250**, P. 295–302.
- [30] Kremer F., Schonhals A. *Broadband dielectric spectroscopy*. Springer, New York, 2003, 430 p.
- [31] Angell C.A., Ngai K.L., et al. Relaxation in glassforming liquids and amorphous solids. *J. Appl. Phys.*, 2000, **88**, P. 3113.
- [32] Pikhurov D.V., Zuev V.V. The effect of fullerene C<sub>60</sub> on the mechanical and dielectric behaviour of epoxy resins at low loading. *Nanosystems: Phys., Chem., Math.*, 2013, **4** (6), P. 834–843.
- [33] Wang C., Guo Z.-X. et al. Polymers containing fullerene or carbon nanotube structures. *Prog. Polym. Sci.*, 2004, **29**, P. 1079–1141.
- [34] Zuev V.V. Polymer nanocomposites containing fullerene C<sub>60</sub> nanofillers. *Macromol. Symp.*, 2011, **301**, P. 157–161.

## Structural hierarchy of $\text{NH}_4\text{V}_3\text{O}_7$ particles prepared under hydrothermal conditions

G. S. Zakharova<sup>1,2</sup>, Y. Liu<sup>3</sup>, I. S. Popov<sup>1</sup>, A. N. Enyashin<sup>1</sup>

<sup>1</sup>Institute of Solid State Chemistry UB RAS, Ekaterinburg, Russia

<sup>2</sup>Kirchhoff Institute for Physics, University of Heidelberg, Germany

<sup>3</sup>Institute of Materials Science and Engineering,

Wuhan University of Technology, PR China

enyashin@ihim.uran.ru

PACS 61.50.Ah, 61.72.Hh, 71.20.Ps

DOI 10.17586/2220-8054-2015-6-4-583-592

Despite having simple stoichiometry,  $\text{NH}_4\text{V}_3\text{O}_7$  still remains an odd compound with poorly resolved structure among the series of known ammonium vanadates. Here, a new hydrothermal synthesis of the product with explicit  $\text{NH}_4\text{V}_3\text{O}_7$  stoichiometry is evaluated. Intricate microstructure of the product is revealed as an aggregate of spherical microparticles consisting of microplatelets via scanning electron microscopy. To further guide the characterization of the  $\text{NH}_4\text{V}_3\text{O}_7$  phase, X-ray diffraction analysis and first-principle calculations were carried out to refine the structure at an atomistic level and to predict electronic properties. The results suggest a complex structural hierarchy with consequent nanodomain organization of prepared  $\text{NH}_4\text{V}_3\text{O}_7$  microplatelets.

**Keywords:** Ammonium vanadates, Hydrothermal synthesis, Microplatelets, Nanodomains, DFT calculations.

*Received: 22 June 2015*

### 1. Introduction

Mixed-valence Vanadium oxides and several of their derivatives form a wide class of functional materials for catalysts, Li-ion batteries, chemosensors, electronic and optical devices [1–3]. A rich variation of  $\text{V}^{4+}$  and  $\text{V}^{5+}$  content, the types of coordination polyhedra and their possible arrangements permit a very large variety of possible V–O frameworks and serve as great opportunity to design new advanced crystalline structures. The chemical nature of V–O frameworks enables hydrothermal (i.e. solvothermal) synthesis as the most outstanding and cost-effective method with widely varying experimental conditions for their fabrication [4,5].

The electroneutrality of a charged V–O framework can be compensated using appropriate amount of intercalated metal or complex cations, such as ammonium [6–9]. Particularly, to date, a few compounds in the family of ammonium polyvanadates are known –  $\text{NH}_4\text{V}_4\text{O}_{10}$  [9–12],  $\text{NH}_4\text{V}_4\text{O}_{14}$  [13],  $(\text{NH}_4)_2\text{V}_3\text{O}_8$  [14],  $\text{NH}_4\text{V}_3\text{O}_7$  [15]. Large  $\text{NH}_4^+$ -ions stabilize the internal pillar-like cavities within the vanadate frameworks, leading to enhanced diffusion rate of lithium ions. The latter is a necessary attribute of the cathode material for high capacity rechargeable Li-ion batteries.

Diammonium trivanadate  $(\text{NH}_4)_2\text{V}_3\text{O}_8$  crystallizes as a fresnoite structure and attracts much attention due to its magnetic properties [16,17]. Ammonium vanadium bronze,  $\text{NH}_4\text{V}_4\text{O}_{10}$  (or  $(\text{NH}_4)_{0.5}\text{V}_2\text{O}_5$ ) has a monoclinic structure. It was suggested as a potential electrode material for high capacity Li-ion batteries because of its good cyclic stability [11].  $\text{NH}_4\text{V}_4\text{O}_{10}$  showed a discharge capacity of 197.5 mAh/g remaining after 11 cycles and excellent cycling stability with the capacity retention of 81.9% after 100 cycles at 150 mAh/g [10]. Bicationic vanadium bronzes,  $(\text{NH}_4)_{0.83}\text{Na}_{0.43}\text{V}_4\text{O}_{10}\cdot 0.26\text{H}_2\text{O}$  [18] and  $(\text{NH}_4)_{0.25}\text{Na}_{0.14}\text{V}_2\text{O}_5$  [19], exhibit advanced

electrochemical properties, which might presumably be attributed to the modulation of the lattice parameters due to the co-intercalation of different cations.

Despite its simple stoichiometry,  $\text{NH}_4\text{V}_3\text{O}_7$  still remains an odd compound with a poorly resolved structure among the known ammonium vanadates. This compound has been synthesized hydrothermally using  $\text{NH}_4\text{VO}_3$ ,  $\text{CuCO}_3\cdot\text{Cu}(\text{OH})_2$  and  $\text{NH}_4\text{F}$  as precursors [15]. Yet, under the reaction conditions chosen,  $\text{NH}_4\text{V}_3\text{O}_7$  was prepared in a mixture with  $(\text{NH}_4)_2\text{V}_4\text{O}_9$  phase, which challenges some credibility of subsequent crystallographic and conductivity measurements.

In recent work, we evaluate a new hydrothermal synthesis of  $\text{NH}_4\text{V}_3\text{O}_7$  compound, which allowed the isolation of a product with explicit  $\text{NH}_4\text{V}_3\text{O}_7$  stoichiometry and with a morphology consisting of microplatelets which were assembled into spherical particles. Such a high texture does not enable us to refine the unit cell parameters. Yet, as a guide for further interpretation of the  $\text{NH}_4\text{V}_3\text{O}_7$  phase, first-principle calculations were carried out to confirm the structure at an atomistic level and to predict its electronic properties. Our calculations reveal that, fabricated  $\text{NH}_4\text{V}_3\text{O}_7$  microplatelets should have a nanodomain structure.

## 2. Experimental part

### 2.1. Chimie douce synthesis

All chemical reagents were purchased from Sigma Aldrich and used without further purification. Ammonium metavanadate  $\text{NH}_4\text{VO}_3$  was used as precursor and citric acid  $\text{C}_6\text{H}_8\text{O}_7$  was used as a mild reductant. The synthesis procedure was as follows:  $\text{NH}_4\text{VO}_3$  powder was dissolved with stirring in deionized water. Then, an appropriate amount of saturated aqueous citric acid was added drop-wise until  $4 \leq \text{pH} \leq 5.5$  is achieved. The homogenous solution was placed into a teflon-lined stainless steel autoclave and maintained at  $180\text{ }^\circ\text{C}$  for 48 hours. After cooling to room temperature, the obtained black sediment was filtered, washed with deionized water and air-dried at  $50\text{ }^\circ\text{C}$ .

### 2.2. Characterization techniques

The morphology of the powder and elemental analysis were studied by scanning electron microscope Nano-SEM (FEI) with integrated energy-dispersive X-ray microspectrometer for analysis (EDX). The product was characterized by powder X-ray diffraction (XRD) by means of Shimadzu diffractometer XRD-7000 S using  $\text{Cu K}_\alpha$  radiation. Thermogravimetry (DSC-TG) was carried out using analyzer DTA 409 PC/PG (Netzsch). The samples were heated at a rate of  $10\text{ K/min}$  up to  $800\text{ }^\circ\text{C}$  under  $\text{N}_2$ .

### 2.3. Computational details

The spin-polarized calculations of  $\text{NH}_4\text{V}_3\text{O}_7$  compound were performed within the framework of the density-functional theory (DFT) [20] using the SIESTA 2.0 implementation [21,22]. The exchange-correlation potential within the Generalized Gradient Approximation (GGA) with the Perdew-Burke-Ernzerhof parametrization was used [23]. The core electrons were treated within the frozen core approximation, applying norm-conserving Troullier–Martins pseudopotentials [24]. The valence electrons were taken as  $3d^34s^24p^0$  for V,  $2s^22p^4$  for O,  $2s^22p^3$  for N and  $1s^1$  for H. The pseudopotential core radii were chosen as  $2.34\text{ a}_B$  for  $\text{V}3d$  and  $\text{V}4s$ ,  $2.50\text{ a}_B$  for  $\text{V}4p$  states,  $1.45\text{ a}_B$  for all O states,  $1.04\text{ a}_B$  for all N states, and  $0.15\text{ a}_B$  for  $\text{H}1s$  states. In all calculations, a double- $\zeta$  polarized basis set was used. The  $k$ -point mesh was generated by the method of Monkhorst and Pack [25]. The real-space grid used for the numeric integrations was set to correspond to the energy cutoff of 300 Ry. For  $k$ -point sampling, a cutoff of  $10\text{ \AA}$  was used [26]. All calculations were performed using variable-cell and atomic

position relaxations, with convergence criteria corresponding to the maximum residual stress of 0.1 GPa for each component of the stress tensor, and the maximum residual force component of  $0.05 \text{ eV/\AA}$ .

The optimized geometry was used to calculate the XRD spectra for the radiation wavelength  $\lambda = 1.5406 \text{ \AA}$  (nickel-filtered  $\text{CuK}\alpha$  radiation). XRD spectra of nanosized  $\text{NH}_4\text{V}_3\text{O}_7$  were calculated in Debye approximation as for ensemble of monodisperse nanoparticles. The smearing of reflection profiles was approximated with correction for the isotropic atomic temperature factor and with regard to the instrumental line broadening [27].

### 3. Results and Discussion

#### 3.1. Scanning microscopy

The microstructure of synthesized ammonium trivanadate ( $\text{NH}_4\text{V}_3\text{O}_7$ ) was characterized using SEM method. The SEM data reveal an insignificant dependence of the compound's morphology on the variation of pH value in the primary reaction mixture. The samples fabricated at pH 4 consist mainly of the spherical-like particles with  $3 - 8 \mu\text{m}$  diameters (Fig. 1a). In turn, these microparticles are assembled of stochastically oriented microplatelets with thickness of  $50 - 200 \text{ nm}$  and with the characteristic edge lengths up to  $3 \mu\text{m}$  (Fig. 1b).

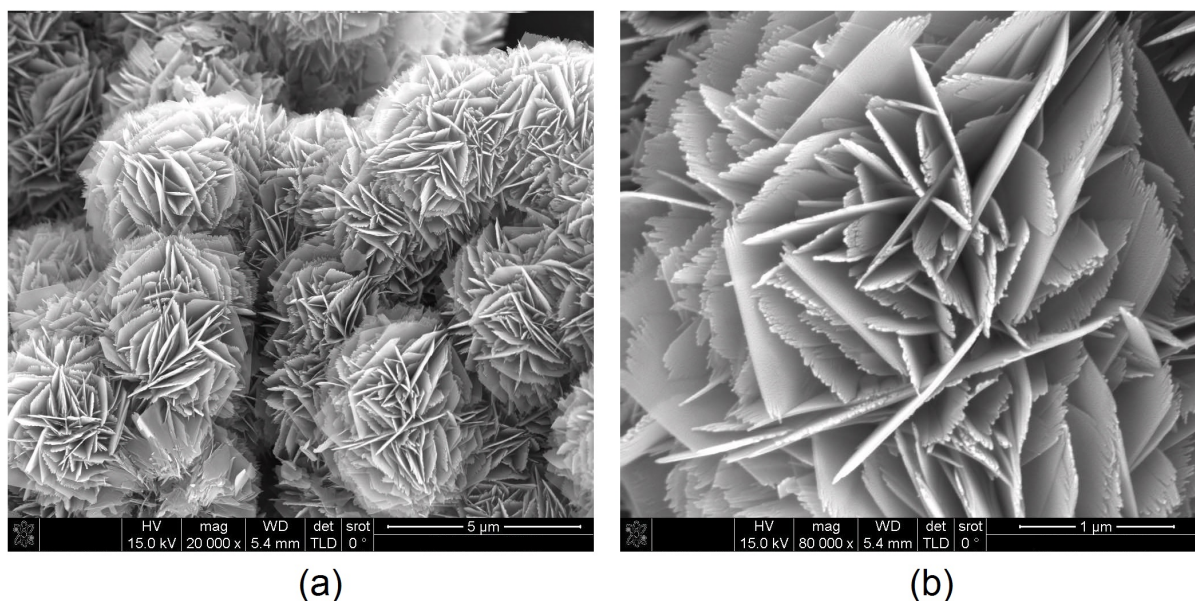


FIG. 1. SEM images of  $\text{NH}_4\text{V}_3\text{O}_7$  powder fabricated from the precursor solution with  $\text{pH} = 4$

The morphology of  $\text{NH}_4\text{V}_3\text{O}_7$  samples isolated from the less acidic precursor solutions ( $\text{pH} < 4$ ) is enriched by the separate single microplatelets. A  $\text{pH}$  value of 5.5 leads to the formation of square-like microplatelets stochastically aggregated into the particles with the diameters of  $20 - 30 \mu\text{m}$ . These platelets have the larger thickness and lengths up to  $250 - 950 \text{ nm}$  and  $5 - 15 \mu\text{m}$ , respectively.

#### 3.2. Thermogravimetric analysis

In order to determine the stoichiometry and the thermal stability of  $\text{NH}_4\text{V}_3\text{O}_7$  samples, DSC study was performed. The data of the mass loss measurements under an inert atmosphere allowed us to adjust the explicit  $\text{NH}_4\text{V}_3\text{O}_7$  stoichiometry for the prepared samples. Upon the

heating of  $\text{NH}_4\text{V}_3\text{O}_7$  powder in a stream of nitrogen, the mass loss is observed as a single stage process, which is finalized at 422 °C (Fig. 2). The decomposition of the samples is an endothermic process with the minimum corresponding to the temperature at 369 °C. In general, the decomposition of  $\text{NH}_4\text{V}_3\text{O}_7$  can be described according to the reaction

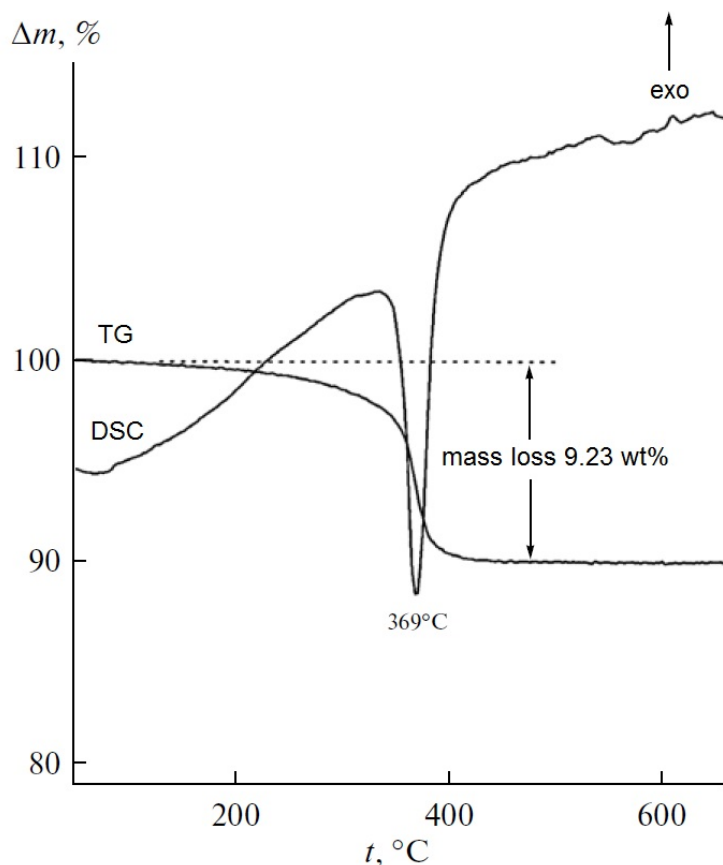
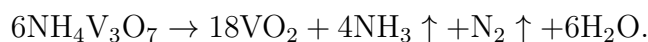


FIG. 2. TG and DSC thermogravimetric curves of  $\text{NH}_4\text{V}_3\text{O}_7$  powder decomposition under a stream of nitrogen

### 3.3. X-ray diffraction

The structure and the lattice type of experimentally observed  $\text{NH}_4\text{V}_3\text{O}_7$  phase have not been validated, yet. The former study after Trombe et al did not describe the texture of the samples in detail and no X-ray diffractogram was quoted [15]. Despite the presence of an admixture of an  $(\text{NH}_4)_2\text{V}_4\text{O}_9$  phase, the lattice parameters of  $\text{NH}_4\text{V}_3\text{O}_7$  were ascribed there to the crystal structure with its own monoclinic type and with lattice parameters of  $a = 12.198 \text{ \AA}$ ,  $b = 3.7530 \text{ \AA}$ ,  $c = 13.178 \text{ \AA}$ ,  $\beta = 100.532^\circ$ ,  $Z = 4$  (ICSD 417589). This lattice was represented as a stack of  $\text{V}_3\text{O}_7$  layers, consisting of sextuple ribbons of distorted  $\text{VO}_6$  octahedra and intercalated by ammonium cations (Fig. 3a).

XRD measurements of our samples prepared at a pH level of 4.0 – 5.5 give evidence that the crystal structure may also be described as a monoclinic phase. Yet, noticeably different lattice parameters are found:  $a = 12.247(5) \text{ \AA}$ ,  $b = 3.4233(1) \text{ \AA}$ ,  $c = 13.899(4) \text{ \AA}$ ,  $\beta = 89.72(3)^\circ$ ,

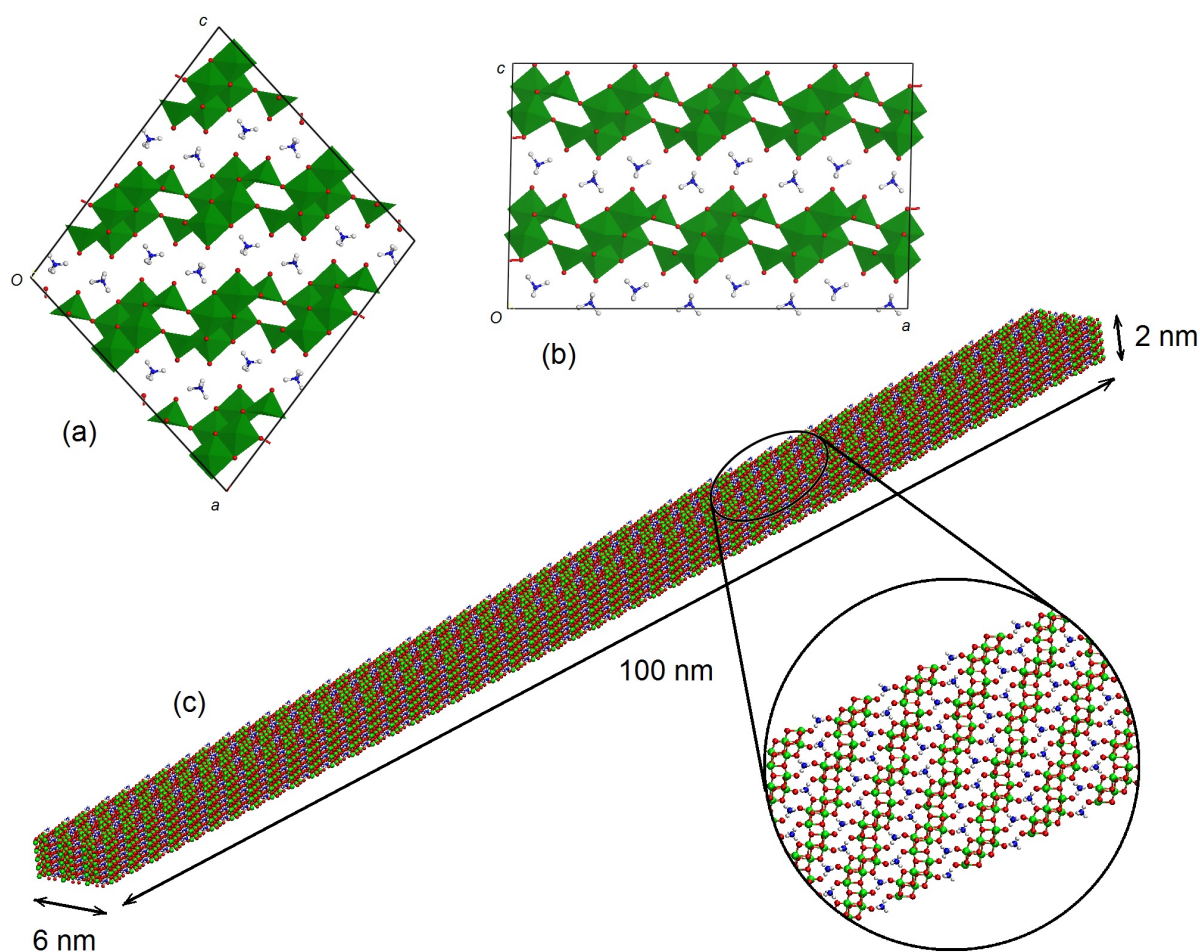


FIG. 3. Polyhedral models for DFT optimized supercells ( $Z = 16$ ) of two polytypic  $\text{NH}_4\text{V}_3\text{O}_7$  forms: (a) the most stable polytype I; (b) hypothetical and less stable polytype II (the views along  $b$ -axes are shown). Ball-and-stick model (c) demonstrates a single needle-like nanoparticle of polytype I with characteristic size  $6 \text{ nm} \times 2 \text{ nm} \times 100 \text{ nm}$  in  $a$ ,  $b$ ,  $c$  directions, respectively.

TABLE 1. Lattice parameters of  $\text{NH}_4\text{V}_3\text{O}_7$  compound concerning to experimental X-ray diffraction data in the recent work and in the work [15] versus the data for two polytypes from DFT calculations.

$\text{NH}_4\text{V}_3\text{O}_7$	$Z$	$a, \text{Å}$	$b, \text{Å}$	$c, \text{Å}$	$\beta, ^\circ$	$V, \text{Å}^3$
exp. [15]	4	12.198	3.753	13.178	100.5	593.1
exp. here	4	12.247	3.423	13.899	89.72	582.3
calc. here polytype I	4	12.211	3.832	12.886	97.8	597.5
calc. here polytype II	4	16.652	3.841	10.204	88.8	652.5

$V = 582.3(4) \text{ Å}^3$  (Table 1). At pH values  $> 5.5$ , the product possesses an admixture of  $\text{NH}_4\text{V}_4\text{O}_{10}$  compound (JCPDS 031-0075) and was not considered henceforth.

Our data suggest that the  $\text{NH}_4\text{V}_3\text{O}_7$  compound, as prepared in a recent work, should have a layered structure composed of  $(\text{V}_3\text{O}_7)$ -layers with an orientation within  $(10\bar{1})$  planes.

Regretably, further XRD structure refinement of our highly textured  $\text{NH}_4\text{V}_3\text{O}_7$  microparticles did allow a detailed view of the internal structure of the lattice. The discrepancy between our data and the previously-obtained data [15] may be attributed either to the poor characterization of highly textured samples or to the formation of a new polymorph. Hence, the first-principle calculations were employed to explore both options and to judge the crystal motif of  $\text{NH}_4\text{V}_3\text{O}_7$ .

### 3.4. Possible polytypism of $\text{NH}_4\text{V}_3\text{O}_7$

Many layered compounds are inclined to a rich polytypism due to unrestrained combination of layers' stacking. To explain the discrepancy between the recent data and earlier data [15], we surmised that another possible crystalline structure, based on the same type of  $\text{V}_3\text{O}_7$  layers may exist. Like the crystal motif suggested by Trombe et al. [15] (hereafter polytype I, Fig. 3a), the hypothetical  $\text{NH}_4\text{V}_3\text{O}_7$  polymorphic modification can be based on the same type of  $\text{V}_3\text{O}_7$  layers, yet, with every second layer shifted on  $b/2$  along [010] direction (polytype II, Fig. 3b). To validate the structure of both polytypes, optimization of their geometry has been carried out and their relative stability has been analyzed using DFT calculations.

Our DFT results are encouraging, showing that the crystal structure of polytype I has the lowest total energy and is the most stable. However, the energy of polytype II is only on 0.14 eV/ $\text{NH}_4\text{V}_3\text{O}_7$  higher than that of polytype I. Such a minor energy difference suggests the existence of at least these two polytypes or even a number of intermediate  $\text{NH}_4\text{V}_3\text{O}_7$  polytypes. The presence of numerous random dislocations along [010] direction may be not excluded, too.

The accurate first-principle calculations permit crystallographic parameter determination for both  $\text{NH}_4\text{V}_3\text{O}_7$  polytypes and comparison of them with experimental data (Table 1). Both experimental datasets do not reproduce the crystallographic properties found for hypothetical polytype II. Yet, the lattice parameters of the most stable  $\text{NH}_4\text{V}_3\text{O}_7$  polytype I may be reliably attributed to and can be found in fair agreement with former experimental values of Trombe et al. [15]. The largest deviation between calculated and these experimental lattice parameters does not exceed 2%. Thus, our experimental data cannot be seemingly assigned to the most stable crystalline phase of  $\text{NH}_4\text{V}_3\text{O}_7$ .

A more detailed insight into the structure of our highly textured samples can be performed by the comparison of experimental X-ray diffractograms with those simulated using the geometries resulted from DFT calculations. Again, theoretical diffractogram of polytype II does not reveal any similarity with the experimental data (Fig. 4). Nonetheless, theoretical diffractogram of polytype I also showed a remarkable difference. Particularly, it contains very strong reflexes missing on our experimental diffractogram at angles  $2\theta = 24^\circ$ ,  $46^\circ$  and, in general, it has a more fine profile. Such a mismatch is a clear indication of poor crystallinity for our  $\text{NH}_4\text{V}_3\text{O}_7$  product. We may surmise that the microplatelets, assembling the spherical particles of our product, should have their own internal organization at the nanoscale; e.g., every microplatelet could be an aggregate of nanoparticles or could have a nanodomain structure.

In addition, X-ray diffraction spectra of  $\text{NH}_4\text{V}_3\text{O}_7$  samples have been simulated as for the sets of monodisperse free-standing nanoparticles or nanodomains of polytype I. Routine fitting has been performed for a wide range of sizes and for several possible morphologies (compact 0D particles, 2D films, 1D needles). Despite the simplicity of all of these models, neglecting the lattice strain and possible surface reconstructions, an evident coincidence with our experimental data has been found for the case of needle-like nanoparticles with characteristic size  $6 \text{ nm} \times 2 \text{ nm} \times \sim 100\text{--}500 \text{ nm}$  along  $a$ ,  $b$ ,  $c$  directions, respectively (Fig. 3c). Some of the peaks on the profile of simulated XRD spectrum may be found as slightly shifted to the lower angles  $2\theta$ , since our DFT calculations may overestimate interlayer distances.

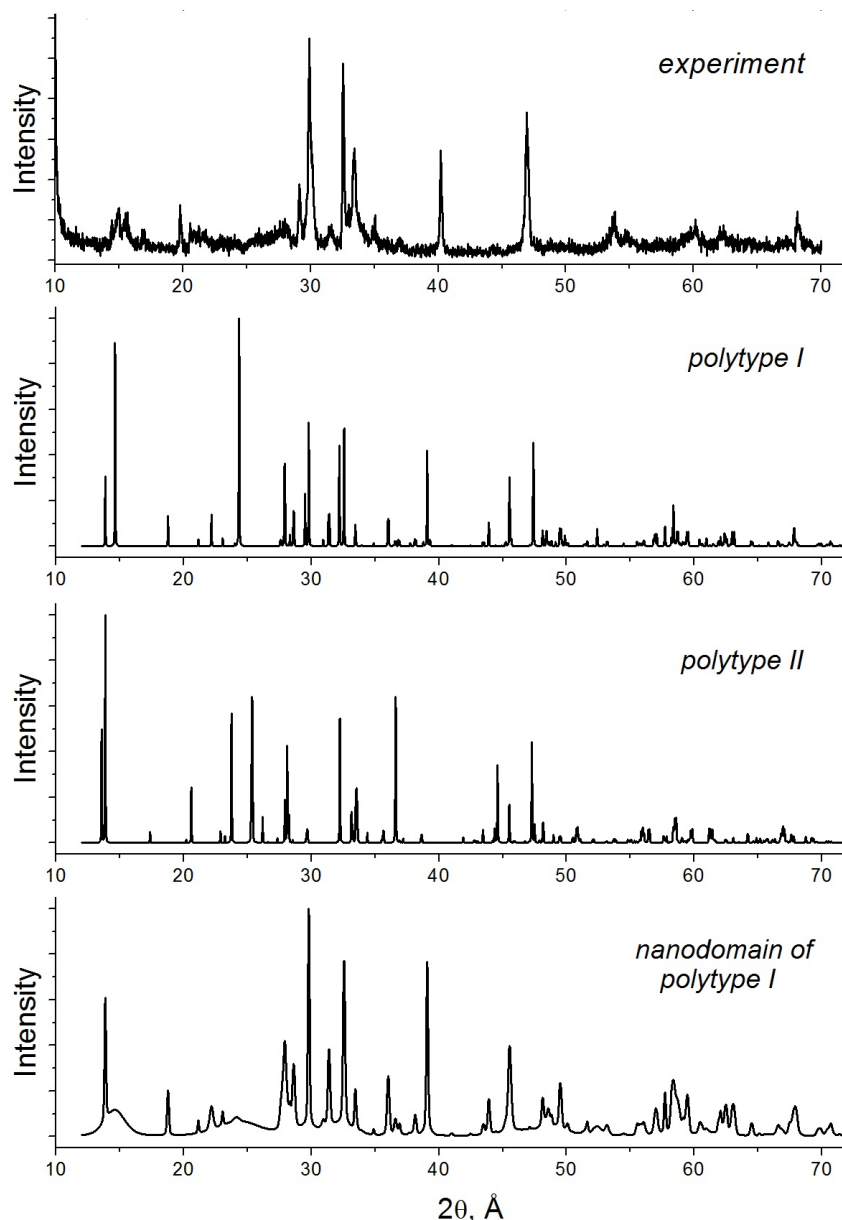


FIG. 4. Comparison between X-ray diffractograms for  $\text{NH}_4\text{V}_3\text{O}_7$  compound as observed for the samples fabricated in this work and as theoretically predicted for the monocrystals of two  $\text{NH}_4\text{V}_3\text{O}_7$  polytypic forms (I and II) and for a single needle-like nanodomain of polytype I with characteristic size of  $6 \text{ nm} \times 2 \text{ nm} \times \sim 100 \text{ nm}$  along  $a$ ,  $b$ ,  $c$  directions, respectively.

Thus, DFT calculations suggest that experimental XRD data, as obtained from our highly textured samples, should be not treated as for the monocrystal. The structural hierarchy of  $\text{NH}_4\text{V}_3\text{O}_7$  compound can be drastically enriched at the nanolevel. The  $\text{NH}_4\text{V}_3\text{O}_7$  microplatelets may have interim nanodomain structure, as the grains of polytype I and numerous low-energy dislocations, as the grain boundaries. As well, they might be assembled of free-standing  $\text{NH}_4\text{V}_3\text{O}_7$  nanoneedles. Further investigation by means of high-resolution electron microscopy could resolve the structural hierarchy of our samples in greater detail.

### 3.5. Electronic properties of $\text{NH}_4\text{V}_3\text{O}_7$

DFT calculations enable us to give prior information about the electronic properties of  $\text{NH}_4\text{V}_3\text{O}_7$  compound. The electronic density of states calculated for the most stable polytype I is visualized in Fig. 5. The studied compound,  $\text{NH}_4\text{V}_3\text{O}_7$ , should be a magnetic semiconductor with a band gap of  $\sim 0.83$  eV. The bottom of splitted conduction band has a dominant  $\text{V}3d$ -character. The top of valence band is also formed by  $\text{V}3d$ -states with an admixture of  $\text{O}2p$ -states, while the remaining wide part of the band at  $-2 \dots -6$  eV is composed predominantly of  $\text{O}2p$ -states. The deep and separated valence band at  $-7 \dots -9$  eV is formed by the mixture of  $\text{N}2p$  and  $\text{H}1s$  states.

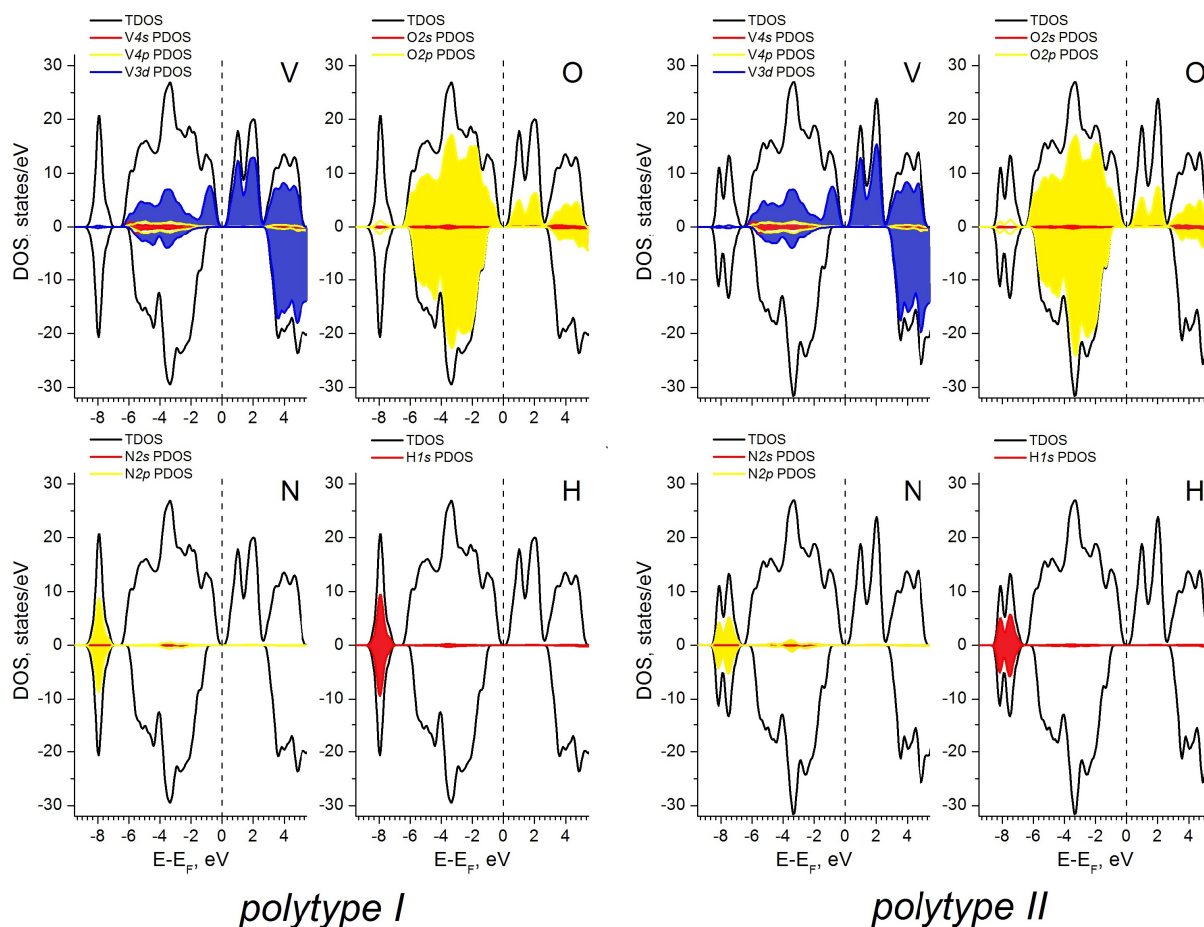


FIG. 5. Total and partial densities-of-states (DOS) for two polytypic  $\text{NH}_4\text{V}_3\text{O}_7$  phases. DFT calculations.

Analysis of the Mulliken charge distribution indicates that two groups of V atoms can be distinguished, with the charges  $+1.11$  and  $+1.14$  respectively. These groups differ in the environment of their second coordination shell. The first group of four V atoms is placed within the middle of a  $\text{V}_3\text{O}_7$  sextuple ribbon as  $\text{VO}_6$  octahedra with shared edges. The second group of two V atoms is placed at the edges of this ribbon as  $\text{VO}_6$  octahedra sharing their vertices with equivalent  $\text{VO}_6$  octahedra of the neighboring ribbon. The coordination polyhedra of the latter group have a heavily distorted geometry, with one of V–O distances at  $2.44 \text{ \AA}$ , the largest of the group. The spin-polarization calculations indicate a magnetization of the compound with the spin density redistribution at the V atoms. The estimated magnetic moments within aforementioned groups of V atoms were found to be  $2.40$  and  $1.73 \mu_B$ .

The charge distribution among the O atoms is wider, yet, a few groups of atoms can be distinguished, depending mainly on the coordination number:  $-0.42$ ,  $-0.49 \dots -0.60$  and  $-0.54 \dots -0.66$  for O atoms within vanadyl groups, for bridging double and for triple coordinated O atoms, respectively. The charges on every N and every H atom are equal to  $-0.68$  and  $+0.28$ , respectively, which amounts to the total formal charge of  $\text{NH}_4^+$  cation as equal to  $+0.44$ .

The results of DFT calculations for polytype II show that the overall qualitative picture of the density of states is preserved (Fig. 5). Both considered  $\text{NH}_4\text{V}_3\text{O}_7$  polytypes should be magnetic semiconductors. In general, the charge distribution and the DOS picture of both polytypes explicitly correspond to the formation of covalent V–O and N–H bonding within anionic  $\text{V}_3\text{O}_7$  framework and ammonium  $\text{NH}_4$  cations. The relative position of dominating  $\text{V}3d\text{--O}2p$  and  $\text{N}2p\text{--H}1s$  overlaps in the valence band gives evidence for a highly versatile  $\text{V}_3\text{O}_7$  network for redox reactions as well as a low ability of  $\text{NH}_4$  cations for reduction, e.g. using alkali metal atoms.

#### 4. Summary

In summary, a facile chimie douce route was evaluated to produce highly textured product of pure ammonium trivanadate  $\text{NH}_4\text{V}_3\text{O}_7$  from the corresponding metavanadate  $\text{NH}_4\text{VO}_3$  as precursor and citric acid  $\text{C}_6\text{H}_8\text{O}_7$  as a mild reductant. The intricate structure of the product was characterized by the combination of experimental SEM, XRD and computational DFT techniques, which uncover a complex structural hierarchy of synthesized  $\text{NH}_4\text{V}_3\text{O}_7$ .

SEM data has revealed the microstructure as an aggregation of spherical-like particles with the diameters of  $\sim 30 \mu\text{m}$ , assembled of stochastically oriented nanoplatelets with thicknesses of  $50 - 200 \text{ nm}$  and edge lengths up to  $2 \mu\text{m}$ . Yet, the values of the lattice parameters derived using recent XRD data and upon assumption of crystalline  $\text{NH}_4\text{V}_3\text{O}_7$  were found to be quite different from previous experimental and recent DFT data. Assuming a domain-like organization of synthesized  $\text{NH}_4\text{V}_3\text{O}_7$ , X-ray diffractograms have been routinely simulated for a wide range of the size and for several possible domain morphologies. Indeed, it suggests even a more deep organization of  $\text{NH}_4\text{V}_3\text{O}_7$  microparticles at the nanoscopic level. Most likely, the lattice of  $\text{NH}_4\text{V}_3\text{O}_7$  studied in this work tends towards the formation of low-energy dislocations or twinning along  $[010]$  direction, which is a prerequisite for the emergence of needle-like nanodomains or a very rich polytypism.

A further study of  $\text{NH}_4\text{V}_3\text{O}_7$  by means of high-resolution electron microscopy could prove the structural hierarchy in more detail. Though, relying on DFT calculations, we predict that the electronic and chemical properties of layered  $\text{NH}_4\text{V}_3\text{O}_7$  would be not altered, even by possible domain-like organization. Two most prominent  $\text{NH}_4\text{V}_3\text{O}_7$  polytypes should be magnetic semiconductors with band gaps of  $\sim 0.8 \text{ eV}$ . Irrespective of their lattice arrangement, the anionic  $\text{V}_3\text{O}_7$  framework should be highly versatile in redox reactions, while  $\text{NH}_4^+$  cations should demonstrate a low ability for reduction, e.g. with alkali metal atoms.

#### Acknowledgments

The support from the Ministry of Science and Education of Russian Federation (unique project identifier RFMEF161314X0002) is gratefully acknowledged.

#### References

- [1] Wu C., Xie Y. Promising Vanadium Oxide and Hydroxide Nanostructures: From Energy Storage to Energy Saving. *Energy & Environmental Science*, 2010, **3**, P. 1191–1206.
- [2] Hellmann I., Zakharova G.S., et al. Static Susceptibility and Heat Capacity Studies on  $\text{V}_3\text{O}_7 \cdot \text{H}_2\text{O}_7$  Nanobelts. *Journal of Magnetism and Magnetic Materials*, 2010, **322**, P. 878–881.

- [3] Strelcov E., Lilach K., Kolmakv A. Gas Sensor Based on Metal-Insulator Transition in VO<sub>2</sub> Nanowire Thermistor. *Nano Letters*, 2009, **9**, P. 2322–2326.
- [4] Wang Y., Cao G.Z., Synthesis and Enhanced Intercalation Properties of Nanostructured Vanadium Oxides. *Chemistry of Materials*, 2006, **18**, P. 2787–2804.
- [5] Balakhonov S.V., Ivanov V.K., Baranchikov A.E., Churagulov B.R. A comparative analysis of physicochemical properties of vanadium-oxide nanomaterials fabricated via hydrothermal and microwave-hydrothermal methods. *Nanosystems: physics, chemistry, mathematics*, 2012, **3**, P. 66–74.
- [6] Rao K.J., Ramakrishnan P.A., Gadagkar R. Microwave Preparation of Oxide Bronzes. *Journal of Solid State Chemistry*, 1999, **148**, P. 100–107.
- [7] Xu Y., Han X.S., et al. Pillar Effect on Cyclability Enhancement for Aqueous Lithium Ion Batteries: a New Material of  $\beta$ -vanadium bronze M<sub>0.33</sub>V<sub>2</sub>O<sub>5</sub> (M = Ag, Na) nanowires. *Journal of Materials Chemistry*, 2011, **21**, P. 14466–14472.
- [8] Oka Y., Yao T., Yamamoto N. Crystal Structures and Lattice Distortions of  $\sigma$ -Type Layered Vanadium Bronzes:  $\sigma$ -M<sub>0.25</sub>V<sub>2</sub>O<sub>5</sub>·H<sub>2</sub>O (M=Mg, Co, Ni). *Journal of Solid State Chemistry*, 1999, **144**, P. 181–187.
- [9] Wu X., Tao Y., Dong L., Hong J. Synthesis and Characterization of Self-ling (NH<sub>4</sub>)<sub>0.5</sub>V<sub>2</sub>O<sub>5</sub> Nanowires. *Journal of Materials Chemistry*, 2004, **14**, P. 901–904.
- [10] Wang H., Huang K., et al. (NH<sub>4</sub>)<sub>0.5</sub>V<sub>2</sub>O<sub>5</sub> Nanobelt with Good Cycling Stability as Cathode Material for Li-ion Battery. *Journal of Power Sources*, 2011, **196**, P. 5645–5650.
- [11] Zhang K.-F., Zhang G.-Q., et al. Large Scale Hydrothermal Synthesis and Electrochemistry of Ammonium Vanadium Bronze Nanobelts. *Journal Power Sources*, 2006, **157**, P. 528–532.
- [12] Wang N., Chen W., Mai L., Dai Y. Selected-Control Hydrothermal Synthesis and Formation Mechanism of 1D Ammonium Vanadate. *Journal of Solid State Chemistry*, 2008, **181**, P. 652–657.
- [13] Zhou R., Zhang Z., et al. Oriented Free-Standing Ammonium Vanadium Oxide Nanobelt Membranes: Highly Selective Absorbent Materials. *Chemistry – A European Journal*, 2010, **16**, P. 14307–14312.
- [14] Ren T.-Z., Yuan Z.-Y., Zou X. Crystal Growth of Mixed-Valence Ammonium Vanadates. *Crystal Research and Technology*, 2007, **42**, P. 317–320.
- [15] Trombe J.C., Szajwaj O., Salles P., Galy J. Synthesis of New Mixed Valence Compounds MV<sup>5+</sup>V<sub>2</sub><sup>4+</sup>O<sub>7</sub> (M = NH<sub>4</sub>, K): Crystal Structure of NH<sub>4</sub>V<sub>3</sub>O<sub>7</sub> and Electrical Properties of KV<sub>3</sub>O<sub>7</sub>. *Journal of Solid State Chemistry*, 2007, **180**, P. 2102–2109.
- [16] Theobald F.R., Theobald J.-G., Vedrine J.C., Clad R., Renard J. Crystal Growth, Structure, Electron Paramagnetic Resonance and Magnetic Properties of (NH<sub>4</sub>)<sub>2</sub>V<sub>3</sub>O<sub>8</sub>. *Journal of Physics and Chemistry of Solids*, 1984, **45**, P. 581–587.
- [17] Liu G., Greedan J.E. Magnetic Properties of Fresnoite-Type Vanadium Oxides: A<sub>2</sub>V<sub>3</sub>O<sub>8</sub> (A = K, Rb, NH<sub>4</sub>). *Journal of Solid State Chemistry*, 1995, **114**, P. 499–505.
- [18] Fei H., Shen Z., et al. Flower-like (NH<sub>4</sub>)<sub>0.83</sub>Na<sub>0.43</sub>V<sub>4</sub>O<sub>10</sub>·0.26H<sub>2</sub>O Nano-structure for Stable Lithium Battery Electrodes. *Journal of Power Sources*, 2009, **189**, P. 1164–1166.
- [19] Fei H.-L., Shen Z.R., et al. Novel Bi-Cation Intercalated Vanadium Bronze Nano-structures for Stable and High Capacity Cathode Materials. *Electrochemistry Communications*, 2008, **10**, P. 1541–1544.
- [20] Hohenberg P., Kohn W. Inhomogeneous Electron Gas. *Physical Review B*, 1964, **136**, P. 864–871.
- [21] Ordejon P., Artacho E., Soler J.M. Self-Consistent Order-N Density-Functional Calculations for Very Large Systems. *Physical Review B*, 1996, **53**, R10441.
- [22] Soler J.M., Artacho E., et al. The SIESTA Method for ab initio Order-N Materials Simulation. *Journal of Physics: Condensed Matter*, 2002, **14**, P. 2745–2779.
- [23] Perdew J.P., Burke K., Ernzerhof M. Generalized Gradient Approximation Made Simple. *Physical Review Letters*, 1996, **77**, P. 3865–3868.
- [24] Troullier N., Martins J.L. Efficient Pseudopotentials for Plane-Wave Calculations. *Physical Review B*, 1991, **43**, P. 1993–2006.
- [25] Monkhorst H.J., Pack J.D. Special Points for Brillouin-Zone Integrations. *Physical Review B*, 1976, **13**, P. 5188–5192.
- [26] Moreno J., Soler J.M. Optimal Meshes for Integrals in Real- and Reciprocal-Space Unit Cells. *Physical Review B*, 1992, **45**, P. 13891–13898.
- [27] Caglioti G., Paoletti A.B., Ricci F.P. Choice of Collimators for a Crystal Spectrometer for Neutron Diffraction. *Nuclear Instruments and Methods in Physics Research*, 1958, **3**, P. 223.

## Nanodisperse oxide compounds of iron formed in the $\text{FeSO}_4 - \text{KOH} - \text{H}_2\text{O} - \text{H}_2\text{O}_2$ system ( $4.0 \leq \text{pH} \leq 13.0$ )

D. A. Zherebtsov<sup>2</sup>, V. Sh. Mirasov<sup>2</sup>, D. G. Kleschev<sup>2</sup>, E. V. Polyakov<sup>1</sup>

<sup>1</sup>Institute of Solid State Chemistry of the Ural Branch of the Russian Academy of Sciences, Ekaterinburg, Russia

<sup>2</sup>South Ural State University (National research university), Chelyabinsk, Russia

zherebtsov\_da@yahoo.com, mirasov@gmail.com,  
dgk1950dgk@mail.ru, rupolyakov@ihim.uran.ru

**PACS 68.55.A**

**DOI 10.17586/2220-8054-2015-6-4-593-604**

The regularities of phase formation during oxidation of aqueous solutions of  $\text{FeSO}_4$  and (or) suspensions of  $\text{Fe}(\text{OH})_2$  at quasi-constant temperature and pH values have been studied for wide intervals of temperature (20 – 85 °C) and (4.0 – 13.0) of the reaction medium. The produced nanodisperse materials have been examined by X-ray phase analysis, IR spectroscopy, scanning electron microscopy and X-ray fluorescence analysis, as well as by thermogravimetric analysis combined with thermal analysis and mass spectrometric analysis of released gases. The dependences of the phase, chemical and disperse compositions of the formed precipitates on the synthesis parameters have been revealed.

**Keywords:**  $\text{FeSO}_4$  solutions;  $\text{Fe}(\text{OH})_2$  suspensions; hydrogen peroxide oxidation; oxide compounds of iron(III).

*Received: 2 May 2015*

*Revised: 13 May 2015*

### 1. Introduction

The oxidation of iron(II) salt solutions and (or) iron(II) hydroxide suspensions leads to the formation of poorly soluble nanodisperse iron(III) compounds exhibiting peculiar and in some cases unique ion-exchange, sorption, magnetic, catalytic and other properties [1–5], attracting much interest of specialists in many different fields. It is established [2, 3, 5–12] that the phase and disperse compositions of these compounds depend on numerous synthetic parameters: the temperature and pH of the reaction medium, concentration of iron(II) ions in solution and of  $\text{Fe}(\text{OH})_2$  in suspension, the nature of salt anion and alkaline agent cation, the presence of uncontrolled or specially introduced impurities in the solution, as well as the feed rate and activity of oxidizing agent. Until now, the question as to which parameters have a determining influence on the phase and disperse compositions of the formed iron(III) compounds remains a point for debate, which restrains the introduction of advanced technologies for the reproducible preparation of products with optimal functional properties.

The aim of this work is to obtain more accurate information about the regularities of phase formation during the oxidation of aqueous solutions of  $\text{FeSO}_4$  and (or) suspensions of  $\text{Fe}(\text{OH})_2$  at quasi-constant values of temperature, total iron(II) concentration in solution (suspension), of reaction medium and average oxidation rate in case the solid solutions K and  $\text{H}_2\text{O}_2$  are used as alkaline and oxidizing agents, respectively (hereafter the system  $\text{FeSO}_4 - \text{H}_2\text{O} - \text{KOH} - \text{H}_2\text{O}_2$ ).

## 2. Experimental

The following reagents were used for synthesis: 1.1 M solution of  $\text{FeSO}_4$  in distilled water, which was preliminarily reduced by iron powder; 3.8 M KOH and 0.9 M  $\text{H}_2\text{O}_2$  solutions in distilled water. All the reagents were chemically pure. Oxidation was carried out in a 0.5 dm<sup>3</sup> cylindrical reactor furnished with a mixer, electric heating, thermostating, continuous KOH and  $\text{H}_2\text{O}_2$  solutions dosing and measuring systems.

In all the experiments, the average oxidation rate of iron(II) ions,  $15 \pm 1$  mmol/(dm<sup>3</sup>·min), and the total concentration of Fe(II) and Fe(III) in oxidized suspension,  $0.51 \pm 0.02$  mol/dm<sup>3</sup>, were maintained constant, while the temperature  $t$  and pH were varied. The experiments were performed in the following sequence: the calculated amount of  $\text{FeSO}_4$  solution was poured into the reactor and heated to preset temperature  $t$  (20, 40, 60 or 85 °C); the required pH value of the reaction medium<sup>1</sup> (4.0; 5.5; 6.5; 8.5; 10.5 or 13.0) was achieved by feeding the KOH solution. After that, the  $\text{H}_2\text{O}_2$  solution was added at a constant rate into the reactor, and in the interval  $4.0 \leq t < 9.0$  the KOH solution was also added to maintain a quasi-constant pH value ( $\pm 0.25$ ). Note that over time, the temperature of the reaction medium gradually increased by  $\Delta t \approx 5$  °C<sup>2</sup> in all the experiments. At the conclusion of oxidation, the precipitate was separated from the mother solution on a Buchner funnel and washed with water until the filtrate contained no sulfate ions; then, it was dried until constant mass at  $\sim 50$  °C and ground.

The obtained samples were examined by X-ray phase analysis (XPA; DRON-3 X-ray unit with digital data recording attachment; filtered  $C_{K\alpha}$  radiation; the powder diffraction electronic database ICSD was used). The average size of the precipitate crystals,  $d$ , was calculated by the Debye formula from the physical broadening of reflections<sup>3</sup>. The samples obtained at fixed values of  $t = 40$  °C ( $4.0 \leq \text{pH} \leq 13.0$ ) and  $\text{pH} = 6.5$  ( $20$  °C  $\leq t \leq 85$  °C) were also studied on a scanning electron microscope JEOL JSM-7001F with an energy-dispersion spectrometer Oxford INCA X-max 80 to determine their elemental (X-ray fluorescence spectral analysis – XSA; random error below 5 %) and disperse compositions (scanning electron microscopy – SEM), as well as by thermogravimetric and thermal analysis methods (synchronous analyzer Netzsch STA 449C Jupiter combined with a mass spectrometer Netzsch QMS 403C Aeolos; the thermograms were recorded over 20 – 900 °C at a heating rate of 10 K/min in air flow of 20 ml/min) and IR spectroscopy (Fourier IR spectrometer Bruker Tensor-27; transmission survey in the 400 – 4000 cm<sup>-1</sup> range in a KBr matrix).

## 3. Results and discussion

When  $\text{H}_2\text{O}_2$  is fed into the reactor, a yellow precipitate is formed (experiments at  $\text{pH} = 4.0$ ) or the  $\text{Fe}(\text{OH})_2$  suspension changes its color ( $\text{pH} \geq 5.5$ ). We note a typical dark-green color of the intermediate samples for suspensions produced at  $\text{pH} 5.5 - 8.5$ , which changes to yellow, orange or brown at the end of oxidation, depending on the temperature and pH. According to [2, 8], in this pH interval corresponding to partial precipitation of iron(II) ions from the solution, an intermediate compound is formed during oxidation, which is known in the literature as “green rust II”. It is this compound which determines the suspension’s color.

The XPA data show that the following nanodisperse phases can be formed in the examined system depending on temperature and pH: iron(III) oxyhydroxides of  $\alpha$ ,  $\gamma$  and  $\delta$  modifications and iron(III) oxide  $\gamma\text{-Fe}_2\text{O}_3$ . The phase and disperse compositions of the precipitates,

<sup>1</sup>The time required to attain a preset pH value was less than 3 min.

<sup>2</sup>Hereafter the value of initial temperature  $t$  is indicated.

<sup>3</sup>Non-overlapping reflections of phases with crystallographic indices (hkl):  $\alpha$  -FeOOH – (110);  $\gamma$  -FeOOH – (120);  $\delta$  -FeOOH – (101);  $\gamma\text{-Fe}_2\text{O}_3$  – (220) were chosen as analytical reflections.

TABLE 1. Phase composition and grain dimension of precipitates as a function of temperature and pH in the system  $\text{FeSO}_4 - \text{H}_2\text{O} - \text{KOH} - \text{H}_2\text{O}_2$ 

pH	Temperature $t$ , °C							
	20		40		60		85	
4.0	$\alpha(100)$ 9		$\alpha(100)$ 12		$\alpha(100)$ 19		$\alpha(100)$ 40	
5.5	$\alpha(40) + \gamma(60)$ 8 7	$\alpha(80) + \gamma(20)$ 12 9		$\alpha(95) + \gamma(5)$ 18 12		$\alpha(5) + \gamma^*(95)$ – 23		
6.5	$\alpha(50) + \gamma(50)$ 8 7	$\alpha(100)$ 10		$\alpha(40) + \gamma^*(60)$ 12 20		$\gamma^*(100)$ 27		
8.5	$\alpha(80) + \gamma(20)$ 9 10	$\gamma^*(100)$ 20		$\gamma^*(100)$ 23		$\gamma^*(100)$ 30		
10.5	$\alpha(10) + \gamma^*(90)$ 10 20	$\gamma^*(100)$ 23		$\gamma^*(100)$ 25		$\gamma^*(100)$ 40		
13.0	$\delta(100)$ 8	$\alpha(40) + \delta(60)$ 10 10		$\alpha(40) + \delta(60)$ 15 16		$\alpha(45) + \gamma^*(45) + \delta(10)$ 15 50 –		

1.  $\alpha$  – phase  $\alpha\text{-FeOOH}$ ;  $\gamma$  – phase  $\gamma\text{-FeOOH}$ ;  $\delta$  – phase  $\delta\text{-FeOOH}$ ;  $\gamma^*$  – phase  $\gamma\text{-Fe}_2\text{O}_3$ .
2. In the parentheses are depicted mass % of the phase, the numbers under the parentheses mean crystal size, calculated from the X-ray diffraction data, nm.

as functions of oxidation parameters, are presented in Table 1 and Fig. 1, in which the regions of formation of these phases are demonstrated in temperature – coordinates. From Fig. 1, it follows that  $\alpha\text{-FeOOH}$  is formed over the whole considered pH interval;  $\gamma\text{-FeOOH}$  – at  $5.5 \leq \text{pH} < 9.0$ ;  $\delta\text{-FeOOH}$  – at  $\text{pH} \geq 10.5$ ; and  $\gamma\text{-Fe}_2\text{O}_3$  – at  $5.5 - 13.0$ . When the temperature is raised, the pH range in which these phases are formed expand for  $\gamma\text{-Fe}_2\text{O}_3$  and  $\alpha\text{-FeOOH}$  and narrow for  $\gamma$ - and  $\delta\text{-FeOOH}$ . With increased temperature, the reflection half-width  $\Delta 2\theta$  of the corresponding phases decreases, which is indicative of an increase in the average size  $d$  of their crystals (Fig. 2).

It follows from the SEM results that each of the synthesized phases has a characteristic crystal morphology, the average size of which depends on the oxidation parameters. In particular, the  $\gamma\text{-Fe}_2\text{O}_3$  and  $\delta\text{-FeOOH}$  phases have an isometric (nearly-spherical) crystal shape. The  $\alpha$ - and  $\gamma\text{-FeOOH}$  crystals are characterized respectively by needle- and plate-like growth forms. Note that the average crystal size determined from the SEM data agrees reasonably well with X-ray analysis data.

The XSA data show that all the synthesized samples consist mainly of iron and oxygen<sup>4</sup>, however, they also contain much smaller amounts of potassium and sulfur atoms. The relative contents of Fe/O and S/O in the most typical samples are given in Table 1.

The data for the phase and chemical compositions of the samples are confirmed by the results of IR spectroscopic and thermogravimetric studies. In particular, the IR spectrum of sample 1 ( $\alpha\text{-FeOOH}$ ), which is monophasic according to XPA data, contains (Fig. 3, curve a): narrow absorption bands of Fe–O bonds with wave numbers  $\nu$  407, 462 and 631  $\text{cm}^{-1}$ ; vibrations of groups (797 and 893 1787  $\text{cm}^{-1}$ ); deformation vibrations of  $\text{H}_2\text{O}$  (1645  $\text{cm}^{-1}$ ), as well

<sup>4</sup>The employed XSA method allows determining the elements with atomic number  $z \geq 5$ . Therefore it should be assumed that along with the above mentioned elements, the examined samples contain also hydrogen.

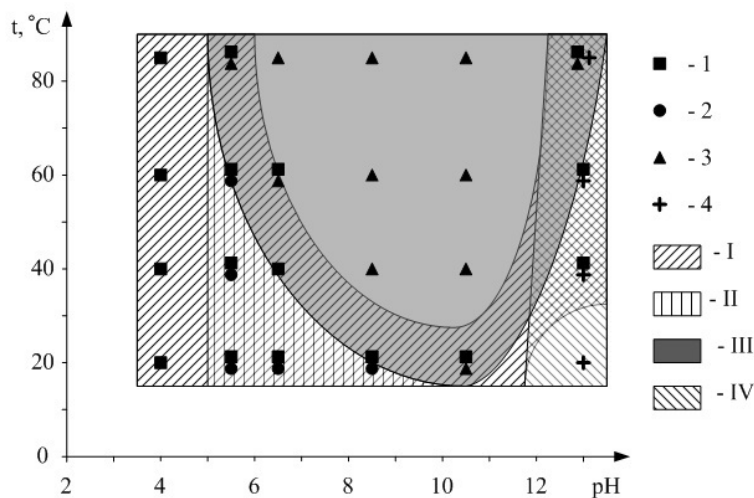


FIG. 1. The phase composition of the precipitate obtained in the system  $\text{FeSO}_4 - \text{H}_2\text{O} - \text{KOH} - \text{H}_2\text{O}_2$  as a function of temperature and pH. Designations of phases contained in the precipitate: 1 –  $\alpha\text{-FeOOH}$ ; 2 –  $\gamma\text{-FeOOH}$ ; 3 –  $\gamma\text{-Fe}_2\text{O}_3$ ; 4 –  $\delta\text{-FeOOH}$ . Phase formation regions: I –  $\alpha\text{-FeOOH}$ ; II –  $\gamma\text{-FeOOH}$ ; III –  $\gamma\text{-Fe}_2\text{O}_3$ ; IV –  $\delta\text{-FeOOH}$ .

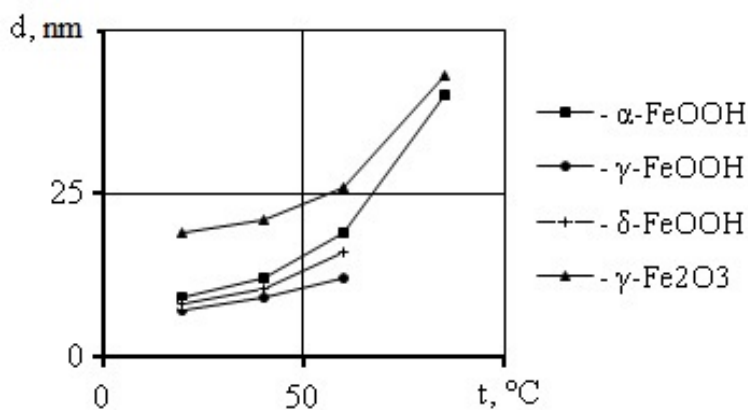


FIG. 2. The average crystal size  $d$  (nm) of phases formed in the system  $\text{FeSO}_4 - \text{KOH} - \text{H}_2\text{O} - \text{H}_2\text{O}_2$  at a fixed pH value as a function of temperature ( $t$ , °C):  $\alpha\text{-FeOOH}$  (pH – 4.0);  $\gamma\text{-FeOOH}$  (pH – 5.5);  $\delta\text{-FeOOH}$  (pH – 13.0);  $\gamma\text{-Fe}_2\text{O}_3$  (pH – 10.5).

as a wide absorption band with a maximum at 3158 stretching vibrations of H–O bonds [13]. Additionally, the spectrum of this sample contains weaker absorption bands with  $\nu$  1053, 1137 and  $1160\text{ cm}^{-1}$ , which can be attributed to the stretching vibrations of  $(\text{SO}_4)^{2-}$  ions [14].

The IR spectra of the binary mixture samples  $\alpha\text{-} + \gamma\text{-FeOOH}$  and  $\alpha\text{-} + \delta\text{-FeOOH}$  (samples 2 and 4, respectively), along with the absorption bands typical of  $\alpha\text{-FeOOH}$ , also contain additional absorption bands (Fig. 3, curves b and c) with wave numbers  $1022\text{ cm}^{-1}$  (sample 2) and  $1050, 1530\text{ cm}^{-1}$  (sample 4). These bands should be attributed to vibrations of groups in  $\gamma\text{-}$  and  $\delta\text{-FeOOH}$ , respectively [15].

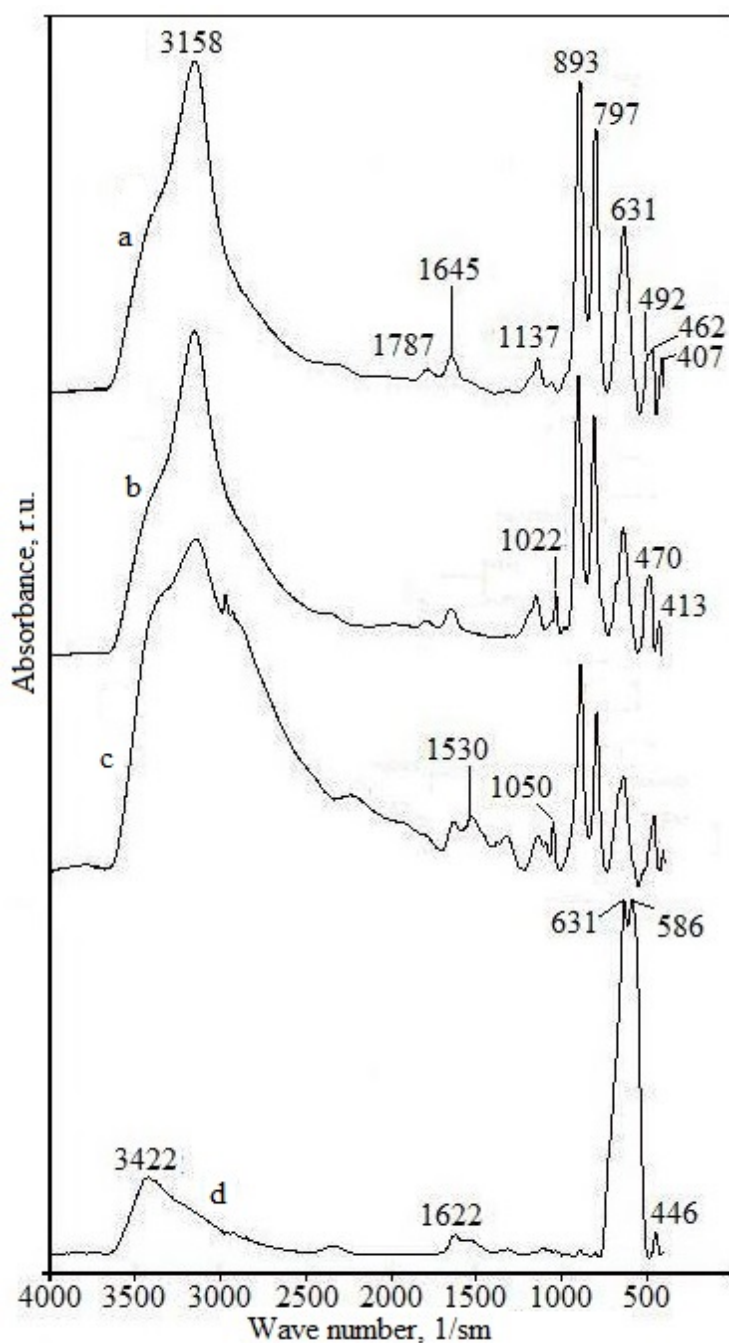
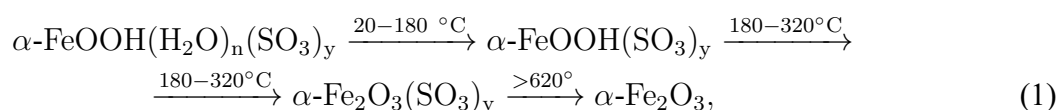


FIG. 3. The IR spectra of samples: a -  $\alpha$ -FeOOH; b -  $\alpha$ - +  $\gamma$ -FeOOH; c -  $\alpha$ - +  $\delta$ -FeOOH; d -  $\gamma$ -Fe<sub>2</sub>O<sub>3</sub>.

The IR spectra of monophase samples of  $\gamma$ -Fe<sub>2</sub>O<sub>3</sub> (Fig. 3, curve d) contain absorption bands of Fe-O bonds with wave numbers 447, 581, 626 cm<sup>-1</sup>, typical of Fe<sub>2</sub>O<sub>3</sub> [16], deformation vibrations of H<sub>2</sub>O (1625 cm<sup>-1</sup>), a broad absorption band with a maximum at 3441 stretching vibrations of H-O bonds and weak absorption bands of stretching vibrations of (SO<sub>4</sub>)<sup>2-</sup> ions.

The thermograms for FeOOH samples are similar in many ways, therefore it is convenient to consider them on the example of thermal transformations of monophase  $\alpha$ -FeOOH (sample 1). According to the TG data (Fig. 4), the relative mass variation in the interval 20 - 900 °C,  $\Delta m_{20-900}/m_0$ , for this sample is 16.49 %. On the differential thermal analysis (DTA)

curves, there are three endothermic effects with maxima at 80, 270 and 750 °C which are accompanied by reduction in mass. Mass-spectrometry studies of the gaseous phase composition revealed (Fig. 4) that the first and the second endothermic effects are due to dehydration and the third effect is caused by the decomposition of sulfate ions. According to the XPA data, at temperatures above 300 °C the  $\alpha$ -FeOOH sample undergoes a transformation into  $\alpha$ -Fe<sub>2</sub>O<sub>3</sub>. From comparison of the obtained findings with the literature data [3, 17], it can be concluded that physically adsorbed water and water of hydration (OH groups) are removed from the sample during the first and second endothermic effects, respectively. Then, the empirical structural formula FeOOH can be represented as FeOOH(H<sub>2</sub>O)<sub>n</sub>(SO<sub>3</sub>)<sub>y</sub> and the thermal transformation of  $\alpha$ -FeOOH during heating occurs as follows:



where  $n$  and  $y$  is the content of adsorbed water and (SO<sub>4</sub>)<sup>2-</sup> ions in the sample expressed in terms of FeO.

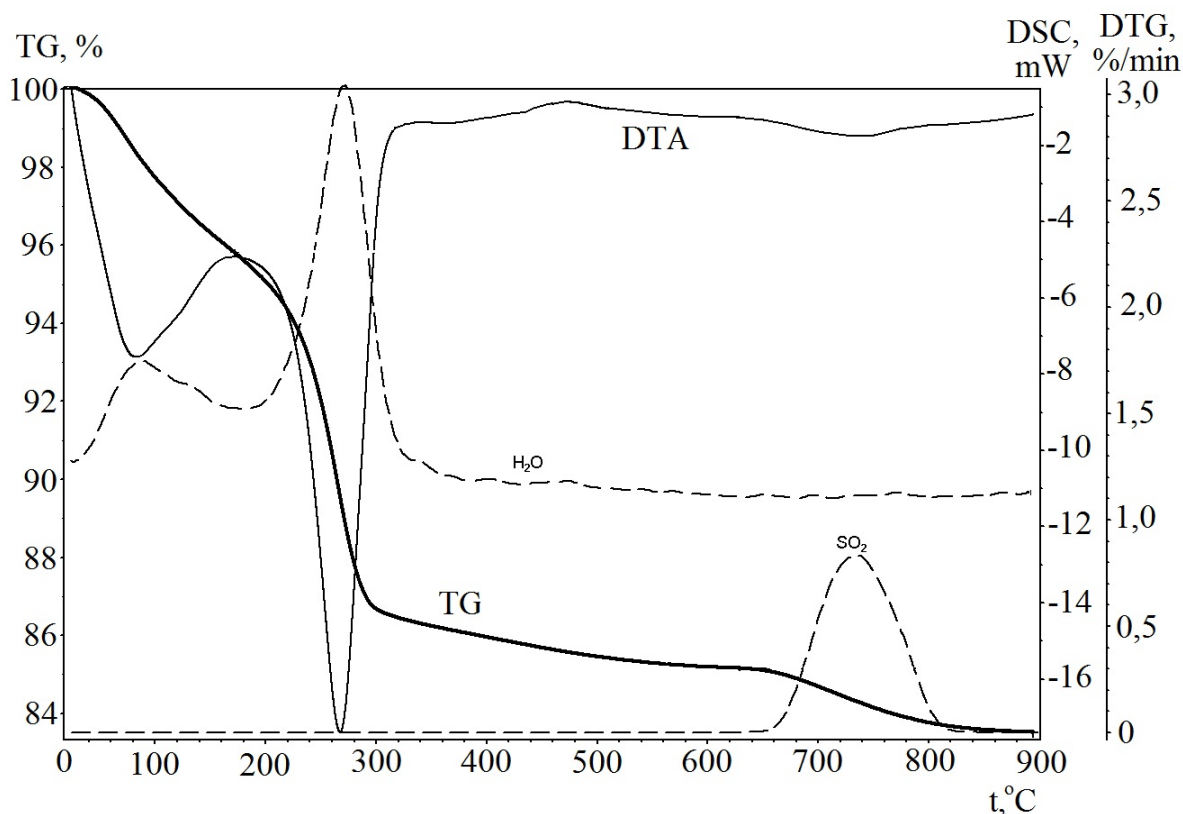


FIG. 4. The data of thermal (TG curve – heavy line, DTA curve – thin line) and mass spectrometric (H<sub>2</sub>O, SO<sub>2</sub> curves – dash lines) analysis of  $\alpha$ -FeOOH sample

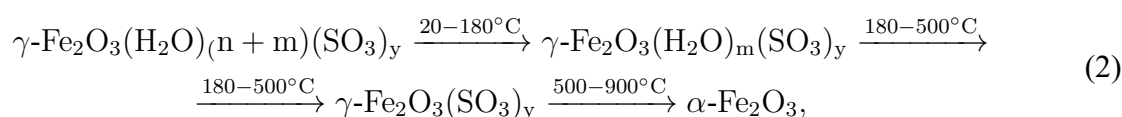
From the TG data on mass variation for FeOOH samples (No. 1–4) at each stage of thermal transformation (Table 2), we calculated the values of  $n$  and  $y$  and, with allowance for the structural formula, the ratios Fe/O and S/O in the initial samples (Table 2). From Table 2, it follows that the data on the chemical composition of FeOOH samples obtained by two independent methods (XSA and TG) coincide within experiment error.

TABLE 2. Phase and chemical composition of the samples

No.	Conditions of synthesis		Phase composition	Chemical composition									
	pH	$t$ , °C		Method PCA		Method TG							
				Fe/O, r.u.	S/O, r.u.	$\Delta m_1/m_0^a$ , r.u.	$\Delta m_2/m_0^b$ , r.u.	$\Delta m_3/m_0^c$ , r.u.	$n$ , r.u.	$m$ , r.u.	$y$ , r.u.	Fe/O <sup>d</sup> , r.u.	S/O, r.u.
1	6.5	40	$\alpha$ -FeOOH <sup>e</sup>	0.47	0.008	0.0474	0.1011	0.0164	0.25	–	0.020	0.49	0.009
2	5.5	40	$\alpha$ - + $\gamma$ -FeOOH	0.47	0.010	0.0444	0.1012	0.0204	0.26	–	0.024	0.48	0.010
3	6.5	20	$\alpha$ - + $\gamma$ -FeOOH	0.46	0.014	0.0738	0.1011	0.0297	0.24	–	0.038	0.47	0.015
4	13.0	40	$\alpha$ - + $\delta$ -FeOOH	0.52	0.001	0.0407	0.1011	–	0.21	–	< 0.001	0.50	–
5	6.5	85	$\gamma$ -Fe <sub>2</sub> O <sub>3</sub> <sup>f</sup>	0.57	0.004	0.021	0.0168	0.0042	0.195	0.156	0.009	0.63	0.003
6	10.5	40	$\gamma$ -Fe <sub>2</sub> O <sub>3</sub>	0.50	0.002	0.0194	0.0155	0.0021	0.179	0.143	0.0044	0.63	0.0015

- a)  $\Delta m_1/m_0$  – relative mass loss of the sample at the temperature (20 – 180 °C, 1<sup>st</sup> end of thermic effect);  
b)  $\Delta m_2/m_0$  – relative mass loss of the sample at the temperature (200 – 500 °C, 2<sup>nd</sup> end of thermic effect);  
c)  $\Delta m_3/m_0$  – relative mass loss of the sample at the temperature 500 – 900°C;  
d) we didn't take into consideration amount of oxygen, participated in the samples in the form of adsorbed water due to total desorption of this form of water molecules in the high vacuum chamber of the PCA analytical installation used.  
e) empirical formula of the  $\alpha$ -,  $\gamma$ -,  $\delta$ -FeOOH contained samples is FeOOH·nH<sub>2</sub>O·SO<sub>3</sub>.  
f) empirical formula of the Fe<sub>2</sub>O<sub>3</sub> contained samples is Fe<sub>2</sub>O<sub>3</sub>·(n + m)H<sub>2</sub>O·ySO.

The DTA curves of monophasic samples of  $\gamma\text{-Fe}_2\text{O}_3$  (Fig. 5) have two endothermic effects with maxima at 80 and 260 °C which are due to removal of physically adsorbed water and water of hydration and are accompanied by mass loss. Also present is a pronounced exothermic effect at 560 °C, occurring without any noticeable variation in the sample mass (the mass reduction from 500 – 900 °C is  $\sim 0.2\%$ ). The XPA data show that the exothermic effect is brought about by the phase transition of  $\gamma\text{-Fe}_2\text{O}_3$  into  $\alpha\text{-Fe}_2\text{O}_3$ . Assuming that the variation of the mass for the  $\text{Fe}_2\text{O}_3$  samples at temperatures above 500 °C, as in the case of  $\text{FeOOH}$ , is caused by the process of desulfation, the structural formula of  $\text{Fe}_2\text{O}_3$  can be represented as  $\text{Fe}_2\text{O}_3(\text{H}_2\text{O})_n(\text{SO}_3)_y$  and its thermal transformation during heating occurs in the following manner:



where  $n$ ,  $m$  and  $y$  are the contents of adsorbed water and water of hydration and  $(\text{SO}_4)^{2-}$  ions in the sample expressed in terms of  $\text{Fe}_2\text{O}_3$ .

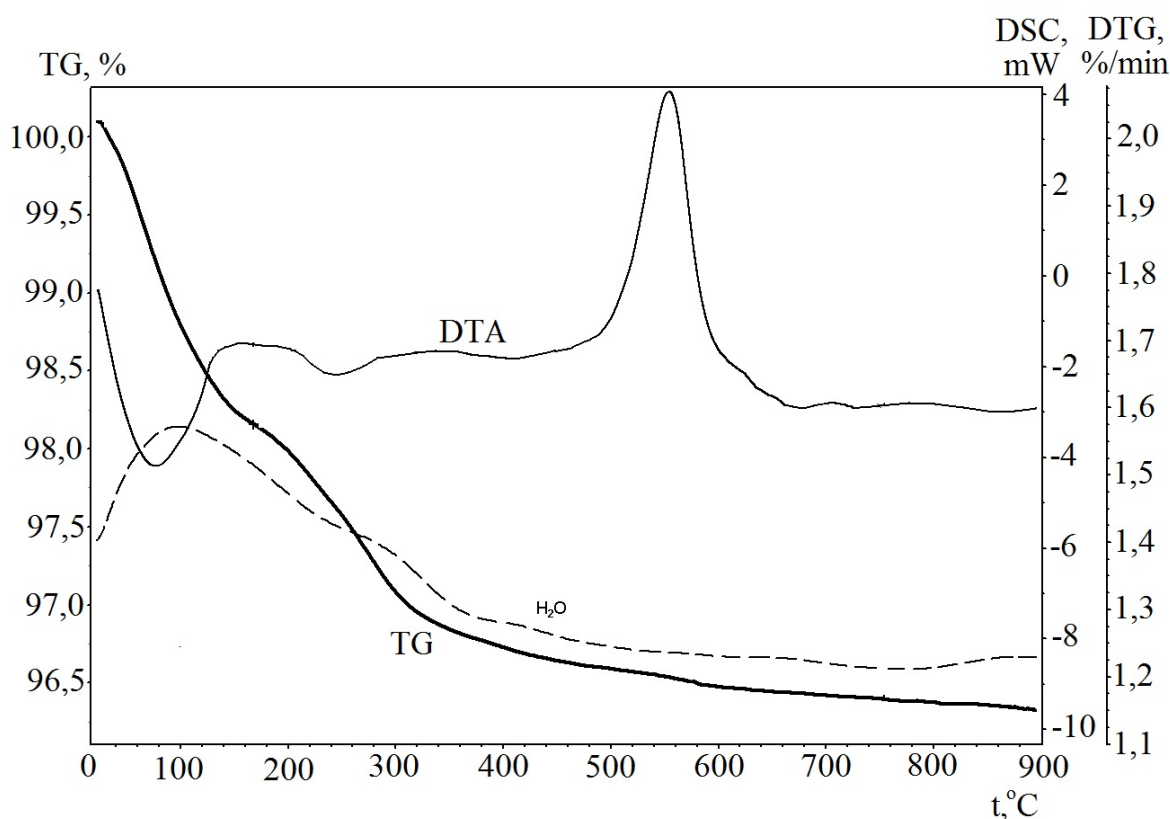


FIG. 5. The data of thermal (TG curve – heavy line, DTA curve – thin line) and mass spectrometric ( $\text{H}_2\text{O}$  curve – dash line) analysis of  $\gamma\text{-Fe}_2\text{O}_3$  sample

As in the case of thermal transformations of  $\text{FeOOH}$ , values for  $m$ ,  $n$  and  $y$  were calculated from the TG data, and the ratios  $\text{Fe}/\text{O}$  and  $\text{S}/\text{O}$  in the initial samples were determined taking into account the structural formula (Table 2). From Table 2, it follows that the XSA method gives a slightly underestimated  $\text{Fe}/\text{O}$  ratio in the  $\gamma\text{-Fe}_2\text{O}_3$  samples as compared to TG analysis.

The established dependence of the phase and disperse compositions of the precipitates formed in the  $\text{FeSO}_4 - \text{H}_2\text{O} - \text{KOH} - \text{H}_2\text{O}_2$  system on the oxidation parameters agrees on the whole with the results obtained from the examination of analogous systems [2, 3, 6–12] and provides evidence that crystal growth during the oxidation of aqueous solutions of iron(II) salts and (or) suspensions of iron(II) hydroxide, especially at low temperatures, takes place under conditions of high supersaturation. As a result, the average size of crystals decreases, their imperfections increase, and phases with disordered crystal structure are formed, in particular,  $\delta\text{-FeOOH}$ . At the same time, it should be noted that our data for  $\gamma\text{-Fe}_2\text{O}_3$  phase formation do not agree with previous results [7, 18] for the formation of the  $\text{Fe}_3\text{O}_4$  phase during the oxidation of  $\text{Fe}(\text{OH})_2$  suspensions by atmospheric air under analogous conditions ( $\text{pH} \approx 9$ ). This contradiction is eliminated if we assume that in our experiments the application of a more active oxidizer ( $\text{H}_2\text{O}_2$ ) originally leads to the formation of the  $\text{Fe}_3\text{O}_4$  phase in a nanodisperse state, which is subsequently oxidized by hydrogen peroxide to  $\gamma\text{-Fe}_2\text{O}_3$  by a topotactical solid-state reaction mechanism. The possibility of  $\text{Fe}_3\text{O}_4 \rightarrow \gamma\text{-Fe}_2\text{O}_3$  transformation occurring in oxygen-containing aqueous media has been reported previously [3, 19].

The synthetic conditions for oxyhydroxide phases in the examined system are characterized by high supersaturation and lead to the formation of nanodisperse primary particles, which, owing to developed specific surface area, are apt to form compact aggregates, whose average size ( $D$ ) increases as  $d$  decreases [3]. In this connection, it is interesting to consider the empirical dependence between the size of primary crystals of new phases and the temperature of synthesis in the framework of the familiar nucleation model [20]. From this dependence, it follows that the relation between the average size of primary crystals  $d$  (nm) of phases formed in the  $\text{FeSO}_4 - \text{KOH} - \text{H}_2\text{O} - \text{H}_2\text{O}_2$  system at a fixed value and temperature (Fig. 2 and Table 1) obeys the Kelvin equation:

$$RT \ln(a/a_0) = 4\gamma\bar{V}/d, \quad (3)$$

in which the average size of primary crystals ( $d$ ) correlates with their relative solubility;  $a$ ,  $a_0$  is the solubility of crystals of size  $d$  under synthetic conditions and of crystals with infinitely large size under equilibrium conditions;  $\gamma$ ,  $\bar{V}$  is the interfacial tension determining the solubility and molar volume of crystal;  $R$  is the universal gaseous constant; and  $T$  is the temperature of formation for crystals of a given size [20]. Then, we transform equation (3) to a form convenient for the analysis of experimental dependences (4) by the least square method:

$$1/d = b[0] + b[1]T, \quad (4)$$

where  $b[0]$  is the empirical constant and  $b[1] = R \ln(a/a_0)/4\gamma\bar{V}$ . It is seen that all the empirical data on the sizes of primary crystals and the synthesis temperature for the  $\text{FeSO}_4 - \text{KOH} - \text{H}_2\text{O} - \text{H}_2\text{O}_2$  system obey equation (4). In Fig. 6, these experimental dependences are represented in the coordinates of equation (4) and are characterized by the correlation coefficient in the range (0.94 – 0.99) and by the Fisher F-criterion parameter for the nucleation model (50 – 120). A peculiar feature of Fig. 6 is a negative value for the parameter  $b[1]$  in eq. (4). This may imply that  $\ln(a/a_0) < 0$  or the relative solubility of primary crystals during synthesis is  $(a/a_0) < 1$ . This dependence contradicts the model of critical nucleus formation both during the condensation of liquid drops from vapor and during primary particle crystallization from aqueous solutions of electrolytes [20] and can be explained by the fact that the majority of primary particles inside the compact aggregates are isolated from the mother solution and do not affect the value of  $a_0$ , while the contribution to the solubility of new phase is made mainly by the small crystals located on the surface of aggregates. Indeed, from Fig. 7, it is seen that the growth of primary crystal sizes and consequently the reduction of the average aggregate size  $D$

results in the disappearance of anomalous relative solubility when the particle size approaches 25 – 35 nm, whereas further increase in the primary particle sizes with the growth of  $d$  may lead to a traditional character of temperature dependence for the relative solubility,  $(a/a_0) > 1$ .

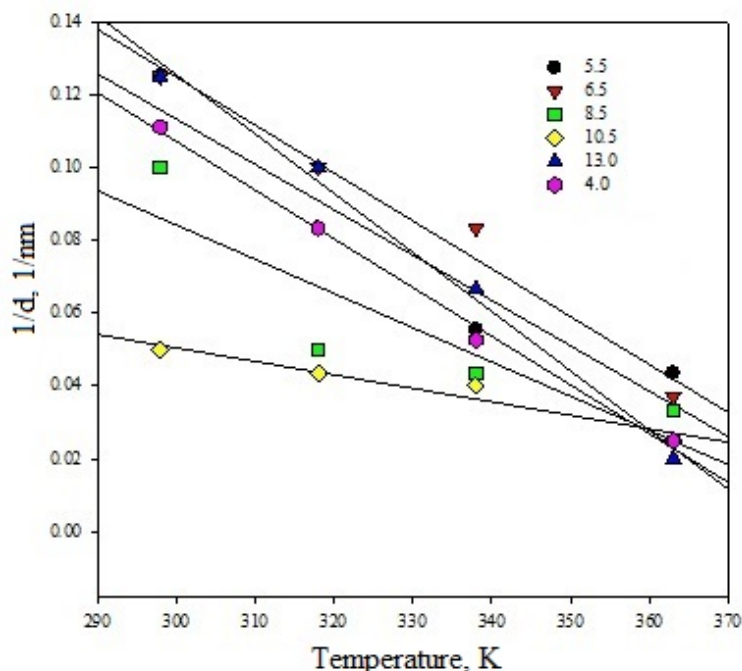


FIG. 6. The average crystal size  $d$  (nm) of phases formed in the system  $\text{FeSO}_4 - \text{KOH} - \text{H}_2\text{O} - \text{H}_2\text{O}_2$  at a fixed pH value as a function of temperature represented in the coordinates of equation (4). Inset: the synthesis pH values are designated by figures.

In conclusion, let us consider the nature of the water of hydration in  $\gamma\text{-Fe}_2\text{O}_3$ . According to [9, 19, 21], the nanodisperse samples of  $\gamma\text{-Fe}_2\text{O}_3$ , as distinct from coarse crystalline ones, have a spinel-type defect structure and regular defects in the cationic sublattice. The structural formula of nanodisperse  $\gamma\text{-Fe}_2\text{O}_3$  is  $\text{Fe}_8\Box_{2.67}\text{Fe}_{13.33}\text{O}_{32}$ , where  $\Box$  is a vacancy in the octahedral cationic positions. In the topochemical oxidation reaction, water molecules of the solution can occupy the vacant positions, forming hydrogen bonds with oxygen anions and thereby stabilize the  $\gamma\text{-Fe}_2\text{O}_3$  lattice. This explains the higher temperatures for removing the water of hydration on the thermograms of  $\gamma\text{-Fe}_2\text{O}_3$  (above 200 °C) as compared to adsorbed water.

#### 4. Conclusion

For wide temperature (20 – 85 °C) and (4.0 – 13.0) intervals of the reaction medium, we have established the regularities for the formation of nanodisperse iron(III) oxide compounds during the oxidation of aqueous  $\text{FeSO}_4$  solutions and (or)  $\text{Fe}(\text{OH})_2$  suspensions by hydrogen peroxide under quasi-stationary conditions with the use of KOH as an alkaline agent. The dependences of the phase, chemical and disperse compositions of the resulting products upon the synthetic conditions have been determined.

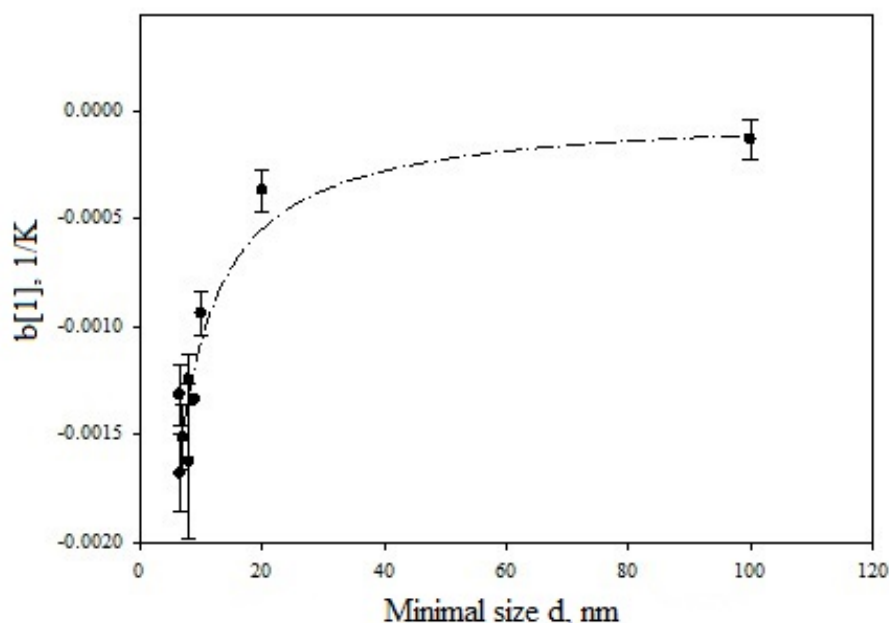


FIG. 7. The variation of the inclination angle  $b[1]$  in the empirical equation (4) as a function of the minimal size of primary crystals registered in each series of experiments at constant pH in the system  $\text{FeSO}_4 - \text{KOH} - \text{H}_2\text{O} - \text{H}_2\text{O}_2$ . The line in the Figure exhibits a tendency towards  $b[1]$  variation with the growth of the size of primary particles.

## References

- [1] Bharat B. *Handbook of Nanotechnology*. Springer-Verlag Heidelberg, Berlin, 2010, 1961 p.
- [2] Cornell R.M. Schwertmann U. *The iron oxides. Structure, properties, reactions, occurrences and uses*. WILEY-VCH Verlag GmbH & Co. KGaA, Weinheim, 2003, 694 p.
- [3] Kleschev D.G., Sheinkman .I., Pletnev R.N. *The effect of medium on the phase and chemical transformations in disperse systems*. UrO AN SSSR, Sverdlovsk, 1990, 248 p. [in Russian]
- [4] Polyakov E.V., Krasilnikov V.N., et al. Synthesis and photocatalytic activity of quasi-one-dimensional (1-D) solid solutions  $\text{Ti}_{1-x}\text{M}_x\text{O}_{2-2x/2}$  (M(III)= Fe(III), Ce(III), Er(III), Tb(III), Eu(III), Nd(III and Sm(III),  $0 \leq x \leq 0.1$ )). *Nanosystems: physics, chemistry, mathematics*, 2014, **5** (4), P. 553–563.
- [5] Mallikarjuna N.N., Manohar S.K., et al. Novel high dielectric constant nanocomposites of polyaniline dispersed with  $\gamma\text{-Fe}_2\text{O}_3$  nanoparticles. *J. Appl. Polym. Sci.*, 2005, **97** (5), P. 1868–1874.
- [6] Feitknecht W. Über die Oxydation von festen Hydroxyverbindungen des Eisens in wabbrigen Losungen. *Zs. Elektrochem*, 1959, **63** (1), P. 34–43.
- [7] Kijama M. Conditions for the formation of  $\text{Fe}_3\text{O}_4$  by the air oxidation of  $\text{Fe}(\text{OH})_2$  suspensions. *Bull. Chem. Soc. Japan.*, 1974, **47** (7), P. 1646–1650.
- [8] Misawa T., Hashimoto K., Shimodaria S. The mechanism of formation of iron oxides and oxihydroxides in aqueous solutions at room temperatures. *Crrsion Sci.*, 1974, **4** (2), P. 131–149.
- [9] Datta N.C. Chemistry of iron(III) oxides and oxyhydroxide. *J. Sci. Industr. Res.*, 1981, **40** (9), P. 571–583.
- [10] Kijama M., Takada T. Iron compounds formed by the aerial oxidation of ferrous salt solutions. *Bull. Chem. Soc. Japan.*, 1972, **45** (10), P. 1923–1924.
- [11] Tolchev A.V., Kleschev D.G., Bagautdinova R.R., Pervushin V.Yu. Temperature and pH effect on composition precipitate formed in  $\text{FeSO}_4 - \text{H}_2\text{O} - \text{H}^+/\text{OH}^- - \text{H}_2\text{O}_2$  system. *Mat. Chem. Phys.*, 2002, **74** (1), P. 336–339.
- [12] Inouye K. What is Iron Oxyhydroxide. *Kagaku to Kogyo*, 1974, **27** (8), P. 571–578.
- [13] Weckler B., Lutz H.D. Lattice vibration spectra. Part XCV. Infrared spectroscopic studies on the iron oxide hydroxides goethite ( $\alpha$ ), akaganeite ( $\beta$ ), lepidocrocite ( $\gamma$ ), and feroxyhite ( $\delta$ ). *Eur. J. Solid State Inorg. Chem.*, 1998, **35** (8–9), P. 531–544.

- [14] Nakamoto K. *Infrared and Raman Spectra of Inorganic and Coordination Compounds*. Sixth edition. WILEY: A John Wiley & Sons, Inc., Publication. Hoboken, New Jersey. 2009, 427 p.
- [15] Weckler B., Lutz H.D. IR spectroscopic studies on iron oxide hydroxides. *Eur. J. Solid state Inorg. Chem.*, 1998, **35**, P. 531–544.
- [16] Sidhu P.S. Transformation of trace element-substituted maghemite to hematite. *Clays and Clay Minerals*, 1988, **36** (1), P. 31–38.
- [17] Koga N., Takamoto Sh., Okada S., Tanaka H. A kinetic study of the thermal decomposition of iron(III) hydroxide oxides. Part 1.  $\alpha$ -FeOOH in banded iron formatins. *Thermochimica Acta*, 1995, **254** (1), P. 193–206.
- [18] Kleshcheva R.R., Kleshchev D.G., et al. The effect of synthesis parameters on the phase formation in the system  $\text{FeSO}_4 - \text{H}_2\text{O} - \text{H}^+/\text{OH}^- - \text{O}_2$  ( $3.5 \leq \text{pH} \leq 13$ ). *Russian Journal of Applied Chemistry*, 2003, **76** (9), P. 1379–1383.
- [19] Gallagher K.S., Feitknecht W., Mannweiler U. Mechanism of oxidation of magnetite to  $\gamma\text{-Fe}_2\text{O}_3$ . *Nature*, 1968, **127** (5134), P. 1118–1121.
- [20] Adamson A.W., Gast A.P. *Physical chemistry of surface*. Sixth edition. A WILEY-INTERSCIENCE PUBLICATION: A John Wiley & Sons, Inc. 1997, 804 p.
- [21] Bernal J.D., Dasgypta D.R., Mackay A.S. The oxides and hydroxides of iron and their structural interrelationships. *Clay miner. Bull.*, 1959, **4** (2), P. 131–149.



# ***NANOSYSTEMS:***

***PHYSICS, CHEMISTRY, MATHEMATICS***

## **Журнал зарегистрирован**

Федеральной службой по надзору в сфере связи, информационных технологий и массовых коммуникаций

(свидетельство ПИ № ФС 77 - 49048 от 22.03.2012 г.)

ISSN 2220-8054

**Учредитель:** федеральное государственное автономное образовательное учреждение высшего образования

«Санкт-Петербургский национальный исследовательский университет информационных технологий, механики и оптики»

**Издатель:** федеральное государственное автономное образовательное учреждение высшего образования

«Санкт-Петербургский национальный исследовательский университет информационных технологий, механики и оптики»

**Отпечатано** в Учреждении «Университетские телекоммуникации»

Адрес: 197101, Санкт-Петербург, Кронверкский пр., 49

## **Подписка на журнал НФХМ**

На первое полугодие 2016 года подписка осуществляется через

ОАО Агентство «Роспечать»

Подписной индекс 57385 в каталоге «Издания органов научно-технической информации»